International Journal of Photoenergy

Energy Storage Technologies and Materials for Solar Energy

Lead Guest Editor: Chuanchang Li
Guest Editors: Zhangxing He, Yi Long, and Hafiz M. Ali

Energy Storage Technologies and Materials for Solar Energy

International Journal of Photoenergy

Energy Storage Technologies and Materials for Solar Energy

Lead Guest Editor: Chuanchang Li
Guest Editors: Zhangxing He, Yi Long, and Hafiz M. Ali

Chief Editor

Academic Editors

Contents

Hindawi
International Journal of Photoenergy
Volume 2020, Article ID 6532820, 13 pages
https://doi.org/10.1155/2020/6532820

Research Article

Effect of Laser Shock Processing and Aluminizing on Microstructure and High-Temperature Creep Properties of 321 Stainless Steel for Solar Thermal Power Generation

Wei Li,[1,2] **Huang Huang**,[1,2] **Dongliang Xu**,[1,2] **Jian Chen**,[1,2] **Lu Zuo**,[1,2] **Guozhi Ma**,[3] **Jianjun He**,[1,2] **Cong Li**,[1,2] **Zhuoyin Peng**,[1,2] **Yanjie Ren**,[1,2] **and Sheng-de Zhang**[4]

[1]*Key Laboratory of Efficient & Clean Energy Utilization, School of Energy and Power Engineering, Changsha University of Science & Technology, Changsha 410114, China*
[2]*Hunan Province 2011 Collaborative Innovation Center of Clean Energy, and Smart Grid, Changsha 410114, China*
[3]*College of Engineering and Designing, Hunan Normal University, Changsha 410006, China*
[4]*Japan Electric Power Central Research Institute, Tokyo 240-0196, Japan*

Correspondence should be addressed to Guozhi Ma; xiagy8520@126.com

Received 6 November 2019; Accepted 1 February 2020; Published 26 February 2020

Academic Editor: Pierluigi Guerriero

The aluminized layer of 321 stainless steel was treated by laser shock processing (LSP). The effects of constituent distribution and microstructure change of the aluminized layer in 321 stainless steel on creep performance at high temperature were investigated. SEM and EDS results reveal that aluminized coating is mainly composed of an Al_2O_3 outer layer, the transition layer of the Fe-Al phase, and the diffusion layer. Additionally, LSP conducted on coating surface not only improves the density of the layer structure, resulting in an increment on the bonding strength of both infiltration layer and substrate, but also leaves higher residual compressive stress in the aluminized layer which improves its creep life effectively. Experimental results indicate that the microhardness of the laser-shocked region is improved strongly by the refined grains and the reconstruction of microstructures. Meanwhile, the roughness and microhardness of aluminized steel are found to increase with the laser impact times. On the other hand, the intermetallic layers, whose microstructure is stable enough to inhibit crack initiation, reinforce strength greatly. The anticreep life of aluminized sample with three times LSP was increased by 232.1% as compared to aluminized steel, which could attribute to the increased dislocation density in the peened sample as well as the decrease of creep voids in size and density.

1. Introduction

To meet increasing global energy demand in an environmentally sustainable manner, greater emphasis is being given to the development and dissemination of renewable energy technologies. Solar energy is an important renewable energy source that is expected to play a significant role in the future energy supply mix. Concentrated solar power (CSP) technology is an important option for acquiring solar energy which draws increasing attention during past several decades [1, 2]. It is internationally believed that for every 1 percentage point increase in the annual average power generation efficiency of solar thermal power generation systems, the average power generation cost will be reduced by 5% to 8%. Therefore, it is vitally significant to improve the power generation efficiency, reduce the cost, and increase service life of the solar thermal power generation system. However, as the key component of CSP, the heat exchange tube should be paid more attention [3–6].

Austenitic stainless steels (ASS) are commonly characterized by favorable ductility and excellent corrosion resistance [7–9]. AISI321, an austenitic stainless steel stabilized with titanium, is a promising material for load-bearing applications in solar thermal power generation, nuclear power reactors, boilers, pressure vessels, expansion bellows, and stack liners [10, 11]. The heat exchange pipes made of AISI321

Table 1: Chemical composition of 321 austenitic stainless steel.

Element	C	Si	Mn	P	S	Cr	Ni	N	Ti
(wt.%)	0.035	0.38	1.08	0.028	0.003	17.02	9.06	0.045	0.22

are prone to have creep damage under long-term high-temperature conditions, coupled with the combined effects of corrosive media and pressure within the pipe, to further accelerate pipeline failure and bursting.

Aluminizing can significantly improve the resistance of stainless steel to high-temperature oxidation, friction, and corrosive medium like atmosphere, hydrogen sulfide, seawater, and liquid metals [12, 13]. Different techniques as chemical vapor deposition (CVD), hot dip aluminizing [14], pack aluminizing [15, 16], electrolytic deposition of Al from ionic liquids [17], and Ar-plasma deposition are applied for depositing Al on the surface of the steel. Among them, the powder pack aluminizing technique is widely used due to its advantages of producing a uniform dense layer on different shapes and sizes of specimens. Ref. [18–21] analyzed the phase composition of the aluminized layer and found the 321 stainless steel with a thicker layer showed a better resistance of oxidation and corrosion. On the other hand, the coating formed with the normal method of application is relatively porous with a multitude of defects and impurities. In particular, the Al_2O_3 film or Fe-Al phase may crack, promoting microcrack propagation at a high temperature and stress, which causes the aluminized steel exhibiting a decrease in the creep life in high temperature. Moreover, the creep behavior of aluminized steel exhibits a higher creep rate and shorter creep rupture life than those of uncoated specimens [22, 23]. Ref. [24] also pointed out that brittle coatings with poor bearing properties were detrimental to the creep properties of the aluminized steel.

Laser shock peening (LSP) is an advanced surface enhancement method for metallic materials to enhance the resistance of creep, fatigue, and corrosion, which can delay the crack nucleation and expansion [25, 26]. In the LSP process, high-amplitude shock waves are generated through rapid expansion of high-temperature plasma induced by the contact between high-power density laser pulse and the material surface. While the shock wave propagates into the material, plastic deformation occurs to a depth where the stress no longer exceeds the elastic limit of the material, which induces residual stresses throughout the affected depth [27, 28]. Yella et al. reported that using an absorbent tape as a sacrificial layer was a good way to perform LSP on the stainless steel and it did not cause surface damage [29]. Vázquez Jiménez et al. pointed out that the best LSP path for extending the high-cycle fatigue life was perpendicular to the rolling direction [30]. Lu et al. found that the treated sample displayed better tensile properties such as stronger flow stress and higher ultimate tensile strength with an increasing LSP impact time [31]. To improve the creep resistance and anti-corrosion performance simultaneously, technology of aluminizing with LSP has been already investigated partially. Lai demonstrated that the fatigue life of material with aluminizing and LSP was increased visibly [32]. Ref. [33–36] also testified that the mechanical property of the aluminized steel was greatly improved by LSP.

In view of the above considerations, many researches mainly focused on the anticorrosion capability, LSP parameters, and the influence on fatigue behaviors. Nevertheless, the studies about high-temperature creep properties of the stainless steel with aluminizing and LSP is rarely reported. Therefore, in order to ensure the stable operation of stainless steel heat exchanger under actual working conditions, the effect of surface modification processes, aluminizing with LSP, on the microstructure and high-temperature creep properties of 321 stainless steel was investigated in this paper.

2. Materials and Methods

2.1. 321 Stainless Steel. The austenitic steel AISI 321 was procured commercially for this investigation. The result of elemental composition analysis is presented in Table 1.

2.2. Powder Pack Aluminizing. The pack powder mixture consisted of 68 wt% Fe-Al powder, 30 wt% Al_2O_3 filler, and 2 wt% NH_4Cl activator. The samples were ground to #2000 grit-sized SiC paper finish and cleaned thoroughly before placing inside the pack, and then, samples were kept inside the pack in an alumina crucible, which was subsequently covered with a lid. Pack aluminizing experiments were carried out in a KSL-1400X box-type sintering furnace, and samples cooled to room temperature after being heated at 950°C for 12 h. The cross-sectional image of the coating layer is shown in Figure 1. The EDS and SEM results indicate that aluminized coating is mainly composed of an Al_2O_3 outer layer, the transition layer of the Fe-Al phase (such as Fe_3Al, FeAl, $FeAl_2$, and a small amount of AlN), and the diffusion layer with the AlFe(Ni) phase and AlCrFe phase. In the case of aluminizing processes, there was a formation of surface layers of a new composition and structure. The formation of such a local transition zone in the form of individual areas or intermetallic compounds directly in aluminizing led to the fact that high-stress microcracks appear in this area and significant local overstresses cause loss of strength of the solid coating system in thermal deformation action on it.

2.3. LSP Treatment. The LSP was performed with the LAMBER-08 pulsed laser which is operating at a 1064 nm wavelength and delivering 7 J pulse energy in 20 ns, with a 2 Hz repetition rate. The diameter of laser spot is 3 mm, the overlapping rate is 50%, and the laser power density is about 4.95 GW/cm^2. In order to protect the surface of the metal material from direct laser burning and couple with the laser energy better, the black adhesive tape is selected as the impact protection layer. The constraining layer is water, to constrain the high-temperature plasma generated by the laser irradiation and increase the shock wave pressure [37].

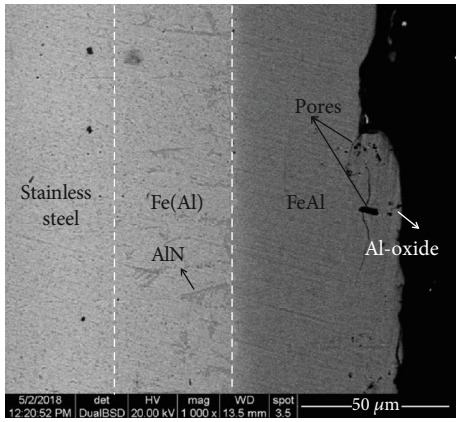

Figure 1: SEM section morphology of the coating layer formed after pack aluminizing at 950° C for 12 h.

2.4. Surface Roughness and Microhardness. A JB-4C precision roughness tester with a 0.8 mm sampling length and a 2 mm/s sensor movement speed was used to measure the surface roughness. 3D surface profiles of samples were observed by the VHX-1000 super-deep 3D microscopic system. The microhardness was tested with a 410MVA Vickers microhardness tester using a load of 300 g and a hold time of 15 s.

2.5. High-Temperature Creep Experiment. Samples treated by different processes, such as aluminizing, aluminizing with single LSP impact, and aluminizing with LSP impacts for three times, were subjected to high-temperature tensile creep tests on a WDML slow tensile tester at the temperature of 620°C and the stress load range of 180-240 MPa. Creep tensile specimens with a gauge length of 24 mm and 4 mm thickness were made.

2.6. XRD and Microstructure. The surface phases of the aluminized steel with different times of LSP impact were analyzed by a TD3000 X-ray diffractometer (XRD). The Quanta 2000 environment scanning electron microscope (SEM) and the attached energy dispersive spectrometer (EDS) were used to examine the creep fracture.

3. Results and Discussion

3.1. Surface Roughness and Microhardness. Surface roughness plays a dominant role in affecting the creep performance and reflecting the collection characteristics of the material surface. Surface roughness is evaluated by three index, including contour arithmetic mean deviation (R_a), contour maximum height (R_z), and contour unit average width (R_{ms}), where R_a can simultaneously reflect the microscopic geometrical features and the height of the convex peak [38]. If these rough peaks are equivalently approximated as microgaps, the stress concentration of the rough peaks can be calculated using the notch stress formula [39]:

$$\sigma = 2k[1 + \ln(1 + m)], \quad (1)$$

Table 2: Surface roughness values of the aluminized steel with different times of LSP impact.

Sample	R_a (μm)	R_z (μm)	R_{ms} (μm)	m (μm)
Aluminizing	0.952	7.174	0.0645	111.2
Aluminizing+single impact	1.856	10.813	0.0930	116.3
Aluminizing+three impacts	3.347	20.718	0.1667	124.3

where k is the material constant and m is the ratio of R_z to R_{ms}. The larger the value of m is, the greater the stress concentration is. Table 2 presents the surface roughness of specimens with different times of LSP impact. As can be seen, the roughness of the aluminized sample is 0.952 μm, and the roughness increases rapidly with the increase of impacts' times. The more the stress concentration is, the easier to generate microcracks, resulting in internal damage of the material. Nevertheless, the roughness is related to the laser absorption, namely, the overly smooth metal surface is not conducive to the absorption of laser [40].

The optical photograph and 3D surface profile for different conditions are shown in Figure 2. It can be seen from Figures 2(a) and 2(d) that the surface of aluminized samples is smooth and flat with regular dimples, and the average pit depth is 7.174 μm. The morphology of the aluminized sample with single LSP impact (Figures 2(b) and 2(e)) displays the existence of obvious pits and steps, whose shapes are square or circle. The shape of the pits depends on the contact pressure between the protective layer and the sample [41]. The average pit depth is 10.813 μm with an increase of 50.7% and the deformation amount is 3.639 μm. The morphology of the sample after three impacts is shown in Figures 2(c) and 2(f). The plastic deformation was aggravated by the plastic loading wave. The depth of the pit is 20.718 μm with an increase of 188.8%, and the deformation amount is 13.544 μm. As the LSP time increases, the roughness and the degree of plastic deformation are alleviated, which attributes to the generation of surface pits predominately. Figure 2(g) is the pulse sequence applied to treat the specimens. It consists of firing pulses in a zigzag-type scanning pattern, covering a total area of 24 × 8 mm in the central zone of the specimens. A laser impact region with a diameter of 1 mm and a depth of 21.5 μm can be observed on the aluminized samples after three LSP impacts, and the plastic deformation is one of the important indexes for evaluating the enhancement effect of LSP.

Figure 3 presents the microhardness of aluminized samples before and after LSP. The microhardness of the aluminized sample gradually increases with increasing distance from the penetrating layer to the surface, which could be imputed to intermetallic compounds formed in the penetrating layer mainly. In addition, the grain grows and the material softening phenomenon occurred during the high-temperature aluminizing process. Therefore, the hardness was found to be lower when the depth of the layer was measured to 180 μm. However, subjected to radial shock waves released by LSP, the surface of the aluminized steel would

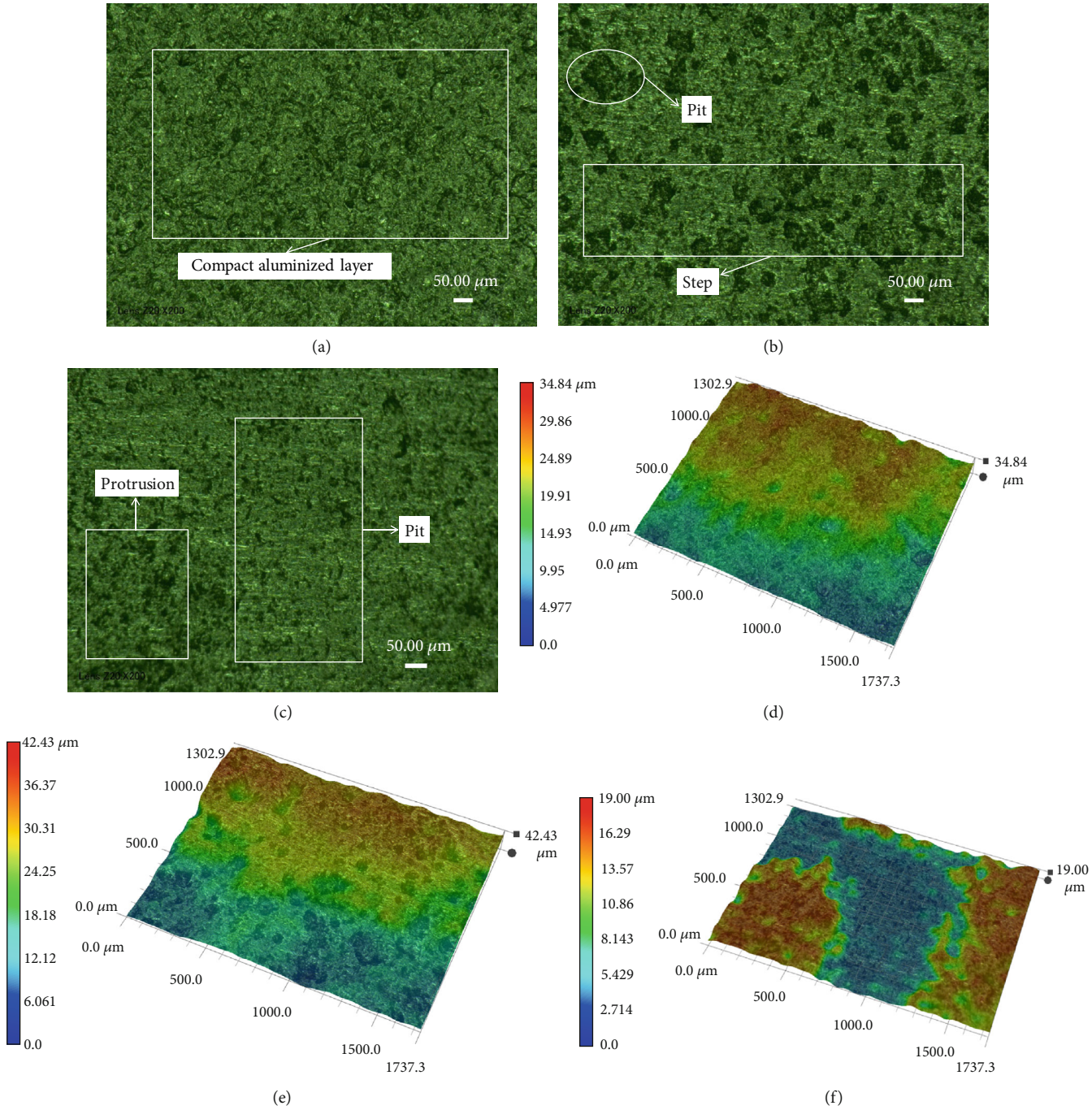

Figure 2: Continued.

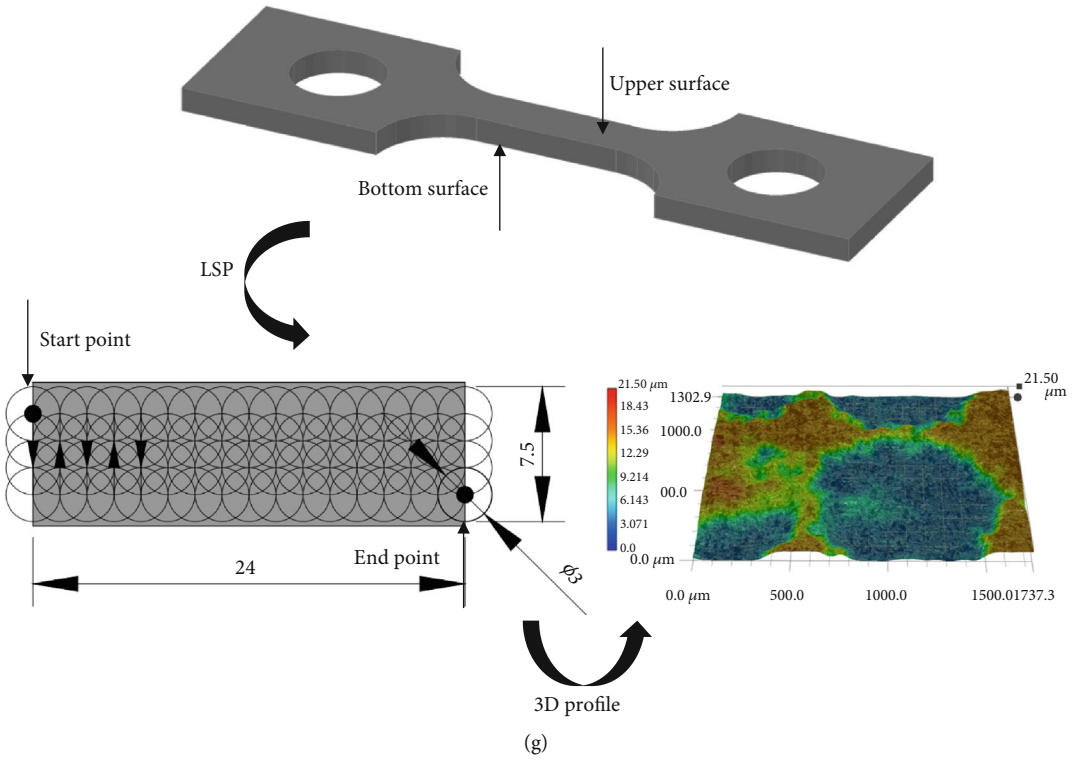

(g)

Figure 2: Optical photograph and corresponding 3D surface profile: (a) optical photograph of aluminized steel; (b) optical photograph of aluminized steel with single LSP impact; (c) optical photograph of aluminized steel with three LSP impacts; (d) 3D surface profile of aluminized steel; (e) 3D surface profile of aluminized steel with single LSP impact; (f) 3D surface profile of aluminized steel with three LSP impacts; and (g) scanning pattern and the enlarged 3D profile of the aluminizing with three LSP impacts sample.

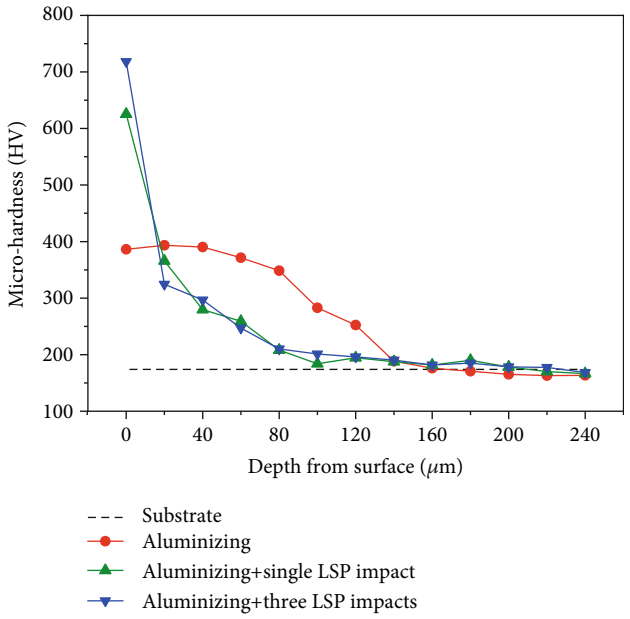

Figure 3: Microhardness variation along the depth of aluminized samples with different times of LSP impact.

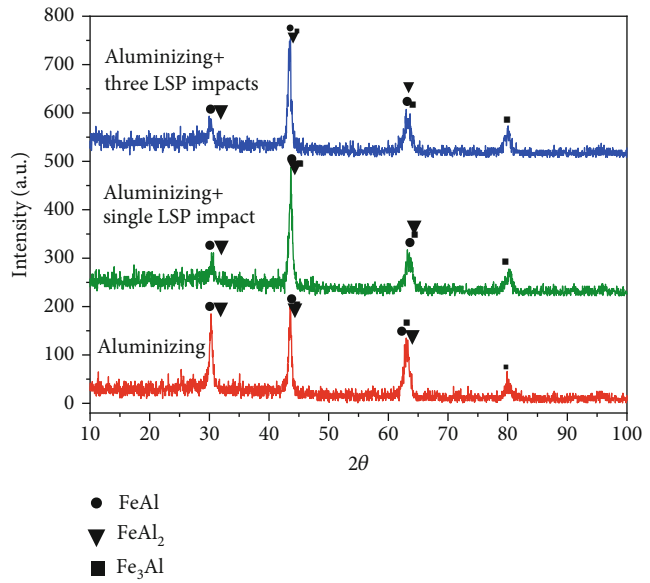

Figure 4: XRD spectra of the aluminized samples with different times of LSP impact.

generate severe plastic deformation, advancing the surface hardness of materials significantly. It is well known that plastic deformation will cause work-hardening effect and grain refinement, thus increases the hardness of the work piece. Similar conclusions have been drawn from Ref. [42, 43]. As the number of impacts increases, the surface microhardness increases from 395 HV of the nonimpacted sample to 625 HV and 718.4 HV. Figure 4 is the XRD pattern of

aluminized samples before and after LSP. There are mainly three phases, FeAl, $FeAl_2$, and Fe_3Al, and none of the new phase is observed after LSP. The position of the crystal surface is hardly changed, while the intensity of the diffraction peak is obviously reduced, and the full-width half maxima (FWHM) become larger. It illustrates that surface grains were refined after LSP, and the grain refinement phenomenon of three-time impact samples was more obvious than single-impact samples, which is consistent with the conclusion of the previous hardness enhancement mechanism.

3.2. Creep Curves. Figure 5 shows the high-temperature creep curves and creep rate curves of the aluminized steels with different times of LSP impact under a series of loading stress. It is observed that all the specimens have similar curve shapes to characterize three stages of typical creep behaviors, namely, the deceleration creep stage, stationary creep stage, and accelerated creep stage. The first stage of creep is shorter while the second stage of creep turns longer. As shown in Figures 5(a) and 5(d), aluminized samples enter the stationary creep stage within 10 h. With the increase of loading stress, the time for samples to enter the steady-state phase is shortened and the creep rate and creep strain increases. When the applied stress reaches 210 MPa, the steady-state creep rate of the aluminized sample rises from 1.05719×10^{-7} to 1.482204×10^{-6} and the creep rupture time degrades from 206 h to 28 h, indicating that the creep resistance of the material was remarkably affected by the stress. The creep curves of aluminized samples with single (Figures 5(b) and 5(e)) and three times (Figures 5(c) and 5(f)) LSP are similar, which implies that the three states of materials were remarkably affected by the external loads. Figure 6 represents the relationship between the applied stress and creep rupture time of the austenitic stainless steel treated with different surface modification processes and all results show that the creep rupture time is inversely correlated to the stress at the creep experimental temperature. At the same time, we found that the steady-state creep rate decreases and creep rupture time extends with the increase of impact times. The steady-state creep rate of specimens with single and three times decreases by an order of magnitude, and their creep rupture lives are increased by 42.8% and 232.1%, respectively, when the applied stress is 210 MPa, which clearly demonstrates that the high-temperature creep resistance of aluminized samples is significantly improved by LSP technology.

In the stationary stage, the effective dislocation density remains unchanged to keep a balance between the material recovering and hardening due to the constant external stress and high-temperature environment. Consequently, the stationary creep rate with the smallest value and the simplest deformation mechanism is the key parameter to reflect the creep behavior of the material. Figure 7 displays that the applied stress is positively relevant to the minimum creep rate of the steady-state creep region. The minimum creep rate and applied stress are well-known to be related by a power law as presented in

$$\dot{\varepsilon} = A_x \sigma^n \exp\left(-\frac{Q_c}{\mathrm{RT}}\right), \tag{2}$$

where $\dot{\varepsilon}$ is the stationary creep strain rate, A_x is a complex constant correlated to the material structure, σ is the applied stress, n is the creep stress index, Q_c is the creep apparent activation energy, R is the molar gas constant ($R = 8.314$ KJ/mol), and T is the absolute temperature. Equation (2) on both sides conducts the logarithmic processing to obtain Equation (3). When the creep temperature T is constant, $\ln\varepsilon$ and $\ln\sigma$ have the linear relationship of slope n (Equation (4)) as follows:

$$\ln \dot{\varepsilon} = \ln A_x + n \ln \sigma - \frac{Q_c}{\mathrm{RT}}, \tag{3}$$

$$n = \left(\frac{\partial \ln \dot{\varepsilon}}{\partial \ln \sigma}\right)_T. \tag{4}$$

Figure 8 exhibits the logarithmic relationship between the steady-state creep rate and the applied stress. It can be concluded that the n values of aluminizing and aluminizing composite single and three-time LSP samples are 13.73, 19.71 and 23.13, respectively. The matrix alloy is 321 austenite stainless steel, and the values 3 and 5 of stress exponent stand for two important creep types of solid solution. When $n \leq 3$, the stress exponent has a typical value of 3, this signifies that the creep behavior is very different from that of a pure metal, which is called the first class of alloy-type creep; when $n = 4 - 7$, its typical value is 5, which indicates that the creep behavior is similar to that of pure metals, which is called the second pure metal creep; when $n \geq 8$, the steady-state creep behavior can no longer be described by power-law equations [44]. Ref. [45] points out that if a metallic had a larger apparent stress exponent, the metal may have a higher creep stress threshold, which can predicate that the aluminizing composite LSP material has a higher creep stress threshold and better creep resistance.

3.3. Fracture Morphology. The creep macroscopic fracture appears the necking phenomenon while the crack-like plastic deformation occurred near the typical ductile fracture. The fracture existence of clear cross-section grains with strong sense of third dimension testifies that it belongs to intergranular fracture. The area shrinkage of impacted specimens is higher than that of nonimpacted specimens, implying that the impacted specimens have a better plasticity. It can be seen from Figure 1 that there are some defects on the coating layer, such as coarse second-phase particles (AlN) and pores. During the high-temperature creep process, the abundant intracrystal cross slips glided to the pore position or grain boundary lattice defects caused by the residual tensile stress, resulting in plenty of micropores. These micropores continued to converge into cracks which caused the expansion and separation of grain boundaries under the tensile stress. According to the SEM morphology of fracture surfaces and the EDS analysis of Figure 9, it can be distinguished that the fracture surface of aluminized steels can be roughly divided into three layers: the outer layer (FeAl), the transition layer (mainly composed of $FeAl_2$ and Fe_3Al), and the

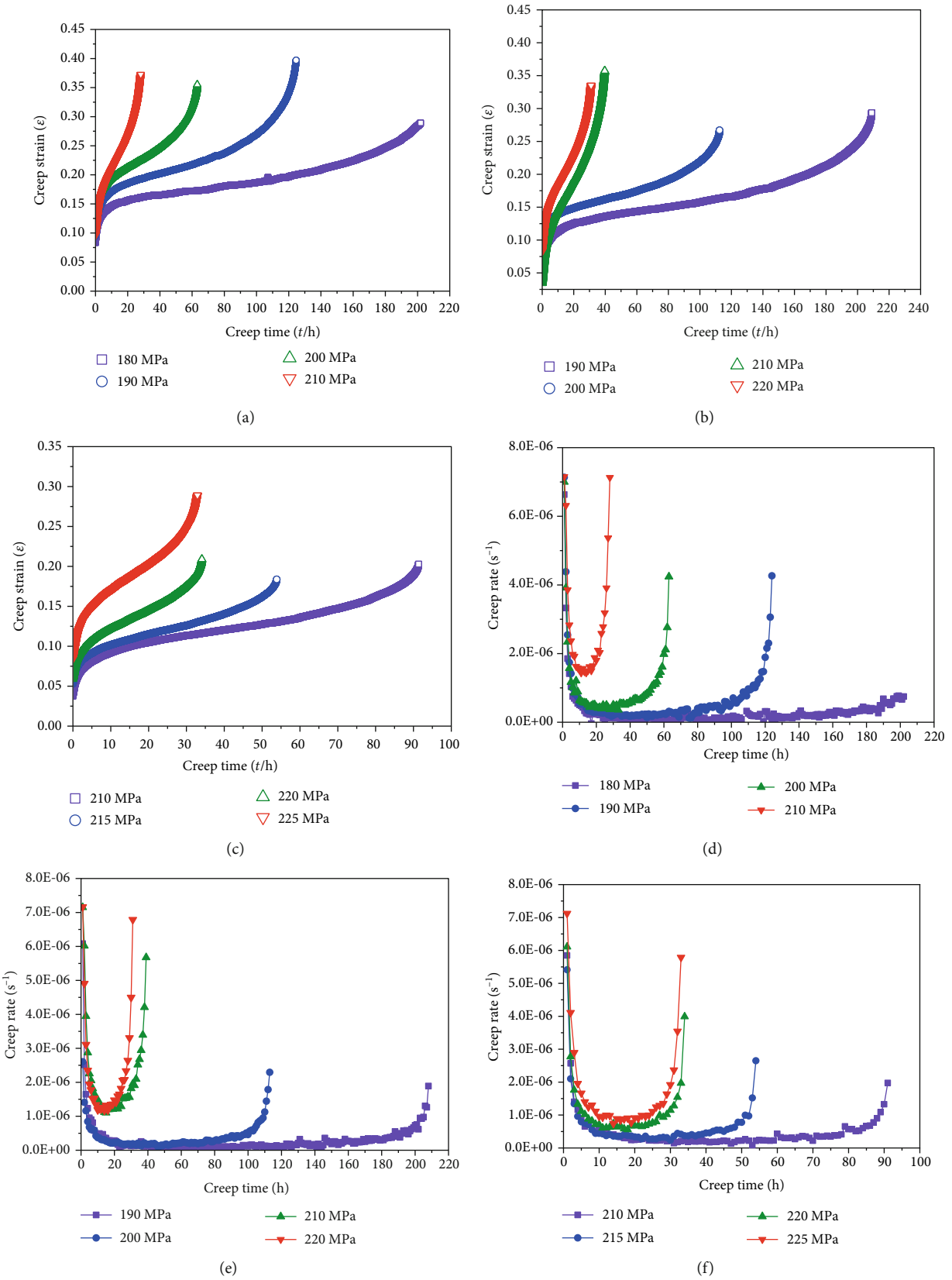

Figure 5: Creep curves and creep rate curves of specimens under different loading stresses: (a) creep curve of aluminized specimen; (b) creep curve of aluminized specimen with single LSP impact; (c) creep curve of aluminized specimen with three LSP impacts; (d) creep rate curve of aluminized specimen; (e) creep rate curve of aluminized specimen with single LSP impact; and (f) creep rate curve of aluminized specimen with three LSP impacts.

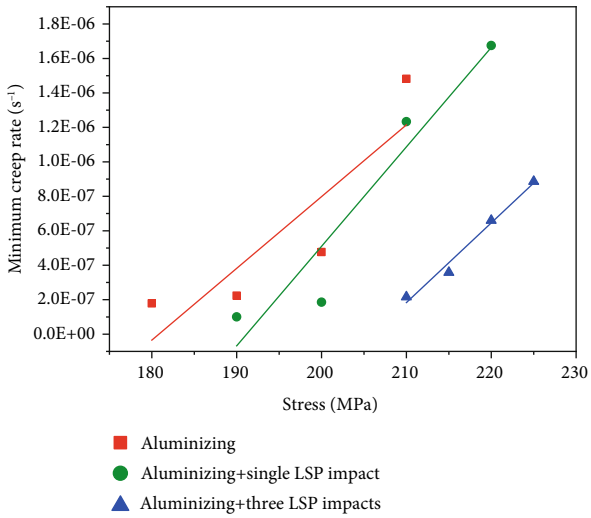

Figure 6: Creep rupture strength of 321 stainless steel treated with different surface modification processes examined at 620° C.

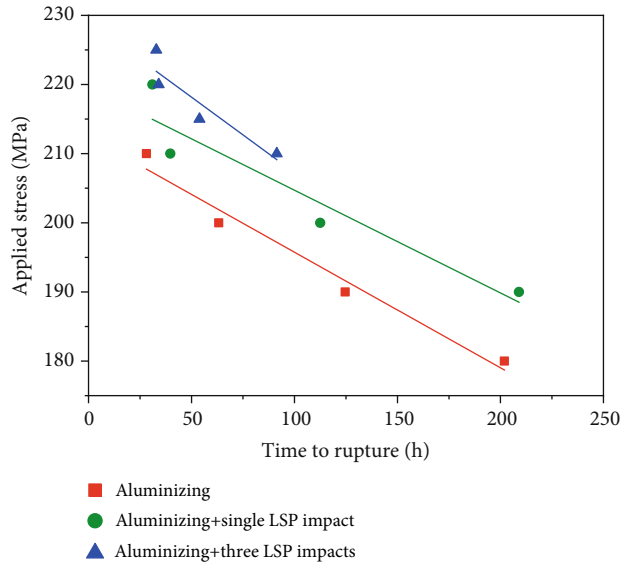

Figure 7: Stress dependence of minimum creep rates for aluminized specimens at different surface modification processes.

austenitic stainless-steel matrix layer. The second phase generated from aluminizing had a large separation tendency from the matrix, which is easily affected by high-temperature environment and the tensile stress. Then, the tendency led to the generation of macropores and eventually fracture. On the one hand, grains of the aluminized layer were refined by the LSP treatment (Figure 9(b)). The rough second phase was evenly distributed on the substrate and the pores' size was narrowed, so that microcracks were difficult to generate. In addition, the laser shock-induced residual compressive stress prevents further creep slips and the separation between crystals. On the other hand, under the impact of high-power lasers, strenuous plastic deformation (Figure 9(c)) accelerates the generation of crystal substructures, changes the direction of grains, and increases the dislocation density. High-density dislocations undergo disorder and discretional slips in all

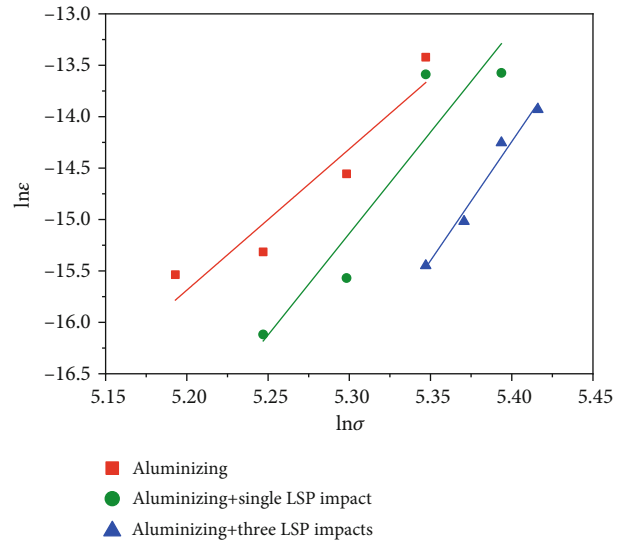

Figure 8: Double logarithmic relationship of creep rate and stress for aluminized specimens at different surface modification processes.

directions at high temperatures to annihilate dislocations with particularly slip orientations. This kind of interaction consumes most time and heat to extend the anticreep life of samples [46]. At the same time, high-density dislocations induce significant differences in orientation amongst grain boundaries, resulting in higher internal stresses impeding dislocations, suppressing grain boundary slippage, and delaying the growth of grains to effectively retard crack initiation [47]. The advance in impact times brings out more obvious grain refinement and plastic deformation; therefore, the creep life of the laser-shocked sample with multiple impacts is vitally improved.

The mechanism of creep damage is the exfoliation, formation, and development of voids followed by the occurrence of failure, which attributes to the plastic deformation incompatibility between intragranular inclusions or second phases and matrix radically. The voids are circular or polygonal, dispersing at the intersection of three grain boundaries or on the grain boundary mainly, where the austenite stainless steel voids preferentially nucleate on the inclined grain boundary [48]. Through connected to one another, some hollows turn into a chain eventually, indicating that the voids formed independently intersect with their growth mutually. In particular, as nucleation centers, inclusion particles are contained in some voids. As can be seen from Figures 10(a) and 10(b), dimples and intergranular cracks are visible in the propagation region. Besides, there are several fracture edges' dimple accumulation, secondary cracks, and parallel stripe structures around. After initiating along grain boundaries, the cracks stretch rapidly and converge into larger cracks during the creep process, leading to the separation among grains. Although creep fractures occur at the grain boundaries predominantly, the creep rupture is influenced by the state, structure, and precipitates of the grain boundary seriously. As described in Figures 10(c) and 10(e), the dimples as well as voids are degraded in size and density with increasing times of LSP impact. Meanwhile, neither rough

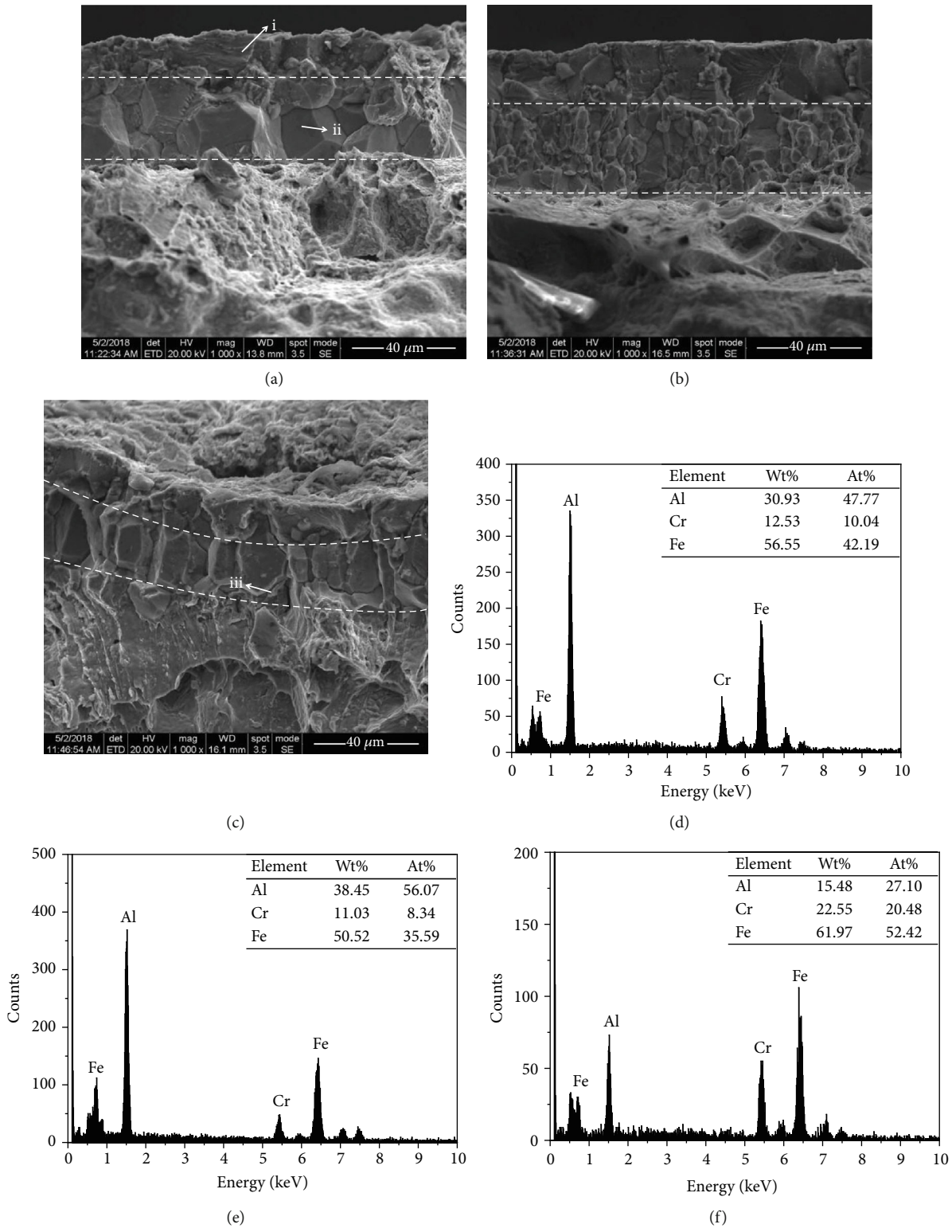

Figure 9: SEM morphology and EDS analysis of fracture surfaces: (a) aluminized steel; (b) aluminized steel with single LSP impact; (c) aluminized steel with three LSP impacts; (d) EDS spectrums of point i in (a); (e) EDS spectrums of point ii in (a); (f) EDS spectrums of point iii in (c).

second-phase particles nor inclusions are observed at magnification (Figures 10(d) and 10(f)). The phenomenon that the fracture toughness of the aluminized steel increases with LSP impacts could be attributed to the rough second-phase particles (or inclusions) with low plasticity, which cannot codeform with the matrix at the same time, resulting in stress

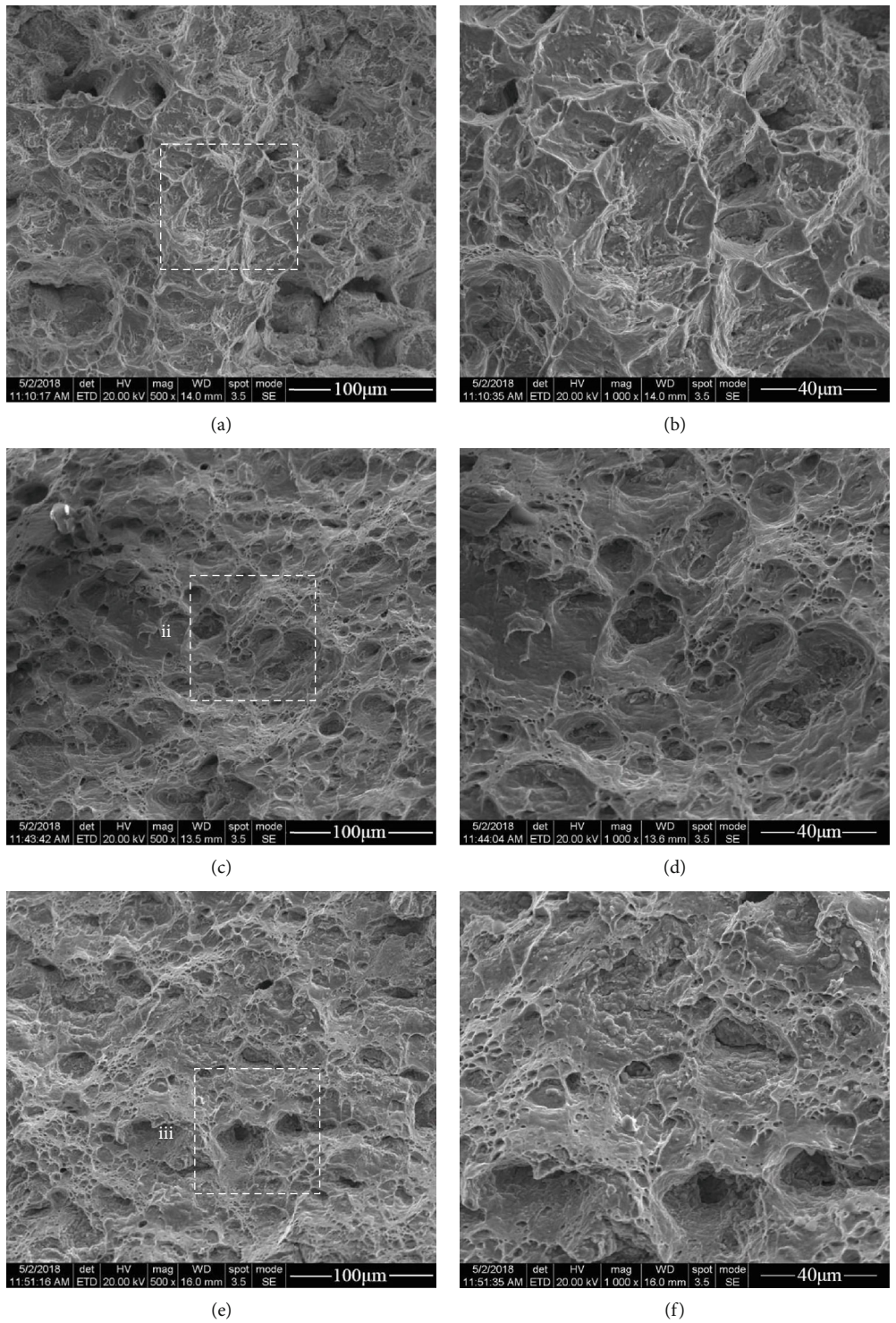

Figure 10: SEM fracture micrographs of the aluminized steel with different impact times of LSP under the stress of 210 MPa: (a) aluminized steel; (b) aluminized steel with single LSP impact; (c) aluminized steel with three LSP impacts; (d) magnification of area i; (e) magnification of area ii; and (f) magnification of area iii.

concentrations around particles to cause breakage. Nevertheless, the grain size of the second-phase particles (or inclusions) in aluminized samples with LSP impacts is significantly refined, and the degree of stress concentration is reduced to enhance the creep resistance. In addition, the austenite stainless steel is subjected to soften during the high-temperature aluminizing process, leading to grain coarsening and plasticity deterioration. But grain refinement increased plasticity after LSP, the plasticity of materials is closely related to creep behaviors. Therefore, the impact of laser on the grain refinement of the aluminized steel is the microscopic reason for the improvement in creep performance.

4. Conclusion

In this study, the effect of laser shock processing and aluminizing on microstructure and high-temperature creep properties of the 321 stainless steel were investigated. The main conclusions are described as follows:

(1) A tightly bounded dense iron-aluminum coating was obtained on the surface of the 321 austenitic stainless steel by powder-embedded aluminizing. The roughness, surface plastic deformation, and surface microhardness of the aluminized specimens were significantly increased after LSP treatment, and the strengthening effect of aluminizing specimens with LSP three times is most obvious

(2) Specimens with different impact times of LSP have similar curve shapes to characterize the three stages of typical creep behaviors. The steady-state creep rate decreased and creep rupture time extended with the increase of impact times, which clearly demonstrates that the high-temperature creep resistance of aluminized samples is significantly improved by LSP technology. The n values of aluminizing and aluminizing composite single and three times LSP samples are 13.73, 19.71, and 23.13 respectively

(3) The dimple size, void size, and density of impacted samples became smaller than those of nonimpacted samples. As the number of LSP increases, the dislocation density and the plasticity of material increase because of the more obvious grain refinement and plastic deformation on the surface, which comprehensively improves the creep performance of the aluminized steel

Data Availability

All data used to support the findings of this study are included within the article.

Disclosure

An earlier version of this paper was partly presented in terms of an invited report at the 25th Congress of International Federation for Heat Treatment and Surface Engineering (http://www.25ifhtse.csp.escience.cn/dct/page/70051).

Conflicts of Interest

The authors declare that there is no conflict of interest regarding the publication of this paper.

Acknowledgments

The authors received financial support from the National Natural Science Foundation of China (No. 51675058 and No. 51801062), the Key Scientific Research Project of the Education Department of Hunan Province (No. 16A002), the Science and Technology Innovation Project of Hunan Province (No. 2018RS3073) and the Hunan Natural Science Foundation (No. 2018JJ3531), and the double first-class scientific research international cooperation project of Changsha University of Science and Technology (No. 2019IC15).

References

[1] S. Mihoub, A. Chermiti, and H. Beltagy, "Methodology of determining the optimum performances of future concentrating solar thermal power plants in Algeria," *Energy*, vol. 122, pp. 801–810, 2017.

[2] S. Kuravi, J. Trahan, D. Y. Goswami, M. M. Rahman, and E. K. Stefanakos, "Thermal energy storage technologies and systems for concentrating solar power plants," *Progress in Energy and Combustion Science*, vol. 39, no. 4, pp. 285–319, 2013.

[3] C. Li, J. Chen, W. Li et al., "Study on the relationship between microstructure and mechanical property in a metastable β titanium alloy," *Journal of Alloys and Compounds*, vol. 627, pp. 222–230, 2015.

[4] C. Li, J. Chen, Y. J. Ren, W. Li, J. J. He, and J. H. Chen, "Effect of solution heat treatment on the stress-induced martensite transformation in two new titanium alloys," *Journal of Alloys and Compounds*, vol. 641, pp. 192–200, 2015.

[5] C. Li, J. Chen, W. Li, Y. J. Ren, J. J. He, and Z. X. Song, "Effect of heat treatment variations on the microstructure evolution and mechanical properties in a β metastable Ti alloy," *Journal of Alloys and Compounds*, vol. 684, no. 5, pp. 466–473, 2016.

[6] W. Li, J. Chen, H. Liang, and C. Li, "Research on high-temperature compression and creep behavior of porous Cu-Ni-Cr alloy for molten carbonate fuel cell anodes," *Materials Science-Poland*, vol. 33, no. 2, pp. 356–362, 2015.

[7] J. Wang, Y. Lin, J. Yan et al., "Influence of time on the microstructure of AISI 321 austenitic stainless steel in salt bath nitriding," *Surface & Coatings Technology*, vol. 206, no. 15, pp. 3399–3404, 2012.

[8] Y. J. Ren, Y. Q. Chen, J. Chen, W. Li, and C. L. Zhang, "Electrochemical impedance studies for intergranular corrosion of super 304H stainless steel," *Materials Performance*, vol. 55, no. 8, pp. 60–63, 2016.

[9] C. Li, J. Chen, W. Li et al., "Investigation on compressive behavior of Cu-35Ni-15Al alloy at high temperatures," *Materials Science-Poland*, vol. 32, no. 3, pp. 341–349, 2014.

[10] K. Guan, X. Xu, H. Xu, and Z. Wang, "Effect of aging at 700 °C on precipitation and toughness of AISI 321 and AISI 347 austenitic stainless steel welds," *Nuclear Engineering and Design*, vol. 235, no. 23, pp. 2485–2494, 2005.

[11] R. K. C. Nkhoma, C. W. Siyasiya, and W. E. Stumpf, "Hot workability of AISI 321 and AISI 304 austenitic stainless steels," *Journal of Alloys and Compounds*, vol. 595, no. 13, pp. 103–112, 2014.

[12] X. Xiang, X. Wang, G. Zhang, T. Tang, and X. Lai, "Preparation technique and alloying effect of aluminide coatings as tritium permeation barriers: a review," *International Journal of Hydrogen Energy*, vol. 40, no. 9, pp. 3697–3707, 2015.

[13] W. Li, J. Chen, J. J. He et al., "Effect of the sic particle orientation anisotropy on the tensile properties of a spray-formed Sicp/Al-Si composite," *Strength of Materials*, vol. 46, no. 2, pp. 221–228, 2014.

[14] K. Singh, A. Fernandes, B. Paul, M. R. Gonal, G. Abraham, and N. Krishnamurthy, "Preparation and investigation of aluminized coating and subsequent heat treatment on 9Cr-1Mo

Grade 91 steel," *Fusion Engineering and Design*, vol. 89, no. 11, pp. 2534–2544, 2014.

[15] M. Mollard, B. Rannou, B. Bouchaud, J. Balmain, G. Bonnet, and F. Pedraza, "Comparative degradation of nickel aluminized by slurry and by pack cementation under isothermal conditions," *Corrosion Science*, vol. 66, no. 1, pp. 118–124, 2013.

[16] S. Guo, Z. B. Wang, L. M. Wang, and K. Lu, "Lower-temperature aluminizing behaviors of a ferritic-martensitic steel processed by means of surface mechanical attrition treatment," *Surface & Coatings Technology*, vol. 258, no. 1, pp. 329–336, 2014.

[17] W. Krauss, J. Konys, and S. E. Wulf, "Corrosion barriers processed by Al electroplating and their resistance against flowing Pb-15.7Li," *Journal of Nuclear Materials*, vol. 455, no. 1–3, pp. 522–526, 2014.

[18] S. Majumdar, B. Paul, V. Kain, and G. K. Dey, "Formation of Al_2O_3/Fe-Al layers on SS 316 surface by pack aluminizing and heat treatment," *Materials Chemistry and Physics*, vol. 190, pp. 31–37, 2017.

[19] S. W. Green and F. H. Stott, "Aluminizing of iron-nickel-base alloys for resistance to high-temperature gaseous environments," *Corrosion Science*, vol. 23, no. 15, pp. 345–359, 1992.

[20] W. J. Cheng and C. J. Wang, "Study of microstructure and phase evolution of hot-dipped aluminide mild steel during high-temperature diffusion using electron backscatter diffraction," *Applied Surface Science*, vol. 257, no. 10, pp. 4663–4668, 2011.

[21] A. R. Rastkar and N. Rezvani, "The effects of processing time on the microstructure and composition of plasma pack-aluminized and -oxidized surface layers on low carbon steel," *Metallurgical and Materials Transactions A*, vol. 46, no. 9, pp. 4132–4142, 2015.

[22] S. Dryepondt, Y. Zhang, and B. A. Pint, "Creep and corrosion testing of aluminide coatings on ferritic-martensitic substrates," *Surface & Coatings Technology*, vol. 201, no. 7, pp. 3880–3884, 2006.

[23] B. L. Bates, Y. Zhang, S. Dryepondt, and B. A. Pint, "Creep behavior of pack cementation aluminide coatings on Grade 91 ferritic- martensitic alloy," *Surface & Coatings Technology*, vol. 240, no. 3, pp. 32–39, 2014.

[24] K. Kakehi, F. H. Latief, and T. Sato, "Influence of primary and secondary orientations on creep rupture behavior of aluminized single crystal Ni-based superalloy," *Materials Science and Engineering A*, vol. 604, no. 604, pp. 148–155, 2014.

[25] J. L. Ocaña, M. Morales, J. J. García-Ballesteros, J. A. Porro, O. García, and C. Molpeceres, "Laser shock microforming of thin metal sheets," *Applied Surface Science*, vol. 255, no. 10, pp. 5633–5636, 2009.

[26] Y. J. Ren, W. Wen, J. Chen, J. L. Chen, W. Qiu, and J. J. He, "Corrosion behaviour of nanochromium coatings deposited by direct current magnetron sputtering," *Surface Engineering*, vol. 32, no. 4, pp. 294–298, 2016.

[27] X. Wu, C. Huang, X. Wang, and H. Song, "A new effective method to estimate the effect of laser shock peening," *International Journal of Impact Engineering*, vol. 38, no. 5, pp. 322–329, 2011.

[28] W. Li, J. Chen, Y. Hu, L. Cong, Y. P. Sun, and J. M. Yang, "Cyclic fatigue fracture behavior of spray-deposited SiCp/Al-Si composite," *Journal of Materials Engineering and Performance*, vol. 23, no. 8, pp. 2871–2876, 2014.

[29] P. Yella, P. Venkateswarlu, R. K. Buddu et al., "Laser shock peening studies on SS316LN plate with various sacrificial layers," *Applied Surface Science*, vol. 435, pp. 271–280, 2018.

[30] C. A. Vázquez Jiménez, G. Gómez Rosas, C. Rubio González, V. Granados Alejo, and S. Hereñú, "Effect of laser shock processing on fatigue life of 2205 duplex stainless steel notched specimens," *Optics Laser Technology*, vol. 97, pp. 308–315, 2017.

[31] J. Z. Lu, J. S. Zhong, K. Y. Luo et al., "Strain rate correspondence of fracture surface features and tensile properties in AISI304 stainless steel under different LSP impact time," *Surface & Coatings Technology*, vol. 221, no. 16, pp. 88–93, 2013.

[32] Z. L. Lai, "Effects of laser shock peening and ultrasonic shot peening on fatigue property of 1Cr11Ni2W2MoV stainless steel," *Laser & Optoelectronics Progress*, vol. 50, no. 5, 2013.

[33] B. P. Fairand and A. H. Clauer, "Laser generation of high-amplitude stress waves in materials," *Journal of Applied Physics*, vol. 50, no. 3, pp. 1497–1502, 1979.

[34] L. Sihai, H. Weifeng, Z. Liucheng, N. Xiangfan, and L. Yinghong, "Aluminizing mechanism on a nickel-based alloy with surface nanostructure produced by laser shock peening and its effect on fatigue strength," *Surface & Coatings Technology*, vol. 342, pp. 29–36, 2018.

[35] W. Li, Y. Ning, J. Chen, Y. Sun, Y. Hu, and J. He, "Investigation on microstructure and fatigue characteristics of spray-formed SiCp/Al-20Si composite," *Transactions of the Indian Institute of Metals*, vol. 68, no. 5, pp. 769–775, 2015.

[36] W. Li, Y. Ning, J. Chen, Y. P. Sun, and C. Li, "Effect of SI content on microstructure and mechanical properties of the spray-formed SiCp/Al-Si composites," *Powder Metallurgy and Metal Ceramics*, vol. 54, no. 5-6, pp. 298–303, 2015.

[37] J. M. Yang, Y. C. Her, N. Han, and A. Clauer, "Laser shock peening on fatigue behavior of 2024-T3 Al alloy with fastener holes and stopholes," *Materials Science and Engineering A*, vol. 298, no. 1-2, pp. 296–299, 2001.

[38] A. L. Wen, S. W. Wang, R. M. Ren, and X. X. Yan, "Effect of combined shot peening process for surface nanocrystallization method on fatigue strength of TC4," *Advanced Materials Research*, vol. 97-101, pp. 2217–2220, 2010.

[39] G. Wang and P. Liaw, *Fatigue and fracture behavior*, Bulk Metallic Glasses Springer US, 2008.

[40] Y. L. Huang, F. H. Yang, G. Y. Liang, and J. Y. Su, "Using in-situ technique to determine laser absorptivity of Al-alloys," *Chinese Journal of Lasers*, vol. 30, no. 5, pp. 449–453, 2003.

[41] F. Z. Dai, J. Z. Lu, Y. K. Zhang, D. P. Wen, X. D. Ren, and J. Z. Zhou, "Surface integrity of micro-dent arrays fabricated by a novel laser shock processing on the surface of ANSI 304 stainless steel," *Vacuum*, vol. 106, no. 5, pp. 69–74, 2014.

[42] Y. Xiong, H. Y. He, K. Y. Luo, G. Zhiqiang, L. Yanjun, and Z. Lingfeng, "Effect of laser shock processing times on microstructure and microhardness of high carbon pearlitic steel," *Chinese Journal of Lasers*, vol. 40, no. 4, 2013.

[43] Z. Ying, F. Bowen, G. Wei, and K. Hui, "Influence of laser shock peening times on microstructure and hardness of TA15 titanium alloy," *Journal of Beijing University of Aeronautics & Astronautics*, vol. 40, no. 4, pp. 444–448, 2014.

[44] M. Pekguleryuz and M. Celikin, "Creep resistance in magnesium alloys," *International Materials Reviews*, vol. 55, no. 4, pp. 197–217, 2010.

[45] J. Tian and Z. Q. Shi, "Creep mechanism and creep constitutive model of aluminum silicate short-fiber- reinforced magnesium matrix composite," *Transactions of Nonferrous Metals Society of China*, vol. 24, no. 3, pp. 632–640, 2014.

[46] W. Li, H. Weifeng, L. Yinghong, W. Cheng, and Y. Zhuojun, "Effects of laser shock processing on vibration fatigue properties of K417 material," *Chinese Journal of Lasers*, vol. 36, no. 8, pp. 2197–2201, 2009.

[47] N. Tao, W. Tong, Z. Wang et al., "Mechanical and wear properties of nanostructured surface layer in iron induced by surface mechanical attrition treatment," *Journal of Materials Science and Technology*, vol. 19, no. 6, pp. 563–566, 2003.

[48] Y. Yang, A. Shan, and D. Lin, "High temperature deformation and fracture of Fe 3Al Ti," *Journal of Shanghai College of Metallurgy*, vol. 20, no. 3, 1999.

Hindawi
International Journal of Photoenergy
Volume 2020, Article ID 4102350, 18 pages
https://doi.org/10.1155/2020/4102350

Research Article

Designing and Optimizing Heat Storage of a Solar-Assisted Ground Source Heat Pump System in China

Yan Gao,[1,2] Zhi Sun,[2] Xinxing Lin,[3] Chuang Wang,[1,2] Zongyu Sun,[4] and Yanhong Chen[5]

[1]*Beijing Advanced Innovation Center for Future Urban Design, Beijing University of Civil Engineering and Architecture, Beijing 100044, China*
[2]*Beijing Key Lab of Heating, Gas Supply, Ventilating and Air Conditioning Engineering, Beijing University of Civil Engineering and Architecture, Beijing 100044, China*
[3]*Key Laboratory of Efficient Utilization of Low and Medium Grade Energy, MOE, Tianjin University, Tianjin 300072, China*
[4]*China Academy of Building Research, Beijing 100013, China*
[5]*Mechanical and Electrical Engineering Institute of Kaifeng University, Kai Feng 475004, China*

Correspondence should be addressed to Chuang Wang; wangchuang@bucea.edu.cn

Received 11 October 2019; Revised 17 November 2019; Accepted 2 December 2019; Published 24 February 2020

Guest Editor: Chuanchang Li

The cold accumulation problem can lead to performance degradation of heat pumps. This paper presents the design and optimization of a solar-assisted storage system to solve this issue. A ground source heat pump (GSHP) project was established using the transient system simulation program (TRNSYS) based on a ground heat exchange theoretical model, which was validated by a previously established experiment in Beijing. The Beijing, Harbin, and Zhengzhou regions were used in numerical simulations to represent three typical cities where buildings require space heating (a cold region, a severe cold region, and a hot summer and cold winter region, respectively). System performance was simulated over periods of ten years. The simulation results showed that the imbalance efficiencies in the Beijing, Harbin, and Zhengzhou regions are 55%, 79%, and 38%, respectively. The annual average soil temperature decreases 7.3°C, 11.0°C, and 5.3°C during ten years of conventional GSHP operation in the Beijing, Harbin, and Zhengzhou regions, respectively. Because of the soil temperature decrease, the minimum heating coefficient of performance (COP) values decrease by 23%, 46%, and 11% over the ten years for GSHP operation in these three regions, respectively. Moreover, the simulation data show that the soil temperature would still be decreasing if based on the previous solar energy area calculation method. Design parameters such as the solar collector size are optimized for the building load and average soil temperature in various cold regions. Long-term operation will test the matching rate of the compensation system with the conventional GSHP system. After the system is optimized, the solar collector area increases of 20% in the Beijing region, 25% in the Harbin region, and 15% in the Zhengzhou region could help to maintain the annual average soil temperature balance. The optimized system could maintain a higher annual average COP because of the steady soil temperature. It provides a method for the design of a solar collector area which needs to be determined in the seasonal heat storage solar ground source heat pump system.

1. Introduction

Compared with outdoor air, the ground retains a relatively stable temperature because of its large heat mass. The ground can be used as a heat source or sink to meet the needs of ground source heat pump (GSHP) systems for heating and cooling of building spaces. In recent years, many GSHP systems have been developed and installed because of their environmentally friendly performance and high efficiency [1]. Ground heat exchangers (GHEs) are an emerging technology, which are an important component of GSHP systems for extracting ground heat during the heating season and

injecting absorbed dwelling heat into the ground during the cooling season [2]. In established GSHP systems, high-performance GHEs result in lower CO_2 emissions and less electrical load on the power grid.

However, under the two main working conditions dominated by heating and cooling, there can be a large gap between the heating and cooling load which the ground self-recovery cannot match [3]. In China, the government has encouraged GSHP systems for conventional heating, ventilation, and air conditioning. Thus, China has become the largest GSHP-system-practicing nation in the world. After several years of continuously increasing sales, the GSHP market share reached 7% of the total central air conditioning market by 2010. However, the market share of GSHP systems has shown a downtrend in recent years and decreased to 2.2% by 2016 [4]. Some GSHP systems installed several years ago have now been decommissioned for not achieving the desired energy savings, especially in typically cold regional cities such as Shenyang in northeast China [5]. When GSHP systems are used in cold regions, more heat is extracted from the ground than is injected back into it. This leads to cold accumulation and long-term decreases in soil temperature. This thermal imbalance over a long-term operation decreases the temperature recovery ability, degrades the heating performance of GSHP systems, and can lead to complete GSHP system failure [6]. Studies indicate that heat injected into the ground and heat extracted from the ground should balance, to preserve the geothermal resource for sustainable utilization as a heat source or sink [7]. To achieve this, studies suggest that partial compensation between winter heating and summer cooling is necessary for a single line or two staggered lines of infinite GHEs, even with a large distance between adjacent GHEs. For a square field of infinite GHEs, near complete compensation of winter and summer loads is necessary [8].

Compensation heat sources such as gas boilers, waste heat sources, and solar collectors can be used to avert this annual energy imbalance and solve this problem in cold regions. To extract less heat from the ground, gas boilers are commonly used during the peak heating load, and the GSHP system provides the remaining heating. Alavy et al. [9] investigated the characteristics of a GSHP system assisted by a gas boiler. A heating load ratio of 60% for the GSHP system and 40% for the gas boiler was found to be the most economical operation and did not lead to any obvious increase in energy consumption.

Another approach of compensating the heat into the ground from another energy source has also been explored. There are two approaches to heat storage: low-temperature storage and high-temperature storage. In the low-temperature heat storage, the heat is mainly used to compensate for the annual heat imbalance or to increase the ground temperature within several degrees K to increase the heat pump COP [10]. High-temperature heat storage is another approach to seasonal heat storage and requires higher input fluid temperature and insulation of a storage medium boundary [11]. Although the ground is rarely used as a high-temperature storage medium, water has proven to be a more effective seasonal heat storage medium. However, if there is no natural reservoir, such a system is more expensive than the ground storage system because of the need for a large tank (usually underground) to store water [12].

Solar energy is the most advantageous renewable energy source. It collects and converts the abundant energy of the sun into available energy. Evacuated tube collectors (and similar devices) convert solar energy into heat energy, which can be applied to the space of residential and commercial buildings or water heating and air conditioning. Hybrid GSHP systems compensate for the ground heat loss by providing additional heat into the soil. Energy storage technology, such as solar energy storage, is commonly applied to store natural underground energy [13]. Solar-assisted GSHPs (SA-GSHPs) installed for a residential building in Tianjin, China (a cold region similar to Beijing), were studied by Wang et al. The system performance during long operating periods was simulated by unit modeling, and its parametric effects were discussed [14]. The experimental results of Bakirci et al. showed that the coefficients of performance (COP) of the heat pump and the overall system were 3.0–3.4 and 2.7–3.0, respectively [15]. The results showed that SA-GSHPs could be used for residential heating in the cold region of Erzurum, Turkey. The study demonstrated that the hybrid GSHP system incorporating solar thermal collectors was feasible for the space conditioning for heating-dominated houses. Rad et al. reported that solar thermal energy storage in the ground could significantly reduce the necessary GHE length [16].

Lazzarin showed that compared with the independent GSHP system, the SA-GSHP system has a shorter length of heat exchanger and a lower investment cost [17]. Macía et al. showed the COP of the heat pump and the efficiency. The design method of the SA-GSHP system is evaluated to generate an analysis model and numerical model [18]. A house with GSHP and a solar seasonal heat storage system was simulated in Harbin, China. This study showed that the vertical ground heat exchanger model has better simulation results than the field data. Therefore, in the heating season, the average soil temperature and inlet and outlet temperature of the vertical surface heat exchanger decreased significantly. In general, the proposed system meets the heating and cooling requirements of buildings [19].

The performance of an SA-GSHP for heating a detached house in Harbin, China, was experimentally studied by Wang et al. The average COPs of the heat pump and overall system were 4.29 and 6.55 for operation in heating mode, respectively [20]. Karagiorgas et al. reported a hybrid system composed of a GSHP system and a solar-assisted GSHP system, along with a simulation model developed in TRNSYS (a transient system simulation tool) for predicting key issues in the design process [21].

Liu et al. carried out experimental research on a GSHP system with thermal energy storage under different loads. The results show that the heating and cooling capacity can be increased by 37.5% and 15.8%, respectively, by integrating heat storage with the GSHP system [22]. The above studies asserted that SA-GSHPs are a promising technology for matching the gap between cooling and heating loads in cold regions, but solutions for GHE heat injection performance

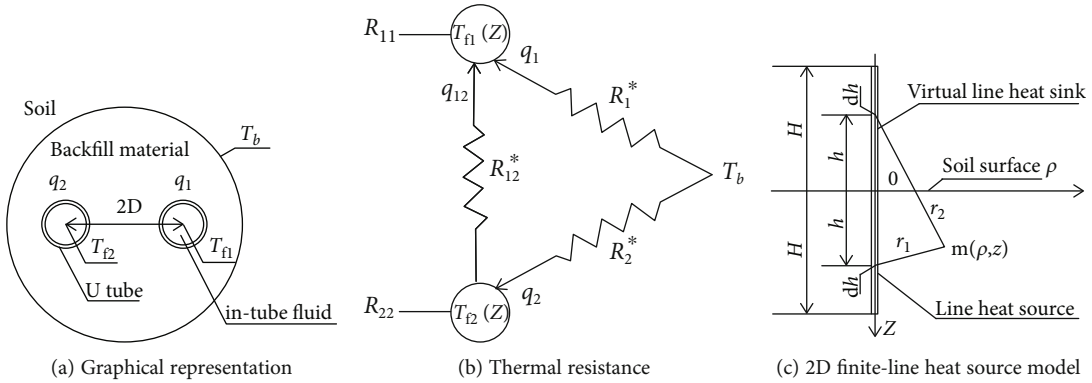

(a) Graphical representation (b) Thermal resistance (c) 2D finite-line heat source model

Figure 1: Heat transfer network of the borehole.

are complex. The thermophysical properties of the ground and the operation of a compensation system are always the determinants of the size of the solar collector and water storage tank system [23].

The thermal transport efficiency of the GHE in the ground plays a vital role in the efficiency of the overall GSHP system, so the operation of GHEs should be examined carefully [24]. To reduce interference on the refrigerating process in summer, the heat storage process is usually applied in autumn. Considering the heat self-recovery in the soil, the sizes of the solar loops are usually optimized based on the results of long-term case studies. Simulation results are analyzed to determine the necessary parameter of the GSHP for storing heat in selected regions. Methods for determining the specific heat storage and heat storage mode are then developed.

A comprehensive review of the relevant literature of SA-GSHP systems shows that a large amount of work has been done in terms of technical feasibility, detailed modeling, and field test experiments with many innovative ideas. It has been shown that the viability of an SA-GSHP system in residential sectors and the demand for heating and cooling are very high. One of the important aspects to be considered in the construction of SA-GSHP is to specify the optimal size of the system. Emmi et al. [25] demonstrated the factors for optimal size of solar hybrid systems and the importance of optimal size in the residential sector.

In this paper, the aim is to confirm whether the system needs specific heat storage and a heat storage mode. Based on the finite-line source model, the performance of GHEs is simulated. The ground thermal performance is studied by injection experiments, and the mathematics model is validated to optimize the energy storage. A simulation of the GSHP system combining solar seasonal energy storage is carried out to predict the long-term ground temperature field variation. The suitability of the systems to three regions in China was simulated. The surface temperature and system efficiency of the regenerative system are compared.

2. Mathematical Modeling of GHEs

Using solar energy for seasonal heat storage can overcome the ground thermal imbalance that occurs over long-term operation. For the long-term simulation of systems that include seasonal solar energy storage in this study, the GHE model needed to connect with other equipment, making the simulation complicated and time-consuming. Analytical methods have advantages in their lower computational expense and higher speed. A typical simulation model involves a composite linear source model to simulate the thermal processes of the borehole and pile. A reasonable prediction can then be made of the thermal behavior of the GHEs [25].

To build a two-dimensional (2D) finite-line source model in cylindrical coordinates, it is practical to determine the equivalent U-tube geometry, as illustrated in Figure 1. Figure 1(a) shows the physical configuration and relative positions of the working fluid, U-tube geometries, concentric grout, and soil. Figure 1(a) also shows the parameters characterizing the heat exchange process, such as the temperature of the borehole wall (T_b), the inlet fluid temperature (T_{f1}), and the outlet fluid temperature (T_{f2}). In Figure 1(b), R_1^* and R_2^* are the equivalent thermal resistances between the fluid of two legs of the U-tube and the borehole wall, respectively. R_{12}^* is the equivalent thermal resistance from the fluid of one leg to another. q_1 and q_2 are the heat transfer rates per unit length from a certain leg to the borehole wall, respectively. q_{12} is the heat rate per unit length pipe between two legs of the U-tube. As shown in Figure 1(c), the classical finite-line heat source model adopted in this study derives an analytical solution for the transient temperature response in a semi-infinite medium. The borehole is treated as a finite-line heat source.

If the thermal interference between the two adjacent legs of the U-tube is not considered, the proposed finite-line heat model can be used to analyze and calculate the heat conduction of the vertical boreholes for their long-term operation in GSHP systems. Therefore, the model is based on typical simplifying assumptions and is commonly utilized to address these types of problems. The specific assumptions are as follows:

(1) The thermal properties of the ground are constant and the soil is assumed to be isotropic

(2) Moisture migration is neglected

(3) The borehole size is neglected, so the borehole can be regarded as a linear heat source

(4) The heat conduction along the borehole axis, including the heat flux through the surface and bottom of the borehole, is neglected to make the heat conduction one-dimensional

(5) There is considered to be no contact thermal resistance between the borehole and the ground

2.1. Heat Transfer Model inside the Borehole. The description of the borehole model consists of the resistances associated with the fluid, pipe, and grout. In accordance with Figure 1, the energy balance equation inside the borehole is given by the following equations:

$$\begin{cases} M_c \dfrac{\partial T_{f1}(Z)}{\partial z} = \dfrac{[T_b - T_{f1}(Z)]}{R_1^*} + \dfrac{[T_{f2}(Z) - T_{f1}(Z)]}{R_{12}^*}, \\ -M_c \dfrac{\partial T_{f1}(Z)}{\partial z} = \dfrac{[T_b - T_{f2}(Z)]}{R_2^*} - \dfrac{[T_{f2}(Z) - T_{f1}(Z)]}{R_{12}^*}, \end{cases} \tag{1}$$

where M_c is the total heat mass of the unit inside the borehole per length. The parameters $R_1{}^*$, $R_2{}^*$, and $R_{12}{}^*$ are expressed as follows [26]:

$$\begin{cases} R_1^* = \dfrac{R_{11}R_{22} - (R_{12})^2}{R_{22} - R_{12}}, \\ R_2^* = \dfrac{R_{11}R_{22} - (R_{12})^2}{R_{11} - R_{12}}, \\ R_{12}^* = \dfrac{R_{11}R_{22} - (R_{12})^2}{R_{12}}, \end{cases} \tag{2}$$

where R_{11} and R_{22} are the thermal resistances between the circulating fluid in a certain U-tube leg and the borehole wall. $R_{11} = R_{22}$ when the U-tube legs are buried in the borehole symmetrically. R_{12} is the resistance between the two individual legs. By analyzing the steady-state conduction problem in the borehole cross-section through the line source, the following relationships can be obtained [27]:

$$\begin{cases} R_{11} = \dfrac{1}{2\pi k_b}\left[\ln\left(\dfrac{r_b}{r_p}\right) + \dfrac{k_b - k}{k_b + k} \cdot \ln\left(\dfrac{r_b^2}{r_b^2 - D^2}\right)\right] + \dfrac{1}{2\pi k_p}\left[\ln\left(\dfrac{r_p}{r_{pi}}\right) + \dfrac{1}{2\pi k_{pi} h}\right], \\ R_{12} = \dfrac{1}{2\pi k_b}\left[\ln\left(\dfrac{r_b}{2D}\right) + \dfrac{k_b - k}{k_b + k} \cdot \ln\left(\dfrac{r_b^2}{r_b^2 + D^2}\right)\right], \\ h = \dfrac{0.023\mathrm{Re}^{0.8}\mathrm{Pr}^n \lambda_f}{d_{pi}}, \end{cases} \tag{3}$$

where r_b is the radius of the borehole; r_p and r_{pi} are the outer and inner radii of the pipe, respectively; k is the conductivity of the grout; k_b is the conductivity of the pipe material; D is the distance between the centers of the pipe and borehole; and h is the convective heat transfer coefficient. Using the method of Diao [28], the inlet and outlet temperatures with time can be obtained as

$$\begin{cases} T_{in}(\tau) = T_b(\tau) + \dfrac{Q}{\varepsilon \dot{m} c}, \\ T_{out}(\tau) = T_{in}(\tau) - \dfrac{Q}{\dot{m} c}, \end{cases} \tag{4}$$

where Q is the total heat transfer rate of the borehole, $\dot{m}$ is the total mass flow rate of the fluid, and the borehole heat transfer efficiency ε and parameter β are expressed as

$$\varepsilon = \frac{(H/M_c\beta)((1/R_1^*) + (1/R_2^*))\mathrm{sh}(\beta)}{\mathrm{ch}(\beta) + (H/2M_c\beta)((1/R_1^*) + (1/R_2^*))\mathrm{sh}(\beta)}, \tag{5}$$

$$\beta = \sqrt{\frac{H^2}{4(M_c)^2}\left(\frac{1}{R_1^*} + \frac{1}{R_2^*}\right)^2 + \frac{H^2}{(M_c)^2 R_{12}^*}\left(\frac{1}{R_1^*} + \frac{1}{R_2^*}\right)}, \tag{6}$$

where $\mathrm{sh}(\beta)$ and $\mathrm{ch}(\beta)$ are the double sine function and double cosine function of parameter β, respectively.

2.2. Heat Transfer Model outside the Borehole. The finite-line source model in this study is based on the solution of the heat conduction exclusively in a homogeneous medium. This problem is solved by using the superposition principle to approximate the borehole as a finite-line source [29]. The model accounts for the influence between boreholes by an intricate superposition of numerical solutions with transient radial-axial heat conduction, one for each borehole. The response to any heat input can be calculated by devolving the heat injected into the ground by a series of step functions. The temperature response (θ) in the ground is then obtained from the sum of the time step responses and calculated by the following equation [30]:

$$\theta(r,z,\tau)=\sum_{i=1}^{n}\frac{q_i-q_{i-1}}{4\lambda\pi}\int_0^H\left\{\frac{\operatorname{erfc}\left(\sqrt{r^2+(z-h)^2}/2\sqrt{\alpha(\tau_n-\tau_{i-1})/h^2}\right)}{\sqrt{r^2+(z-h)^2}}-\frac{\operatorname{erfc}\left(\sqrt{r^2+(z+h)^2}/2\sqrt{\alpha(\tau_n-\tau_{i-1})/h^2}\right)}{\sqrt{r^2+(z+h)^2}}\right\}\mathrm{d}h, \tag{7}$$

where the heat transfer rate per length in extracted or injected heat in time τ_i step is q_i, the radius r and depth z express the position of the aiming point, and α is the thermal diffusion coefficient. The temperature response at the boundary of the borehole (θ_b) is therefore

$$\theta_b=\theta(r_b,z,\tau). \tag{8}$$

The temperature response θ_b presented above is for a single borehole. For the case of multiple boreholes with n GHEs, the total temperature response on the borehole wall or other position of a certain GHE, $\theta_{b,n}$, can be obtained by summing all the temperature responses [31]:

$$\theta_{b,n}=\sum_{j=1}^{n}\theta\left(r_j,z,\tau\right). \tag{9}$$

The advantage of this model is that a spatial superimposition is used to account for the temperature responses for multiple boreholes. In addition, the sequential temporal superimposition is used to calculate the temperature response for any arbitrary heat injection or extraction, which can be decomposed into a set of single pulses. In other words, the overall temperature response of the GHEs to any heat injection or extraction at any time can be determined by the spatial and temporal superimpositions.

3. Experimental System Description and Verification

3.1. Experimental System. An experimental system of GHEs was set up in Beijing, China (altitude 40 m, latitude 39.95°N, longitude 116.35°E). A schematic diagram of the experimental system is shown in Figure 2. The system consists of three components: (1) GHEs, (2) monitoring devices, and (3) thermostatic water bath as a heat source.

The GHE system consisted of four boreholes (Figure 2) that were drilled to an average depth of 70 m. In the vertical heat exchanger, a U-tube of DN32 (nominal diameter) made from high-density polyethylene was buried in the ground, and the boreholes were back filled with grout.

The monitoring system included PT1000 temperature sensors (shown in Figure 3(a)) that were attached to the tube exterior wall at intervals of 10 m in each borehole. Two further temperature sensors were placed to allow the measurement of the GHE inlet fluid temperature T_{in} and outlet fluid temperature T_{out}.

Figures 3(c) and 3(d) show digital photographs of soil samples taken during drilling. The installation of the water separator makes it possible to run each GHE individually or in combination.

Some boreholes were used to test the action of thermal fluids, while others were used to observe the surface temperature of inactive thermal fluids. The working fluid flow rates were measured by a metal tube flowmeter (Figure 4(e)). All measured variables were recorded using an Agilent data acquisition device every ten minutes as shown in Figure 4(f). Before installation of the sensor device, all temperature sensors were calibrated by a constant-temperature water bath with a water temperature accuracy of 0.1°C.

A constant-temperature water bath, which provides a constant inlet temperature for the buried heated tube through insulated pipes, was used as the storage source. This instrument was equipped with an electric water heater and a rotary compressor. The maximum heating and cooling outputs were 9 and 5 kW, respectively. The operating temperature of the water tank and the operation mass flow rate were both measured. The accuracy and measuring range of the sensor used in the experiment are shown in Table 1. To avoid freezing, the fluid was an antifreeze mixture of propylene glycol (20%) and water.

In the heat storage experiment in this study, the surrounding borehole played a monitoring role when some of the GHEs were in action. From the autumn of 2015, a series of heat injection experiments were performed, as shown in Table 2. This study focused on the heat storage performance of GHEs under existing geological conditions, for which the performance of the GHEs is strongly dependent on the real-world situation. The test parameters of the experiment are shown in Table 3.

The recording of experimental data was completed in September 2016. The initial soil temperature was monitored without thermal disturbance from the heat source. The ground temperature profile in July 2015 is shown in Figure 5. The curve shows that the soil temperature was about 16°C and that the soil below 35 m was slightly cooler.

3.2. Verification of the Simulation Result by Comparison with Experimental Data. In the heat storage operation, verification of the simulation result against the experimental data consists of two aspects: the GHE fluid outlet temperature (T) and the soil temperature variation caused by heat injection at different depths. Figure 4 shows the simulation and experimental results during the process of this operation.

In Experiment 1, Borehole 4# is the working GHE and Borehole 2# is used for observation. The two boreholes are spaced by a distance of 2.5 m. The fluid inlet temperature T_{in}, fluid outlet temperatures T_{out} (exp.) and T_{out} (num.),

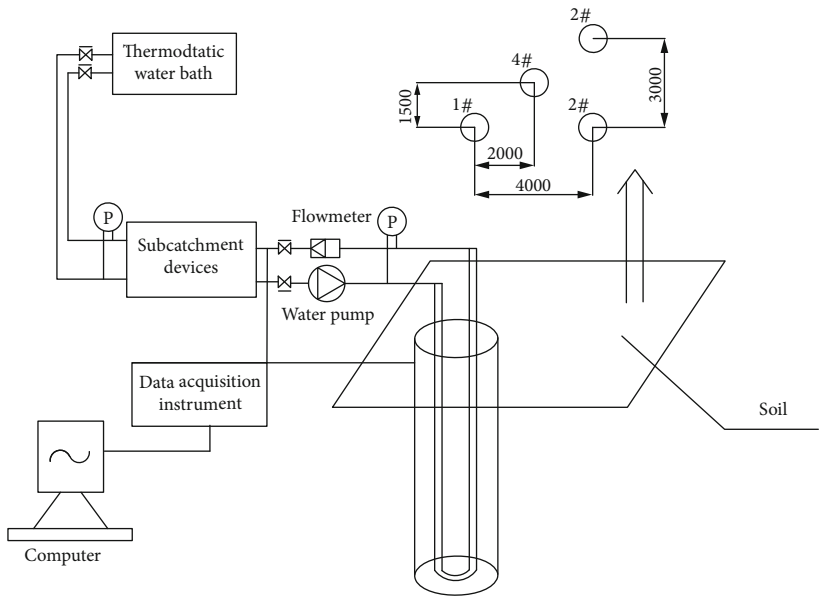

Figure 2: Schematic diagram of the experimental system.

Figure 3: Digital photographs of the soil sampling process.

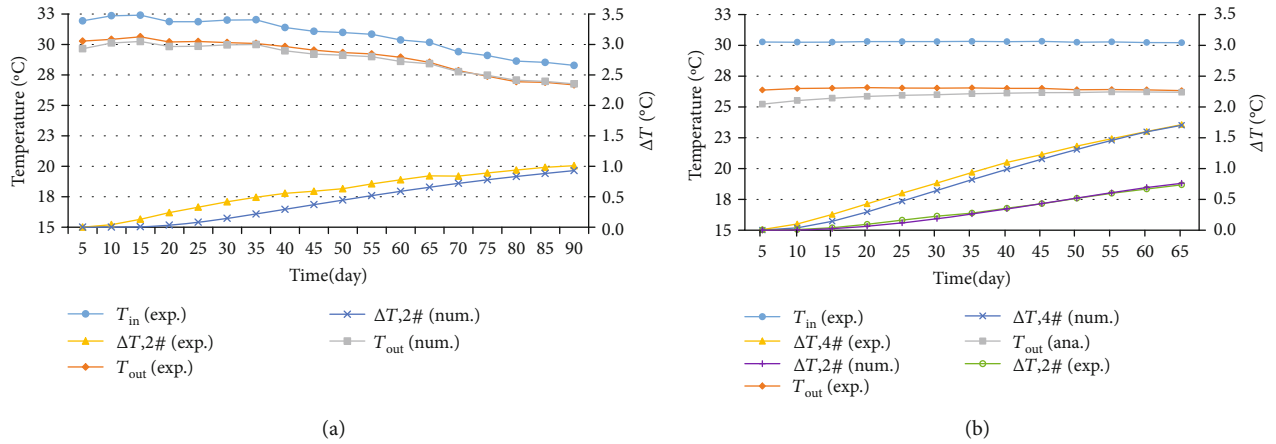

Figure 4: (a) Inlet and outlet temperatures in borehole 2#. (b) Inlet and outlet temperatures in boreholes 2# and 4#.

Table 1: Accuracies and measuring ranges of the sensors in the experimental system.

	Temperature	Volume flow rate
Instrument measuring accuracy	±0.1°C	±0.5%
Measuring range	−100–100°C	1–30 m^3/h

and soil temperature increases ΔT (exp.) and ΔT (num.) for the numerical model and experimental data are shown in Figure 4(a). The absolute error values of the outlet temperatures between the experimental and simulated results are less than 0.6°C. The absolute error values of the 3# borehole temperature increases are less than 0.3°C.

Figure 4(b) shows the validation of the inlet and outlet temperatures from the numerical model against those from the experimental data for the constant input test. Based on the experimental data from this constant input test, the inlet and outlet temperatures of the numerical model were verified.

In Experiment 2, the 1# and 3# boreholes are the working GHEs and the 2# and 4# boreholes are used for soil temperature observation. The inlet temperature T_{in}, outlet temperatures T_{out} (exp.) and T_{out} (num.), and soil temperature increases ΔT,2# (exp.), ΔT,2# (num.), ΔT,4# (exp.), and ΔT,4# (num.) from the numerical model and experimental data are shown in Figure 4(b). The absolute error values of the outlet temperatures are between 0.13°C and 1.15°C. The absolute error values for the 2# borehole and 4# borehole temperatures increase by 0.01°C to 0.13°C and by −0.02°C to 0.04°C, respectively.

The maximum relative percentage error for the soil simulation tests is relatively small, at 4.4% for all verifications. Maximum percentage error of 4.4% could explain the mismatch between the experimental and simulated results. The above discussion demonstrates the effectiveness of the developed model.

4. Case Study

Different combinations of solar-assisted auxiliary heat source and conventional GSHP can lead to different soil temperature properties and system efficiencies. The main objective of this study is to analyze the performance of SA-GSHP systems and to optimize the solar collector size for SA-GSHP systems operating in cold regions. The main components of the SA-GSHP system are the heat pump, borehole heat exchangers, solar collectors, and storage tank. The overall system was dynamically simulated in the TRNSYS software package. The GHEs validated above and experimental data were modeled in MATLAB and linked to the main TRNSYS project. Other components (such as the heat loads, solar thermal collectors, storage tank, weather calculator, valves, pumps, and controllers) were simulated using TRNSYS built-in models. When the location characterized by a cold climate was confirmed, the building load profile was calculated. That load was then used to simulate the plant system, which consists of a GSHP coupled with or without solar thermal collectors. The building and its characteristics were the same for all simulations in each of the three regions. TRNSYS can be used to study each subsystem of the whole power plant in detail and consider the actual coupling and control strategy in a step-by-step manner. The proposed system is shown in Figure 6. The thermal plant system was initially designed by selecting the surface size of the solar thermal collectors, the volume of the storage tank, and the total borehole length.

4.1. Heating Load. The cities of Beijing, Harbin, and Zhengzhou in China are regions in which GSHP systems cause cold accumulation and decreased soil temperature. These three regions are characterized by different climates and were used for analysis [32], which is appropriate because SA-GSHP systems are aimed at meeting building heating loads. The ambient dry-bulb temperature and wet-bulb temperature (i.e., humidity) for these three regions are shown in the left diagrams of Figure 7. The hourly heating and cooling loads for a 2000 m^2 residential building are simulated using the DeST software package, and the results are shown in the right diagrams of Figure 7. Figures 7(a)–7(c) show the peak heating loads for the Beijing, Harbin, and Zhengzhou regions when the building is used for residential heating.

4.2. Heat Pump. The heat pump is connected to the GHEs on the evaporator side and connected to the building on the

Table 2: Experimental conditions.

Experiment no.	Continuous experiment period	Borehole in action	Operation mode	Flow rate (kg/s)	Average inlet temperature (°C)
1	16 Aug. 2015–15 Oct. 2015	#4	Single-U heat injection (storage mode)	0.34	30.3
2	14 Jul. 2016–17 Sep. 2016	#1 and #3	Single-U heat injection (storage mode)	0.34	30.3

Table 3: Experimental parameters of the GHEs.

Parameter	Value
Grout conductivity	1.7 W/(m·K)
Soil conductivity	1.43 W/(m·K)
Pipe conductivity	0.39 W/(m·K)
Soil density	1900 kg/m^3
Soil specific capacity	2.086 kJ/(kg·°C)
Working fluid capacity	3.7 kJ/(kg·°C)
Working fluid density	1027 kg/m^3
Test flow rates	1.224 m^3/h

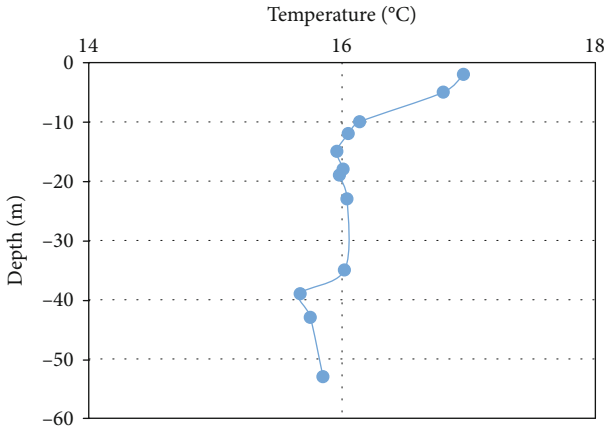

Figure 5: Plot of the initial soil temperature with depth.

condenser side. The type 668 models used a water-to-water heat pump that can operate with any kind of liquid (not necessarily water). Thus, the heat pump can be used as a geothermal heat pump if coupled with a GHE. This component reads an external file prepared by the user, consisting of the load, source temperature, and COP of the heat pump. These data are available from the manufacturer's catalog. Table 4 shows the data file used for the GSHP heating capacity of 44 kW, which can satisfy the peak heating load and peak cooling load. The number of heat pumps in different regions was adjusted according to the maximum load. Specifically, two heat pumps were used in the Beijing region, three were used in the Harbin region, and one was used in the Zhengzhou region.

These values are a function of the source and load temperatures. All the data were processed, and the simulation results show the COP, heating capacity, and return temperature from the evaporator to the storage tank (on the heat source side) for each time step.

In the previous section, the GHE model was validated by comparing simulated results with the experimental data. In the current section, the calculation code implemented in MATLAB was linked to the main TRNSYS project and integrated with the other components. The total length of the GHEs required to meet the heating and cooling loads is the main parameter in the GSHP design process. In typical ground conditions for a borehole heat exchanger, the borehole length is sized for a heat extraction rate (q_{design}) of 50 W/m of borehole length [32]. Consequently, the GHE's total length can be calculated by

$$\begin{cases} L_{\text{heating}} = \dfrac{q_{\text{heating,max}}}{q_{\text{design}}} \times \left(1 - \dfrac{1}{\text{COP}_{\text{heating}}}\right), \\ L_{\text{cooling}} = \dfrac{q_{\text{cooling,max}}}{q_{\text{design}}} \times \left(1 + \dfrac{1}{\text{COP}_{\text{heating}}}\right), \\ L = \text{Max}\langle L_{\text{heating}}, L_{\text{cooling}}\rangle, \end{cases} \tag{10}$$

where $q_{\text{heating,max}}$ and $q_{\text{cooling,max}}$ are the peak heating load and peak cooling load, respectively; $\text{COP}_{\text{heating}}$ and $\text{COP}_{\text{cooling}}$ are the COPs under heating and cooling conditions, respectively; and L_{heating}, L_{cooling} and L are the designed GHE total length under heating conditions, cooling conditions, and the final selected GHE length, respectively. The characteristics of the borehole GHEs and the thermal properties of the ground are summarized in Table 5. The initial soil temperature was set to 16°C, as shown in Figure 5.

4.3. Solar Collectors. The heat from solar radiation was captured by solar thermal collectors installed on the south-facing roof at a 45° slope. The properties of this system are summarized in Table 6. The heat-carrier fluid of the solar thermal collectors is a 50% propylene glycol in water, and its mass flow rate (pump no. 1 in Figure 1(a)) is 1.65 kg/s. The thermal behavior of the solar thermal collectors was simulated by the Type 1c function of the TRNSYS tool, which models the thermal performance of flat-plate solar collectors utilizing the g_0, a_1, and a_2 coefficients, as declared by the manufacturer. The thermal performance of the collector array is determined by the number of modules in series and the characteristics of each module. The effects of off-normal solar incidence radiation are evaluated by incidence angle modifiers which are read from an external data file as a function of the incidence angle. In the simulation, the surface areas of solar collectors in the different

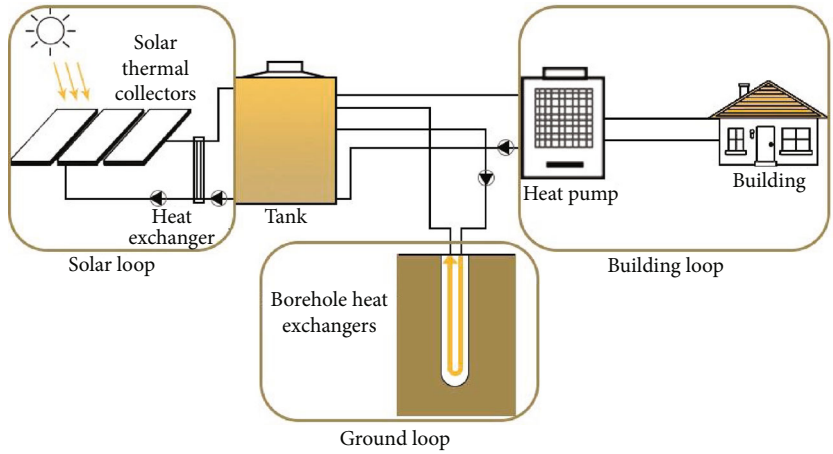

Figure 6: Proposed system involving GSHP and solar thermal collectors.

regions need to be calculated. This is achieved using the following equations:

$$q_{\text{gap}} = q_{\text{heating,total}} \times \left(1 - \frac{1}{\text{COP}_{\text{heating}}}\right) - q_{\text{cooling,total}} \times \left(1 + \frac{1}{\text{COP}_{\text{cooling}}}\right), \tag{11}$$

$$A = \frac{k_c \times f \times q_{\text{gap}}}{90 \times 3600 \times S_y \times U \times \Delta t}, \tag{12}$$

where f is the solar energy guarantee rate (%); k_c is the time-varying coefficient of solar radiation illumination, which is 1.5–1.8 (this benefits the utilization of solar energy but increases the cost); S_y is the local average daily sunshine hours per year (h); U is the heat transfer coefficient of the heat exchanger, which is determined according to the technical parameters of the heat exchanger; A is the heat exchanger area (m^2); and q_{gap} is the average daily heat supply of the solar heating system during the heating season (kW) [26].

4.4. Heat Storage Tank. Heat storage is important in solar systems to compensate for time differences between the availability of the heat source and the availability of the heating demand. A stratified fluid storage tank was considered in the current study. The storage tank was modeled using the TRNSYS software Type 4d function [33], based on the assumption that the tank can be divided into N fully mixed equal subvolumes. The tank is also equipped with a pressure relief valve, to consider boiling effects. The model also considers the energy released by the fluid flowing through the valve, whereas the corresponding loss of mass is neglected. This subroutine simulates a fluid-filled constant-volume storage tank and simulates a cylindrical tank with a vertical configuration. The fluid in the storage tank interacts with the fluid that may exist in the heat exchanger, with the ambient air, and with flow streams that pass into and out of the storage tank [34].

4.5. Control Strategy. In the simulation, the imbalance efficiency need to be calculated. This is achieved using the following equations:

$$\eta_{\text{ie}} = \left| \frac{Q_{\text{heating,total}} - Q_{\text{cooling,total}}}{Q_{\text{heating,total}}} \right|, \tag{13}$$

where η_{ie} is the imbalance efficiency, $Q_{\text{heating,total}}$ is the sum of the energy storage during the ten years, and $Q_{\text{cooling,total}}$ is the sum of the energy absorbed during the ten years.

In this paper, a method for optimization of the area of the solar collector for a seasonal heat storage solar ground source heat pump system is proposed. The specific calculation steps are shown in Figure 8.

The initial solar thermal collector area is first put into the seasonal heat storage SA-GSHP system and it is determined whether the efficiency is less than 1%. If $Q_{\text{heating,total}} < Q_{\text{cooling,total}}$ and the efficiency are greater than 1%, the area will increase by 5%. Otherwise, it should be reduced by 5% to obtain a new solar thermal collector area, and then simulation calculation can be carried out.

Figure 9 shows the control strategy. In the heating season, if the average temperature of the building is lower than 18°C, the heat pump is turned on. When the temperature is higher than 24°C, the heat pump is turned off.

In the cooling season, if the average temperature of the building is lower than 18°C, the heat pump is turned off. When the temperature exceeds 24°C, the heat pump is turned on.

In the nonheating (cooling) season, the heat exchanger of the solar energy system unit is connected with the GHE circuit for heat storage.

5. Simulation Results and Discussion

Based on the model discussed in the previous section, case studies were conducted in Beijing, Harbin, and Zhengzhou. The main purpose of the long-term simulation was to compare the performance of the proposed SA-GSHP combined system with that of the conventional GSHP system.

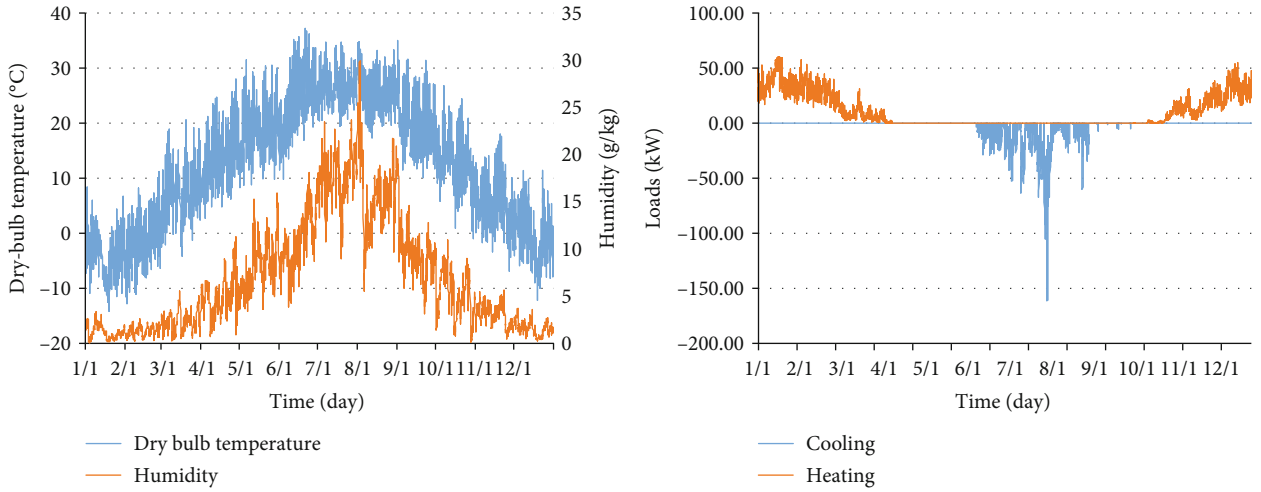

(a) Case 1 (Beijing)

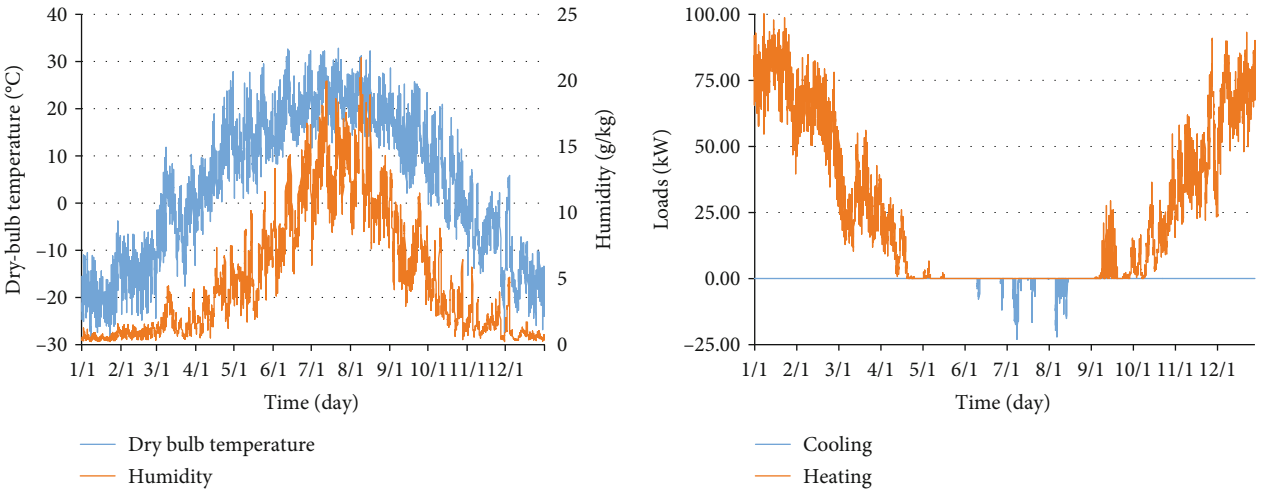

(b) Case 2 (Harbin)

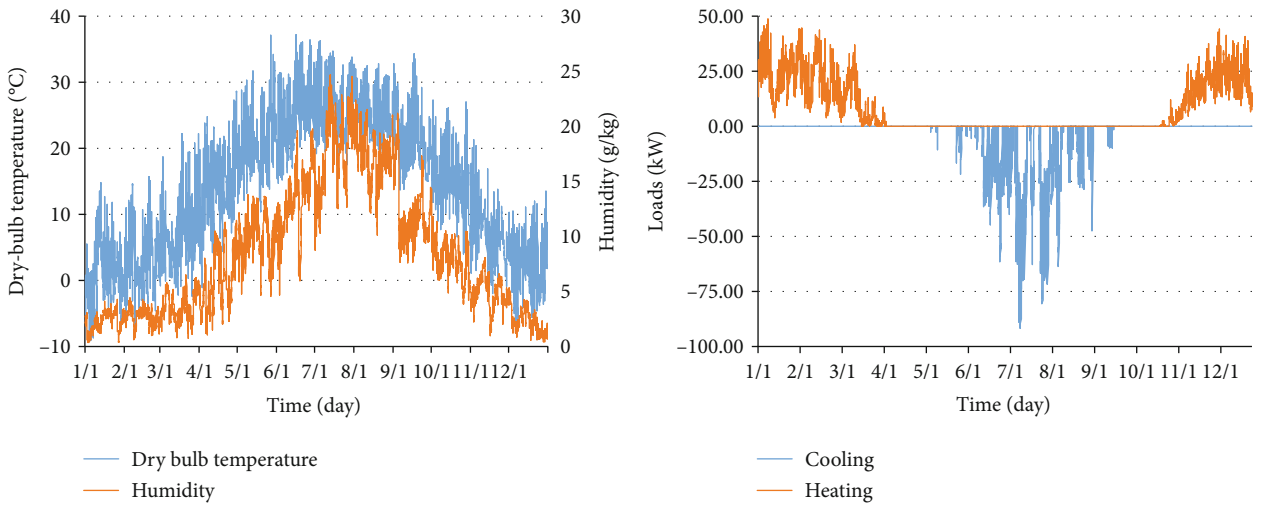

(c) Case 3 (Zhengzhou)

Figure 7: Climate characteristics and dynamic building loads for different uses in the Beijing, Harbin, and Zhengzhou regions.

Table 4

(a) Cooling characteristics of the heat pump

T_{source} (°C)	0		6		12		18	
	Power	COP	Power	COP	Power	COP	Power	COP
T_{load} (°C)								
5	17.43	2.66	19.64	2.70	21.85	2.78	24.05	2.84
10	17.49	2.83	19.33	2.87	21.19	2.90	23.03	2.93
20	15.82	3.43	17.40	3.50	17.92	3.56	21.56	3.63
29	14.31	3.80	15.92	3.85	17.52	3.90	19.13	3.95
32	14.24	3.98	15.68	4.03	17.13	4.08	19.57	4.13
38	13.32	4.30	14.66	4.33	15.99	4.36	17.33	4.40

(b) Heating characteristics of the heat pump

T_{load} (°C)	35		40		45		50	
	Power	COP	Power	COP	Power	COP	Power	COP
T_{source} (°C)								
−4	18.72	2.52	18.22	2.80	17.72	3.08	17.21	3.36
0	22.37	2.71	21.77	3.00	21.17	3.29	20.57	3.58
4	26.02	2.90	25.32	3.20	24.63	3.50	23.93	3.80
10	30.27	3.37	29.46	3.69	28.66	4.00	27.85	4.32
20	39.22	4.24	38.17	4.60	37.12	4.96	36.07	4.32
29	43.71	4.82	42.55	5.20	41.39	4.58	40.23	4.96

Table 5: Characteristics of the double U-tube heat exchanger.

Pipe		
Material		High-density polyethylene
Thermal conductivity	W/(m·K)	0.4
Outside diameter	mm	26.0
Inside diameter	mm	32.0
Number of pipes		4
Distance between pipes (center to center)	mm	50.0
Borehole diameter	mm	140.0
Connection between the two U tubes		Parallel
Grout thermal conductivity	W/(m·K)	2.0
Heat-carrier fluid		50% mixture of propylene glycol

The imbalance efficiency in the three regions was simulated, as shown in Figure 10. The imbalance efficiency in the three places is obviously different from that shown in the figure.

In the Beijing region, the $Q_{heating,total}$ is 4.99×10^8 kWh, the $Q_{cooling,total}$ is 11.2×10^8 kWh, and the imbalance efficiency is 55%. In the Harbin region, the $Q_{heating,total}$ is 14.3×10^8 kWh, the $Q_{cooling,total}$ is 2.98×10^8 kWh, and the imbalance efficiency is 79%. In the Zhengzhou region, the $Q_{heating,total}$ is 9.63×10^8 kWh, the $Q_{cooling,total}$ is 5.97×10^8 kWh, and the imbalance efficiency is 38%.

The temperature of soil in the three regions was simulated, as shown in Figure 11. The x-axis represents time in hours, and the y-axis represents soil temperature.

The soil temperatures in the different regions all show significant decreases, especially in the Harbin region where the soil is needed to store heat [35].

In the Beijing region, for the conventional GSHP system, the annual average soil temperature decreases from 15.8°C to 8.5°C during ten years of operation. As heat extracted by the heat pump unit from the ground decreases yearly, the rate of reduction in the average soil temperature slows. For the SA-GSHP system, the soil temperature fluctuates between 13.1°C and 17.9°C.

In the Harbin region, for the conventional GSHP system, the annual average soil temperature decreases from 10.6°C to 3.1°C during the ten years of operation. For the SA-GSHP system, the soil temperature fluctuates between 8.2°C and 12.5°C. The annual average soil temperature remains stable over the decade.

In the Zhengzhou region, for the conventional GSHP system, the annual average soil temperature decreases from 18.3°C to 14.1°C during the ten years of operation. For the SA-GSHP system, the soil temperature fluctuates between 10.9°C and 16.2°C.

Figure 12 shows the ten-year trend in dynamic quality during heating for the GSHP and SA-GSHP systems. The x-axis represents time in hours, and the y-axis represents COP.

Table 6

(a) Characteristics of the solar thermal collectors in the Beijing region

Total area of solar thermal collectors	m^2	300.58
Area of the single collector	m^2	2.26
Number of collectors		133
Number of collectors in series		6
η_0		0.768
α_1	$W/(m^2 \cdot K)$	3.4
α_2	$W/(m^2 \cdot K)$	0.0089
Heat-carrier fluid		50% mixture of propylene glycol

(b) Characteristics of the solar thermal collectors in the Harbin region

Total area of solar thermal collectors	m^2	800.04
Area of the single collector	m^2	2.26
Number of collectors		354
Number of collectors in series		6
η_0		0.768
α_1	$W/(m^2 \cdot K)$	3.4
α_2	$W/(m^2 \cdot K)$	0.0089
Heat-carrier fluid		50% mixture of propylene glycol

(c) Characteristics of the solar thermal collectors in the Zhengzhou region

Total area of solar thermal collectors	m^2	201.14
Area of the single collector	m^2	2.26
Number of collectors		177
Number of collectors in series		6
η_0		0.768
α_1	$W/(m^2 \cdot K)$	3.4
α_2	$W/(m^2 \cdot K)$	0.0089
Heat-carrier fluid		50% mixture of propylene glycol

In the Beijing region, the average annual COP in winter for the first year is 3.9, while in the tenth year, it is 2.9 and the COP decreases by 23%. For the SA-GSHP system, the relatively stable soil temperature results in the average annual COP of the heat pump unit remaining at around 3.9 over the ten years.

In the Harbin region, the average annual COP in the first year is 3.7, while in the tenth year, it is 2.0 and the COP decreases by 46%. For the SA-GSHP system, the annual average COP of the heat pump unit remains at around 3.6 over the ten years, because of the relatively stable soil temperature.

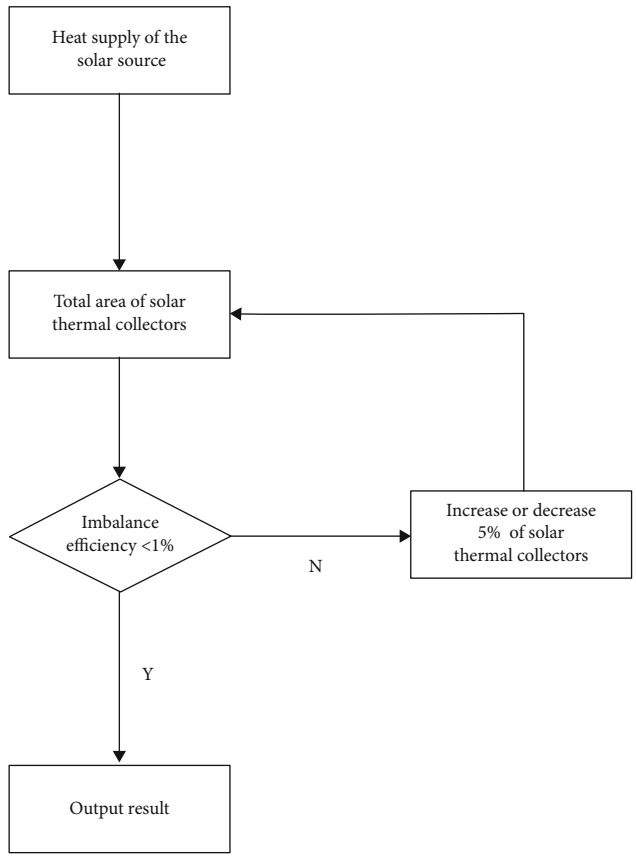

Figure 8: Optimization of solar collector area.

In the Zhengzhou region, the average annual COP in the first year is 3.8, while in the tenth year, it is 3.4 and the COP decreases by 11%. For the SA-GSHP system, the relatively stable soil temperature results in the average annual COP of the heat pump unit remaining at around 3.8 over ten years.

Figure 13 shows the first year and the tenth year during heating for the GSHP and SA-GSHP systems. The x-axis represents time in hours, and the y-axis represents the on/off state of the heat pump.

In the Beijing region, as the soil temperature decreases, the operating time of the heat pump unit of the conventional GSHP system increases from 2626 hours in the first year to 2767 hours in the tenth year. In contrast, the heat pump unit of the SA-GSHP system has a running time of approximately 2581 hours per year. The operating time of the heat pump unit of the SA-GSHP system is 45 hours lower in the first year and 186 hours lower in the tenth year, when compared with the conventional GSHP system. The total operating time over ten years of the heat pump units in the GSHP and SA-GSHP systems is 27,120 and 25,917 hours, respectively.

In the Harbin region, the operating time of the heat pump unit for the traditional GSHP system increases from 2855 hours in the first year to 3221 hours in the tenth year. In contrast, the heat pump unit of the SA-GSHP system operates for approximately 2784 hours per year. The operating time of the heat pump unit for the SA-GSHP system decreases by 71 hours in the first year and by 437 hours in the tenth year, compared with the conventional GSHP

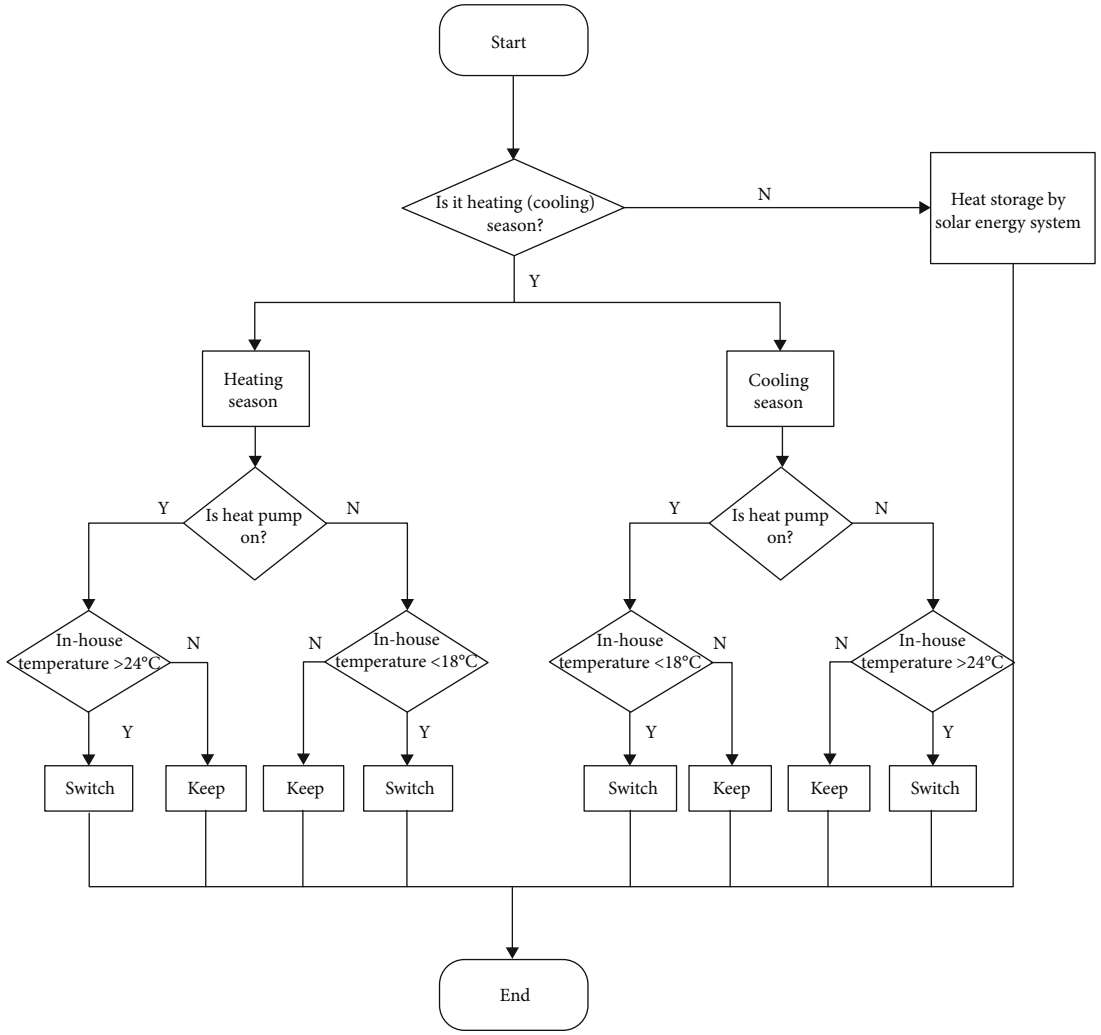

Figure 9: Control strategy of the system.

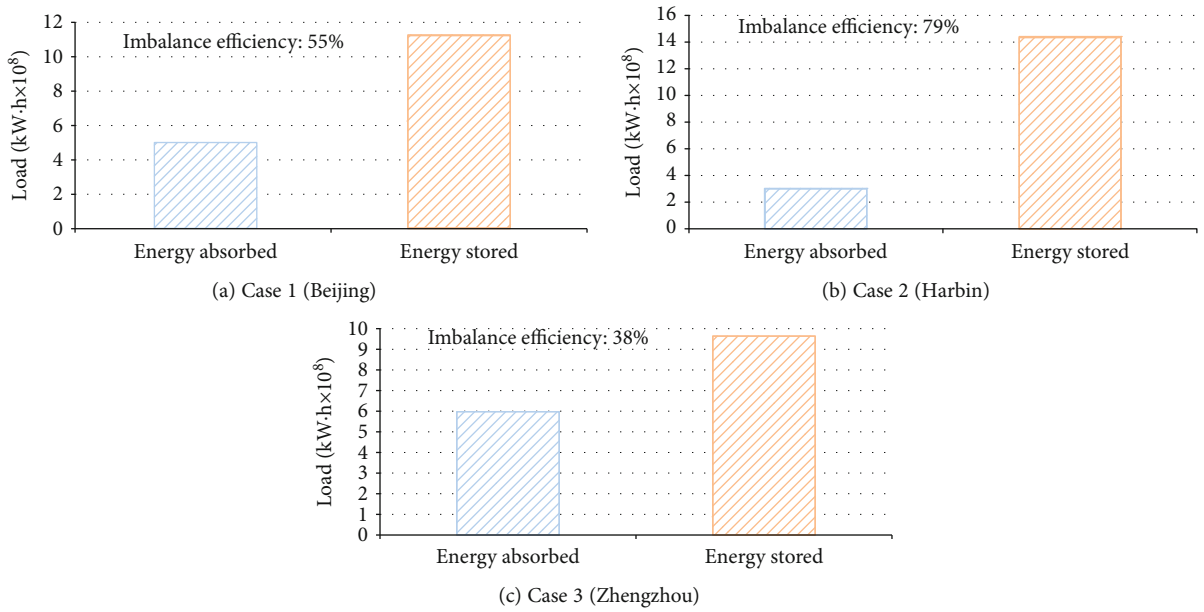

Figure 10: Imbalance efficiency in the Beijing, Harbin, and Zhengzhou regions.

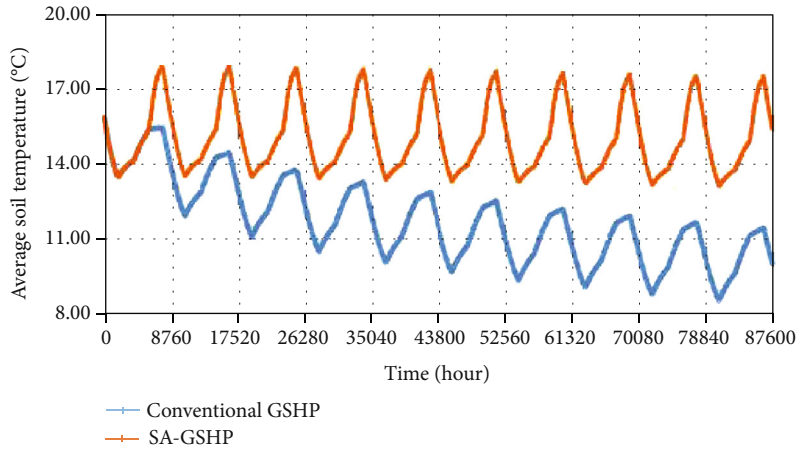

(a) Case 1 (Beijing)

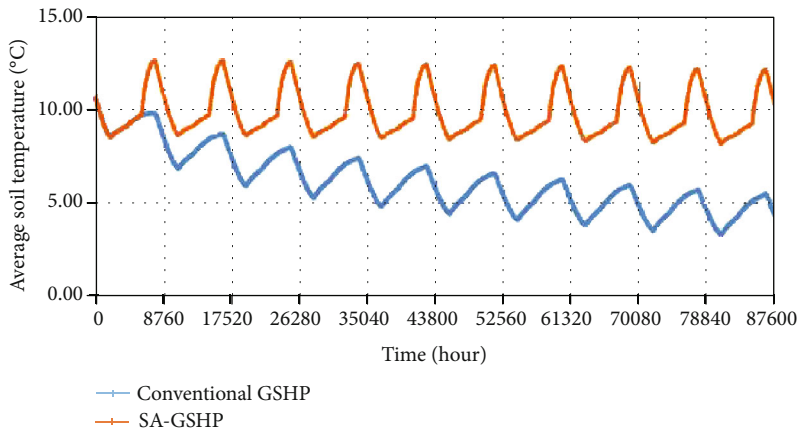

(b) Case 2 (Harbin)

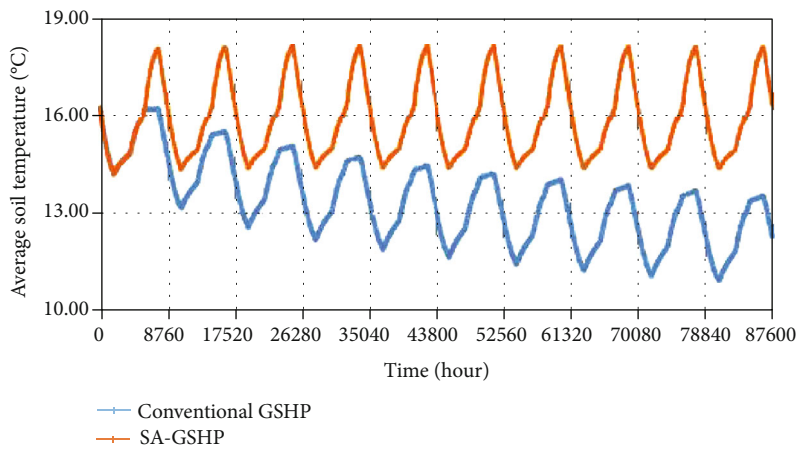

(c) Case 3 (Zhengzhou)

Figure 11: Soil temperature in the Beijing, Harbin, and Zhengzhou regions.

system. The total operating time over ten years of the heat pump units for the GSHP and SA-GSHP systems is 29,433 and 27,853 hours, respectively.

In the Zhengzhou region, the operating time of the heat pump unit for the traditional GSHP system increases from 2379 hours in the first year to 2443 hours in the tenth year. In contrast, the heat pump unit of the SA-GSHP system operates for approximately 2355 hours per year. The total operating time over 10 years of the heat pump units for the GSHP and SA-GSHP systems is 24,183 and 23,535 hours, respectively. There is not much difference between the two systems.

Among the three cities, they have different building loads. Harbin has the smallest cooling loads in summer and the largest heating loads in winter. So the problem of soil cold accumulation is very serious. Compared with Harbin, Beijing

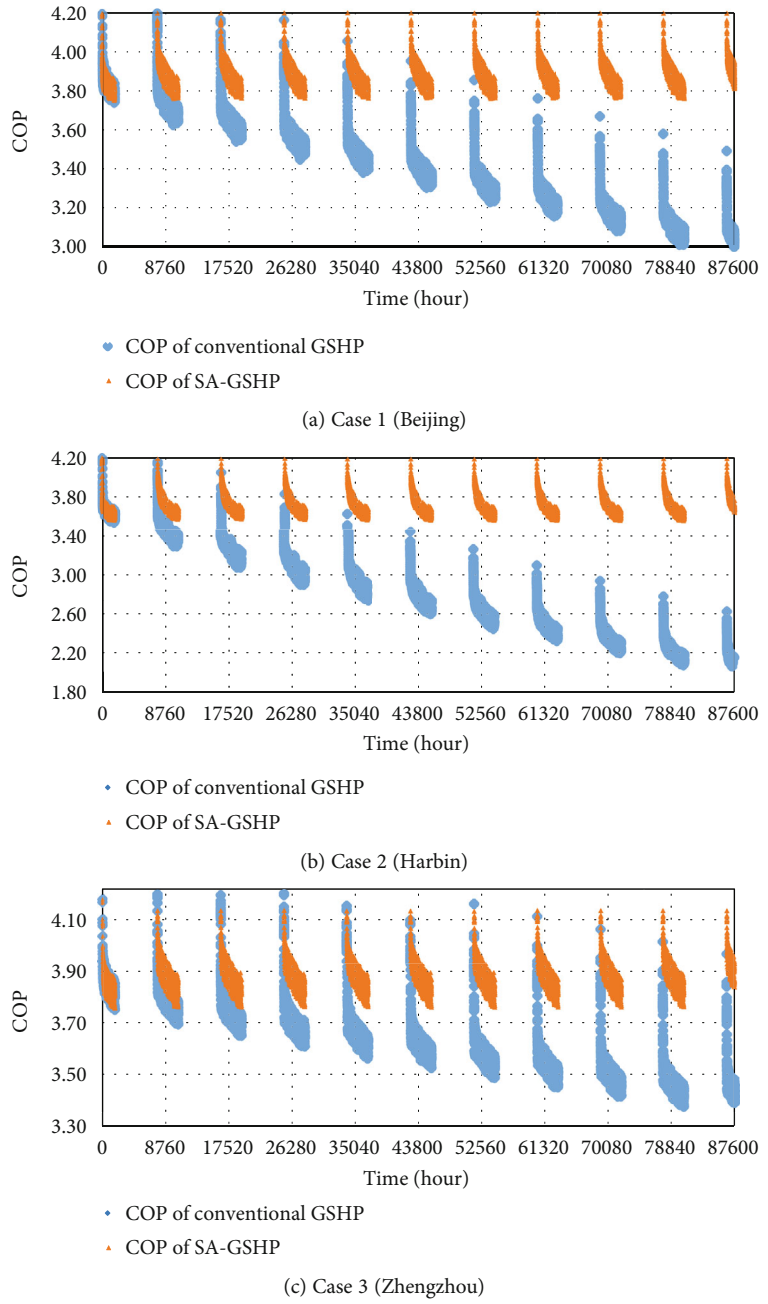

Figure 12: Ten-year trend in dynamic quality during heating for the GSHP and SA-GSHP systems.

has more cooling loads in summer and less heating loads in winter. Zhengzhou has the largest cooling loads in summer and the smallest heating loads in winter; the soil temperature drops less and the system is relatively stable.

6. Conclusion

This paper reports a method for analyzing the imbalance efficiency, specifically, to determine whether a GSHP system requires additional heat storage. Three typical cities, Beijing, Harbin, and Zhengzhou, are selected from the cold region, the severe cold region, and the hot summer and the cold winter region for simulation, and the performance and parameter variations of GSHP systems are analyzed.

It was found that the imbalance efficiency of Beijing, Harbin, and Zhengzhou is 55%, 79%, and 38%, respectively, after 10 years of operation. The average soil temperature decreased by 7.3°C, 11°C, and 4.3°C, respectively, which resulted in obvious cold accumulation. The COP of the heat pump also decreased by 23%, 46%, and 11%, respectively. By the tenth year, the operation time of the system is increased by 186 hours, 437 hours, and 88 hours compared with the first year, respectively.

The dynamic simulation results in TRNSYS show that the proposed SA-GSHP system has great energy saving

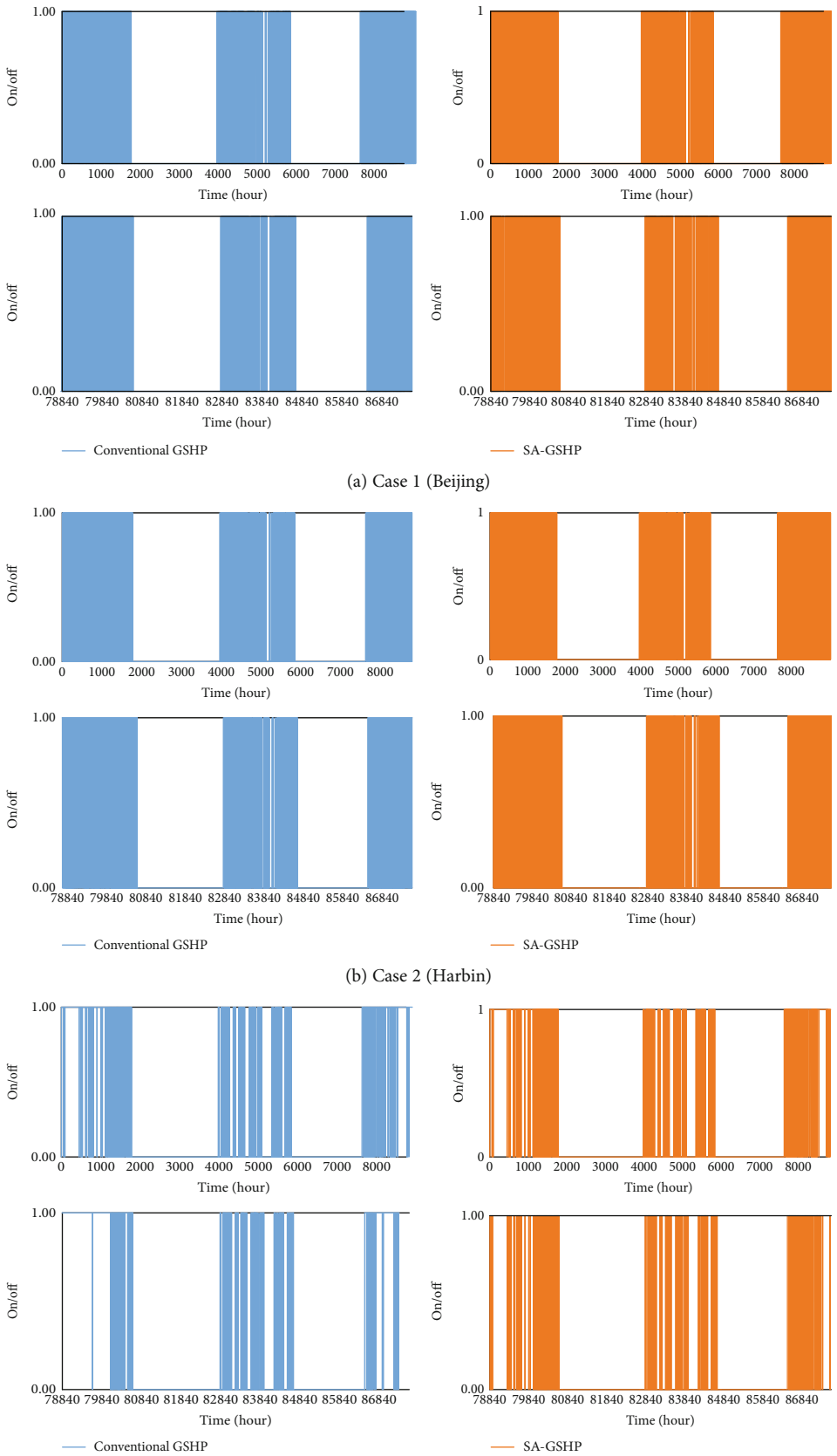

(a) Case 1 (Beijing)

(b) Case 2 (Harbin)

(c) Case 3 (Zhengzhou)

Figure 13: Ten-year trend in pump operating signal during heating for the GSHP and SA-GSHP systems.

potential. The system operation time of SA-GSHP is shorter than that of GSHP which could save more energy. After the system is optimized, the solar collector area increases by 20% in the Beijing region, 25% in the Harbin region, and 15% in the Zhengzhou region could help to maintain the annual average soil temperature balance. The simulation results show that the system can stabilize space heating. By storing solar energy into the soil in the transitional season, the imbalance efficiency can be kept at 1% to decrease the phenomenon of cold accumulation in the soil and ensure the COP stability of the heat pump unit.

For the cold and severe cold region represented by Beijing and Harbin, it is suggested to add heat storage equipment to the GSHP system because soil temperature and COP decrease greatly. For a hot summer and cold winter region like Zhengzhou, soil temperature and COP have little change and there is no significant impact on equipment operation; it is not recommended to conduct heat storage.

Nomenclature

A: Heat transfer area (m^2)
cp: Specific heat capacity (kJ/(kg·K))
D: Distance (m)
f: Solar energy guarantee rate (%)
k_c: Time-varying coefficient
h: Heat transfer coefficient ($W/m^2 \cdot K$)
L: Length (m)
M_c: Total heat mass of the unit inside the borehole (W/m^2)
$\dot{m}$: Fluid flow rate (kg/s)
p: Pressure (kPa)
P: Power (kW)
Pr: Prandtl number
Q: Heat transfer quantity (kW)
q: Heat transfer rate per unit ($W/m^2 \cdot K$)
r: Radius (m)
R: Thermal resistance ($m^2 \cdot K/W$)
Re: Reynolds number
S_y: Local average daily sunshine hours (h)
T: Temperature (K)
U: Coefficient of heat transfer ($W/(m^2 \cdot K)$)
v: Specific volume (m^3/kg)
w: Specific work (kW/kg)
W: Work (kW)
z: Depth (m)
τ: Transmission coefficient.

Subscripts

B: Borehole
Con: Condensation
Cooling: Cooling season
Crit: Critical pressure
Exp: Experiment
Evp: Evaporation
Ex: Exothermic process
Heating: Heating season
In: Tube inlet
Num: Numerical
Min: Minimum
Max: Maximum
Natural: Natural convection
Out: Tube outlet
Pump: Pump.

Greek Symbols

α: Convective heat transfer coefficient ($W/(m^2 \cdot K)$)
ε: Efficiency of the heat exchanger
η: Efficiency
ρ: Density (kg/m^3)
λ: Thermal conductivity
θ: Temperature response.

Acronyms

COP: Coefficient of performance
GHE: Ground heat exchanger
GSHP: Ground source heat pump
SA-GSHP: Solar-assisted ground source heat pump.

Data Availability

The data used to support the findings of this study are available from the corresponding author upon request.

Conflicts of Interest

The authors declare no conflict of interest.

Acknowledgments

This work was financially supported by the National Natural Science Foundation of China (No. 51678024 and No. 51338006), High Level Innovation Team of Beijing Municipal Education Commission (No. IDHT20180512), and Fundamental Research Funds for Beijing University of Civil Engineering and Architecture (No. X18111 and No. X18301). We thank the Liwen Bianji, Edanz Editing China Office (http://www.liwenbianji.cn/ac), for editing the English text of a draft of this manuscript.

References

[1] I. Sarbu and C. Sebarchievici, "General review of ground-source heat pump systems for heating and cooling of buildings," *Energy and Buildings*, vol. 70, no. 1, pp. 441–454, 2014.

[2] C. Naldi, G. L. Morini, and E. Zanchini, "A method for the choice of the optimal balance-point temperature of air-to-water heat pumps for heating," *Sustainable Cities and Society*, vol. 12, pp. 85–91, 2014.

[3] W. Choi, R. Ooka, and Y. Nam, "Impact of long-term operation of ground-source heat pump on subsurface thermal state in urban areas," *Sustainable Cities and Society*, vol. 38, pp. 429–439, 2018.

[4] Y. Bi, L. Chen, and F. Sun, "Comparative performance analysis for endoreversible simple air heat pump cycles considering ecological, exergetic efficiency and heating load objectives," *International Journal of Exergy*, vol. 6, no. 4, pp. 550–566, 2009.

[5] A. Michopoulos, T. Zachariadis, and N. Kyriakis, "Operation characteristics and experience of a ground source heat pump system with a vertical ground heat exchanger," *Energy*, vol. 51, no. 51, pp. 349–357, 2013.

[6] W. Li, X. Lin, C. Cao, Z. Gong, and Y. Gao, "Organic Rankine cycle-assisted ground source heat pump combisystem for space heating in cold regions," *Energy Conversion and Management*, vol. 165, no. 1, pp. 195–205, 2018.

[7] S. Lazzari, A. Priarone, and E. Zanchini, "Long-term performance of BHE (borehole heat exchanger) fields with negligible groundwater movement," *Energy*, vol. 35, no. 12, pp. 4966–4974, 2010.

[8] Y. Geng, J. Sarkis, X. Wang, H. Zhao, and Y. Zhong, "Regional application of ground source heat pump in China: a case of Shenyang," *Renewable & Sustainable Energy Reviews*, vol. 18, no. 2, pp. 95–102, 2013.

[9] M. Alavy, H. V. Nguyen, W. H. Leong, and S. B. Dworkin, "A methodology and computerized approach for optimizing hybrid ground source heat pump system design," *Renewable Energy*, vol. 57, no. 3, pp. 404–412, 2013.

[10] N. Zhu, P. Hu, L. Xu, Z. Jiang, and F. Lei, "Recent research and applications of ground source heat pump integrated with thermal energy storage systems: a review," *Applied Thermal Engineering*, vol. 71, no. 1, pp. 142–151, 2014.

[11] S. Paiho, H. Hoang, and M. Hukkalainen, "Energy and emission analyses of solar assisted local energy solutions with seasonal heat storage in a Finnish case district," *Renewable Energy*, vol. 107, pp. 147–155, 2017.

[12] S. Colclough and P. Griffiths, "Financial analysis of an installed small scale seasonal thermal energy store," *Renewable Energy*, vol. 86, pp. 422–428, 2016.

[13] W. Yang, J. Zhou, W. Xu, and G. Zhang, "Current status of ground-source heat pumps in China," *Energy Policy*, vol. 38, no. 1, pp. 323–332, 2010.

[14] S. Bae, Y. Nam, J. Choi, K. Lee, and J. Choi, "Analysis on thermal performance of ground heat exchanger according to design type based on thermal response test," *Energies*, vol. 12, no. 4, p. 651, 2019.

[15] K. Bakirci, O. Ozyurt, K. Comakli, and O. Comakli, "Energy analysis of a solar-ground source heat pump system with vertical closed-loop for heating applications," *Energy*, vol. 36, no. 5, pp. 3224–3232, 2011.

[16] F. M. Rad, A. S. Fung, and W. H. Leong, "Feasibility of combined solar thermal and ground source heat pump systems in cold climate, Canada," *Energy and Buildings*, vol. 61, no. 3, pp. 224–232, 2013.

[17] R. M. Lazzarin, "Dual source heat pump systems: operation and performance," *Energy and Buildings*, vol. 52, pp. 77–85, 2012.

[18] A. Macía, L. A. Bujedo, T. Magraner, and C. R. Chamorro, "Influence parameters on the performance of an experimental solar-assisted ground-coupled absorption heat pump in cooling operation," *Energy and Buildings*, vol. 66, pp. 282–288, 2013.

[19] C. Lyu, W. H. Leong, M. Zheng, G. Chen, S. Ye, and Y. Liu, "Verification and analysis of a dynamic simulation model of ground-coupled heat pump with solar seasonal heat storage system," *Procedia Engineering*, vol. 205, pp. 3154–3161, 2017.

[20] X. Wang, M. Zheng, W. Zhang, S. Zhang, and T. Yang, "Experimental study of a solar-assisted ground-coupled heat pump system with solar seasonal thermal storage in severe cold areas," *Energy and Buildings*, vol. 42, no. 11, pp. 2104–2110, 2010.

[21] M. Karagiorgas, K. Galatis, M. Tsagouri, T. Tsoutsos, and A. Botzios-Valaskakis, "Solar assisted heat pump on air collectors: a simulation tool," *Solar Energy*, vol. 84, no. 1, pp. 66–78, 2010.

[22] W. Liu, G. Chen, B. Yan, Z. Zhou, H. Du, and J. Zuo, "Hourly operation strategy of a CCHP system with GSHP and thermal energy storage (TES) under variable loads: a case study," *Energy and Buildings*, vol. 93, pp. 143–153, 2015.

[23] H. J. L. Witte, G. J. V. Gelder, and J. D. Spitler, "In situ measurement of ground thermal conductivity: the Dutch perspective," *ASHRAE Transactions*, vol. 108, no. 1, pp. 263–272, 2002.

[24] J. Luo, H. Zhao, J. Jia, W. Xiang, J. Rohn, and P. Blum, "Study on operation management of borehole heat exchangers for a large-scale hybrid ground source heat pump system in China," *Energy*, vol. 123, pp. 340–352, 2017.

[25] G. Emmi, A. Zarrella, M. De Carli, and A. Galgaro, "An analysis of solar assisted ground source heat pumps in cold climates," *Energy Conversion and Management*, vol. 106, pp. 660–675, 2015.

[26] W. Yang, M. Shi, G. Liu, and Z. Chen, "A two-region simulation model of vertical U-tube ground heat exchanger and its experimental verification," *Applied Energy*, vol. 86, no. 10, pp. 2005–2012, 2009.

[27] W. Yang, S. Zhang, and Y. Chen, "A dynamic simulation method of ground coupled heat pump system based on borehole heat exchange effectiveness," *Energy and Buildings*, vol. 77, no. 77, pp. 17–27, 2014.

[28] N. Diao, *Heat Transfer Analyses of Ground Heat Exchanger and Their Engineering Applications[D]*, Tsinghua university, China, 2004.

[29] P. Hu, Z. Yu, N. Zhu, F. Lei, and X. Yuan, "Performance study of a ground heat exchanger based on the multipole theory heat transfer model," *Energy and Buildings*, vol. 65, no. 10, pp. 231–241, 2013.

[30] M. Guo, N. Diao, Y. Man, and Z. Fang, "Research and development of the hybrid ground-coupled heat pump technology in China," *Renewable Energy*, vol. 87, pp. 1033–1044, 2016.

[31] T. Katsura, K. Nagano, S. Narita, S. Takeda, Y. Nakamura, and A. Okamoto, "Calculation algorithm of the temperatures for pipe arrangement of multiple ground heat exchangers," *Applied Thermal Engineering*, vol. 29, no. 5–6, pp. 906–919, 2009.

[32] A. F. Handbook, *American Society of Heating, Refrigerating and Air-Conditioning Engineers*, Inc, Atlanta, GA, USA, 2009.

[33] S. A. Klein, *A Transient System Simulation Program*, Solar Energy Laboratory, TRNSYS, University of Wisconsin, Madison, 2006.

[34] G. Florides and S. Kalogirou, "Ground heat exchangers–a review of systems, models and applications," *Renewable Energy*, vol. 32, no. 15, pp. 2461–2478, 2007.

[35] China Academy of Architectural Sciences, *GB 50495-2009 Technical Specification for Solar Heating and Heating Engineering*, China Construction Industry Press, Beijing, 2009.

Hindawi
International Journal of Photoenergy
Volume 2020, Article ID 6150794, 11 pages
https://doi.org/10.1155/2020/6150794

Research Article

Thermomechanical Fatigue Behavior of Spray-Deposited SiC_p/Al-Si Composite Applied in the High-Speed Railway Brake Disc

Wei Li,[1,2] **Huitao Chen**,[1,2] **Lu Zuo**,[1,2] **Jian Chen**,[1,2] **Dongliang Xu**,[1,2] **Jianjun He**,[1,2] **Cong Li**,[1,2] **Zhuoyin Peng**,[1,2] **Yanjie Ren**,[1,2] **and Sheng-de Zhang**[3]

[1]*Key Laboratory of Efficient & Clean Energy Utilization, School of Energy and Power Engineering, Changsha University of Science & Technology, Changsha 410114, China*
[2]*Hunan Province 2011 Collaborative Innovation Center of Clean Energy, and Smart Grid, Changsha 410114, China*
[3]*Japan Electric Power Central Research Institute, Tokyo 240-0196, Japan*

Correspondence should be addressed to Wei Li; lwzzgjajie@126.com and Jian Chen; chenjian_513@126.com

Received 6 November 2019; Accepted 10 January 2020; Published 7 February 2020

Guest Editor: Hafiz M. Ali

The thermomechanical fatigue (TMF) behaviors of spray-deposited SiC_p-reinforced Al-Si alloy were investigated in terms of the size of Si particles and the Si content. Thermomechanical fatigue experiments were conducted in the temperature range of 150-400°C. The cyclic response behavior indicated that the continuous cyclic softening was exhibited for all materials, and the increase in SiC particles size and Si content aggravated the softening degree, which was attributed to dislocation generation due to differential thermal contraction at the Al matrix/Si phase interface or Al matrix/SiC particle interface. Meanwhile, the TMF life and stress amplitude of SiC_p/Al-7Si composites were greater than those of Al-7Si alloy, and increased with the increasing SiC particle size, which was associated with "load sharing" of the direct strengthening mechanism. The stress amplitude of 4.5μmSiC_p/Al-Si composite increased as the Si content increased; however, the influence of Si content on the TMF life was not so significant. The TMF failure mechanism revealed that the crack mainly initiated at the agglomeration of small-particulate SiC and the breakage of large-particulate SiC, and the broken primary Si and the exfoliated eutectic Si accelerated the crack propagation.

1. Introduction

The depletion of natural resources and environmental pollution are major challenges facing humanity today. It is urgent to study new energy sources instead of traditional fossil energy sources. The use of clean energy such as solar energy has been very extensive. For instance, new energy vehicles are using clean energy to save resources and protect the environment [1]. However, the development of new technologies has improved the requirements of materials. For instance, the light-weight, wear resistance, and thermomechanical fatigue properties of composites for automotive brake discs are very important [2–4]. The traditional metal brake discs are easy to crack and cannot ensure the safety of the vehicles due to the high temperature produced by friction between wheel and rail with high driving speed (≥400 km/h). Some new composites like carbon/carbon fiber-reinforced carbon matrix composites have excellent high-temperature wear resistance, but oxidation and high manufacturing cost restrict their widespread application. SiC_p/Al-Si composite, owing to advantages such as high-specific strength, excellent thermal conductivity, and low expansion coefficient, is considered as an ideal metal matrix composite (MMC) for brake disc [5–8]. In the process of actual braking, the residual stress caused by the mismatch in thermal-expansion coefficient (CTE) between SiC particle and Al-Si alloy while the composites are subjected to mechanical load leads to thermomechanical fatigue (TMF) collaboratively.

Several methods can be adopted to prepare the SiC_p/Al-Si composites such as stir casting [9], powder metallurgy [10], and spray deposition [11]. Spray deposition is a rapid prototyping process to gas atomize a stream of molten metal by mean of high velocity gases (i.e., Ar or N_2) and to direct the resulting spray into a cold substrate [12]. Not only can this

Table 1: Composition of materials.

Materials	SiC particle size (μm)	Si (wt%)	Mg (wt%)	Mn (wt%)	Cu (wt%)	Al (wt%)
Al-7Si	0	7	0.3	0.01	0.01	Bal.
20μmSiC_p/Al-7Si	20	7	0.3	0.01	0.01	Bal.
4.5μmSiC_p/Al-7Si	4.5	7	0.3	0.01	0.01	Bal.
4.5μmSiC_p/Al-13Si SiC_p/Al-13Si	4.5	13	0.3	0.01	0.01	Bal.
4.5μmSiC_p/Al-20Si	4.5	20	0.3	0.01	0.01	Bal.

method avoid the oxidation reaction between molten metal and bubbles during stirring process [13] but also make some microstructure improvements such as refining the grains, decreasing the segregated phase, and making the internal SiC particles more evenly distributed in SiC_p/Al-Si composite [14]. Generally, the material prepared by spray deposition has high strength, good plasticity, and strong wear resistance [15].

There are many factors affecting the TMF properties of MMCs, involving complex mechanism. The in-phase (IP) and out-of-phase (OP) experiments are conducted to simulate the temperature, strain, and phase relationship generally [16]; therefore, previous work about TMF of MMCs has been investigated mainly on the influence of phase, the volume fraction of reinforcement, and stress level on the fracture mechanism. Qian et al. [17–19] researched the TMF behavior of SiC_W/6061Al composites with SiC_W volume fraction of 15% and 28% and found that cyclic softening occurred in both composites during IP- and OP-TMF, and the cyclic stress range of high-volume-fraction composites was greater than that of low-volume-fraction composites at an equivalent strain range. In addition, the 15% SiC_W composite revealed a longer life than 28% SiC_W composite in the case of IP-TMF, but the fatigue life curves of the two composites passed across each other in the case of OP-TMF, and the damage mechanism consists of initiation, growth, and coalescence of voids in the matrix around whiskers. Eun [20] reported that the IP-TMF life of Ti-48Al-2V alloy and TiB_2 particles reinforced Ti-48Al-2V composites became longer as the maximum temperature and the stress range decreased, and the TMF mechanism was nucleation and growth of voids on interlamellar plate, twin, and grain boundaries; their interlamellar, translamellar, and intergranular linkage; intergranular separation and disintegration of lamellar structure. The IP- and OP-TMF behavior of SiC_p/Al 2xxx-T4 between 100°C and 300°C composites has been investigated by Karayaka and Sehitoglu [16]. They found that the failure mechanism was creep-fatigue damage in short-life areas and oxidation damage in long-life areas. Sehitoglu [21] found that the TMF life of Al/SiC composites became longer with smaller SiC particle size. It was investigated by Wang et al. that the TMF damage behavior of Al-Si piston alloy was affected by temperature ranges; the cracks mainly initiated from the broken primary silicon in the temperature range of 120~350°C and nucleated from the interface between matrix and primary Si in the temperature range of 120~425°C [22]. However, the effect of particle size and Si contents on the TMF behavior of spray-deposited SiC particles reinforced Al-Si alloy has rarely been investigated.

Thus, the cyclic stress behavior, particulate strengthening mechanism, and thermomechanical fatigue fracture of SiC_p/Al-Si composites in terms of different SiC particle sizes and Si contents were investigated.

2. Experimental Materials and Procedures

The Al-Si alloy and composites reinforced with 15 vol.% SiC particles were prepared by multilayer spray deposition technology; the details of which have been shown in the previous studies [23]. The nominal composition of investigated samples is given in Table 1. The sprayed ingots were extruded at the ratio of 17.3, and T6 heat treatment was performed at 535°C for 2.5 h followed by quenching in room-temperature water and natural aging more than 12 h, finally artificial aging at 160°C for 7 h. All of samples were treated by the abovementioned process.

The machined specimens had a rectangular section of 5 mm × 8 mm and a gauge length of 25 mm, according to ASMT standard E8. TMF tests were examined on a computer-controlled servo hydraulic test machine. As can be seen in Figure 1, the temperature was controlled by triangle wave and detected by thermocouple. Mechanical strain was controlled by cosine waves and measured with 25 mm high-temperature extensometer. The total strain amplitude is 0.3% and R of stress ratio is 0.1. Considering that the disc surface temperature is generally 150-400°C, sometimes up to 450°C [24], specimens were heated using induction heater from minimum temperature of 150°C to a maximum temperature of 400°C. The cycle period (total heating and cooling times) was 100 s for the TMF experiments. After TMF experiments, the fracture morphology was observed by the Quanta 2000 environment scanning electron microscope (SEM).

3. Results

3.1. Microstructure. Some typical phases of Al-7Si alloy and SiC_p/Al-Si composites are identified and marked briefly in the optical micrographs (Figure 2). The Al-7Si alloy is mainly consisted of α-Al matrix and Si particles with white color, which cluster together forming the eutectic Si phase marked in Figure 2(a). SiC particles with an average size of 4.5 μm were distributed evenly in the 4.5μmSiC_p/Al-7Si composite (Figure 2(b)). In Figure 3(c), the SiC particles with grey color and a mean particle size of 20 μm were irregular shaped, and interparticle spacing is smaller than 4.5μmSiC_p/Al-7Si obviously. The morphology of Si phase changed with an increase in Si content; it can be seen a few block-like primary Si phase

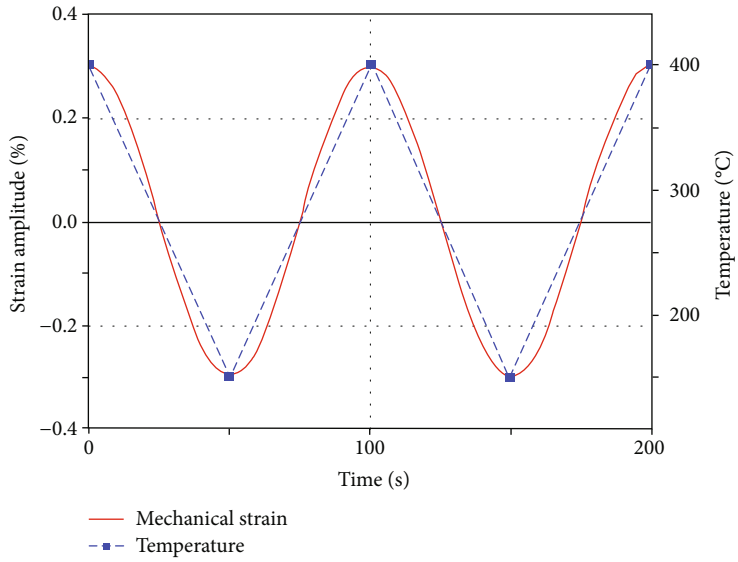

Figure 1: Schematic diagram of IF-TMF.

with an average of 5.85 μm and many round eutectic Si phase with an average of 2.51 μm in the 4.5μmSiC_p/Al-13Si composite (Figure 2(d)). While for 4.5μmSiC_p/Al-20Si composite, the average size of primary Si phase is 7.85 μm and the shape is more random. More details about microstructure have been reported in previous investigations [25, 26].

3.2. Stress-Mechanical Strain Hysteresis Loop. Figure 3 shows the hysteresis loop for the first- and half-life time of SiC_p/Al-7Si composites with different particle sizes during TMF loading. During the heating period of the first cycle, the stress increases with increasing temperature and strain value. When the temperature and strain value first reach the maximum and then both decrease to minimum value, the stress amplitude first reaches the maximum positive value and then decreases to the maximum negative value, correspondingly. In addition, the maximum tensile stress is greater than the maximum compressive stress for the all materials. It can be seen from the Figures 3(a)–3(c) that the stress amplitude of the first cycle life is greater than that of the half-life cycle for all samples, which means that softening occurs once the first cycle begins. Comparison of Figures 2(a)–2(c) shows that the softening degree of Al-7Si alloy is more obvious than other two composites. Especially, the 4.5μmSiC_p/Al-7Si composites have the lowest softening degree.

Typical first- and half-life hysteresis of 4.5μmSiC_p/Al-Si composites with different Si contents for TMF are given in Figure 4. The stress amplitude of the half-life cycle is lower than that of the first cycle life and softening occurs after the first cycle loading for all specimens. It can be also observed that the cyclic softening degree increases with an increase in Si content. The maximum tensile stress is greater than the maximum compressive stress for the same materials during TMF loading process.

3.3. Cyclic Stress Response. Figure 5 shows the cyclic stress response of the studied SiC_p/Al-Si composites at the total mechanical strain amplitude of 0.3%. It can be observed that the cyclic response stress of Al-7Si alloy has the similar trend to those of SiC_p/Al-7Si composites from Figures 5(a) and 5(b), i.e., cyclic softening. While there are a few differences between the details, for Al-7Si alloy, the onset of slight cyclic softening stage occurs from 1 to 10 cycles, and then the softening degree becomes more significant, and finally rapid softening occurred from about 300 cycles to rupture time. For 4.5μmSiC_p/Al-7Si composite, rapid cyclic softening occurs during the first 20 cycles, nearly followed by saturation around 700 cycles and rapid softening till failure. The 20μmSiC_p/Al-7Si composites show rapid cyclic softening during the first 30 cycles, followed by slight softening till about 800 cycles and then failure. In addition, the stress ranges are the largest in the first cycle and then decrease rapidly in the following cycles for all samples. It can be found that the stress amplitude of Al-7Si alloy is obviously lower than that of SiC particle-reinforced Al-7Si composites, of which the stress amplitude of 20μmSiC_p/Al-7Si composite is the highest. Thereafter, it is worth noting that an increase in SiC particle size leads to an increase in the TMF life. The 4.5μmSiC_p/Al-Si composites with different Si content also exhibit softening tendency from initial cycles to final rupture, and an increase in Si content results in a more pronounced cycle softening (Figure 5(b)). In terms of stress amplitude, a similar trend also appears. The higher the Si content, the greater the stress amplitude. However, there is no significant difference in the TMF life of these composites; the TMF life of 4.5μmSiC_p/Al-7Si composite is slightly longer than the other two composites, while the TMF life of 4.5μmSiC_p/Al-13Si composites and 4.5μmSiC_p/Al-20Si composites is similar.

3.4. Fractographical Observation. The TMF fractography of Al-7Si alloy and SiC_p/Al-Si composites is shown in Figure 6. The rough fracture surface consists of many micropores with 3-5 μm in size uniformly distributed in the region of stable fatigue crack propagation (Figure 6(a)). Figure 6(b) is the magnified view of the region of fatigue crack

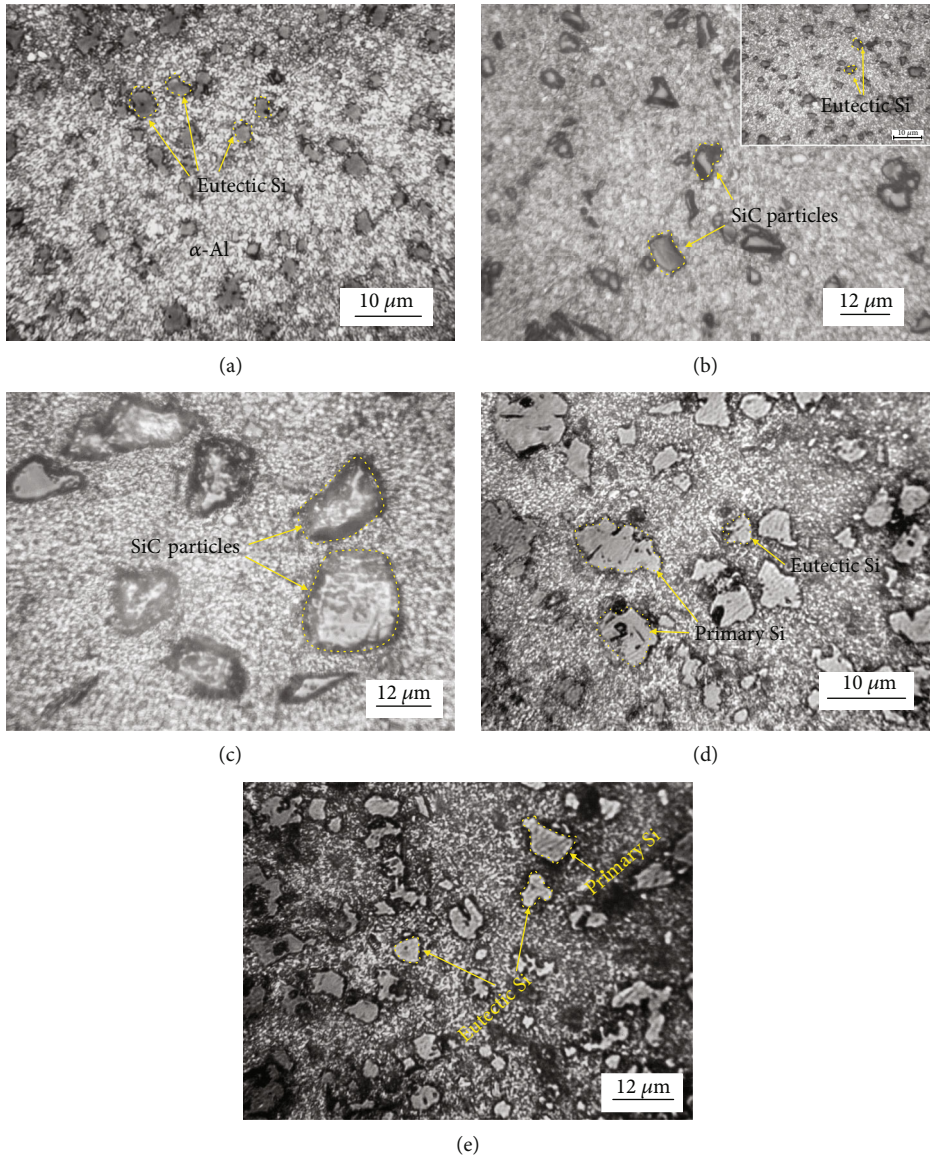

Figure 2: Microstructures of (a) Al-7Si alloy; (b) 4.5μmSiC_p/Al-7Si (eutectic); (c) 20μmSiC_p/Al-7Si; (d) 4.5μmSiC_p/Al-13Si (eutectic); (e) 4.5μmSiC_p/Al-20Si (hypereutectic).

propagation, and there are many small eutectic Si particles scattering around the micropores, which is probably associated with debonding during TMF loading. Crack tip factor increases as the cycles increases, which results in the sharp rising amount of micropores and dimples. Fatigue striation and micropores distributed alternatively on the rough fracture surface of 4.5μmSiC_p/Al-7Si composite can be presented in Figure 6(c), and the direction of fatigue crack propagation is perpendicular to fatigue striation. Plenty of complete SiC particles and several Si particles can be observed at transient fracture zone (Figure 6(d)), which indicates that SiC particles debond from Al-Si matrix and form aggregation accelerating fatigue crack initiation and propagation during TMF loading. Figure 6(e) shows rougher fracture surface of 20μmSiC_p/Al-7Si composites in the region of crack propagation than that of Al-7Si alloy and 4.5μmSiC_p/Al-7Si composite, and the propagation paths are more tortuous. There are some broken primary SiC particles distributing on the fracture plane, where the decohesion of SiC particles and Si particles also occurs peripherally. Besides, many voids form around the particles, and cavities and pits accumulate together with the increase in TMF cycles. The contiguous holes interlink with each other due to the tearing of different phases in the monolithic alloy, thus forming many microcracks (Figure 6(f)).

Similar to 4.5μmSiC_p/Al-7Si composite, typical fatigue striation should have been observed in the region of crack propagation for the 4.5μmSiC_p/Al-13Si composite; however, there is no such characterization probably because some free SiC particles and Si phases concealed the fatigue striation, but plenty of homogeneous cavities and dimples also can be seen in the fracture surface. These SiC particles agglomerate together more tightly to form a large cluster, like a big

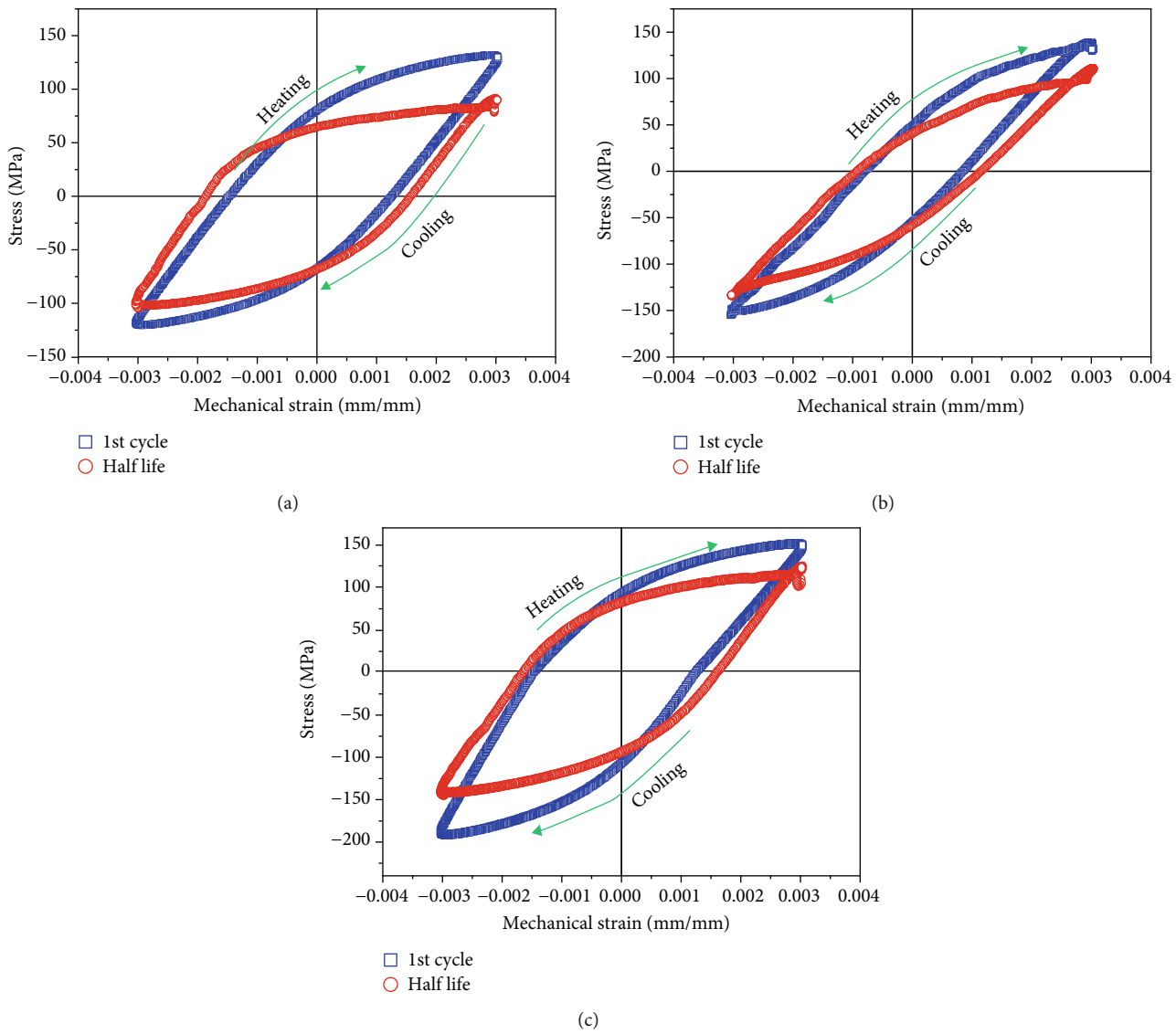

FIGURE 3: The stress-mechanical strain hysteresis loop of (a) Al-7Si alloy; (b) 4.5μmSiC$_p$/Al-7Si composite; (c) 20μmSiC$_p$/Al-7Si composite ($\Delta\varepsilon_m = 0.3\%$).

particle, which results in the crack initiation more easily (Figure 6(g)). In addition, the fracture of some free primary Si possibly takes place at crack growth stage (Figure 6(h)). The striations and cavities appear alternatively in the TMF fractographs of 4.5μmSiC$_p$/Al-20Si composites (Figure 6(i)), and the reason for the formation of cavities may be related to SiC particles and Si particles debonding from Al-Si matrix. The size of primary Si particles increases as Si content increases, and cracks nucleate primary Si particles with larger size, which results in many microcracks in Figure 6(j).

4. Discussion

4.1. The Effect of Thermal Expansion Coefficient on Fatigue Life. Karayaka and Sehitoglu [16] investigated the thermomechanical fatigue of metal matrix composite and found that temperature and mechanical strain always changed momentarily in the TMF process. Lloyd [27] also pointed out that the total strain was the sum of thermal and mechanical strain components:

$$\varepsilon_{net} = \varepsilon_{th} + \varepsilon_{mech} = \alpha(T - T_0) + \varepsilon_{mech}, \quad (1)$$

where ε_{net} is the total strain, ε_{th} is the thermal strain, ε_{mech} is the mechanical strain, T_0 is the initial temperature at the beginning of experiment, T is the real-time temperature of experiment, and α is the thermal expansion coefficient of composites.

SiC$_p$/Al-Si composites are composed of the Al matrix, Si phases, and SiC particles. The difference in Si content and SiC particle size will lead to a great difference in thermal expansion coefficient of materials, which will directly affect the dislocation and residual internal stress of materials. Elomari et al. [28] indicated that the addition of SiC reinforced particles could effectively reduce the thermal expansion

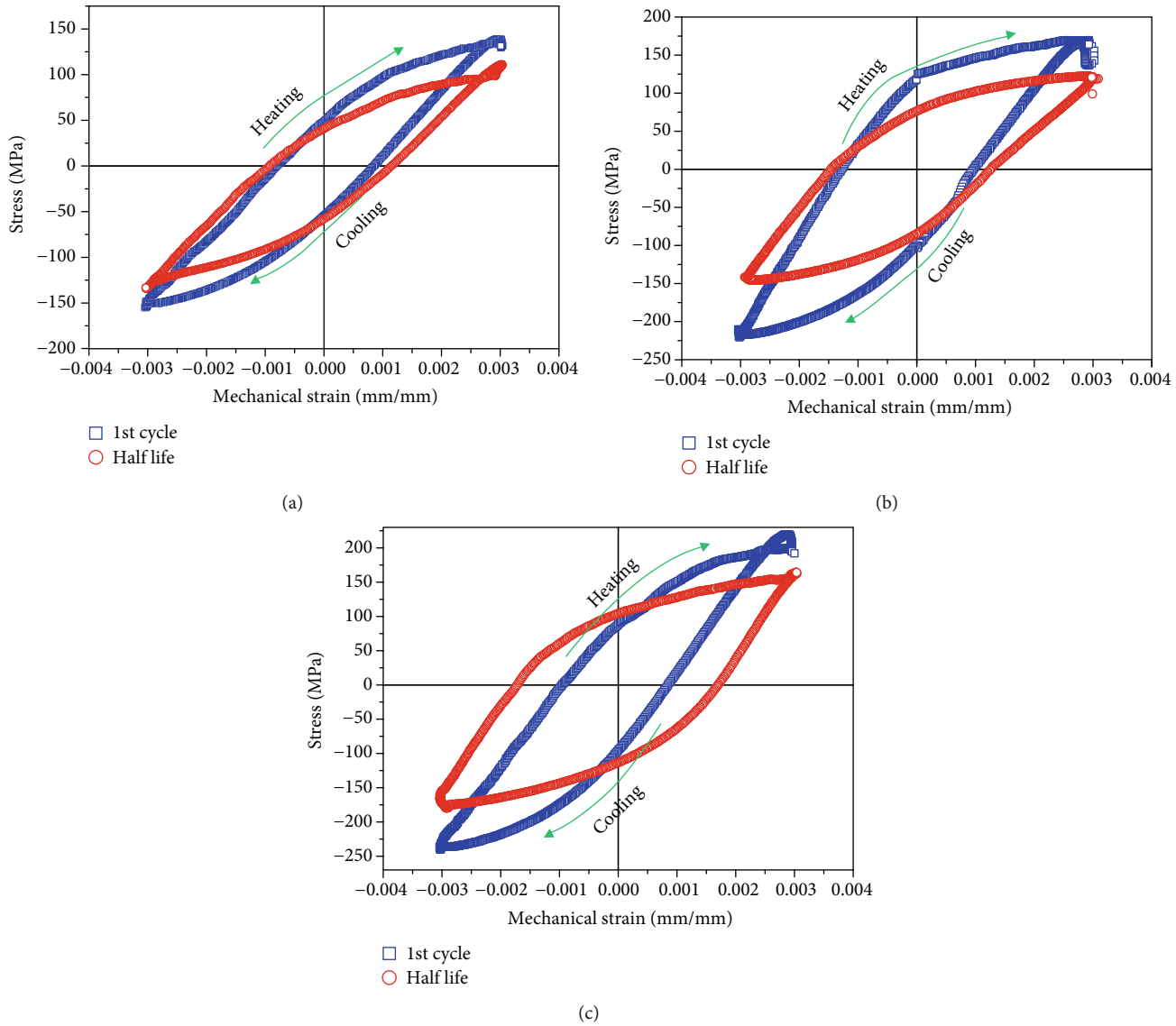

FIGURE 4: The stress-mechanical strain hysteresis loop of (a) 4.5μmSiC$_p$/Al-Si composite; (b) 4.5μmSiC$_p$/Al-13Si composite; (c) 4.5μmSiC$_p$/Al-20Si composite ($\Delta\varepsilon_m = 0.3\%$).

coefficient of the material. When the volume fraction of reinforced particles was constant, the thermal expansion coefficient of composites decreased with the decrease of SiC particle size. Thus, it can be concluded that the thermal expansion coefficient of Al-7Si alloy in this paper is the highest, followed by composite with 20 μm SiC particles and composite reinforced with 4.5 μm SiC particles. When the cyclic loading temperature is applied between 150 and 400°C, the Al-7Si alloy exhibited the most obvious thermoplastic deformation, which is attributed to the highest thermal strain and residual thermal stress, leading to the lowest fatigue life.

4.2. The Effect of SiC Particle Size. The stress amplitude and TMF life of SiC$_p$/Al-7Si composite are both greater than that of Al-7Si alloy, which is closely related to the strengthening mechanism of reinforced particles. Generally, there are two kinds of strengthening mechanisms, direct strengthening and indirect strengthening. The load transmission between matrix and reinforced particles is taken into account for direct strengthening, and the effect of reinforcement on microstructure and deformation mode of matrix is concerned about indirect strengthening [29]. From the perspective of direct strengthening, elastic modulus of matrix is lower than that of SiC particles; thus, SiC particles can undertake the loading partly from matrix, which improves the strength of materials. According to the shear lag model proposed by Nardone and Prewo [30],

$$\sigma_{cy} = \sigma_{my}\left(\frac{V_p(S+4)}{4} + V_m\right), \tag{2}$$

where σ_{cy} is the yield strength of composites, σ_{my} is the yield strength of alloys, S is the length-to-diameter aspect ratio of reinforced particles, and V_p and V_m are the volume fraction of reinforced particles and matrix, respectively.

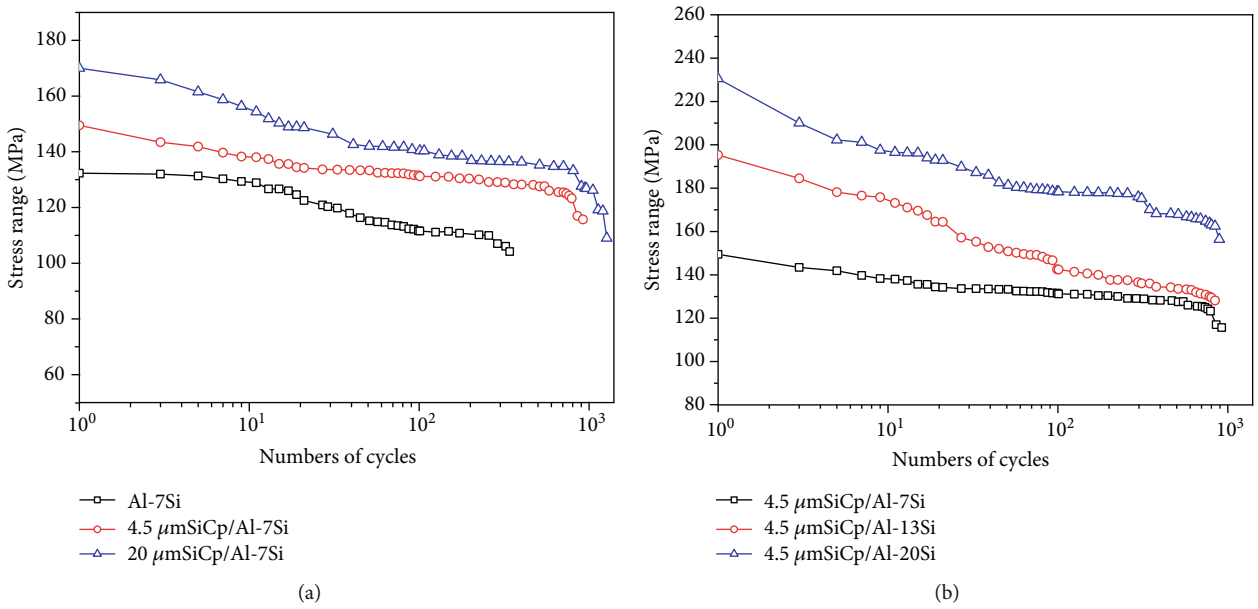

FIGURE 5: Cyclic stress response curves of SiC_p/Al-Si composite ($\Delta\varepsilon_m = 0.3\%$).

In accordance with the microstructure of SiC_p/Al-7Si composites, the aspect ratio S can be measured to be 1.38 and 1.94 for 4.5 μm SiC particle and 20 μm SiC particles, respectively. It can be calculated from formula (2) that composite with 20 μm SiC reinforcement exhibits the highest yield strength, which is consistent with the mechanical properties measured experimentally in literature [23], leading to a higher cyclic stress response.

In this study, the indirect strengthening mainly caused by the geometric dislocation resulted from the mismatch of the thermal expansion coefficient between the refractory-phase reinforced particles SiC and the deformable-phase Al-7Si alloy. Especially, the thermal expansion coefficient induced by smaller particles results in higher geometrically dislocation density, discussed in Ref. [21]. Consequently, the geometrically dislocation density of 4.5μmSiC_p/Al-7Si composite is greater than that of 20μmSiC_p/Al-7Si composite. Based on the constitutive relationship between shear flow stress and dislocation proposed by Fleck et al. [31],

$$\tau = \kappa G b \sqrt{\rho} \tag{3}$$

where G is the elastic modulus of Al-7Si alloy, GPa; κ is the scalar coefficient; b is the Burgers vector. Thus, the increase in dislocation density results in an increase in flow stress, namely, the yield strength of 4.5μmSiC_p/Al-7Si composite is greater than that of 20μmSiC_p/Al-7Si composite; in ordinary, the TMF behaviors have the same rule as yield strength. Similar results are also reported in Ref. [21]. However, the observations in cyclic stress response are different from the above accepted point, which could be predominantly correlated to the lower yield strength resulted from the formation of fine particle clusters [23]. Load transfers from the matrix to the SiC particles in the TMF process, but when the aggregated SiC particles form loose microstructure, crack initiation and propagation occur more easily, which accelerates the failure of the material. While SiC particles are distributed uniformly in the 20μmSiC_p/Al-7Si composite, cracks initiate the defects of particles. Reference [24] indicates that the SiC particles with small size result in void nucleation, increasing the low-cycle fatigue life at the high strain amplitude (>0.3%). In summary, the direct strengthening mechanism is dominant in Al-7Si alloy and SiC_p/Al-7Si composites.

4.3. The Effect of Si Content. Generally, the Si species, including primary Si phase and eutectic Si phase, differ from Si contents in composites, which results in different TMF properties. The microstructure of 4.5μmSiC_p/Al-Si composites shows that the volume fraction and average size of Si phase increase with an increase in Si content. The SEM images of the fracture surface on the TMF samples indicate two distinctly crack growth mechanisms of primary Si particle and eutectic Si, which are summarized in Figure 7. It can be described that the TMF cracks will propagate through the primary Si particles and along the interface between eutectic Si and α-Al matrix, which is related to the crack-tip driving forces [32]. Besides, continuous thermal cycle will result in expansion of Si particles and local microplasticity around the α-Al/Si interface accelerating the deformation of composites, the concept has also been reported in Ref. [22]. Therefore, in this study, the fracture modes of 4.5μmSiC_p/Al-7Si composite are debonding and aggregation of SiC particles, along with the detachment of eutectic Si phase, while for 4.5μmSiC_p/Al-13Si composite, the detachment of eutectic Si phase is the main fracture mode; meanwhile, the broken primary Si phases are very rare. The fracture tendency of primary Si increases with increasing Si content; thus, plenty broken primary Si phases can be seen for 4.5μmSiC_p/Al-20Si composite. In addition, the loading distribution between particles and matrix is largely decided by the Si interparticle distance, and the interparticle

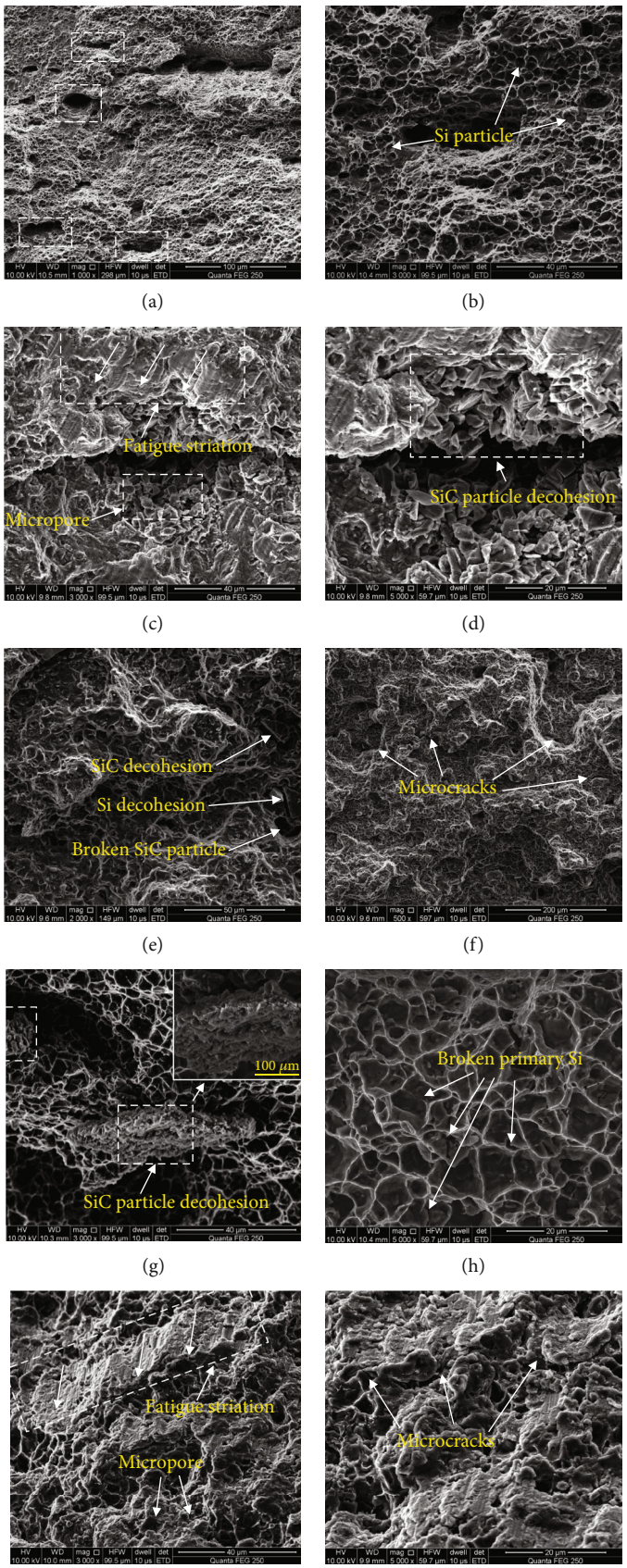

(a) (b) (c) (d) (e) (f) (g) (h) (i) (j)

Figure 6: SEM micrograph of samples of TMF fracture surface (a, b) Al-7Si; (c, d) 4.5μmSiC_p/Al-7Si; (e, f) 20μmSiC_p/Al-7Si; (g, h) 4.5μmSiC_p/Al-13Si; (i, j) 4.5μmSiC_p/Al-20Si.

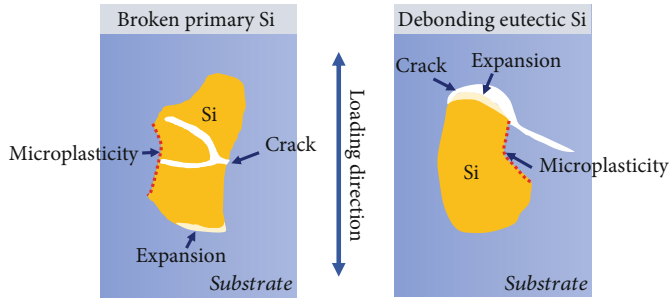

Figure 7: Schematic of the TMF crack growth mechanism.

distance of 4.5μmSiC$_p$/Al-20Si composite is the smallest. Once the plastic deformation occurs in the local matrix, Si phase can impede the dislocation sliding movement due to more difficult deformation than α-Al matrix, which can slow down the overall plastic deformation of composite. Therefore, 4.5μmSiC$_p$/Al-20Si composite possesses the best performance to resist the plastic deformation. Moreover, the stress amplitude of composite, which meets the movable dislocation amount bypassing the obstacles, increases with increasing Si content; therefore, the stress amplitude of 4.5μmSiC$_p$/Al-20Si composites is the highest.

When the composite is cooled from high temperature or processing, the α-Al matrix near the Si phase and SiC particles is easily deformed; thus, dislocations are generated, moved, and stored. The main reason of dislocation generation is differential thermal contraction at the Al-Si-SiC$_p$ interface due to the CTE mismatch among α-Al matrix, Si phase, and SiC particles [33, 34]. If the size and volume fraction of SiC particles is constant, the effect of Si content on the dislocation should be considered carefully. Figure 8 is the schematic of geometrically necessary dislocation model. Assuming that (1) the Al-Si-SiC interface is well-bonded and (2) Si particles and SiC particles are simplified as sphere, the strain gradient is produced in the transition area from the Si-phase interface to the region far away the interface in the matrix; thus, the geometrically necessary dislocation decreases with the increasing interparticle spacing, namely, the $\lambda/2$ in Figure 8. It can be examined that the interparticle distance (λ) of Si phase increases with Si content in Figure 2. In addition, the presence of strain gradient results in geometrically necessary dislocation to adapt to lattice distortion for composites, and the relationship can be expressed as formula (4) proposed by Arsenlis and Parks [35]:

$$\rho^{G} = \frac{N\eta}{b}, \tag{4}$$

where ρ^{G} is the geometrically necessary dislocation, N is the Nye factor, and usually $N = 2$ for polycrystalline materials, η is the strain gradient, and b is the Burgers vector. Therefore, the geometrically necessary dislocation increases as the strain gradient increases, the same to Si contents. Therefore, the dislocation density of 4.5μmSiC$_p$/Al-20Si composite is the greatest, which is the dominant reason of high-degree softening.

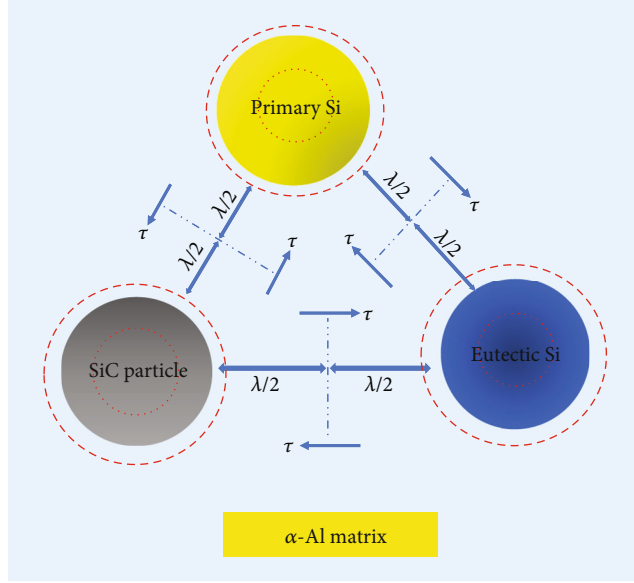

Figure 8: Schematic of geometrically necessary dislocation model.

5. Conclusion

The thermomechanical fatigue behaviors of spray-deposited SiC$_p$/Al-Si composites were investigated in terms of the size of SiC particles and the Si content in the temperature range of 150-400°C. The main findings are listed below:

(1) Hysteresis loop reveals that the stress amplitude of the first cycle life is greater than that of the half-life cycle for all samples, which means that softening occurs since the first cycle begins. And the maximum compressive stress is generally lower than the maximum tensile stress for the same materials during TMF loading process

(2) There exists a continuous cyclic softening in Al-7Si alloy and SiC$_p$/Al-Si composite. Both the increase in SiC particle size and Si content can aggravate the softening degree obviously, which is correlated with the dislocation generation in differential thermal contraction at the Al matrix/Si phase and Al matrix/SiC particles. Besides, the stress amplitude of SiC$_p$/Al-7Si composites increases with increasing SiC particle size or Si content, which is attributed to the abilities to meet the movable dislocation amount bypassing the obstacles

(3) The TMF life is remarkably enhanced by an increase in SiC particle size, which is associated with "load sharing" of the direct strengthening mechanism. Nevertheless, little or no influence on the TMF life is found through increasing Si content

(4) Compared to Al-7Si alloy and 4.5μmSiC_p/Al-7Si composite, 20μmSiC_p/Al-7Si composite presents a rougher fracture surface in the region of crack propagation. As Si content increases, the fracture tendency of primary Si increases, resulting in an increase in microcrack nucleation. The failure mechanism of SiC_p/Al-7Si composites reveals that the agglomeration of small-particulate SiC and the breakage of large-particulate SiC are the main crack initiation sites. The broken primary Si and the exfoliated eutectic Si accelerate the crack propagation

Data Availability

All data used to sustain the findings of this study are included in the article.

Conflicts of Interest

The authors declare that they have no conflicts of interest.

Acknowledgments

The authors received financial support from the National Natural Science Foundation of China (No. 51675058), the Key Scientific Research Project of the Education Department of Hunan Province (No. 16A002), the Science and Technology Innovation Project of Hunan Province (No. 2018RS3073) and the Natural Science Foundation of Hunan Province (No. 2018JJ3531), and the Double First-Class Scientific Research International Cooperation Project of Changsha University of Science and Technology (2019IC15).

References

[1] M. Kenisarin and K. Mahkamov, "Solar energy storage using phase change materials," *Renewable and Sustainable Energy Reviews*, vol. 11, no. 9, pp. 1913–1965, 2007.

[2] A. Adamowicz and P. Grzes, "Influence of convective cooling on a disc brake temperature distribution during repetitive braking," *Applied Thermal Engineering*, vol. 31, no. 14-15, pp. 2177–2185, 2011.

[3] C. Li, L. Qin, M. Li, H. Xiao, Q. Wang, and J. Chen, "Influence of deformation strain rate on the mechanical response in a metastable β titanium alloy with various microstructures," *Journal of Alloy Compounds*, vol. 815, article 152426, 2020.

[4] C. Li, H. Li, and S. van der Zwaag, "Unravelling the abrasion resistance of two novel meta-stable titanium alloys on the basis of multi-pass-dual-indenter tests," *Wear*, vol. 440-441, p. 203094, 2019.

[5] W. Li, Y. Ning, J. Chen, Y. Sun, Y. Hu, and J. He, "Investigation on microstructure and fatigue characteristics of spray-formed SiC_p/Al–20Si composite," *Transactions of the Indian Institute of Metals*, vol. 68, no. 5, pp. 769–775, 2015.

[6] W. Li, Y. Ning, J. Chen, Y. P. Sun, and C. Li, "Effect of Si content on microstructure and mechanical properties of the spray-formed SiC_p/Al–Si composites," *Powder Metallurgy and Metal Ceramics*, vol. 54, no. 5-6, pp. 298–303, 2015.

[7] W. Li, J. Chen, J. J. He et al., "Effect of the SiC particle orientation anisotropy on the tensile properties of a spray-formed SiCp/Al-Si composite," *Strength of Materials*, vol. 46, no. 2, pp. 221–228, 2014.

[8] W. Li, Z. H. Chen, D. Chen, and J. Teng, "Growth behavior of fatigue crack in spray-formed SiC_p/Al-7Si composite," *Acta Metallurgica Sinica*, vol. 47, no. 1, pp. 102–108, 2011.

[9] S. Y. Wang, Q. Tang, D. J. Li et al., "The hot workability of SiC_p/2024 Al composite by stir casting," *Materials and Manufacturing Processes*, vol. 30, no. 5, pp. 624–630, 2015.

[10] M. Günay and U. Şeker, "Evaluation of surface integrity during machining with different tool grades of Sic_p/Al-Si composites produced by powder metallurgy," *Materials Science Forum*, vol. 672, pp. 319–322, 2011.

[11] Y. P. Sun, J. Han, Y. Tu, Z. Bai, and Y. Q. He, "Microstructure and mechanical properties of a spray deposited SiC_p/Al composite processed by hot extrusion and equal channel angular pressing," *Materials Research Innovations*, vol. 18, Supplement 4, pp. S4-220–S4-223, 2014.

[12] E. J. Lavernia and N. J. Grant, "Spray deposition of metals: a review," *Materials Science and Engineering*, vol. 98, pp. 381–394, 1988.

[13] R. Yang, X. J. Wang, X. P. Wu, M. H. Chen, N. Liu, and Q. W. Li, "Progress in stir-casting process for fabricating SiC_p/Al composites," *Materials Review*, vol. 27, no. 9, pp. 131–136, 2013.

[14] W. B. Hu, C. C. Jia, B. F. Hu, and G. F. Tian, "The previous particle boundaries (PPB) of FGH96 superalloy and its effects on impact property," *Powder Metallurgy Technology*, vol. 30, no. 5, pp. 327–333, 2012.

[15] J. L. Estrada, "Microstructure characterization of Al-Si and MMCs preforms processed by spray atomization and deposition," *Journal of Materials Science*, vol. 33, no. 16, pp. 4029–4033, 1998.

[16] M. Karayaka and H. Sehitoglu, "Thermo-mechanical fatigue of metal matrix composites," *Low Cycle Fatigue and Elasto-Plastic Behaviour of Materials—3*, pp. 13–18, Springer, Netherlands, 1992.

[17] L. H. Qian, Z. G. Wang, H. Toda, and T. Kobayashi, "Thermo-mechanical fatigue of SiC whisker reinforced 6061Al composites: I. Stress and strain during cycling," *Acta Metallurgica Sinica*, vol. 37, no. 11, pp. 1198–1202, 2001.

[18] L. H. Qian, Z. G. Wang, H. Toda, and T. Kobayashi, "Thermo-mechanical fatigue of SiC whisker reinforced 6061al composites: II. Fatigue life and damage," *Acta Metallurgica Sinica*, vol. 37, no. 11, pp. 1206-1207, 2001.

[19] L. H. Qian, Z. G. Wang, H. Toda, and T. Kobayashi, "Effect of reinforcement volume fraction on the thermo-mechanical fatigue behavior of SiC_w/6061Al composites," *Materials Science and Engineering: A*, vol. 357, no. 1-2, pp. 240–247, 2003.

[20] L. U. Eun, "Thermal-mechanical fatigue of Ti-48Al-2V alloy and its composite," *Metallurgical and Materials Transactions A*, vol. 25, no. 10, article 2207, 1994.

[21] H. Sehitoglu, "The effect of particle size on thermo-mechanical fatigue of Al/SiC metal matrix composites," *Fatigue under*

Thermal and Mechanical Loading: Mechanisms, Mechanics and Modelling, pp. 371–380, Springer, Netherlands, 1996.

[22] M. Wang, J. C. Pang, M. X. Zhang, H. Q. Liu, S. X. Li, and Z. F. Zhang, "Thermo-mechanical fatigue behavior and life prediction of the Al-Si piston alloy," *Materials Science and Engineering: A*, vol. 715, pp. 62–72, 2018.

[23] W. Li, Z. H. Chen, D. Chen, J. Teng, and L. Changhao, "Understanding the influence of particle size on strain versus fatigue life, and fracture behavior of aluminum alloy composites produced by spray deposition," *Journal of Materials Science*, vol. 46, no. 5, pp. 1153–1160, 2011.

[24] L. A. Boatner, J. S. Neal, J. A. Kolopus, J. O. Ramey, and H. Akkurt, "The characterization of scintillator performance at temperatures up to 400 degrees centigrade," *Nuclear Instruments and Methods in Physics Research Section A: Accelerators, Spectrometers, Detectors and Associated Equipment*, vol. 709, pp. 95–107, 2013.

[25] W. Li, C. Jian, Y. Hu, L. Cong, Y. P. Sun, and J. M. Yang, "Cyclic fatigue fracture behavior of spray-deposited SiC_p/Al-Si composite," *Journal of Materials Engineering and Performance*, vol. 23, no. 8, pp. 2871–2876, 2014.

[26] W. Li, Z. H. Chen, D. Chen, J. Teng, and C. Fan, "Low-cycle fatigue behavior of SiC_p/Al-Si composites produced by spray deposition," *Materials Science and Engineering: A*, vol. 527, no. 29-30, pp. 7631–7637, 2010.

[27] D. J. Lloyd, "Particle reinforced aluminium and magnesium matrix composites," *International Materials Reviews*, vol. 39, no. 1, pp. 1–23, 1994.

[28] S. Elomari, M. D. Skibo, A. Sundarrajan, and H. Richards, "Thermal expansion behavior of particulate metal-matrix composites," *Composites Science and Technology*, vol. 58, no. 3-4, pp. 369–376, 1998.

[29] J. E. Allison and J. W. Jones, "Chapter 15 – fatigue behavior of discontinuously reinforced metal-matrix composites," *Fundamentals of Metal-Matrix Composites*, vol. 14, no. 3, pp. 269–294, 1993.

[30] V. C. Nardone and K. Prewo, "On the strength of discontinuous silicon carbide reinforced aluminum composites," *Scripta Metallurgica*, vol. 20, no. 1, pp. 43–48, 1986.

[31] N. A. Fleck, G. M. Muller, M. F. Ashby, and J. W. Hutchinson, "Strain gradient plasticity: theory and experiment," *Acta Metallurgica et Materialia*, vol. 42, no. 2, pp. 475–487, 1994.

[32] K. Gall, N. Yang, M. Horstemeyer, D. L. McDowell, and J. Fan, "The debonding and fracture of Si particles during the fatigue of a cast Al-Si alloy," *Metallurgical and Materials Transactions A*, vol. 30, no. 12, pp. 3079–3088, 1999.

[33] M. Kouzeli and A. Mortensen, "Size dependent strengthening in particle reinforced aluminium," *Acta Materialia*, vol. 50, no. 1, pp. 39–51, 2002.

[34] R. J. Arsenault and N. Shi, "Dislocation generation due to differences between the coefficients of thermal expansion," *Materials Science and Engineering*, vol. 81, pp. 175–187, 1986.

[35] A. Arsenlis and D. M. Parks, "Crystallographic aspects of geometrically-necessary and statistically-stored dislocation density," *Acta Materialia*, vol. 47, no. 5, pp. 1597–1611, 1999.

Hindawi
International Journal of Photoenergy
Volume 2020, Article ID 3846157, 8 pages
https://doi.org/10.1155/2020/3846157

Research Article

Investigation to Improve the Pool Boiling Heat Transfer Characteristics Using Laser-Textured Copper-Grooved Surfaces

Dharmendra Mani,[1] Suresh Sivan ,[1] Hafiz Muhammad Ali,[2] and Udaya Kumar Ganesan[3]

[1]*Nanotechnology Research Laboratory, Department of Mechanical Engineering, National Institute of Technology, Tiruchirappalli 620015, India*
[2]*Department of Mechanical Engineering, King Fahd University of Petroleum and Minerals, Dhahran, Saudi Arabia*
[3]*Two-Phase Flow Laboratory, Department of Mechanical Engineering, Kookmin University, Seoul, Republic of Korea*

Correspondence should be addressed to Suresh Sivan; ssuresh@nitt.edu

Received 18 November 2019; Accepted 27 December 2019; Published 4 February 2020

Guest Editor: Chuanchang Li

Improving the performance of pool boiling with critical heat flux of pool boiling and enhancing the coefficient of heat transfer through surface modification technique have gained a lot of attention. These surface modifications can be done at different scales using various techniques. However, along with the performance improvement, the durability and stability of the surface modification are very crucial. Laser machining is an attractive option in this aspect and is gaining a lot of attention. In the present experimentation research work, pool boiling attributed performance of copper-grooved surfaces obtained through picosecond laser machining method is investigated. The performance of the modified surfaces was compared with the plain surface serving as reference. In this, three square grooved patterns with the same pitch (100 μm) and width (100 μm) but different depths (30, 70, and 100 μm) were investigated. Different depths were obtained by varying the scanning speed of the laser machine. In addition to the microchannel effect, the grain structuring during the laser machining process creates additional nucleation sites which has proven its effectiveness in improving the pool boiling performance. In all aspects, the pool boiling performance of the grooved laser-textured surface has showed increased surface characterisation as compared with the surface of copper.

1. Introduction

Pool boiling is a complex methodology associated with heat transfer in which the boiling surface is immersed and exposed to the pool of saturated liquid and the transfer of heat occurs on the heating element surface. It is also possible to enhance the heat transfer by surface modification [1]. The latent heat of vaporisation is the reason for the observation of high heat transfer coefficient that occurred in the boiling process. Nucleate boiling is a highly efficient process for removal of large quantities of heat from heated surface with minimal variation in surface temperature [2]. Notable applications of this process are two-phase heat exchangers and evaporators, boilers and steam generators, electronics cooling, nuclear fuel reactors, etc. [3]. The most important pool boiling heat transfer process techniques include heat transfer coefficient (HTC), superheat boiling incipience temperature, and the critical heat flux (CHF). Efforts are made in process to lower various parameters which include increasing the CHF, boiling incipience superheat, and HTC [4].

In the past decades, researchers have focused much attention on the development of surface modification techniques. It is considered as the boiling phenomenon profoundly depends upon the surface and its interaction with the fluid used. The effect could enhance the pool boiling parameters of both the HTC and the CHF [5]. Surface modification at different scales is gaining a lot of attention among researchers to enhance the heat transfer characteristics of pool boiling. These structures modify the surface morphology, surface roughness, and the wettability of the surfaces. Although these techniques produce improved performance, their durability and endurance are a serious issue and this necessitates the application of durable surface modification methods. Laser machining is an effective method to modify the boiling surface, and many works are reported in this aspect [6].

The micro/nanostructure of pool boiling surfaces and the wettability effect on the surfaces can be altered using laser texturing. Functionalized metallic surfaces can be generated using an ultrafast picosecond laser processing technique which modifies the pool boiling heat transfer process by the creation of self-controlled micro/nanostructures by machining [7]. In this study, we focus on investigating the effect of cross-linked grooves in heat transfer associated with pool boiling. Most importantly, the effect of the depth of grooves is investigated in this experimental work. Grooves with constant width and pitch and with different depths were fabricated on copper surface using picosecond laser texturing. Investigation of surfaces processed with laser machining is already carried out by several researchers in the past, and they found improved pool boiling performance. Piasecka [8] conducted a study on the enhancement of heat transfer by boiling of FC-72. A laser microdrilling technique is applied in this technique to create a microchannel on the Haynes-230 alloy-based metal foil for flowing of FC-72, which could enhance the boiling performances. The 355 nm wavelength of a Nd:YAG laser emitting light is used to cover and drill the matrix of grooves on the Haynes-230 alloy-based metal foil. Materials melted as a circle-shaped layer that is micro grooved with input diameter as 10 μm and depth 3-2 as μm are uniformly arranged on both directions for every 100 μm which results in the boiling incipience that occurred for the heat fluxes inferior to the plain metal foil. This forms the augmentation of heat flux due to the boiling incipience which occurred earlier from the examined surfaces.

Sommers and Yerkes [9] investigated on the comparative studies in the enhancement of flow boiling performance via convective heat transfer using R-134a working fluid on aluminium surfaces through two distinct techniques: laser ablation and reactive ion etching. About 90-100% of pool boiling HTC is enhanced on Al metal surfaces by laser ablation. The laser-ablated surface pool boiling HTC is higher than the reactive ion-etched aluminium surface pool boiling HTC and also very higher than the bare metal surface. Kruse et al. [10] performed an experimental investigation on the functionalized multiscale micro/nanostructured metallic surfaces of pool boiling heat transfer. A femtosecond laser surface process (FLSP) technique is used for the fabrication of the mount-like multiscale micro/nanostructures, which are coated layer by layer by the self-arranged nanoparticles. The maximum CHF (142 W/cm^2) and the maximum HTC (67,400 W/m^2 K) at 29°C are obtained for the processed samples. These obtained high CHF and high HTC are exaggerated by the increase of both nucleation associated with site density and surface areas. These are the highlighted major reasons for upgraded CHF and heat transfer.

Zupančič et al. [11] conducted a study on the effect of pool boiling on biphilic surfaces. The pool boiling effect is induced on the boiling surfaces by the formation of biphilic surfaces on stainless steel foil, which are fabricated using laser treatment. Initially, the pool boiling surfaces (stainless steel foil) are highly coated with hydrophobic coating in nature. Subsequently, the hydrophobic-coated boiling surfaces are surface modified by the laser treatment which gets altered into superhydrophilic surfaces. A high CHF (350%) is achieved for the laser-treated biphilic surface than bare stainless steel foil. The nucleated bubble diameter is reduced, and further, the nucleation frequency is increased by the design of smaller hydrophobic spots. However, the boiling incipience and high HTC are promoted with larger hydrophobic regions at low heat fluxes. The homogeneous and inhomogeneous wettable surfaces are patterned on the surface of the boiling heat transfer by laser texturing, and the effect on homogeneous and inhomogeneous wettable surfaces is investigated. It is found that the enhancement of pool boiling behaviour is more effective and highly activated in inhomogeneous wettability [12].

Grabas [13] examined the heat transfer effect by pool boiling on laser-melted surface with DDH_2O as working fluid. This laser melting procedure has been found to modify the surface roughness of the boiling surface to a greater extent, and the result has been obtained as more than four-fold enhancement in the HTC and CHF. Recently, many other works were reported involving laser-treated surfaces and their effect on the pool boiling heat transfer technique. Hence, it is clearly stipulated that laser-treated surfaces are highly efficient in improving the pool boiling performance. Thus, this work provides a novel approach to study the effect of laser-treated surfaces to optimize the depth of the grooves using picosecond laser machining which changes the wettability of the working fluid to obtain superhydrophilic surface. This study conducts the pool boiling heat transfer studies on laser-textured surface with different depths of grooves and concluded the pool boiling heat transfer enhancement in contrast to bare copper surface.

2. Pool Boiling Experimental Setup

Experimentations were performed on copper surface with bare medium in association with laser-treated surfaces along the experimental setup which was modelled and fabricated to study the pool boiling characteristics involving with DI H_2O as working fluid. The experimental setup as shown in Figure 1 has the arrangements which include boiling chamber, heat input system, data acquisition system, and temperature and pressure modulator systems. The heat input arrangement consists of blocks of copper which are embedded with six cartridge heaters (WATLOW Firerod) on the bottom side of the copper block, so as to produce constant heat flux. Regulated DC power supply is used to operate the cartridge heaters to heat the copper block. To eliminate the heat losses in radial direction, the copper heater block was insulated with Teflon fittings which confirmed the conduction of heat flow for the temperature in one dimension at various heat fluxes. It can be ensured by its linearity which is obtained that R^2 is 1 at various heat flux values. A stepped copper sample of 5 mm top radius was considered as test specimen. The bottom of the test specimen was perfectly aligned with high thermal conductive paste ($k = 2.7$ W/mK) on the top of the copper heater block of test specimen and heater block. Thereby, thermocouples (K-type) with a dimension of radius 0.5 mm and accuracy of ±0.5°C were inserted to calculate the heat flux in axial direction of the

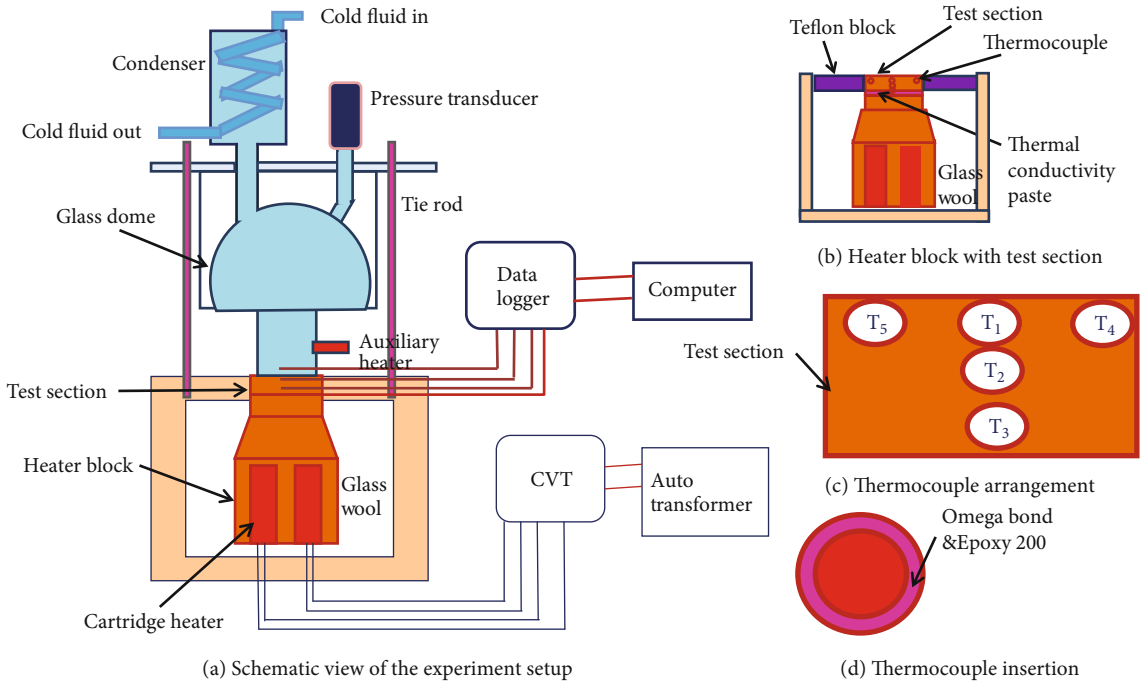

Figure 1: Pool boiling experimental setup.

copper test specimen. The copper specimen surface temperature can be observed by these readings from thermocouples; it is used to find out the heat flux, temperature gradient, and heat transfer coefficient as well.

Saturated condition of the water was attained by secondary heater (500 W) which is fixed inside the boiling chamber. The secondary heater is used to maintain the saturated critical point of boiling fluid by using a temperature controller which receives the temperature of boiling fluid through RTD. The chiller unit and condenser coil were used to maintain the boiling chamber in an atmospheric pressure condition by condensing the evaporating vapor, and this arrangement is used to maintain the boiling fluid of the chamber at standard level. During the experiments, pressure in the boiling chamber is continuously monitored by the pressure transmitter (WIKA, S-10). Thermocouple and pressure sensor readings were recorded by a data logger with the use of a computer. Condenser coil, pressure transmitter, and a RTD were strongly fixed in the chamber lid as well to avoid flow of vapor to the outside of the chamber.

3. Experimental Procedure

Initially, filled DI water in the boiling chamber was heated to remove noncondensable gases. After removal of gases, a chiller was employed to maintain the liquid level and the chamber pressure. As liquid reaches the saturation condition, the cartridge heaters were supplied with power. Bubble incipience event was captured by a high-speed camera. Once the boiling initiates, the temperature values were noted for all heat flux increment at steady state conditions. While taking reading, the auxiliary heater was switched off to avoid turbulence. A sudden temperature shoot in the surface was observed. Resemblance to the heat flux prior to the point is considered as the critical heat flux. This procedure is repeated for all the modified surfaces, and the performance was compared. Thermal linear test was conducted in the heating chamber to confirm the one-dimensional heat conduction. Also, repeatability test was confirmed by carrying out the boiling test for three times for each individual surface.

4. Data Analysis

The copper heater block cylindrical side was tightly insulated with Teflon fitting and glass wool to ensure the conduction of heat in one dimension. The performance of pool boiling can be investigated with the help of heat flux, surface temperature, and heat transfer coefficient. As the experimental condition states, the heat conduction in one dimension results in determining the heat flux by calculating the gradient of temperature in axial direction of the testing specimen by Equation (1) [14]

$$q = -k\frac{dT}{dx}, \tag{1}$$

where k stipulates thermal conductivity of copper (390 W/mK), slope temperature (dT/dx) can be retrieved from the approximation series (Taylor backward series) as in equation (2), and q is the critical heat flux to the projected area (W/cm^2) of copper specimen.

$$\frac{dt}{dx} = \frac{3T_1 - 4T_2 + T_3}{2\Delta x}, \tag{2}$$

where temperatures of T_1, T_2, and T_3 can be calculated for the distance x between the thermocouples which are fixed axially along the copper test specimen (3 mm distance

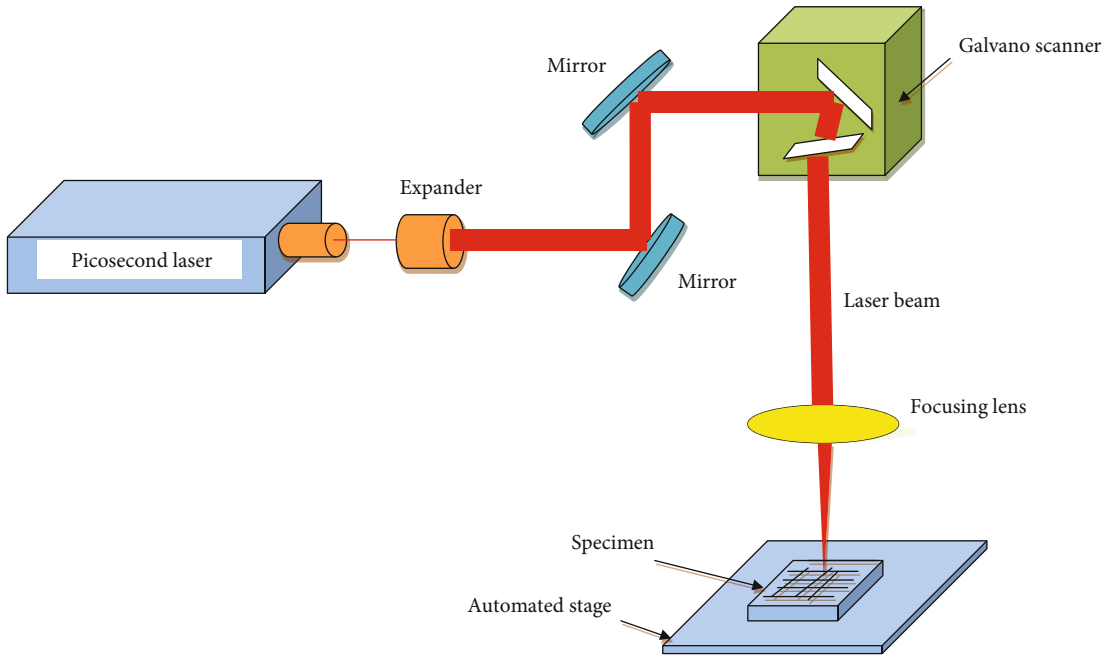

Figure 2: Schematic representation of the picosecond laser surface processing facility.

between T_1, T_2 and T_2, T_3). One-dimensional heat conduction equation can be rearranged to measure the surface temperature of the copper test specimen using Equation (3),

$$T_s = T_1 + q\frac{t}{K}. \tag{3}$$

T_1 is the measured temperature by the thermocouple which has been embedded at 3 mm distance from the top of the surface of the copper test specimen. Equation (4) is used to calculate the coefficient of heat transfer for convective boundary layer with respect to heat flux and temperature difference between surface and fluid [15].

$$h = \frac{q}{(T_s - T_f)}, \tag{4}$$

where T_s is the surface temperature and T_f is the temperature of the fluid at the saturated condition.

5. Fabrication of Modified Surface

A schematic representation of the picosecond laser facility is shown in Figure 2 To attain the grooved surfaces, picosecond-pulsed Nd:YAG laser with the wavelength 532 nm, pulse frequency 45 kHz, pulse width 650 ps, and beam diameter 90 μm was employed in this study. The depth of the microgrooves was changed by varying the output power (0.7, 1.5, and 2.9 J/cm^2) of the laser [1]. The output power of the picosecond laser was kept constant at 3 W and scanning speed at 30 mm/s. In this experiment, we have varied the number of pass as 1, 3, and 5 to obtain different depths. The specimens were placed on a programmable computer-controlled automated motion stage. During laser structuring, the specimen was placed in a well-sealed chamber under ambient conditions. It should be noted that the samples are placed in atmospheric conditions before and after the laser irradiation. Scan separation line or pitch which is denoted by "a" resembles the distance between two adjacent laser lines. Similarly, width and depth of the laser lines are denoted as "w" and "d," respectively. In this case, three modified surfaces with constant width and pitch and varying depths were used as shown in Table 1.

Table 1: Dimensions of modified surfaces.

Name	Pitch (μm)	Width (μm)	Depth (μm)	No. of pass
LTs_1	100	100	30	1
LTs_2	100	100	70	3
LTs_3	100	100	100	5

Figure 3 resembles the optical image of the laser-textured surfaces. We can clearly see the cross-linked grooved patterns. The wettability tests indicated that all the modified surfaces were hydrophilic in nature and the wettability has considerably increased as compared to the copper surface with plane textures.

Figure 4 shows scanning electron microscopy images of the laser-textured surface which were observed using SEM technique. Since LTs_1 has a depth of 80 microns which is the least of the three samples, the melted copper flows without much obstruction which provides smooth surfaces (in other words, less protrusions or less relative roughness). However, the LTs_2 sample has a depth of 100 microns which does not allow the flow easily. Hence, the resulting protrusions in these samples are more. In LTs_3, the depth of the sample is further increased to 120 microns. Not only

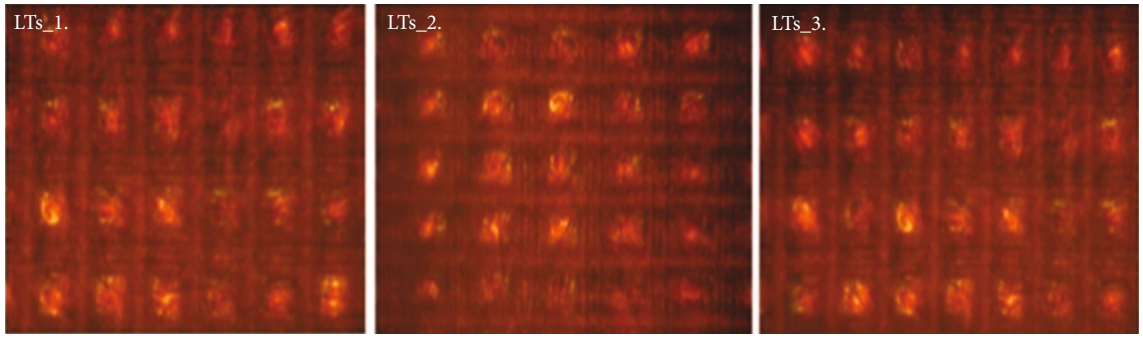

Figure 3: Optical images of laser-textured surfaces.

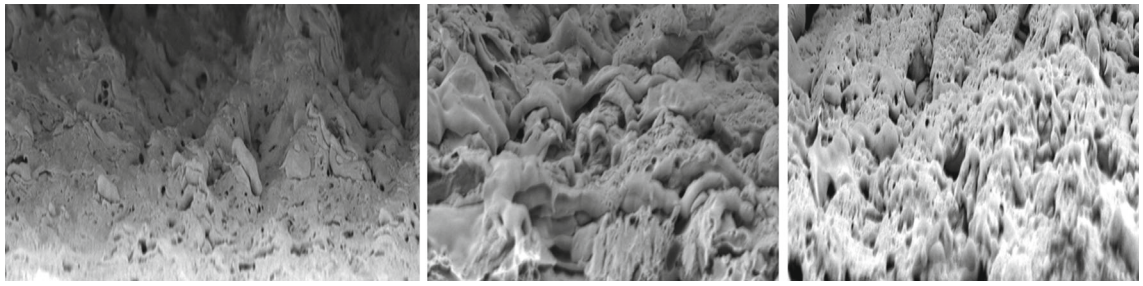

Figure 4: SEM images of laser-textured surface.

is the melted copper obstructed, but the dendrite formation also coagulated to form deeper protrusions (in other words, the relative roughness increases).

6. Results and Discussion

The basic objective is to enunciate the effect of pool boiling heat transfer characteristics on laser-textured grooved surfaces. These grooved surfaces have been fabricated using picosecond laser surface processing which formulates the surface roughness on both the micrometer and nanometer scales [16]. During the boiling process, cavities formed due to surface roughness which influences the bubble dynamics by removing the heat from the laser-textured surface. The depth of laser-textured surfaces was influenced by the density and size of the cavities. Thus, the role of the depth of laser-textured surfaces is interesting to examine the pool boiling heat transfer performance. Bare copper and three laser-textured surfaces with variable depth (~30 μm, ~70 μm, and ~100 μm) were used to conduct the experiments to observe the pool boiling performance. Experiments were conducted initially for very low heat flux, and further considerable increase of heat flux was incremented slowly until it reaches the critical heat flux in all sample surfaces.

Boiling performance of the laser-textured surfaces was compared by treating DI water as fluid with the baseline for the bare copper surface. Figures 5 and 6 clearly explain the performance of pool boiling for different laser-textured surfaces and bare copper surface. There is a drastic difference between the heat transfer characteristics of processed and unprocessed surfaces which can be analysed through Figures 5 and 6. At every surface temperature, processed surface pool boiling performances were consistently improved than those of unprocessed surface. It is evidenced that the laser-textured surfaces have shown better boiling performance than bare copper surface as its curves moved towards leftward and upward.

Boiling incipience superheat initiates the bubble generation for the laser-textured surfaces at very low wall superheat values than bare copper surface as well. Figure 5 indicates that the boiling incipience which occurs in the bare copper surface was around 10.9°C; equivalent heat flux of 7.7 W/cm^2 but at 7.0°C boiling initiates for laser-textured surface LTs_1 and further decreases with the increase in the depth of grid textured to 6.3°C and 5.2°C for corresponding laser-textured surfaces LTs_2 and LTs_3, respectively. The percentage of boiling incipience of the depth of the grid laser-textured surfaces is reduced with bare surface to 33.9%, 42.2%, and 52.2%, respectively.

Nucleation site density has the major role to reduce the percentage of boiling incipience superheat for laser-textured surfaces [17]. Due to laser texturing, melting of metal takes place which results into solidification as nanocrystals [18]. Also, the grooved area influenced the nucleation sites with increases in surface area. This increases the nucleation sites as a whole. Laser texturing on the copper surface increases the occurrence of a large number of cavities which produce the results as discussed above. These cavities increase the

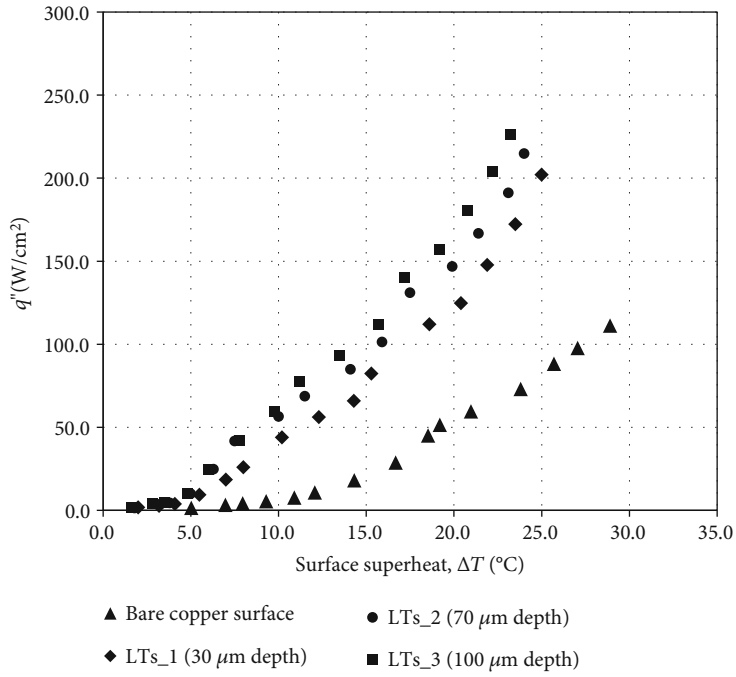

Figure 5: Heat flux variation with superheated surface for plain copper surface and laser-textured surfaces.

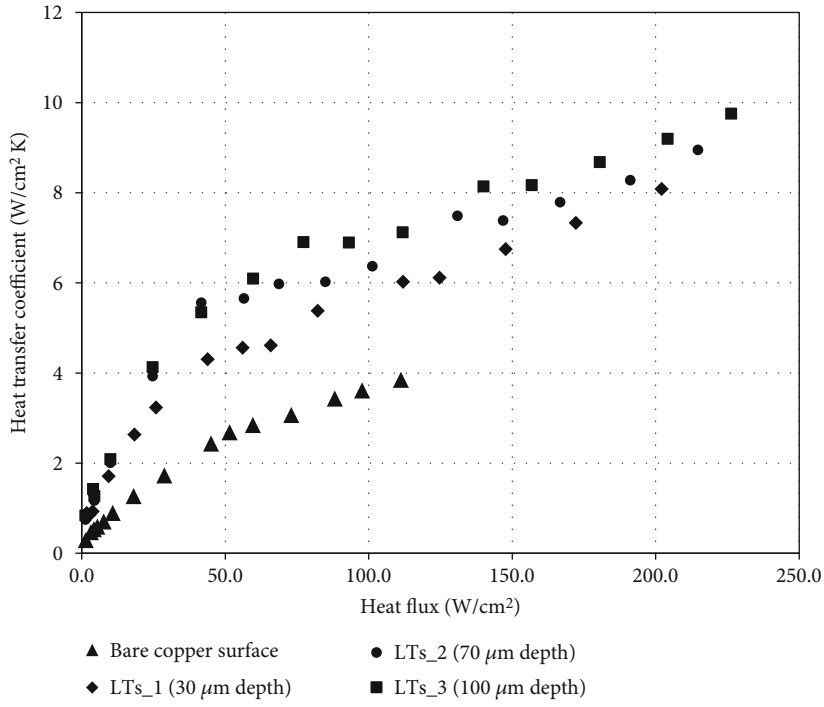

Figure 6: Heat transfer coefficient variation concerning with heat flux.

number of air entrapment sites which leads to the reduction of the percentage of the boiling incipience superheat. Nano- and microscale features on the processed surfaces increase the large number of micron-sized cavities which generate more nucleation sites that gets activated with lesser energy. The number of effective nucleation site can be increased while the depth of laser-textured surface increases with wide range of cavity sizes. This formulates to create more active sites of nucleation easily under low surface superheat values. Safer limit to operate heat transfer enhancement in pool boiling technique was up to reach the CHF.

Figure 5 clearly indicates that the CHF values for the laser-textured surface are increased with reference to the bare copper surfaces. CHF for bare copper surface was 111.3 W/cm^2 at

the superheated surface of 28.9°C, while the percentage increase of CHF for laser-textured surface is 81.5%, 92.9%, and 103.3% corresponding to the surfaces LTs_1, LTs_2, and LTs_3, respectively. From Figure 5, the surface superheat temperature was reduced for different laser-textured surface. It is clearly observed that the bare copper surface significantly decreases in which the surface superheat was observed and this reduction is improved further with an increase in the depth of laser-textured surfaces. This obviously stated that the increasing depth of laser-textured surface has an optimistic effect on the improvement of CHF. Microstructure geometry can further explain the reason why laser-textured surface has more CHF values. From Figure 3, the area between the microstructures increases from the samples LTs_1 to LTs_3. Among the samples, LTs_3 has more area by the formation network by densely packed deep valley structures, narrow channels, and micro cracks which formed between microstructures. During the machining, picosecond laser has settled more nanoparticles in the network channels of the microstructures on LTs_3 due to its higher depth when compared to LTs_2 and LTs_1. It develops elevated capillary wicking effects to speedy top up the heated surface using cold fluid followed by the occurrence of local evaporation causing the delay of critical heat flux. Conversely, in other samples, channels are not formed properly due to increased microstructure size which results in deep pit formation between microstructures. Wicking potential of the surface is reduced due to the formation of deep pits and holes, and the presence of a nanoparticle layer covering the mound structure dominates the wicking effect. The highest CHF value of 226.3 W/cm^2 was observed in the LTs_3 sample even if it had a larger peak valley height. But the wicking ability that is lacking due to the larger microstructure spacing of the LTs_3 sample can be compensated by the dense microstructure of the surface area. Hence, the capillary wicking effect and surface wettability of the surfaces cause the enhancement of CHF for the laser-textured surface.

Laser-textured surfaces also enhance the value of heat transfer coefficient in comparison to the results shown for bare copper surface. From Figure 6, it clearly indicates that increasing the depth of laser texture on the copper surface increases the heat transfer coefficient and was found to be 3.85 W/cm^2K. The percentage increase in the HTC for LTs_1, LTs_2, and LTs_3 with bare copper surface is 109.9%, 132.4%, and 153.4%, respectively. The formation of microstructures during the picosecond laser machining on the copper surface acts like cooling fins to remove the heat from the surface. As the height of the microstructures increased, heat removal from the surface has also increased which has improved the cooling of the surface efficiently, and thus, HTC is increased. HTC's value is consistently higher for the LTs_3 sample than the LTs_1 and LTs_2 samples. The overall enhancement of the HTC of the surface is promoted with an increase in the cavity density and capable nucleate boiling. The slope of the curves which increased over than the divergent point (120 W/cm^2) is related with the peak valley height of the microstructure. It can be seen that the slope change in the curve increases with the increasing of the height of the microstructure. During high heat fluxes, to activate the enhancement of heat transfer coefficients, laser-textured grooved surfaces are activated by the mixture of higher surface area ratio and prominent nature of tall microstructures as well as higher nucleation sites.

7. Conclusion

The experimental investigation for pool boiling heat transfer performance was studied by influencing the effect of depth in laser-textured grooved surfaces. Also, it results in the increases of CHF and HTC in the case of the laser-textured surfaces. It has been proved that the characteristics of CHF and heat transfer coefficients can be increased with the increase in depth of grooves of the laser-textured surface. The boiling incipience temperature is ultimately getting reduced by the cavities with micron size which act as nucleation sites for boiling.

Data Availability

The data used to support the findings of this study are available from the corresponding author upon request.

Conflicts of Interest

The authors declare that they have no conflicts of interest.

Acknowledgments

The authors would like to acknowledge the ASME 2019 ICNMM 17th International Conference on Nanochannels, Microchannels, and Minichannels for accepting the topic in their prepresentation poster.

References

[1] D. Venkata Krishnan, G. Udaya Kumar, S. Suresh, M. Jubal, M. R. Thansekhar, and R. Ramesh, "Wetting transition in laser-fabricated hierarchical surface structures and its impact on condensation heat transfer characteristics," *International Journal of Heat and Mass Transfer*, vol. 140, pp. 886–896, 2019.

[2] J. Voglar, M. Zupančič, A. Peperko, P. Birbarah, N. Miljkovic, and I. Golobič, "Analysis of heater-wall temperature distributions during the saturated pool boiling of water," *Experimental Thermal and Fluid Science*, vol. 102, pp. 205–214, 2019.

[3] S. P. Rodrigues, C. F. A. Alves, A. Cavaleiro, and S. Carvalho, "Water and oil wettability of anodized 6016 aluminum alloy surface," *Applied Surface Science*, vol. 422, pp. 430–442, 2017.

[4] A. Karthikeyan, S. Coulombe, and A. M. Kietzig, "Boiling heat transfer enhancement with stable nanofluids and laser textured copper surfaces," *International Journal of Heat and Mass Transfer*, vol. 126, pp. 287–296, 2018.

[5] G. Liang and I. Mudawar, "Review of pool boiling enhancement by surface modification," *International Journal of Heat and Mass Transfer*, vol. 128, pp. 892–933, 2019.

[6] L. Ventola, L. Scaltrito, S. Ferrero, G. Maccioni, E. Chiavazzo, and P. Asinari, "Micro-structured rough surfaces by laser etching for heat transfer enhancement on flush mounted heat sinks," *Journal of Physics: Conference Series*, vol. 525, no. 1, 2014.

[7] H. S. Ahn, H. J. Jo, S. H. Kang, and M. H. Kim, "Effect of liquid spreading due to nano/microstructures on the critical heat flux during pool boiling," *Applied Physics Letters*, vol. 98, no. 7, article 071908, 2011.

[8] M. Piasecka, "Flow boiling heat transfer in a minichannel with enhanced heating surface," *Heat Transfer Engineering*, vol. 35, no. 10, pp. 903–912, 2013.

[9] A. D. Sommers and K. L. Yerkes, "Using micro-structural surface features to enhance the convective flow boiling heat transfer of R-134a on aluminum," *International Journal of Heat and Mass Transfer*, vol. 64, pp. 1053–1063, 2013.

[10] C. M. Kruse, T. Anderson, C. Wilson et al., "Enhanced pool-boiling heat transfer and critical heat flux on femtosecond laser processed stainless steel surfaces," *International Journal of Heat and Mass Transfer*, vol. 82, pp. 109–116, 2015.

[11] M. Zupančič, M. Steinbücher, P. Gregorčič, and I. Golobič, "Enhanced pool-boiling heat transfer on laser-made hydrophobic/superhydrophilic polydimethylsiloxane-silica patterned surfaces," *Applied Thermal Engineering*, vol. 91, pp. 288–297, 2015.

[12] M. Zupančič, M. Može, P. Gregorčič, and I. Golobič, "Nanosecond laser texturing of uniformly and non-uniformly wettable micro structured metal surfaces for enhanced boiling heat transfer," *Applied Surface Science*, vol. 399, pp. 480–490, 2017.

[13] B. Grabas, "Vibration-assisted laser surface texturing of metals as a passive method for heat transfer enhancement," *Experimental Thermal and Fluid Science*, vol. 68, pp. 499–508, 2015.

[14] G. Udaya Kumar, K. Soni, S. Suresh, K. Ghosh, M. R. Thansekhar, and P. Dinesh Babu, "Modified surfaces using seamless graphene/carbon nanotubes based nanostructures for enhancing pool boiling heat transfer," *Experimental Thermal and Fluid Science*, vol. 96, pp. 493–506, 2018.

[15] M. Dharmendra, S. Suresh, C. S. Sujith Kumar, and Q. Yang, "Pool boiling heat transfer enhancement using vertically aligned carbon nanotube coatings on a copper substrate," *Applied Thermal Engineering*, vol. 99, pp. 61–71, 2016.

[16] B. Wang, Y. Hua, Y. Ye, R. Chen, and Z. Li, "Transparent superhydrophobic solar glass prepared by fabricating groove-shaped arrays on the surface," *Applied Surface Science*, vol. 426, pp. 957–964, 2017.

[17] C. H. Wang and V. K. Dhir, "On the gas entrapment and nucleation site density during pool boiling of saturated water," *Journal of Heat Transfer*, vol. 115, no. 3, pp. 670–679, 1993.

[18] S. Vemuri and K. J. Kim, "Pool boiling of saturated FC-72 on nano-porous surface," *International Communications in Heat and Mass Transfer*, vol. 32, no. 1–2, pp. 27–31, 2005.

Hindawi
International Journal of Photoenergy
Volume 2020, Article ID 2478579, 7 pages
https://doi.org/10.1155/2020/2478579

Research Article

Calculation Method of Specific Surface Area of Foam Metal Based on an Ideal Tetradecahedron Model for Lithium Ion Battery

Jian Chen,[1] Xiao Zhang,[1] Cong Li,[1,2] Xinyuan Zhang,[1] Yanjie Ren,[1] Jianjun He,[1] and Jianlin Chen[1]

[1]*School of Energy and Power Engineering, Changsha University of Science and Technology, Changsha 410014, China*
[2]*Guanxi Key Laboratory of Electrochemical Energy Materials, Guangxi University, Nanning 530004, China*

Correspondence should be addressed to Cong Li; liconghntu@csust.edu.cn

Received 4 December 2019; Accepted 10 January 2020; Published 28 January 2020

Guest Editor: Hafiz M. Ali

A novel calculation method of specific surface area of tetrahedral foam metal is established. The expressions of the two basic parameters of the foam metal with respect to porosity and pore size are derived by using the geometrical relationship of this model; consequently, the specific surface area of the metal foam is easily calculated. The theoretical calculation data are compared with the experimental results; it shows that the specific surface area of various porous metals, such as nickel foam and copper foam prepared by electrodeposition and aluminum foam produced by high-pressure infiltration casting, can be well calculated by the formula proposed in this paper. Compared with other similar equations, the calculation results of this method possess lower deviation and greater practicability.

1. Introduction

Facing the double pressure of global environmental pollution and fossil fuel depletion, the development and utilization of renewable clean energy and high-efficient energy storage technology have become the main theme in this century. Lithium ion battery is recognized as an efficient secondary battery. After 30 years of development, lithium ion battery has been widely used in a variety of portable electronic devices. Foam metal is expected to become a potential electrode material for lithium ion batteries due to its excellent properties such as high porosity, high specific surface area, and low bulk density. The excellent performance of porous metals in silencing, separation, filtration, heat exchange, electrochemical processes, and catalytic reaction engineering strongly depends on the structural morphology of surfaces and the specific surface area of porous materials [1–5]. Therefore, the determination of its specific surface area has increasingly attracted the attention of relevant scholars. The specific surface area of a material refers to the surface area per unit volume or unit mass, the former being a volume specific surface area and the latter being a mass specific surface area. For corrosion performance, it could obtain accurate results by combining the results of surface area and corrosion morphology and can also compare the difference of corrosion behavior between diverse metal foams qualitatively [6]. For fatigue performance, the mechanical properties are directly influenced by two main parameters, including porosity and pore diameter, which determine the surface area of metal foams. Thus, it suggests that there are numerical links between surface area and fatigue performance of porous metal materials [7, 8]. At present, methods for measuring the specific surface area of porous materials include gas adsorption, mercury intrusion, and fluid permeation. Among them, the fluid permeation method is better than the gas adsorption method in terms of the upper and lower limits of measurement and measurement range [9–11]. The mercury intrusion method is a simplified calculation of the specific surface area of the pore body after the pore is assumed to be a uniform cylinder and has a certain error. In reality, the experimental measurement of the specific surface area of materials is often affected by factors such as sample states and equipment conditions, and the theoretical calculations are limited to simple cases where the porosity and pore size

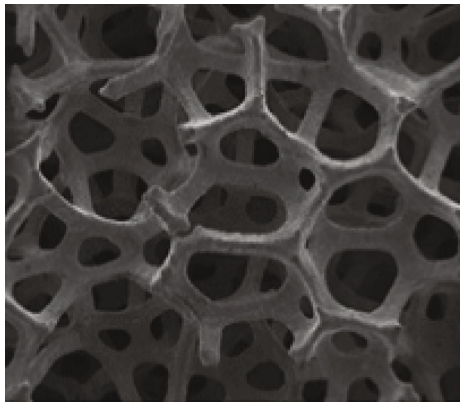

Figure 1: Microscopic geometry of foamed copper under electron microscopy.

are known [12]. Therefore, there is an urgent need to develop a specific area measurement or calculation method that is accurate and can be universally applied to practice. Porosity and pore size are basic properties of porous materials and can be determined directly or simply measured [13]. Until now, some researchers have done investigation on the calculation of specific surface area of foam materials, but there are some limitations in practical applications [14, 15]. Liu [16] calculated the specific surface area of the foam metal based on the ideal model of the regular octahedron, but it still needs further improvement in accuracy. Based on the dodecahedron model, Duan et al. [17] provided a method for calculating the specific surface area of foamed metal. However, this method requires measuring the width of the pores first, and the calculation procedure is cumbersome. Based on the above situation, a calculation method which is related to the pore size and porosity for estimating the specific surface area of porous metal based on the tetrakaidecahedron model is proposed.

2. Theoretical Models and Expressions

The high-porosity porous metal can be assumed to be an irregular three-dimensional network structure connected by filamentous metals. The shapes of pores are different, and the struts are interlaced. The directions of the struts in the material are different. However, in an isotropic porous material, the distribution angle of the inner wires is equal. The structural model is simplified to an isotropic high-porosity metal material according to the comprehensive properties of the porous material. An observed microstructure under an electron microscope is shown in Figure 1; it can be seen that the porous material is composed of a large number of small cells; a tetradecahedron structure which is more similar to the actual situation is selected as the basic cell of the metal.

As shown in Figure 2, the surface of the Kelvin tetradecahedron is composed of six regularograms and eight regular hexagons [18], which ensures that the porous material maintains the sameness in the up and down, left and right, and front and back directions. In this paper, the unit cell structure of the porous material is simplified to a tetradecahedron, and the pore edge is a cylinder. It is assumed that the porosity is θ (%), l is the rib length, r is the radius of the hole, and a is the length of a cube containing the tetradecahedron. The effective specific surface area of the porous metal is the ratio of the surface area sum of tetradecahedral struts to the corresponding porous volume.

Taking Figure 2 as an example, the geometrical method is used to calculate the specific surface area of the unit tetradecahedron. Figure 3 is a projection view of a single cell of a porous material, which is an orthographic projection of a certain angle of the tetradecahedron. The expression of the radius of the tetradecahedron and the radius of the hole can be derived from the geometric relationship shown in the figure.

$$l = \frac{1}{2\sqrt{2}} \cdot a, \tag{1}$$

$$r = \sqrt{\frac{1-\theta}{18\sqrt{2}}} \cdot a. \tag{2}$$

Combine the orthographic projection with the node profile as shown in Figure 4 (the orthographic projection of a node of the unitary tetradecahedron). Using the relevant dimensions to calculate the geometric method, the actual edge length of the porous struts can be expressed as

$$l' \approx l - \mathrm{AB} \approx \left(\frac{1}{2\sqrt{2}} - \frac{\sqrt{6}}{9}\sqrt{\frac{1-\theta}{\sqrt{2}\pi}}\right) \cdot a \tag{3}$$

From formulas (2) and (3), the total external surface area of a single tetradecahedron can be calculated as

$$S = \left\{6\left[\frac{\pi(1-\theta)}{\sqrt{2}}\right]^{1/2} - \frac{4\sqrt{6}}{3}(1-\theta)\right\}a^2. \tag{4}$$

Since the inner surface area of the prism is small and the overall influence on the properties related to the porous specific surface area is negligible, in formula (4), the surface area inside the cylindrical rib of a unit cell is ignored. Therefore, the specific surface area of the entire porous structure can be expressed equivalently by the specific surface area of the unit cell tetradecahedron:

$$S_v = \frac{\left\{12\left[(1-\theta)\pi/\sqrt{2}\right]^{1/2} - \left(8\sqrt{6}/3\right)(1-\theta)\right\}}{a}. \tag{5}$$

From Figure 5 (forward projection of the tetradecahedron), the projected area of the unit tetradecahedron can be drawn; thus, the equivalent circular aperture can be

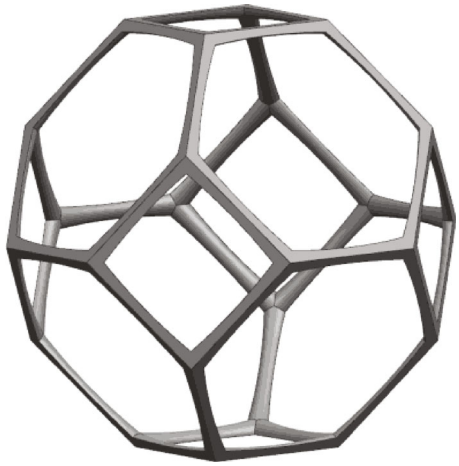

Figure 2: Ideal tetrahedral model of foam metal.

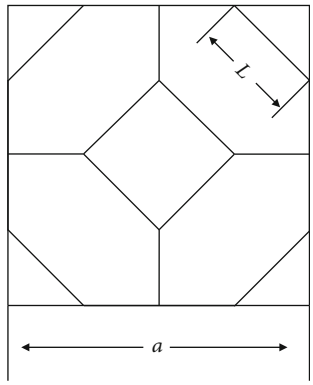

Figure 3: Unit cell orthographic projection.

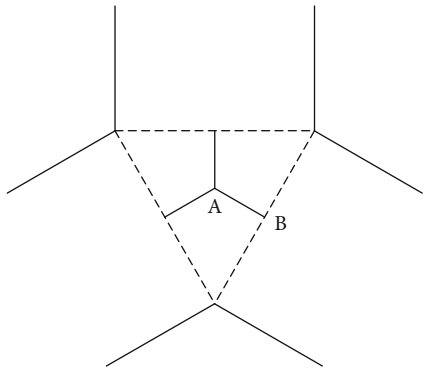

Figure 4: Sectional view of the node.

calculated from the projected area, and the relationship between the aperture and the side length a is obtained:

$$S_d = S_o - S_e = \frac{7}{8}a^2 - \left(2 + 3\sqrt{2}\right) \cdot r \cdot a - 4r^2. \quad (6)$$

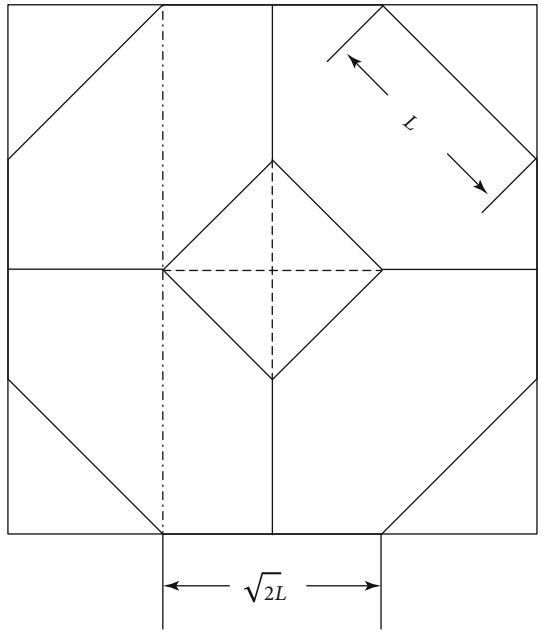

Figure 5: Aperture analysis diagram.

Assuming that the projection octahedron equivalent circular aperture is "d'," formula (7) can be obtained:

$$\left(\frac{d'}{2}\right)^2 \pi = S_d. \quad (7)$$

Combined with formula (2), the relationship between d and a can be obtained.

$$d' = \frac{2a}{\pi}\left[\frac{7}{8} - \frac{1+2\sqrt{2}}{3\sqrt{\pi}} \cdot (1-\theta)^{1/2}\right]^{1/2}. \quad (8)$$

Considering that the fluid flows through the inside of the porous body and it is affected by the structure of the porous body, a coefficient "ε" is introduced to correct that influence. Normally, the "ε" depends on the material and its manufacturing process.

$$d = \varepsilon d'. \quad (9)$$

Through formulas (8) and (9), the relationship between a and d is introduced:

$$a = \frac{d\pi}{2\varepsilon}\left[\frac{7}{8} - \frac{1+2\sqrt{2}}{3\sqrt{\pi}} \cdot (1-\theta)^{1/2}\right]^{1/2}. \quad (10)$$

Combined with formulas (5) and (10), the specific surface area can be simplified and approximated:

$$S_v = \frac{0.596\varepsilon}{d}\left[17.885(1-\theta)^{1/2} - 6.532(1-\theta)\right]. \quad (11)$$

Table 1: Experimental data and theoretical calculation data of copper foam.

Sample number	1	2	3	4	5	6
Porosity θ (%)	91.5	92.26	92.74	94.57	96.23	96.35
Pore size d (mm)	1.256	1.15	0.755	0.93	0.656	2.385
S_{Ev} (cm^2/cm^3) experimental value	269.07	306.287	456.08	404.43	591.03	165.747
S_{cv} (cm^2/cm^3) calculated value	270.8	301.27	463.9	396.74	598.67	165.55

Since the actual hole edge is not a smooth cylinder, it is an irregular triangular prism type; according to different surface states, a variety of shape changing can be exhibited depending on the material and the preparation process, thereby causing different degrees of surface area increase. Therefore, the above formula should be modified by a coefficient "δ" depending on the material and the manufacturing process. If the progress is simplified, then the S_v can be written as follows:

$$S_v = \frac{3.893\varepsilon\delta}{d}\left[2.74(1-\theta)^{1/2} - (1-\theta)\right]. \quad (12)$$

For the convenience of calculation, the K is defined as follows:

$$K = 3.893\varepsilon\delta. \quad (13)$$

Then, formula (12) can be expressed as

$$S_v = \frac{K}{d}\left[2.74(1-\theta)^{1/2} - (1-\theta)\right]. \quad (14)$$

Among them, "d (mm)" is the pore size of the porous body, and "K" is a constant depending on the material and process of the material. From the experimental perspective, it was proved that the specific surface area increases sharply with the increase of the porosity while the pore diameter of the material does not change much. But formula (14) does not conform to the actual situation. Therefore, a correction factor "$(1-\theta)^n$" is introduced to modify the formula to make it fit for the specific surface area of the actual porous material [13]. Among them, the constant "n" is also a material coefficient, which is related to the regularity and geometry of a single unit of porous material, so the formula can be further optimized to

$$S_v = \frac{K}{d}\left[2.74(1-\theta)^{1/2} - (1-\theta)\right](1-\theta)^n. \quad (15)$$

It is considered that the specific surface area of the porous material is affected by factors such as material, preparation, and geometry. The formula introduces two parameters: "K" (material constants related to the material itself and the preparation method) and "n" (a constant related to the regularity and geometry of a single unit of porous material). These two material constants are affected by the material preparation process. Theoretically, for the ideal porous materials, the value of "n" is zero. It can be deduced from formula (15) that when the porosity of the porous material is kept constant, the number of unit bodies and the specific surface area decrease as the pore diameter increases. When the pore diameter is kept constant, the number of unit bodies and the specific surface area both increase with the increase of the porosity. However, when the porosity reaches a certain value, the void walls become thinner and thinner until they pass.

This results in a reduction in surface area. Therefore, when the pore diameter is constant, the specific surface area will increase first and then decrease as the pore volume increases.

3. Calculation Results and Analysis

The experimental materials were foamed metal products obtained by electrodeposition and high-pressure percolation casting, respectively. Nickel foam and copper foam with the porosity between 89% and 99% were produced by electrodeposition. Aluminum foam with good connectivity is prepared by high-pressure seepage casting, the porosity is between 73% and 87%, and the pore diameter ranges from 2.68 mm to 2.87 mm.

3.1. Comparison between Experimental Data and Calculated Data. A Micromeritics ASAP 2020 automatic physical and chemical adsorption instrument was used. The instrument can not only measure the single point, multipoint BET specific surface area, Langmuir specific surface area, BJH mesopores, pore distribution, pore size and total pore volume and area, and density function theory (DFT) but also analyze various data such as adsorption heat and average pore size. The working principle of the instrument is the static volumetric method of isothermal physical adsorption. In this experiment, the BET gas adsorption method was used to measure the size parameters of copper foam, including specific surface area and average pore diameter as recorded in Table 1.

Using equation (16), the specific surface area of cooper foam can be calculated (take $K = 101.1$, $n = -0.6289$); the result is listed in Table 1.

$$S_v = \frac{101.1}{d}\left[2.74(1-\theta)^{1/2} - (1-\theta)\right](1-\theta)^{-0.6289}. \quad (16)$$

The comparison between the experimental value and the calculated value is plotted in Figure 6. It can be seen that the calculated results are in line with the experimental data; the deviation is less than 1.2%. The formula presents a high precision.

3.2. Reference Experimental Data and Calculation Results Analysis. The relevant parameters for aluminum foam and nickel foam given in [12, 16] are listed in Tables 2 and 3.

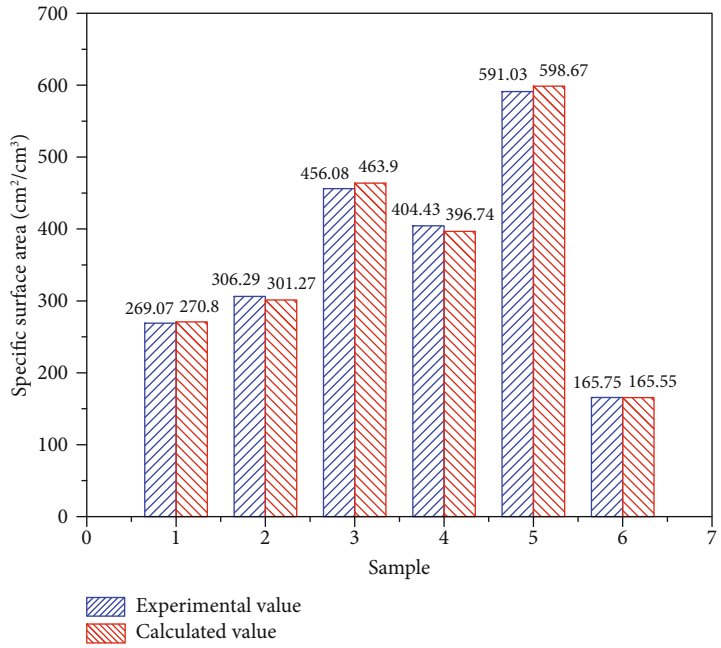

Figure 6: Comparison of experimental and calculated values of foamed copper specific surface area.

Table 2: Experimental data and theoretical calculation data of aluminum foam.

Sample number	1	2	3	4	5
θ (%)	73.5	76.5	79	82.5	86.5
d (mm)	2.68	2.72	2.75	2.80	2.87
S_{Ev} (cm^2/cm^3) experimental value	15.7	14.7	13.8	12.5	10.7
S_{cv} (cm^2/cm^3) calculated value	16.07	14.91	13.93	12.46	10.6

Table 3: Experimental data and theoretical calculation data of foamed nickel.

Sample number	1	2	3	4	5
θ (%)	89.66	92.55	95.79	97.15	98.84
d (mm)	0.5735	0.6008	0.6802	0.7242	0.7378
S_{Ev} (cm^2/cm^3) experimental value	1197.38	1637.48	2649.22	3727.77	9146.05
S_{cv} (cm^2/cm^3) calculated value	1218.898	1646.187	2640.549	3713.126	9150.164

The data are substituted into formula (15) to obtain the corresponding values of n and K, and the calculation result S_{cv} is shown in the last row of the table and compared with the experimental data S_{Ev}. The deviation between the experimental value and the calculated value is plotted in Figure 7.

Using the data given by Reference [16], the specific surface area of porous nickel can be calculated (take $K = 30.03$, $n = -1.4979$).

The result is shown in Table 3. The deviation between the experimental value and the calculated value is plotted in Figure 8.

It can be seen that there is a high consistency between the theoretical results calculated by formula (15) and the actual experimental results. The average deviation of the three sets of data is 1.2%, and the maximum deviation is less than 1.8%, which proves the accuracy of formula (15).

It can be seen from the comparison of the above data that the formula can be well adapted to the electrodeposition type foam metal and the seepage casting type foam metal, indicating that the formula has good versatility. In the study of this paper, because the metal foam is produced by two different processes, there is a huge difference in its product form. The mesostructure, surface features, nodes, and internal state of the cell body may be quite different, but this formula successfully translates these specific factors which depend on the material type and process conditions into the material constants "δ" and "ε". So the formula can be applied to different materials with different processes.

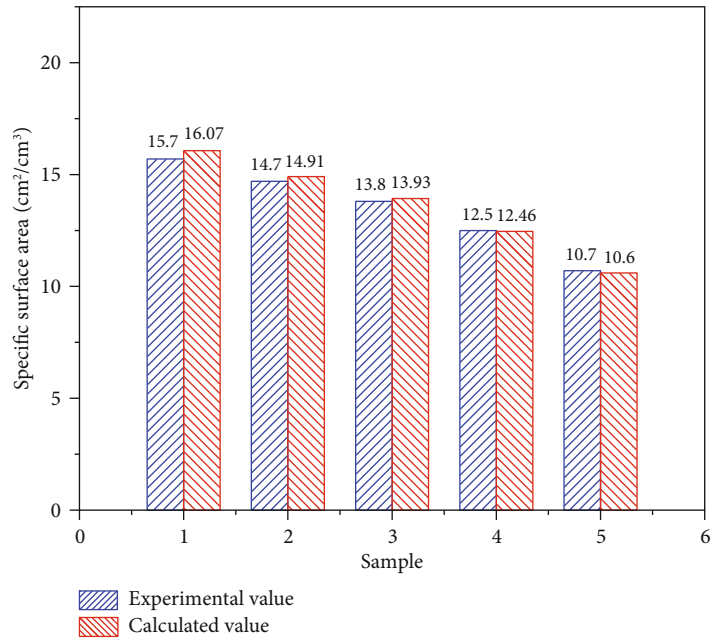

Figure 7: Comparison of experimental and calculated values of foamed aluminum specific surface area.

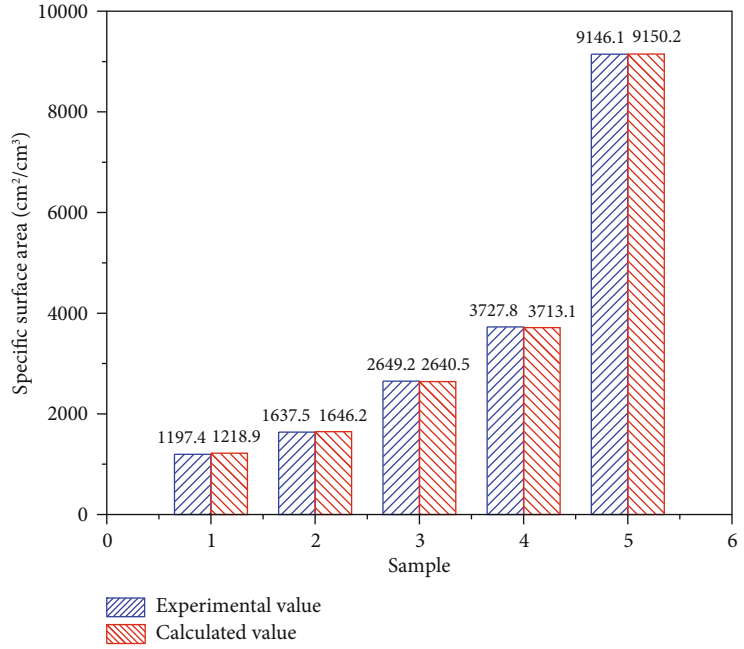

Figure 8: Comparison of experimental and calculated values of foamed nickel specific surface area.

The specific values of "n" and "K" above are obtained by fitting experimental data, the fitting values are used in the formula, and satisfactory results are gained. Both the average deviation and the range of deviation between the calculated and experimental results are very small. Compared with the theoretical octahedral model [16] and the dodecahedron model [17], this model is based on the actual microstructure of foam metal; the calculation results are more accurate.

4. Conclusion

Porosity and pore size are two basic parameters of metal foam. The two parameters of the metal foam are always easy to measure. But sometimes data such as specific surface area is not easy to measure. Using equation (15) herein, the constants n and K of the material can be obtained easily. Then, a specific equation is established, and the value of the

unmeasured specific surface area of the material can be calculated indirectly from the porosity and the pore diameter.

Considering the factors such as material type and preparation process, the material constant was introduced, and the specific surface area expression of porous metal based on porosity and pore size was established. The specific surface area of the electrodeposited porous metal and the high-pressure percolation cast type porous metal was calculated separately. By comparing with the experimental results, it is found that the theoretical calculation error is small and the applicability of the formula is obviously improved.

Data Availability

The data used to support the findings of this study are included within the article.

Conflicts of Interest

The authors declare no conflict of interest with respect to this publication.

Acknowledgments

This work was supported by the National Natural Science Foundation of China (Nos. 51471036 and 51675058), Scientific Research Projects of Education Department of Hunan Province (No. 16A002), and Open Foundation of Hunan Provincial Key Laboratory of Energy Efficiency and Clean Utilization (No. 2016NGQ007).

References

[1] P. S. Liu, T. F. Li, and C. Fu, "Application of porous metal materials," *Journal of Functional Materials*, vol. 32, no. 1, pp. 12–15, 2001.

[2] J. M. Chen, P. Tan, and J. Y. Wang, "Characterization of specific surface area and pore structure of porous materials by gas adsorption," *Powder Metallurgy Industry*, vol. 21, no. 2, pp. 45–49, 2011.

[3] C. Li, M. Li, H. Li, J. Chen, and H. Xiao, "Influence of solution treatment on microstructural evolution and mechanical properties of a new titanium alloy," *Kovové materiály- Metallic Materials*, vol. 58, pp. 1–8, 2020.

[4] C. Li, L. Qin, M. Li, H. Xiao, Q. Wang, and J. Chen, "Influence of deformation strain rate on the mechanical response in a metastable β titanium alloy with various microstructures," *Journal of Alloys and Compounds*, vol. 815, article 152426, 2020.

[5] C. Li, H. Li, and S. van der Zwaag, "Unravelling the abrasion resistance of two novel meta-stable titanium alloys on the basis of multi-pass-dual-indenter tests," *Wear*, vol. 440-441, article 203094, 2019.

[6] S. W. Dai, J. Chen, and Y. J. Ren, "Electrochemical corrosion behavior of the copper current collector in the electrolyte of lithium-ion batteries," *International Journal of Electrochemical Science*, vol. 12, pp. 10589–10598, 2017.

[7] J. Chen, S. Dai, C. Li, W. Li, and Y. Ren, "Effects of pore size on fatigue deformation mechanism of open-cell copper foam at low stress amplitude," *Materials*, vol. 11, no. 9, pp. 1639–1648, 2018.

[8] J. Chen, X. Li, W. Li et al., "Study on the compression properties and deformation failure mechanism of open-cell copper foam," *Advanced Engineering Materials*, vol. 19, no. 11, pp. 1600861–1600868, 2017.

[9] P. S. Liu, "Method for determination of specific surface area and pore morphology of porous materials," *Rare Metal Materials and Engineering*, vol. 35, no. S2, pp. 25–29, 2006.

[10] H. Wang, X. P. Song, and J. J. Liu, "Research progress on specific surface area and pore structure standard materials of porous and highly dispersed materials," *China Powder Science and Technology*, vol. 14, no. 3, pp. 52–55, 2008.

[11] X. H. Liu, "Experimental study on magnetic properties of porous foam metal and its influence on magnetic field," *Foundry Technology*, vol. 32, no. 6, pp. 815–817, 2011.

[12] L. Ma and D. He, "Fabrication and pore structure control of new type aluminium foams," *Chinese Journal of Material Research*, vol. 8, no. 1, pp. 11–17, 1994.

[13] Y. Ding, "Nanoporous metal: a new energy nanomaterial," *Journal of Shandong University (Natural Science)*, vol. 46, no. 10, pp. 121–133, 2011.

[14] S. J. Zhuang, "A new probe into the calculation method of specific surface area of porous solids," *Chinese Journal of Chromatography*, vol. 4, no. 1, pp. 89–92, 1986.

[15] Y. Guan, Q. L. Sun, and X. Y. Wu, "Improvement of measurement and calculation methods for specific surface area and pore size distribution," *Acta Chimica Sinica*, vol. 48, no. 5, pp. 424–430, 1990.

[16] P. S. Liu, "A new method for calculating the specific surface area of porous metal foams," *Philosophical Magazine Letters*, vol. 90, no. 6, pp. 447–453, 2010.

[17] D. L. Duan, R. L. Zhang, X. J. Ding, and S. Li, "Calculation of specific surface area of foam metals using dodecahedron model," *Materials Science and Technology*, vol. 22, no. 11, pp. 1364–1367, 2006.

[18] Y. Q. Tu, L. L. Liu, and J. F. Wan, "Improvement of the tetradecahedral model of closed-cell foamed aluminum material," *Chinese Journal of Computational Mechanics*, vol. 27, no. 2, pp. 275–279, 2010.

Hindawi
International Journal of Photoenergy
Volume 2020, Article ID 7085497, 9 pages
https://doi.org/10.1155/2020/7085497

Research Article

Optical and Thermal Properties of Therminol 55-TiO_2 Nanofluids for Solar Energy Storage

P. Kalidoss, S. Venkatachalapathy, and S. Suresh

Department of Mechanical Engineering, National Institute of Technology, Tiruchirappalli, 620015 Tamil Nadu, India

Correspondence should be addressed to P. Kalidoss; kalidossmech1991@gmail.com

Received 5 November 2019; Revised 10 December 2019; Accepted 6 January 2020; Published 22 January 2020

Guest Editor: Chuanchang Li

The present experimental study focuses on the energy storage performance of Therminol 55-TiO_2 nanofluids for the absorption of solar energy. Photothermal conversion efficiency is enhanced using Fresnel lens and secondary reflectors with a glass-type evacuated absorber tube. The focal length of the Fresnel lens is 150 mm, and that of the secondary reflector is 70 mm. The optical absorbance, extinction coefficient, and thermal conductivity of nanofluids at 100, 250, 350, and 500 ppm are reported. The optical path length of the energy storage medium is 1 cm. The optical performance of the nanofluids is analyzed in the range of 400 to 800 nm. Compared to base fluid, the prepared concentrations show higher absorbance in the measured range of wavelength. The optimum concentration is found to be 250 ppm, and its specific heat is measured in the temperature range of 27 to 117°C and is found to vary from 1.85 to 2.19 J/g°C. The thermal conductivity of the maximum concentration of nanofluid is 0.134 W/mK. The optical absorbance test confirms the stability of nanofluids. Maximum temperature and photothermal conversion efficiency are obtained.

1. Introduction

Liquids are normally used as energy transfer medium for solar thermal collectors. The commonly used liquids are water, silicon oil, Therminol, and mixture of two liquids. The addition of small amounts of nanoparticles to these fluids (low-concentration nanofluids) improves the optical and thermal properties which play a vital role in photothermal conversion. Chen et al. [1] investigated the optical and thermal properties and photothermal conversion of graphene oxide/water-based nanofluids with different mass fractions. They obtained maximum efficiencies of 97.45 and 48.92% at 30 and 80°C for a concentration of 0.02%. The optical absorbance of DI water and ethylene glycol mixture (70 : 30) as base fluid with CuO as a nanoadditive was investigated by Karami et al. [2] for solar applications. Measurements showed that the optical absorbance of nanofluid in the wavelength range of 200 to 2500 nm was 4 times higher than that of the base fluid at 100 ppm concentration. At the same concentration, the enhancement in thermal conductivity was 13.7% at 60°C. The optimum concentration of graphene-water nanofluids was experimentally investigated by Rose et al. [3] in the visible range for solar thermal applications. The volume fraction varied from 0.004 to 0.016%. The maximum absorbance was found at 0.012% with minimum reflectance. The thermal and optical properties of Therminol-Al_2O_3 nanofluid were experimentally investigated by Muraleedharan et al. [4] in the volume concentration ranges from 0.025 to 0.3%. Volume fraction of 0.1% showed maximum absorbance at 501 nm, and the enhancement in thermal conductivity was 11.7%. For the same concentration, the maximum thermal efficiency was 62.7%. To harvest a maximum amount of solar energy, a solar selective volumetric receiver (SSVR) plays an important role as reported by Khullar et al. [5]. In this study, water/MWCNT (multiwalled carbon nanotube) nanofluid was used and its optical transmittance was reported for concentrations of 9, 18, 45, and 75 mg/l. For wavelengths ranging from 300 to 1400 nm, the maximum concentration showed transmittance close to zero indicating maximum absorbance. Wang et al. [6] used paraffin and water-ethanol-based microencapsulated phase change material (MPCM) slurry added with multiwalled carbon nanotubes (MWCNTs) for photothermal conversion. The optical transmittance of the ethanol/water, MWCNT nanofluid (0.005 wt.%), MPCM (1 wt.%), and

hybrid MWCNT-MPCM slurry was reported in the wavelength ranges between 200 and 1400 nm. In the range of wavelength studied, the hybrid nanofluid slurry and MPCM showed 100% absorbance, whereas it was 90% for MWCNT nanofluid in the visible range. The maximum photothermal conversion temperature observed was 80°C after 50 min for MWCNT nanofluid.

The optical properties of MWCNT/water nanofluids of concentration from 0.0015 to 0.25 wt.% were reported by Qu et al. [7]. They measured the optical transmittance in the wavelength range of 200 to 2000 nm. The results revealed that the addition of nanoparticles led to reduction in transmittance. The transmittance was zero for the maximum concentration whereas it was 100% for base fluid up to 900 nm. They also reported a reduction in receiver tube efficiency with increasing time of irradiation. For 0.01 wt.% and an irradiation time of 5 minutes, the receiver tube efficiency was 96.4%. Chen et al. [8] used MWCNT nanofluids with water as base fluid in their studies. They used a concentration of 0.01 wt.% and a temperature range of 10 to 60°C to analyze the stability of pure MWCNT and treated (acid-treated and milling-treated) MWCNT. In the measured range of temperature, the milling treatment showed better stability and higher extinction coefficient (55 mV and 7.49 cm^{-1}, respectively).

Chen et al. [9] studied the thermophysical and optical properties of 0.01, 0.03, and 0.06 wt.% percentage of SiC (silicon carbide) nanofluids with ionic liquid as base fluid. The thermal conductivity and specific heat were also measured. The maximum thermal conductivity for the higher concentration was 0.20 W/mK at 65°C, and the specific heat was 2.5 J/g K at 80°C. The optical properties were studied in the range of 200-1100 nm. The results revealed a transmittance of zero and an extinction coefficient of 7 cm^{-1} for maximum concentration. The optical properties of Al_2O_3 and TiO_2/DI water nanofluids of 0.1 and 0.3% concentration were studied by Said et al. [10]. The extinction coefficient of TiO_2 nanofluid was higher than that of Al_2O_3 nanofluid. The authors found a deviation of nearly 10 times between analytical and experimental results. Khosrojerdi et al. [11] used graphene oxide nanofluid of concentration 0.045 wt.% and thickness of 3 cm in their study and found that 99.6% of incoming solar energy was absorbed. The maximum extinction coefficient was 14 cm^{-1} at 300 nm.

Mahbubul et al. [12] studied the thermal efficiency enhancement of an evacuated tube solar collector using water and CNT/water nanofluids. The thermal conductivity and specific heat of water and 0.05, 0.10, and 0.20 vol.% of nanofluids were measured for the temperatures ranging from 20 to 70°C. For the maximum concentration, the thermal conductivity was 0.9 W/mK at 70°C and the efficiency was 66% which is 10% higher than that of water. The thermal conductivity of Al_2O_3-CuO hybrid nanofluids was reported by Yagnem and Venkatachalapathy [13]. The concentration of nanofluid varied from 0.01 to 0.1%. They obtained a maximum enhancement of 15.72% for 0.1% concentration compared to base fluid. The thermal conductivity of low-concentration nanofluids was investigated by Sundar et al. [14]. They used a mixture of ethylene glycol and water in the proportion of 50 : 50 as base fluid, and the thermal conductivity was measured in the temperature range of 15 to 50°C. For the maximum volume concentration of 0.8%, the enhancement in thermal conductivity was found to vary from 9.8 to 17.89% for Al_2O_3 nanofluid and 15.6 to 24.56% for CuO nanofluid, respectively. The viscosity of water-based single-walled carbon nanohorn (SWCNH) and TiO_2 nanofluids of concentrations 0.001, 0.1, and 1 wt.% was studied by Bobbo et al. [15]. Sodium dodecyl sulphate (SDS) and polyethylene glycol (PEG) were used as stabilizers for SWCNH and TiO_2, respectively. Both the nanofluids showed Newtonian behavior at all concentrations. Zeta potential was reported for all the concentrations, which lies between 57 and 50 mV for SWCNH and 40 and 37 mV for TiO_2 nanofluid. The efficiency was increased by 10% for nanofluid compared to water. Anbu et al. [16] studied heat transfer and pressure drop characteristics of DI water/TiO_2 nanofluids and reported negligible pressure drop for the concentrations 0.1, 0.15, 0.2, and 0.25% compared to base fluid. The heat transfer enhancement was 23 and 4% for tubes with inserts and without inserts for 0.2% volume concentration. Chen et al. [17] reported the absorbance of water-based low-concentration Ag, Au, and Ag-Au nanofluids in the wavelength range of 300 to 800 nm using UV-Spectrophotometer. The concentration used was 0.5 and 2.5 ppm, and a maximum photothermal conversion of 30.97% was obtained for the blended Ag-Au nanofluid. The concentration and thickness of nanofluids play a major role for the maximum absorption of energy radiated by the sun. Thermooptical properties of low-concentration (2.04×10^{-4} and 4.26×10^{-4} volume fraction) gold and silver nanofluids were used by Moreira et al. [18] in their experiments. They obtained an enhancement of 16 and 20% in thermal diffusivity for nanofluids compared to base fluid (DI water). Khullar et al. [19] theoretically studied the thermal efficiency of a concentrated solar parabolic collector using nanofluids. The finite difference method was used for solving the governing equations. Aluminum nanoparticles of concentration 0.05% were used with Therminol VP-1 as base fluid. An evacuated receiver tube was used as the absorber tube. They obtained efficiencies of 19 and 78% for base fluid and nanofluid, respectively, for the average fluid temperature of about 230°C. Tyagi et al. [20] numerically studied heat transfer in a direct absorption solar collector. The authors used water/aluminum nanofluids of volume fraction up to 2%. The collector efficiency depends on its geometry, nanoparticle size, and concentration.

Matuska and Sourek [21] compared the performance of the water heating system using a solar photovoltaic (PV) array (with and without tracking) and a solar photothermal collector. The PV array was connected to the resistive heating elements, and the annual resistance load increase was 20 to 35% for the tracking system. The photothermal conversion efficiency was found to vary between 35 and 68%. The authors concluded that the area required for the photothermal system will be lesser than that for the PV system. The performance of the solar ventilation system coupled with the low-temperature organic Rankine cycle (ORC) was experimentally and numerically investigated by Hung et al. [22]. The dimensions of the system were 4-meter length

and 15° air flow angle. The results of CFD simulations were within the acceptable limit which proved that the CFD is the acceptable tool for predicting the efficiency of the ventilation system. The experimental efficiency of the ORC was 6.2%, and the power generated was 11.43 KWh/day. The optimum concentration for the optical absorbance of Therminol 55-MWCNTs was reported by Kalidoss et al. [23]. The authors concluded that 100 ppm concentration had an absorbance of 0.75 in the visible range and the corresponding photothermal conversion efficiency was 17.36%.

The performance of the solar flat-plate collector was investigated using the reflectors by Bhowmik and Amin [24]. The maximum outlet temperature of water was 52°C for the collector with a reflector. The authors obtained a maximum efficiency of 61% with a reflector which was 10% higher compared to that of a collector without a reflector. Thermal efficiency enhancement of a booster secondary reflector was studied by Bellos and Tzivanidis [25]. They used solid work flow simulation software with syltherm800 as working medium. Turbulent flow was considered in the study, and the authors concluded that the thermal efficiency enhancement varied with an incident angle. The maximum enhancement in efficiency was 150%, and the useful heat gain for the corresponding angle was 10.8 kW. The ray tracking method was used by Prasad et al. [26] to optimize the configuration of the solar Fresnel lens coupled with the secondary reflector system to overcome the improper distribution of heat flux. Optical efficiencies of four different secondary reflectors were reported. The results showed maximum optical efficiency of 75% with a zero-degree tracking error for the compound parabolic concentrator. The minimum optical efficiency was 32% for the trapezoidal secondary concentrator with the tracking error of 0.25 degree.

The major findings on optical absorbance and photothermal conversion efficiency using different nanofluids are given in Table 1.

Many studies have been carried out on the use of low-concentration nanofluids for light to heat conversion. Only few research papers are available with secondary reflectors, and not much work has been done on the combined effects of the above two. The present study focuses on low-concentration nanofluids coupled with secondary reflectors for photothermal conversion.

2. Experiment

2.1. Materials and Characterization. Therminol 55, manufactured by Eastman Chemical Company, USA, is used as base fluid. The chemical name of Therminol 55 is benzene, C14-30-alkyl derivatives, and the molecular formula is $C_{28}H_{50}$. TiO_2 (titanium dioxide) nanoparticles, purchased from Sisco Research Laboratories, India, are used, and the average particle size is 32 nm. The X-ray diffraction (XRD) test is carried out to identify the crystalline structure of TiO_2 nanoparticles, shown in Figure 1. The analysis is carried out in the range of 0-100°, and the peak occurs at 22°. The results reveal that there are no impurities in the nanoparticles.

2.2. Preparation of Nanofluids. Low-concentration nanofluids of 100, 250, 350, and 500 ppm concentrations are prepared by the dilution process shown in Figure 2. 500 ppm is taken as stock solution which is prepared by adding 50 mg of nanoparticles in 100 ml of the base fluid.

The following equation gives the dilution process adopted in this study:

$$C_1 \times V_1 = C_2 \times V_2, \tag{1}$$

where C_1 is the concentration of stock solution prepared (ppm), C_2 is the required concentration of solution to be prepared (ppm), V_1 is the volume of solution required for dilution from stock solution (ml), and $V_2$is the volume of solution to be prepared (ml).

To overcome the agglomeration and also to prevent the settling of nanoparticles, the prepared nanofluid is kept in a magnetic stirrer (REMI make) for 1-hour duration. The nanofluid is then kept in an ultrasonicator (LARK make) for 45 minutes. No surfactant is added to the nanofluid.

2.3. Uncertainty in Measurement. The difference between actual and measured values of the experiments is evaluated, and it is reported as error. The main parameter for photothermal conversion is temperature, which is measured using T-type thermocouples connected to a data logger. To evaluate the error in temperature measurement, the root sum squares (RSS) method is used [27]. The thermocouples are calibrated using a drywell calibrator (Fluke 9100S), and the accuracy of the calibrator is ±0.25°C.

The bias and resolution of the data logger used in this study are ±0.1°C and 0.1°C, respectively. The error in the data logger is found using the following equations.

$$\begin{aligned} e_{\text{DAQ}} &= \sqrt{(e_{\text{bias}})^2 + (e_{\text{precision}})^2}, \\ e_{\text{thermocouple}} &= \sqrt{(e_{\text{bias}})^2 + (e_{\text{precision}})^2}, \\ e_{\text{Temp}} &= \sqrt{\left((e_{\text{thermocouple}})^2 + e_{\text{DAQ}}\right)^2 + (e_{\text{calibrator}})^2}. \end{aligned} \tag{2}$$

The overall uncertainty in temperature measurement is found by combining the errors of the thermocouple, data logger, and drywell calibrator, and the error in temperature is found to be ±1.12°C.

2.4. Description of the Experiment

2.4.1. Experimental Setup. Though nanofluids are used as working medium in the direct solar absorber, their stability plays an important role. To confirm the stability of 250 ppm Therminol-TiO_2 nanofluid, the absorbance test is carried out for every 2 hrs for a duration of 12 hrs using a UV-Vis spectrophotometer. A marginal change in absorbance is observed indicating that there is no precipitation of nanoparticles. The experimental facility consists of secondary reflectors, evacuated tubes, a solar tracker with a time-dependent tracking system, and a Fresnel lens. In order to

Table 1

Author	Base fluid and nanoparticles	Optimum concentration	Optical absorbance (visible range)	Photothermal conversion efficiency	Receiver tube
Chen et al. [1]	Water-graphene oxide	0.02 mass fraction	60% (abs)	48.92%	Cylindrical quartz glass
Karami et al. [2]	Water and ethylene glycol-(70% : 30%) CuO	100 ppm	98% (abs)	—	—
Rose et al. [3]	Ethylene glycol-graphene oxide	0.012 vol. fraction	3 AU	—	—
Muraleedharan et al. [4]	Therminol 55-Al_2O_3	0.1% vol. concentration	1.4 AU	62.7%	Glass-to-glass type (evacuated)
Wang et al. [6]	MPCM slurry/water-ethanol-MWCNTs	0.005 wt.%	100% (abs)	79.8°C (maximum temperature)	Glass-to-glass type (evacuated)
Qu et al. [7].	Water-MWCNTs	0.01 wt.%	100% (abs)	96.4%	Glass tubes
Chen et al. [8]	Water-MWCNTs (milling treated)	0.02 wt.%	100% (abs)	95%	Acrylic receiver
Chen et al. [9]	Ionic liquid-silicon carbide	0.03 wt.%	100% (abs)	—	—
Khosrojerdi et al. [11]	Water-graphene oxide	0.045 wt.%	0.9 AU	—	—
Chen et al. [17]	Water-Ag and Au (hybrid)	2.5 ppm	0.5 AU	30.97%	Glass beakers
Tyagi et al. [19]	Therminol VP-1-Al_2O_3	0.05% vol. concentration	—	78%	Glass-to-glass type (evacuated)
Kalidoss et al. [23]	Therminol 55-MWCNTs	100 ppm	0.75 AU	17.36%	Glass-to-copper type (evacuated)

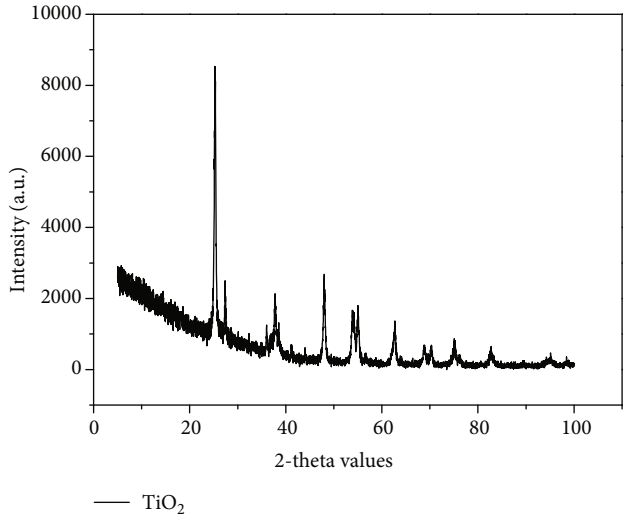

Figure 1: XRD pattern of TiO_2.

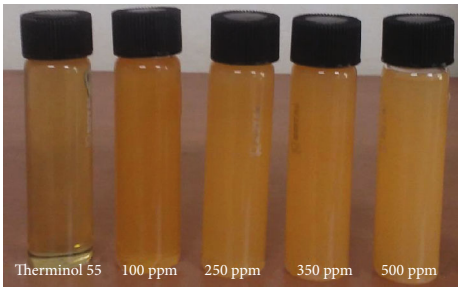

Figure 2: Photographic view of Therminol 55-TiO_2 nanofluids.

fix the secondary reflector at its focal length, a separate arrangement is provided. The schematic diagram of the secondary reflector is shown in Figure 3, and its detailed specifications are given in Table 2. Spacing of 25 mm is given on either side of the Fresnel lens to increase the solar irradiation on the secondary reflectors. Figure 4 shows the top view of the Fresnel lens with spacing.

The photographic view of the experimental setup is depicted in Figure 5. The flow rate of the nanofluid used in the experiment is 0.5 lps, and a rotameter is used to measure the flow rate. The system is supported by an aluminum frame of a rectangular section and the lens side by a square section. The fluid is circulated by a pump, and the circulated fluid is stored in a well-insulated tank. The insulation has a thickness of 40 mm, and its thermal conductivity is 0.03 W/mK. T-type thermocouples are used to measure the temperature of the secondary reflector and nanofluids, and the data are recorded using a Keysight 34972 data logger. The details of the instruments used in the experiment are given in Tables 3 and 4.

The geometrical concentration ratio (CR_g) of the secondary reflector is given by Abdel-Rehim and Lasheen [28].

$$CR_g = \frac{A_a}{A_r}, \tag{3}$$

$$A_a = L \times d, \tag{4}$$

$$A_r = \frac{2}{3} d \times h, \tag{5}$$

$$h = \frac{d^2}{16f}. \tag{6}$$

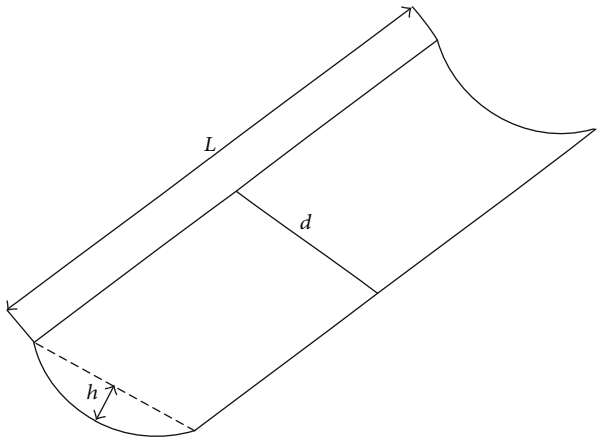

Figure 3: Schematic view of the secondary reflector.

Table 2: Specifications of the secondary reflector.

Parameters	Values
Reflectivity	0.913
Thickness	0.5 mm
Length (L)	550 mm
Width of the receiver (d)	200 mm
Depth (h)	170 mm
Concentration ratio	4.863
Focal length (f)	70 mm

2.4.2. Photothermal Conversion Efficiency. The experiments are carried out during the first 10 days of April 2019. The hourly temperature and the solar insolation are monitored. During the first five days, only the Fresnel lens is used, and for the remaining period, the Fresnel lens is coupled with secondary reflectors and the average values are reported. The recorded temperature values at the specific time are added and divided by the number of days (five days each) for extracting the average values. The same procedure was followed in the research work of Kalidoss et al. [23]. The experimental setup is placed in the surface azimuth angle 0° which is the true north-south direction. A single-axis solar tracking system will track the east-west axis along the movement of the sun. Figure 6 shows the fluid temperature in the storage tank, and the temperature is always higher with secondary reflectors. Maximum temperatures of 110.4 and 93.5°C are obtained at 15:00 p.m. with and without secondary reflectors.

The photothermal conversion efficiency of the Fresnel lens alone and coupled with secondary reflectors is depicted in Figure 7. The efficiency is calculated based on the heat gain by the collector and radiation energy incident on the absorber tubes, given in equation (4). Better photothermal conversion is obtained in both the cases, due to glass-to-glass evacuated tubes which help overcome the convective losses from the absorber tubes. Harding et al. [29] also reported a maximum efficiency of 61.4% for fluid in a glass-to-glass absorber tube compared to other kinds of receiver tubes without secondary reflectors. For the same type of absorber tubes, the maximum efficiency was 62.7% for Therminol 55-Al_2O_3 nanofluid [4].

$$\dot{\eta} = \frac{m_{\mathrm{nf}}\, C_{\mathrm{nf}}}{G\, A}\, \frac{\Delta T}{\Delta t}. \tag{7}$$

The intensity of radiation is measured using a pyranometer. The average values of solar intensity for both the studies are close to 750 W/m^2, shown in Figure 8. The maximum temperature observed for the secondary reflectors is 85°C. The maximum efficiency of the solar collector with and without secondary reflectors is 82.63% at 13:30 p.m. and 61.46% at 13:00 p.m., respectively.

3. Results and Discussion

3.1. Absorbance and Extinction Coefficient. The optical absorbance is measured at a room temperature of 25°C using a Shimadzu UV-2600 spectrophotometer in the wavelength ranging from 400 to 800 nm. Therminol 55 is used as the reference sample throughout the measurement, and a quartz cuvette with path length of 1 cm is used as a sample holder. The spectrophotometer works on the principle of Beer-Lambert's law. According to this law, light absorbed in the sample is directly proportional to the concentration of the sample in which light is radiated. The equation for the absorbance is given as

$$A = \log_{10} \frac{I_{\mathrm{o}}}{I}\, \alpha\, C, \tag{8}$$

where I and I_{o} are the intensities of incident and transmitted light, respectively. The absorbance of the nanofluids with various concentrations is depicted in Figure 9. It is found that the optimum absorbance occurs at 250 ppm concentration in the visible range. The sum of absorption and scattering coefficient is the extinction coefficient and is shown in Figure 10. Though the absorbance and extinction coefficient are higher for 100 ppm concentration, its thermal conductivity is lower. For 350 and 500 ppm, the optical properties are higher in a narrow range and lower in the remaining spectrum in comparison with 250 ppm. Hence, 250 ppm is taken as the optimum concentration for further studies. From absorbance results, transmittance is calculated using the following equation [11]:

$$A = 2 - \log\,(T\%). \tag{9}$$

The extinction coefficient (σ) is calculated by

$$T = \frac{I}{I_{\mathrm{o}}} = \exp^{-L\sigma_{\mathrm{total}}}. \tag{10}$$

The particle size parameter (α) is given by the following equation and is always less than one for solar applications:

$$\alpha = \frac{\pi D}{\lambda}. \tag{11}$$

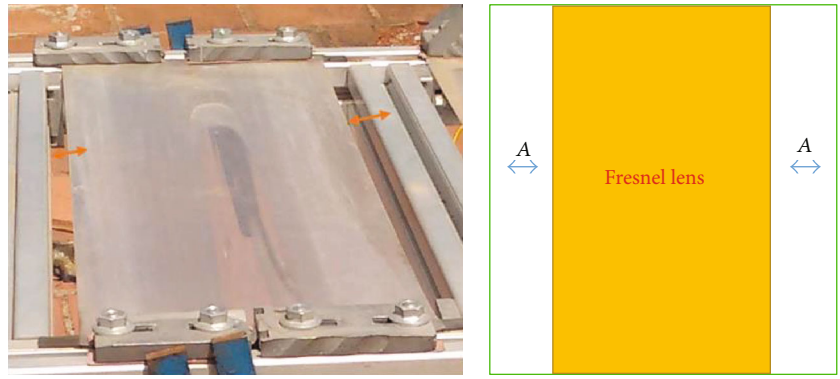

(a) (b)

Figure 4: Top view of the Fresnel lens: (a) photograph and (b) line diagram.

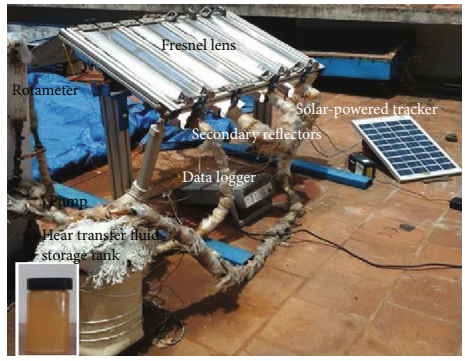

Figure 5: Photographic view of the experimental setup.

Table 3: Specifications of the experimental setup.

Component	Specifications
Fresnel lens	Thickness (250 μm), focal length (150 mm)
Holder (square block)	Aluminum (45 mm)
Absorber tube	Evacuated glass in a glass tube (outer diameter (25 mm), inner diameter (10 mm))
Absorber tube length	550 mm
Thermocouple	T-type

3.2. Thermal Conductivity. The thermal conductivity of Therminol 55-TiO_2 nanofluid is determined using a KD2 Pro Thermal Properties Analyzer (Decagon Devices, Inc., USA). The sensor needle KS-1 is used for measuring the thermal conductivity. The sensor is made of stainless steel, and its dimensions are 60 mm length and 1.3 mm diameter. The sensor needle's measuring range is 0.2-2 W/mK with an accuracy of ±5%. The sensor needle has a heating element and a thermistor. Before starting the measurements, it should be calibrated by standard glycerine solution, prescribed by the manufacturer. The time taken to measure the thermal conductivity of the fluid is 90 seconds, and the instrument requires a 16-bit microcontroller/AD converter. The conductivity is computed from the data in the form of change in temperature and time, given by equation (3).

$$k = \frac{q(\ln t2 - \ln t1)}{4\pi(\Delta T2 - \Delta T1)}. \quad (12)$$

The thermal conductivity of 250 ppm concentration is measured to be 0.129 W/mK. For 350 and 500 ppm, the conductivity values are 0.131 and 0.134 W/mK, respectively.

3.3. Specific Heat. Specific heat of 250 ppm TiO_2 nanofluid is measured with a modulated differential scanning calorimeter (DSC) at IISc, Bangalore. The measurement temperature ranging from 27 to 117°C is shown in Figure 11. The temperature increases at a rate of 10°C/min, and the sample is kept in isothermal condition for 5 min. The TOPEM method is used for finding the specific heat. The sample holder is aluminum whose weight is 49.71 g, and the quantity of the sample used is 29.60 mg. Due to increase in temperature, the specific heat of the nanofluid increases from 1.85 to 2.19 J/g K.

4. Conclusions

The optical and thermal properties of low-concentration Therminol 55-TiO_2 nanofluids are experimentally investigated. The nanofluid concentration varied from 250 to 500 ppm. In the visible range, the absorbance is maximum in a narrow band and remains close to 2.5-3.0 for the remaining wavelength (450-800 nm). Optical stability confirms the suitability of Therminol 55-TiO_2 nanofluid for light to heat conversion in the visible spectrum. The addition of nanoparticles shows changes in thermal conductivity, and an enhancement of 1.57% is found for 250 ppm compared to base fluid. The specific heat measurement shows a marginal change in the temperature range studied. The temperature and photothermal conversion efficiency are enhanced by the use of secondary reflectors, and a maximum efficiency of 82.63% is obtained.

Table 4: Specifications of the instruments used in the experiment.

Instrument	Accuracy
Shimadzu UV-2600 spectrophotometer	±0.1 nm (200 to 1400 nm)
Thermocouples	±0.5°C
Pyranometer	<0.15%
KD2 Pro (thermal conductivity)	±5%
METTLER TOLEDO DSC 1	±0.2°C

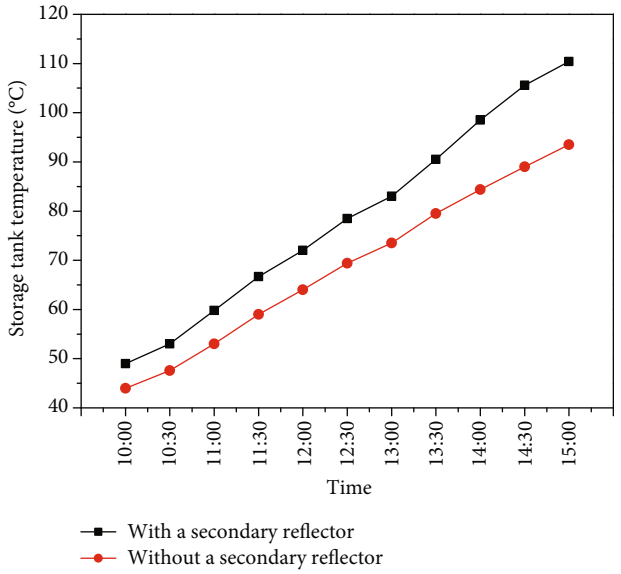

Figure 6: Variation of fluid temperature with time.

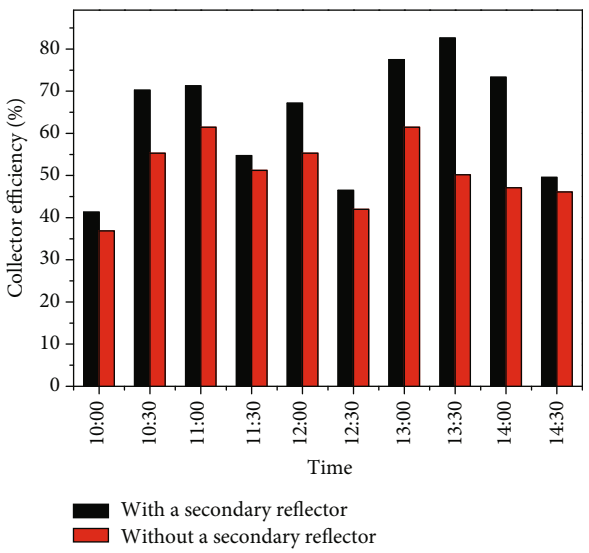

Figure 7: Variation of collector efficiency with time.

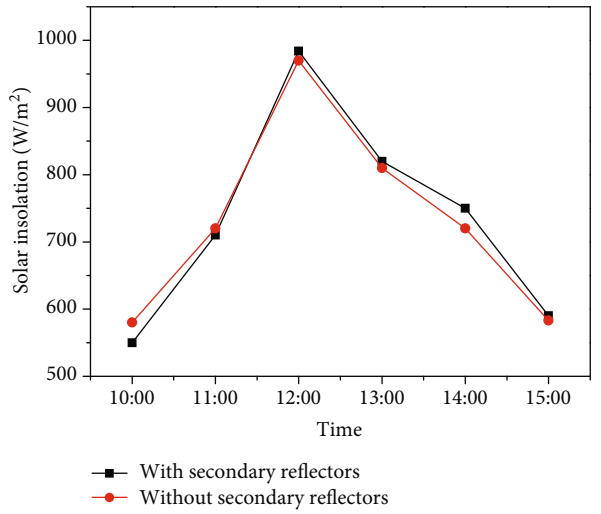

Figure 8: Solar insolation with and without secondary reflectors.

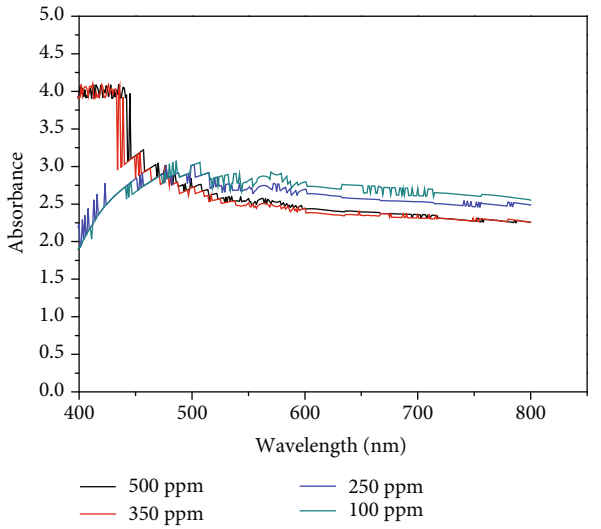

Figure 9: Absorbance of Therminol 55-TiO_2 nanofluids.

Abbreviations

A: Absorbance
A_{total}: Surface area of the receiver tube (m^2)
A_r, A_a: Receiver area and aperture area (m^2)
C: Concentration
C_{nf}: Specific heat of nanofluid (J/g K)
d: Aperture diameter of the secondary reflector (m)
f: Focal length (m)
G: Solar flux on the receiver tube (W/m^2)
h: Depth of the secondary reflector (m)
I_r: Average radiant flux (W/m^2)
I: Intensity of transmitted light
I_o: Intensity of incident light
k: Thermal conductivity (W/m K)
L: Thickness of the sample (cm)
m_{nf}: Mass of nanofluid (kg)
q: Heat flux (W/m^2)

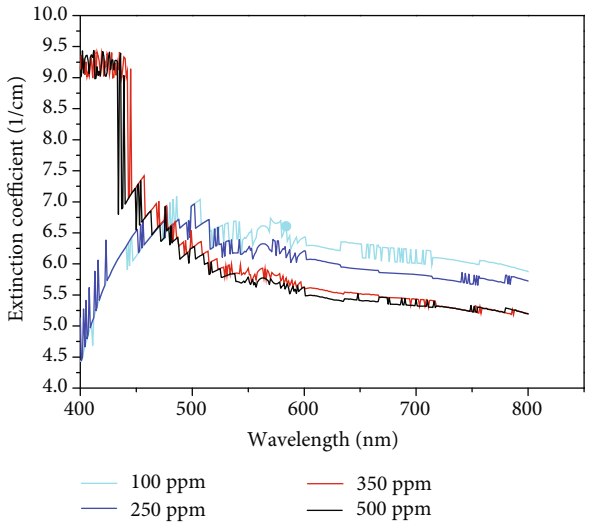

Figure 10: Extinction coefficient of Therminol 55-TiO_2 nanofluids.

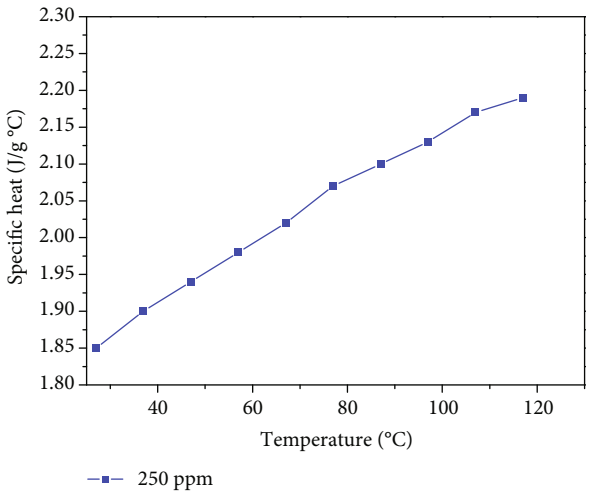

Figure 11: Specific heat variation of 250 ppm Therminol 55-TiO_2 nanofluids.

T: Temperature (K)
t: Time (s)
w: Uncertainty (%)
α: Absorption coefficient
σ: Extinction coefficient (1/cm)
ΔT: Rise in temperature inside the absorber tube (K)
Δt: Exposed time (s).

Data Availability

The data (results) used to support the findings of this study are available from the corresponding author upon request.

Conflicts of Interest

The authors declare that they have no conflicts of interest.

References

[1] L. Chen, C. Xu, J. Liu, X. Fang, and Z. Zhang, "Optical absorption property and photo-thermal conversion performance of graphene oxide/water nanofluids with excellent dispersion stability," *Solar Energy*, vol. 148, pp. 17–24, 2017.

[2] M. Karami, M. A. Akhavan-Behabadi, M. Raisee Dehkordi, and S. Delfani, "Thermo-optical properties of copper oxide nanofluids for direct absorption of solar radiation," *Solar Energy Materials & Solar Cells*, vol. 144, pp. 136–142, 2016.

[3] B. A. J. Rose, H. Singh, N. Verma et al., "Investigations into nanofluids as direct solar radiation collectors," *Solar Energy*, vol. 147, pp. 426–431, 2017.

[4] M. Muraleedharan, H. Singh, S. Suresh, and M. Udayakumar, "Directly absorbing Therminol-Al_2O_3 nano heat transfer fluid for linear solar concentrating collectors," *Solar Energy*, vol. 137, pp. 134–142, 2016.

[5] V. Khullar, H. Tyagi, T. P. Otanicar, Y. L. Hewakuruppu, and R. A. Taylor, "Solar selective volumetric receivers for harnessing solar thermal energy," *Journal of Heat Transfer*, vol. 140, no. 6, 2018.

[6] Z. Wang, J. Qu, R. Zhang, X. Han, and J. Wu, "Photo-thermal performance evaluation on MWCNTs-dispersed microencapsulated PCM slurries for direct absorption solar collectors," *Journal of Energy Storage*, vol. 26, p. 100793, 2019.

[7] J. Qu, M. Tian, X. Han, R. Zhang, and Q. Wang, "Photo-thermal conversion characteristics of MWCNT-H_2O nanofluids for direct solar thermal energy absorption applications," *Applied Thermal Engineering*, vol. 124, pp. 486–493, 2017.

[8] W. Chen, C. Zou, and X. Li, "Application of large-scale prepared MWCNTs nanofluids in solar energy system as volumetric solar absorber," *Solar Energy Materials and Solar Cells*, vol. 200, no. 8, p. 109931, 2019.

[9] W. Chen, C. Zou, and X. Li, "An investigation into the thermophysical and optical properties of SiC/ionic liquid nanofluid for direct absorption solar collector," *Solar Energy Materials and Solar Cells*, vol. 163, pp. 157–163, 2017.

[10] Z. Said, R. Saidur, and N. A. Rahim, "Optical properties of metal oxides based nanofluids," *International Communications in Heat and Mass Transfer*, vol. 59, pp. 46–54, 2014.

[11] S. Khosrojerdi, A. M. Lavasani, and M. Vakili, "Experimental study of photothermal specifications and stability of graphene oxide nanoplatelets nanofluid as working fluid for low-temperature direct absorption solar collectors (DASCs)," *Solar Energy Materials and Solar Cells*, vol. 164, pp. 32–39, 2017.

[12] I. M. Mahbubul, M. M. A. Khan, N. I. Ibrahim, H. M. Ali, F. A. Al-Sulaiman, and R. J. R. E. Saidur, "Carbon nanotube nanofluid in enhancing the efficiency of evacuated tube solar collector," *Renewable Energy*, vol. 121, pp. 36–44, 2018.

[13] A. R. Yagnem and S. Venkatachalapathy, "Heat transfer enhancement studies in pool boiling using hybrid nanofluids," *Thermochimica Acta*, vol. 672, pp. 93–100, 2019.

[14] L. S. Sundar, M. H. Farooky, S. N. Sarada, and M. K. Singh, "Experimental thermal conductivity of ethylene glycol and water mixture based low volume concentration of Al_2O_3 and CuO nanofluids," *International Communications in Heat and Mass Transfer*, vol. 41, pp. 41–46, 2013.

[15] S. Bobbo, L. Fedele, A. Benetti et al., "Viscosity of water based SWCNH and TiO_2 nanofluids," *Experimental Thermal and Fluid Science*, vol. 36, pp. 65–71, 2012.

[16] S. Anbu, S. Venkatachalapathy, and S. Suresh, "Heat transfer and pressure drop studies of TiO 2/DI water nanofluids in helically corrugated tubes using spiraled rod inserts," *Heat and Mass Transfer*, vol. 54, no. 5, pp. 1301–1311, 2018.

[17] M. Chen, Y. He, J. Huang, and J. Zhu, "Synthesis and solar photo-thermal conversion of Au, Ag, and Au-Ag blended plasmonic nanoparticles," *Energy Conversion and Management*, vol. 127, pp. 293–300, 2016.

[18] L. M. Moreira, E. A. Carvalho, M. J. V. Bell et al., "Thermo-optical properties of silver and gold nanofluids," *Journal of Thermal Analysis and Calorimetry*, vol. 114, no. 2, pp. 557–564, 2013.

[19] V. Khullar, H. Tyagi, P. E. Phelan, T. P. Otanicar, H. Singh, and R. A. Taylor, "Solar energy harvesting using nanofluids-based concentrating solar collector," *Journal of Nanotechnology in Engineering and Medicine*, vol. 3, no. 3, 2012.

[20] H. Tyagi, P. Phelan, and R. Prasher, "Predicted efficiency of a low-temperature nanofluid-based direct absorption solar collector," *Journal of Solar Energy Engineering*, vol. 131, no. 4, 2009.

[21] T. Matuska and B. Sourek, "Performance analysis of photovoltaic water heating system," *International Journal of Photoenergy*, vol. 2017, 10 pages, 2017.

[22] T.-C. Hung, D.-S. Lee, and J.-R. Lin, "An innovative application of a solar storage wall combined with the low-temperature organic Rankine cycle," *International Journal of Photoenergy*, vol. 2014, 12 pages, 2014.

[23] P. Kalidoss, S. Venkatachalapathy, and S. Suresh, "Photothermal energy conversion enhancement studies using low concentration nanofluids," *Journal of Solar Energy Engineering*, vol. 141, no. 6, 2019.

[24] H. Bhowmik and R. Amin, "Efficiency improvement of flat plate solar collector using reflector," *Energy Reports*, vol. 3, pp. 119–123, 2017.

[25] E. Bellos and C. Tzivanidis, "Investigation of a booster secondary reflector for a parabolic trough solar collector," *Solar Energy*, vol. 179, pp. 174–185, 2019.

[26] G. S. C. Prasad, K. S. Reddy, and T. Sundararajan, "Optimization of solar linear Fresnel reflector system with secondary concentrator for uniform flux distribution over absorber tube," *Solar Energy*, vol. 150, pp. 1–12, 2017.

[27] B. Praveen and S. Suresh, "Experimental study on heat transfer performance of neopentyl glycol/CuO composite solid-solid PCM in TES based heat sink," *Engineering Science and Technology, an International Journal*, vol. 21, no. 5, pp. 1086–1094, 2018.

[28] Z. S. Abdel-Rehim and A. Lasheen, "Experimental and theoretical study of a solar desalination system located in Cairo, Egypt," *Desalination*, vol. 217, no. 1-3, pp. 52–64, 2007.

[29] G. L. Harding, Y. Zhiqiang, and D. W. Mackey, "Heat extraction efficiency of a concentric glass tubular evacuated collector," *Solar Energy*, vol. 35, no. 1, pp. 71–79, 1985.

Hindawi
International Journal of Photoenergy
Volume 2020, Article ID 8450737, 9 pages
https://doi.org/10.1155/2020/8450737

Research Article

Study of the Tensile Damage of 321 Stainless Steel for Solar Thermal Power Generation by Acoustic Emission

Lida Liao and Qi Tan

School of Energy and Power Engineering, Changsha University of Science and Technology, Changsha 410114, China

Correspondence should be addressed to Qi Tan; tq2012@stu.csust.edu.cn

Received 8 November 2019; Accepted 27 December 2019; Published 10 January 2020

Guest Editor: Zhangxing He

In this paper, the acoustic emission technique was used to study the signal during the tensile damage of 321 stainless steel for solar thermal power generation. It was found that the peak frequency can effectively distinguish different types of signals during the tensile test. The interference signals generated during the tensile test are effectively resolved by combining the amplitude-peak frequency distribution map and the energy-peak frequency distribution map. The amplitude-time map of the acoustic emission signal is successfully divided into three stages by using peak frequency parameter.

1. Introduction

The massive use of fossil fuels has intensified the problem such as energy shortage and environment pollution; therefore, vigorous development of renewable energy is around the corner [1]. Statistics from the International Energy Agency show that electricity production accounts for most of global greenhouse gas emissions, and accordingly, 25,000 GW of low-carbon energy will be required by 2050 to meet the sustainable life on earth [2, 3]. To mitigate the environmental problems associated with this, it is increasingly important to reduce the use of fossil fuels by developing more cost-effective renewable energy technologies. Among all kinds of renewable energy, solar energy accounts for a large proportion [4]. At present, solar photovoltaic power generation and solar thermal power generation are two main technologies of solar energy utilization. Compared with solar photovoltaic power generation technology, solar thermal power generation technology has the advantages of strong controllability and high flexibility [5], so it is regarded as the preferred equipment for flexible power supply of large-scale power grid [6].

Solar thermal power system includes a solar collector, solar receiver, and power conversion device. A solar receiver absorbs concentrated solar radiation through a collector and transmits it to a heat transfer fluid used to transfer high-temperature heat to a power conversion system. The pipelines used in solar thermal power plants to transport thermal fluid require high material stability. 321 stainless steel is a stable and ductile Ti-austenitic stainless steel, and Ti can effectively mitigate the sensitization effect of materials under high temperature. Therefore, 321 stainless steel is widely used in such important parts as pipelines and heat exchangers of solar thermal power system [7]. In order to ensure the safety and reliability of the structure, it is of great significance to study the tensile damage behavior of 321 stainless steel.

Acoustic emission (AE) is an efficient structural health monitoring technology, which is defined as a phenomenon of rapid energy release and transient elastic wave generation [8, 9]. Acoustic emission technology based on Kaiser's [10] research uses sensors and preamplifiers to detect elastic waves propagating through the material. The AE monitors through several sensors and preamplifiers to detect elastic waves propagated inside a material, as shown in Figure 1. The signal waves are directly transmitted to the AE system, where these signals would be analyzed and transferred to digital signals. At present, the nondestructive testing methods commonly used for tensile damage include ultrasonic testing, X-ray inspection, computed tomography (CT) detection, infrared thermography techniques, and magnetic memory

Figure 1: Principles of AE detection. Acoustic emission signal is collected by the sensor, and the preamplifier transmits it to the acoustic emission system.

methods. However, ultrasonic testing requires different probes for different defects, and ultrasonic testing has high requirements on the shape and thickness of the material. X-ray inspection is harmful to the human body, an operator who has special training experience is needed. The disadvantage of CT detection is that it is inconvenient for on-site inspection of large components; furthermore, CT detection is inefficient and costly. The infrared thermography technique has high requirements for the surface heat absorption rate of materials, so it is not suitable for many materials. For magnetic memory testing, the magnetic memory signal is weak, and it is seriously affected by the environmental magnetic field. As a real-time testing method, the acoustic emission technique is more suitable for dynamic evaluation and real-time diagnosis than the abovementioned detection methods. And the acoustic emission technique has characteristics that it is not limited by materials, geometries, and working conditions. Furthermore, acoustic emission detection is a passive detection method; acoustic emission signals come from the detected object, so the detection process will not affect the normal operation of the device. Therefore, acoustic emission technology is widely applied in the detection of deformation and fracture process of various materials. Barile et al. [11] monitored the fatigue process of stainless steel specimens by using AE technology and infrared thermography (IT) technology, and they found that AE technology was more effective than IT technology. A typical AE signal includes many parameters, which are commonly used such as amplitude and count. Amplitude is defined as the peak voltage magnitude of the maximum offset obtained from the signal waveform of the acoustic emission event. Threshold is a voltage level on an electronic comparator such that signals with amplitudes larger than this level will be recognized. Count is defined as the number of times the acoustic emission signal exceeds the threshold. Heiple et al. [12] found that count in the characteristic parameters of the signal can effectively reflect the damage of the material. However, the parameters such as amplitude and count are related to the threshold setting, so analysis by a single parameter is not enough. Acoustic emission energy is the area under the signal detection envelope and is not sensitive to threshold, operating frequency, and propagation characteristics. Roberts and Talebzadeh [13] found that the energy of the signal is less affected by the threshold setting and coupling conditions and the change in the signal energy value can reflect the phase changes inside the material. With the development of acoustic emission technology, many researchers have used acoustic emission technology to study the fatigue process of different materials, such as stainless steel [14], aluminum alloy [15], titanium alloy [16], self-compacting concrete [17], wood material [18], and SIC/SIC composites [19]. In recent years, many researchers have conducted acoustic emission studies on the tensile behavior of various materials and achieved certain results. Sun et al. [20] studied the acoustic emission of tensile damage of high-strength aluminum alloy materials used in the gearbox shell of high-speed train, quantified the evolution of tensile damage of aluminum alloy, and proved the effectiveness of this method. Kumar et al. [21] found that changes in AE parameters could well reflect changes in microstructure of titanium alloy during the tensile process. Sayar et al. [22] investigated damage mechanisms in the open-hole laminated carbon/epoxy composite by using the acoustic emission technology. The results show that different damage stages can be determined by the frequency range of the acoustic emission signal. Njuhovic et al. [23] found that there exists a correlation between the cumulative absolute AE energy and tensile damage of metallised glass fibre-reinforced epoxy composites and different mechanisms of damage can be identified by the peak frequency parameters of the acoustic emission signal. Yao et al. [24] studied the cracking behavior and fracture process of thermal barrier coating under tensile load through acoustic emission technology, and the results showed that acoustic emission signals could reveal the fracture type and failure mechanism. However, at present, there are few researches on tensile damage of 321 stainless steel for solar thermal power generation. Acoustic emission signals contain damage information of material. We can know the internal damage of the material in time by analyzing the parameter of acoustic emission signals. However, the commonly used parameters of acoustic emission signal can easily be affected by various factors, such as parameters of amplitude and count will be affected by the threshold, which cannot accurately characterize the internal damage of the material.

In this paper, we study the tensile damage of 321 stainless steel for solar thermal power generation by using acoustic emission technology. In order to accurately obtain the information of 321 stainless steel for solar thermal power generation during tensile damage, we use the parameter of peak frequency to analyze the tensile damage process of 321 stainless steel. The peak frequency parameters are used to distinguish different types of signals during the tensile test. Peak frequency corresponds to the maximum amplitude of Fourier transform of acoustic emission waveform, which is a parameter sensitive to damage. The peak frequency of acoustic emission signals is not affected by threshold setting, which is more reliable than other parameters. Peak frequency can characterize the types of different acoustic emission sources. The interference signals generated during the tensile test are effectively resolved by combining the amplitude-peak frequency distribution map and the energy-peak frequency distribution map. The amplitude-time map of the acoustic emission signal is divided into three stages by using the peak frequency parameter. The rest of the paper is organized

Table 1: Chemical compositions (wt.%) of 321 stainless steel.

Composition	C	Si	Mn	P	S	Cr	Ni	Ti
Wt.%	0.08	1.00	2.00	0.035	0.03	17-19	9-12	5*C%

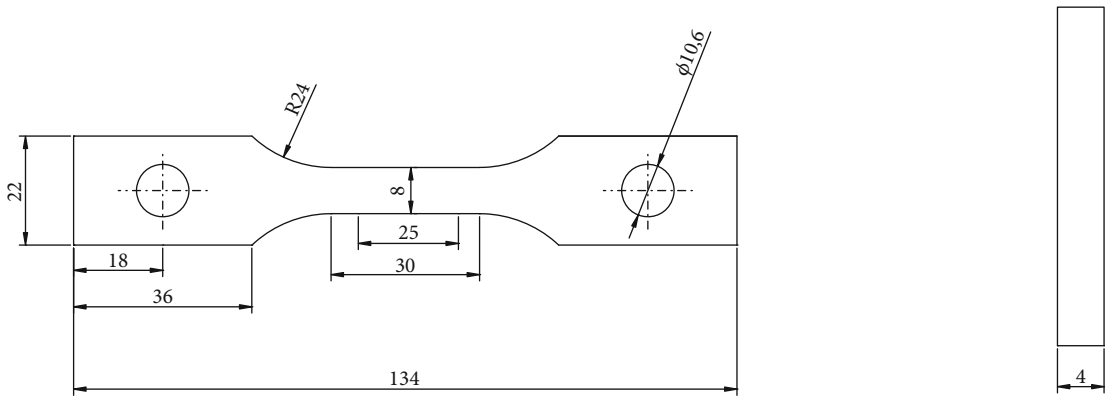

Figure 2: Geometry of tensile specimen. The specimen was machined to a thickness of 4 mm.

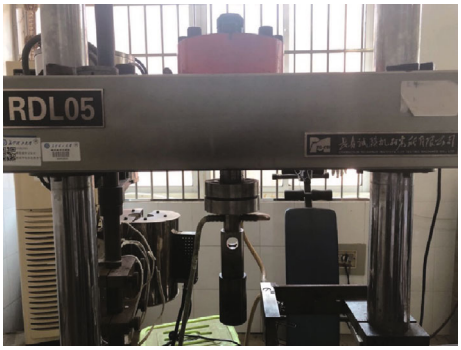

Figure 3: RDL05 testing machine of the tensile experiment. The maximum load of the machine is 50 kN.

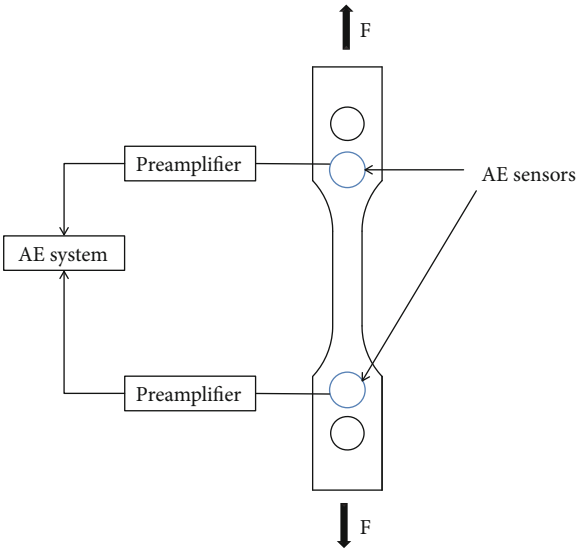

Figure 4: Schematic of the experimental process. Two acoustic emission sensors are fixed on the surface of the specimen to collect signals.

as follows: in the second part, the materials used in the experiment are introduced, the third part is the analysis and discussion of the acoustic emission signals obtained from the tensile test, and the fourth part summarizes the results obtained.

2. Materials and Methods

2.1. Materials and Specimen. The material used in this study is 321 stainless steel used for solar thermal power generation, which is a Ti-containing austenite stainless steel. The 321 stainless steel has stable and ductile characteristics. Its chemical composition is shown in Table 1.

The specimen was machined from the stainless steel plates to a thickness of 4 mm in accordance with GB/T228.1-2010 standard. The 321 stainless steel plate is cut in the rolling direction, with the section size of 4 mm ∗ 8 mm. Figure 2 shows the geometry of the sample.

2.2. Tensile Tests. Tensile tests were carried out according to GB/T228.1-2010 standard on a RDL05 testing machine at ambient temperature. The maximum load of the machine is 50 kN. Specimens were tested with a loading rate controlled at 0.3 mm/min. The machine of the tensile experiment is shown in Figure 3.

2.3. AE Monitoring Setup. The AE signals generated from the tensile tests were recorded and analyzed by PCI-2 AEwin system, supplied by Physical Acoustic Corporation (PAC). Schematic of the experimental process is shown in Figure 4. Acoustic emission signals generated by 321 stainless steel

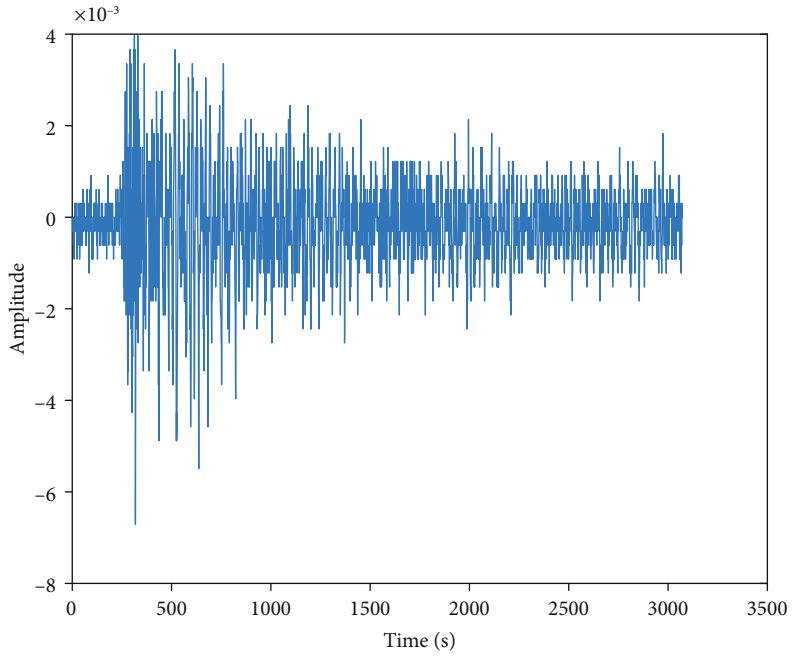

Figure 5: Time-domain graphic of the original signal. Time-domain figure obtained through processing the signals collected by the acoustic emission equipment.

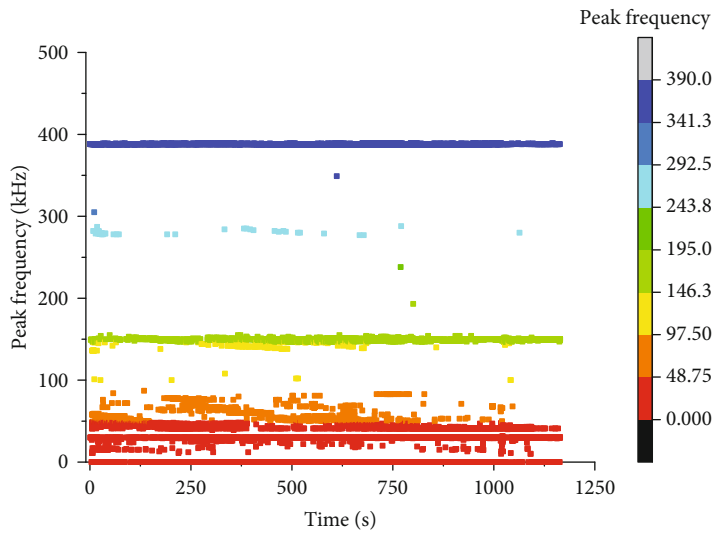

Figure 6: Distribution of peak frequency during tensile test. There are five types of peak frequency signals during the tensile test, which are distributed in five ranges: 0-48 kHz, 50-97 kHz, near 149 kHz, around 284 kHz, and near 388 kHz.

during tensile damage are collected by two acoustic emission sensors (R15a) and then transmitted to the acoustic emission system through two 2/4/6 preamplifiers with a gain of 40 dB. Figure 5 is the time-domain graphic of the original signal. Acoustic emission sensors installed on the specimen surface, using vacuum grease as the coupling agent. The peak determination time (PDT), hit determination time (HDT), and hit observation time (HLT) were set to 300, 600, and 1000, respectively. The collection of these time-driven parameters was performed using standard lead core fracture. Based on these preparation, we set the threshold value at 25 dB to eliminate the external noise. An acoustic emission test was carried out until the final fracture appeared.

3. Results and Discussion

3.1. Analysis of the Peak Frequency-Time Map of Acoustic Emission Signals. An acoustic emission device was used to monitor the tensile damage process of 321 stainless steel, and the acoustic emission signals were collected and recorded

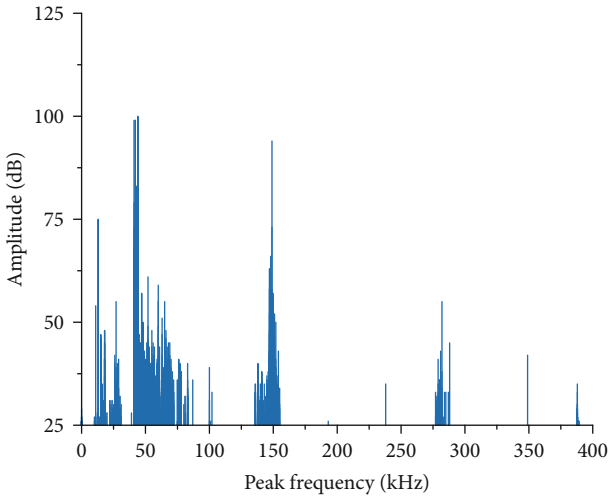

Figure 7: Distribution of amplitude with peak frequency. There are three concentrated sub-ranges in the range 0-48 kHz.

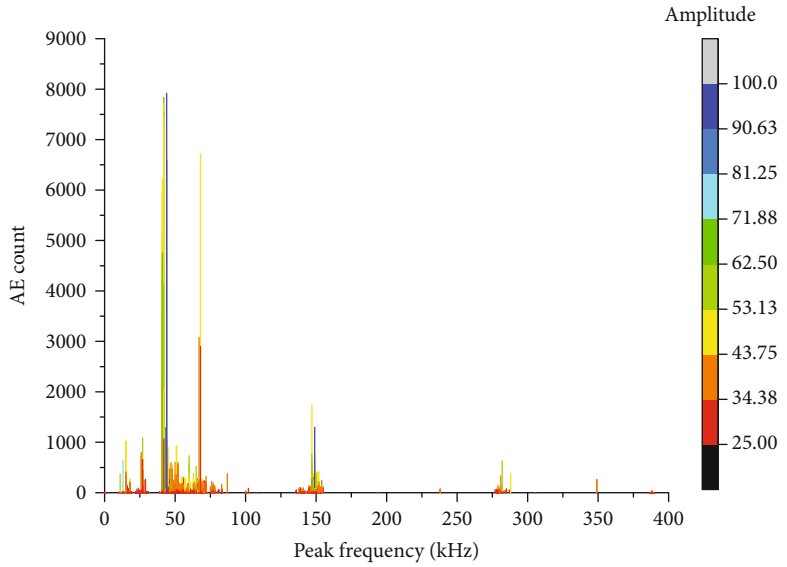

Figure 8: Distribution of AE count with peak frequency. The acoustic emission count of range near 388 kHz was very low.

by acoustic emission system. We obtained a distribution plot of the peak frequency during the tensile damage process by extracting the peak frequency parameters of the collected acoustic emission signals and correlating the peak frequency parameters with time. Figure 6 shows a typical plot of peak frequency vs. time for specimen during the tensile test. It can be clearly found that there are five different ranges of peak frequency signals throughout the tensile test. In range 1, about 0-48 kHz, the distribution of the peak frequency parameter is scattered. In range 2, 50-97 kHz, the distribution of peak frequency parameters concentrated relative to range 1. In range 3, near 149 kHz, its peak frequency distribution is more concentrated. In range 4, around 284 kHz, the peak frequency signal of this range appears intermittently throughout the tensile test, but the frequency is concentrated. In range 5, near 388 kHz, the peak frequency is very concentrated. It can be seen that the peak frequency parameters can distinguish different types of signals well.

3.2. Analysis of the Peak Frequency Distribution. Due to amplitude parameters and count parameters can intuitively show the characteristics of the signal, in order to know the difference in parameter of amplitude and count between types of peak frequency signals, we obtained a plot about the distribution of peak frequency with these two parameters during the tensile test by correlating amplitude parameters and counting parameters with peak frequency parameters, as shown in Figures 7 and 8. It is apparent that there are three concentrated subranges in the range 1 (0-48 kHz), respectively, around 13 kHz, around 27 kHz, and around 44 kHz. Obviously, the highest value of amplitude is around 44 kHz, reaching 100 dB, and has a very high value of count.

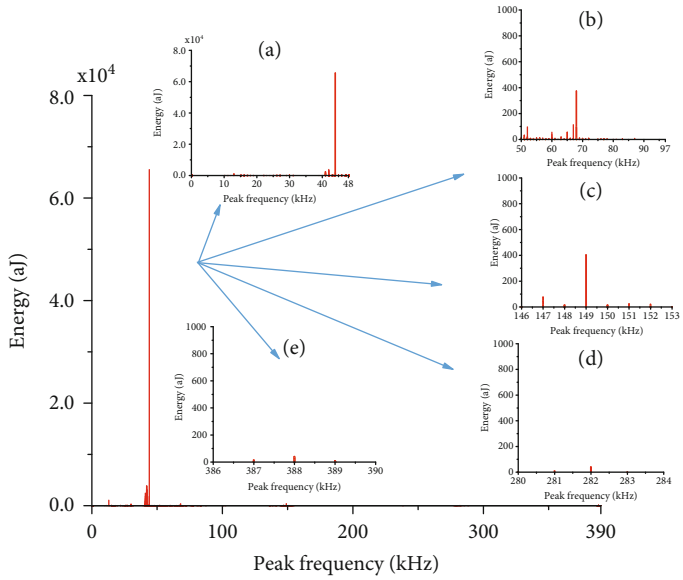

Figure 9: Distribution of AE energy with peak frequency: (a) range 0-48 kHz, (b) range 50-97 kHz, (c) near 149 kHz, (d) around 284 kHz, and (e) near 388 kHz.

However, because the amplitude and count parameters are affected by the threshold setting, analysis based on these two parameters alone will cause inaccurate results. Therefore, peak frequency signals in different ranges are analyzed by combining with energy parameter, which is not affected by the threshold setting. Figure 9 shows an energy distribution plot of the peak frequency signal appearing during tensile damage, which is obtained by corresponding acoustic emission signals of different peak frequencies with the released energy. Furthermore, the energy of value distribution figure in five different peak frequency ranges was obtained. In range 1(0-48 kHz), the energy released is the highest in the whole test. The signal of range 2 (peak frequency 50-97 kHz) exhibits low amplitude and high count characteristics, wherein the signal with a peak frequency at 68 kHz releases the acoustic emission count only after 44 kHz, and the energy is low. The amplitude of the signal in range 3 (the peak frequency is around 149 kHz) is on the rise, and the amplitude is concentrated in the range below 50 dB, and the energy is low. The range of sound emission signals in range 4 (the peak frequency is around 284 kHz) is relatively low, and the energy is extremely low compared to other types of peak frequencies. However, when the peak frequency is in range 4 (near 388 kHz), the amplitude is extremely low, the acoustic emission count is very small, and the energy is extremely low. Therefore, signals with peak frequencies around 284 kHz and 388 kHz are classified as interference signals.

In range 1, the amplitude of the signal near 13 kHz is concentrated in the range of more than 50 dB, and the amplitude of the signal near the peak of 27 kHz is mostly less than 50 dB. However, it is impossible to judge from the amplitude distribution that which peak frequency is generated by the material itself, and therefore, the distribution of the energy of the two is found. It can be seen from Figures 10 and 11 that

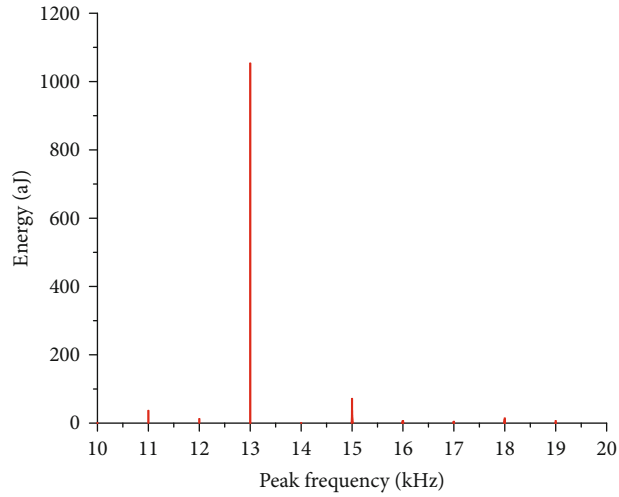

Figure 10: Distribution of AE energy with peak frequency (around 13 kHz). The range near 13 kHz is where the high acoustic emission energy is released.

the energy of the peak frequency near 27 kHz is extremely low, close to zero, and the energy at 13 kHz is much higher. Therefore, it can be judged that the peak frequency is an interference signal at 27 kHz. Finally, four peak frequency ranges capable of expressing the tensile damage signal of the material were obtained: 13 kHz, 44 kHz, 68 kHz, and 149 kHz.

It can be found that the signal source can not be accurately judged by the amplitude and peak frequency distribution map, and a large error will occur. The energy and peak frequency distribution map can find the interference signal, but it has no obvious distribution characteristics of the former. Therefore, by combining the amplitude-peak frequency

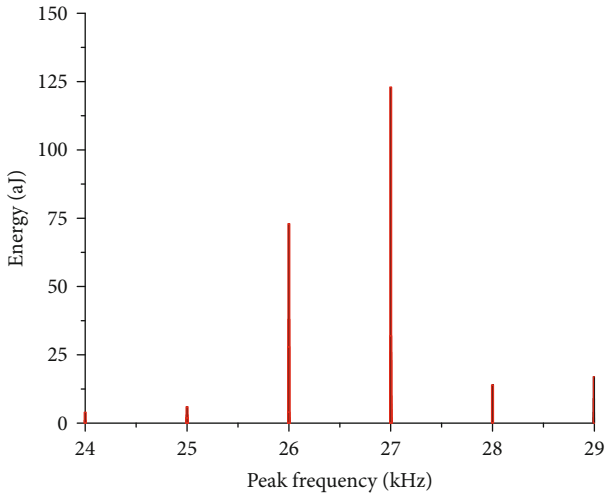

Figure 11: Distribution of AE energy with peak frequency (around 27 kHz). The range near 27 kHz of acoustic emission energy released in a very low level.

distribution map and the energy-peak frequency distribution map, it is possible to effectively distinguish the interference signal from the material self-damage signal.

3.3. Analysis of Amplitude History of Different Types of Peak Frequency Signals. Figure 12 shows the trend of amplitude with time during tensile test, which is divided into three stages according to the peak frequency. The peak frequency appears in the initial set of stages (stage1) and the stage of the break (stage3) in the signal set of range 1, indicating that the signals produced by the two stages are of the same type. In phase 2, signals with peak frequencies in the range of 68 kHz and 149 kHz are simultaneously present, indicating that two different types of acoustic emission signals are generated at this stage. The damage mechanism at each stage of the material stretching process is different, so different types of signals represent different damage mechanisms. The peak frequency can well classify the amplitude history map of the acoustic emission signal into different stages and can understand the type of material damage.

4. Conclusions

In this paper, we used acoustic emission technology to study the tensile damage signal of 321 stainless steel for solar thermal power generation. 321 stainless steel is a ductile Ti-austenitic stainless steel, which is widely used in pipelines and heat exchangers of solar thermal power system. However, there is little research on tensile damage of 321 stainless steel by using a more convenient and efficient method. We detect tensile damage of 321 stainless steel for solar thermal power generation by using an acoustic emission technique. As a real-time testing method, the advantage of the acoustic emission technique is that it is not limited by the type of material and geometry. Compared with current detection methods for material tensile damage, we can detect 321 stainless steel for solar energy more efficiently and conveniently by using acoustic emission technology. Through the analysis of the amplitude and frequency history of the acoustic emission signal, the peak frequency distribution map, and the amplitude history of different types of peak frequency signals, the following conclusions can be drawn:

(1) The peak frequency can distinguish different types of signals better than parameters of amplitude and count during the tensile damage test. It can effectively distinguish the interference signal from the material damage signal by combining the peak frequency and energy parameters of the acoustic emission signal during the tensile damage of 321 stainless steel

(2) From the results, we found that the peak frequency of the 321 stainless steel tensile damage process is mainly concentrated in the following five ranges: 0-48 kHz, 50-97 kHz, around 149 kHz, around 284 kHz, and around 388 kHz. And there are three subranges in the range 0-48 kHz: around 13 kHz, around 27 kHz, and around 44 kHz. According to the distribution of AE energy with peak frequency, we found that the range of peak frequency near 27 kHz is an interference signal with a very low level of energy. Combining the values of the count and energy parameters, we found that the count and energy values of the signal with peak frequency range around 284 kHz and 388 kHz are extremely low, which also are interference signals. Finally, we obtained four kinds of peak frequency ranges that can represent the tensile damage signal of the material: around 13 kHz, 44 kHz, 68 kHz, and 149 kHz

(3) The tensile damage process is divided into three stages by combining the trend of amplitude and peak frequency over time. The peak frequencies of the signals appearing in stages 1 and 3 are concentrated in the range of 0-48 kHz, which are mainly composed of signals with peak frequencies around 13 kHz and 44 kHz. The peak frequency of the signal appearing in stage 2 is in the range of around 68 kHz and around 149 kHz. The first stage is the initial stage of tensile damage of 321 stainless steel, and the third stage is the fracture stage. The appearance of signals with peak frequency ranges around 13 kHz and 44 kHz can serve as a reminder that the 321 stainless steel is entering the fracture stage, which allows us to understand the damage of the equipment in advance so that safety measures can be taken before the accident

At present, we have known that there are five types of peak frequency during the tensile damage process of 321 stainless steel, which are related to the tensile damage source mechanism of 321 stainless steel. Therefore, further work is to quantify tensile damage of 321 stainless steel by establishing relationship between the peak frequency of acoustic emission signals and the tensile damage mechanism. In addition,

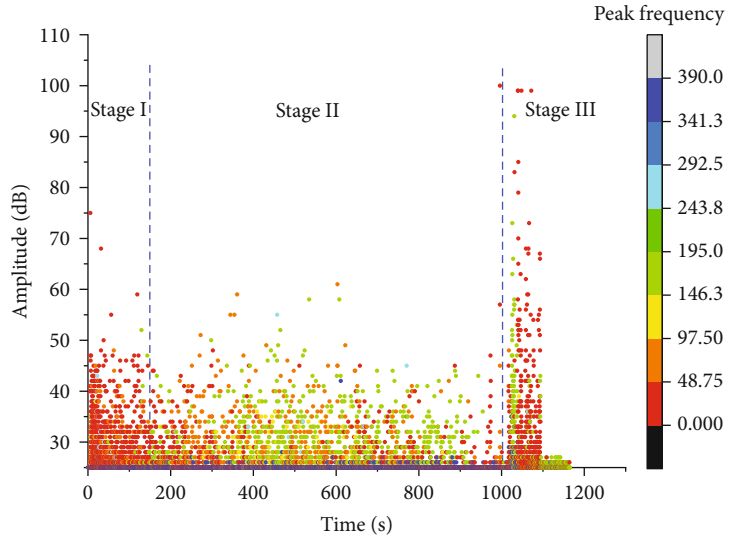

Figure 12: Trend of amplitude with time. The whole test was divided into three stages by the peak frequency.

this testing method has not been applied to actual solar thermal storage system and associated pipelines. There is still work to be done in the application of acoustic emission technique in actual solar thermal storage system.

Data Availability

The data used to support the findings of this study are available from the corresponding author upon request.

Conflicts of Interest

The authors declare that they have no conflicts of interest.

Acknowledgments

Funding that permitted this research was granted by the Key Laboratory of Renewable Energy Electric-Technology of Hunan Province (Grant No. 2015ZNDL007), Key Laboratory of Efficient & Clean Energy Utilization at Changsha University of Science and Technology (Grant No. 2013NGQ009), "Practice Innovation and Entrepreneurship Enhancement Program" for Changsha University of Science and Technology (Grant No. SJCX201957), "International Collaborative Research Underpin Double-First-Class University Development" (Grant No. 2019IC17), and the Education Department of Hunan Province (Grant No. 19B021). The authors would like to acknowledge the Education Department of Hunan Province and Changsha University of Science & Technology for the funding opportunities and financial support.

References

[1] O. Behar, A. Khellaf, and K. Mohammedi, "A review of studies on central receiver solar thermal power plants," *Renewable & Sustainable Energy Reviews*, vol. 23, pp. 12–39, 2013.

[2] "The future of solar energy- an interdisciplinary MIT study," *Energy Initiative Massachusetts Institute of Technology*, 2015.

[3] *CO_2 ermissions from fuel combustion highlights*, International Energy Agency, Paris, 2015.

[4] A. F. Regin, S. C. Solanki, and J. S. Saini, "Heat transfer characteristics of thermal energy storage system using PCM capsules: a review," *Renewable & Sustainable Energy Reviews*, vol. 12, no. 9, pp. 2438–2458, 2008.

[5] B. Xu, P. W. Li, and C. Chan, "Application of phase change materials for thermal energy storage in concentrated solar thermal power plants: a review to recent developments," *Applied Energy*, vol. 160, pp. 286–307, 2015.

[6] J. Sun, Q. B. Liu, and H. Hong, "Numerical study of parabolic-trough direct steam generation loop in recirculation mode: characteristics, performance and general operation strategy," *Energy Conversion and Management*, vol. 96, pp. 287–302, 2015.

[7] M. Lang, J. Johnson, J. Schreiber et al., "Cyclic deformation behaviour of AISI 321 austenitic steel and its characterization by means of HTC-SQUID," *Nuclear Engineering and Design*, vol. 198, no. 1-2, pp. 185–191, 2000.

[8] ASTM E976-10, *Standard Guide for Determining the Reproducibility of Acoustic Emission Sensor Response*, ASTM International, West Conshohocken, PA, USA, 2010.

[9] ASTM E1316-14, *Standard Terminology for Nondestructive Examinations*, ASTM International, West Conshohocken, PA, USA, 2014.

[10] W. Kaiser, "Recent progress in stimulated Raman scattering," *Ieee Journal of Quantum Electronics*, vol. 4, no. 5, p. 381, 1968.

[11] C. Barile, C. Casavola, G. Pappalettera, and C. Pappalettere, "Analysis of crack propagation in stainless steel by comparing acoustic emissions and infrared thermography data," *Engineering Failure Analysis*, vol. 69, pp. 35–42, 2016.

[12] C. R. Heiple, S. H. Carpenter, and M. J. Carr, "Acoustic emission from dislocation motion in precipitation-strengthened alloys," *Metal Science*, vol. 15, no. 11-12, pp. 587–598, 1981.

[13] T. M. Roberts and M. Talebzadeh, "Acoustic emission monitoring of fatigue crack propagation," *Journal of Constructional Steel Research*, vol. 59, no. 6, pp. 695–712, 2003.

[14] M. Y. Chai, Z. X. Zhang, Q. Duan, and Y. Song, "Assessment of fatigue crack growth in 316LN stainless steel based on acoustic

emission entropy," *International Journal of Fatigue*, vol. 109, pp. 145–156, 2018.

[15] M. Y. Bhuiyan and V. Giurgiutiu, "The signatures of acoustic emission waveforms from fatigue crack advancing in thin metallic plates," *Smart Materials and Structures*, vol. 27, no. 1, p. 015019, 2018.

[16] M. Strantza, D. Van Hemelrijck, P. Guillaume, and D. G. Aggelis, "Acoustic emission monitoring of crack propagation in additively manufactured and conventional titanium components," *Mechanics Research Communications*, vol. 84, pp. 8–13, 2017.

[17] C. Chen, X. D. Chen, and S. S. Guo, "Experimental study on acoustic emission characteristic of fatigue crack growth of self-compacting concrete," *Structural Control & Health Monitoring*, vol. 26, no. 4, p. e2332, 2019.

[18] M. Diakhate, N. Angellier, R. M. Pitti, and F. Dubois, "On the crack tip propagation monitoring within wood material: cluster analysis of acoustic emission data compared with numerical modelling," *Construction and Building Materials*, vol. 156, pp. 911–920, 2017.

[19] G. N. Morscher and R. Maxwell, "Monitoring tensile fatigue crack growth and fiber failure around a notch in laminate SIC/SIC composites utilizing acoustic emission, electrical resistance, and digital image correlation," *Journal of the European Ceramic Society*, vol. 39, no. 2-3, pp. 229–239, 2019.

[20] C. Sun, W. D. Zhang, Y. B. Ai, and H. Que, "Study of the tensile damage of high-strength aluminum alloy by acoustic emission," *Metals*, vol. 5, no. 4, pp. 2186–2199, 2015.

[21] J. Kumar, S. Punnose, C. K. Mukhopadhyay, T. Jayakumar, and V. Kumar, "Acoustic emission during tensile deformation of smooth and notched specimens of near alpha titanium alloy," *Research in Nondestructive Evaluation*, vol. 23, no. 1, pp. 17–31, 2012.

[22] H. Sayar, M. Azadi, A. Ghasemi-Ghalebahman, and S. M. Jafari, "Clustering effect on damage mechanisms in open-hole laminated carbon/epoxy composite under constant tensile loading rate, using acoustic emission," *Composite Structures*, vol. 204, pp. 1–11, 2018.

[23] E. Njuhovic, M. Brau, F. Wolff-Fabris, K. Starzynski, and V. Altstädt, "Identification of failure mechanisms of metallised glass fibre reinforced composites under tensile loading using acoustic emission analysis," *Composites Part B: Engineering*, vol. 81, pp. 1–13, 2015.

[24] W. B. Yao, C. Y. Dai, W. G. Mao, C. Lu, L. Yang, and Y. C. Zhou, "Acoustic emission analysis on tensile failure of air plasma-sprayed thermal barrier coatings," *Surface & Coatings Technology*, vol. 206, no. 18, pp. 3803–3807, 2012.

Hindawi
International Journal of Photoenergy
Volume 2019, Article ID 2730849, 13 pages
https://doi.org/10.1155/2019/2730849

Review Article

Review of Modified Nickel-Cobalt Lithium Aluminate Cathode Materials for Lithium-Ion Batteries

Ding Wang,[1] Weihong Liu,[1] Xuhong Zhang,[2] Yue Huang,[1] Mingbiao Xu ,[1,2] and Wei Xiao [3]

[1]*School of Petroleum Engineering, Yangtze University, Wuhan 430100, China*
[2]*Jingzhou Jiahua Technology Co. Ltd., Jingzhou 434000, China*
[3]*School of Chemistry and Environmental Engineering, Yangtze University, Jingzhou 434000, China*

Correspondence should be addressed to Mingbiao Xu; xumingbiao2019@126.com and Wei Xiao; xwylyq2006@126.com

Received 4 November 2019; Accepted 4 December 2019; Published 29 December 2019

Guest Editor: Zhangxing He

Ternary nickel-cobalt lithium aluminate $LiNi_xCo_yAl_{1-x-y}O_2$ (NCA, $x \geq 0.8$) is an essential cathode material with many vital advantages, such as lower cost and higher specific capacity compared with lithium cobaltate and lithium iron phosphate materials. However, the noticeably irreversible capacity and reduced cycle performance of NCA cathode materials have restricted their further development. To solve these problems and further improve the electrochemical performance, numerous research studies on material modification have been conducted, achieving promising results in recent years. In this work, the progress of NCA cathode materials is examined from the aspects of surface coating and bulk doping. Furthermore, future research directions for NCA cathode materials are proposed.

1. Introduction

Lithium-ion batteries (LIBs), an energy storage device that combines high-energy density and flexible operation, have been widely used in mobile and wireless electronic devices, power tools, hybrids, and electric vehicles [1–3]. It is known that the performance of LIBs mainly depends on the cathode materials for the battery capacity, and it involves the electrochemical reactions of intercalation and deintercalation of lithium ions. Moreover, the cathode materials play a vital role in their electrochemical performance and account for more than 30% of the cost of the entire battery system. Therefore, it is very important to research and develop cathode materials with high performance and low cost [4, 5].

Layered structural $LiCoO_2$ materials with a theoretical specific capacity of 274 m Ah g^{-1} are the leading cathode in commercial LIBs, such as the first commercial LIBs prepared by Sony in 1991 [6], which can deliver approximately 137 m Ah g^{-1} of discharge specific capacity with up to 100% coulombic efficiency. However, the depletion and high cost of cobalt resources severely restrict practical applications of $LiCoO_2$ materials [7]. At present, all companies try to avoid using $LiCoO_2$ and develop new materials with a high potential. $LiNiO_2$ has the similar structure to $LiCoO_2$, and it possesses a higher theoretical specific capacity (275 m Ah g^{-1}) at lower cost [8, 9]. However, it is still impossible to synthesize a stoichiometric ratio of $LiNiO_2$ by a simple process because Ni^{2+} is difficult to completely oxidize to Ni^{3+}, and its electronic structure, magnetic structure, and local structure are still highly controversial, severely limiting this positive electrode from practical applications. It is feasible that a layered nickel-rich oxide replacing Ni with other heteroatoms, such as Co [10, 11], Fe [12, 13], Mn [14, 15], Ti [16], Zr [17], Mg [18], and Al [19], can deliver a sizeable reversible capacity, and it is one of the most attractive strategies in the field of cathode materials. These substitutions mainly affect the layered crystal structure, the electrochemical stability, and the capacity with the intercalation and deintercalation of lithium ions, especially for the thermal stability in the case of extreme charge-discharge processes.

The incorporation of Co significantly enhances the structural order of the nickel-based positive electrode materials [20], which could achieve a high voltage platform. When the molar ratio of Ni and Co components is 8 : 2, the as-prepared $LiNi_{0.8}Co_{0.2}O_2$ material may possess the best performance and the degree of cation mixing is less than 2% [21]. However, its performance is greatly affected by high temperature. The capacity and potential of the nickel-rich-layered oxide rapidly deteriorate during long-term cycles, which inevitably affect the stable output of energy. The addition of a small amount of Al stabilizes the material structure and improves the thermal stability of the material. The $LiNi_xCo_yAl_{1-x-y}O_2$ (NCA) material obtained by doping Co and Al elements exhibits exceptional electrochemical properties [22, 23]. Among the series of materials with different ratios of Ni, Co, and Al elements, $LiNi_{0.8}Co_{0.15}Al_{0.05}O_2$ is the most widely researched material and has attracted full attention and commercialization due to its low cost, nontoxicity, and high-energy density [24]. Tesla is the first company to employ NCA cathode materials to power cars, and it has achieved remarkable success in the electric vehicle industry [25].

NCA is a promising cathode material due to its excellent structural stability and high capacity. However, the cycle and rate performance of NCA materials still limit its large-scale application. The layered rock salt cathode material affects the electrochemical performance due to structural defects. The common structural defects in nickel-based compounds are excess nickel, Li-Ni interlayer mixing, and oxygen vacancy defects [26–28]. The NCA material also has some shortcomings. On the one hand, the poor thermal stability of Ni^{3+} causes the reduction of Ni^{3+} to Ni^{2+}. With the release of Li^+, some Ni^{2+} ions could easily occupy the vacancy of Li^+ ions during the charging process because the Ni^{2+} radius (0.69 Å) is similar to the Li^+ radius (0.76 Å) [29], which may cause lithium nickel-mixing effects and generate irreversible phases to result in material capacity loss [30, 31]. On the other hand, Ni^{3+} and Ni^{4+} in the high oxidation state are extremely unstable under high-temperature conditions, and they easily react with the HF released by the electrolyte to cause the material structure to change or even collapse, thus affecting the specific capacity and cycle performance of the NCA material [32, 33]. Given these shortcomings, it is necessary to modify the NCA material, and the main modification methods can be summarized and described as surface coating and bulk phase doping.

2. Surface Coating of NCA

To overcome the aforementioned shortcomings of NCA materials, surface coating is a feasible target to lower the electron transport paths, change the transmission mechanism, and improve the electrode material interface reactions. Generally, the coating material needs to present excellent Li^+ and electronic transmission performance, as well as not react with the electrolyte [34, 35]. The surface-coating mechanism of NCA materials can be described in Figure 1, in which the surface coating acts like a shield that protects the structure of the NCA from rogue side reactions. Therefore,

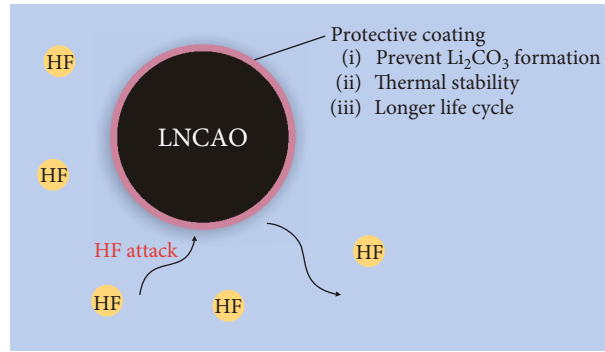

Figure 1: Possible function mechanism of NCA material surface coated by carbon.

the cladding layer prevents the crystal structure from collapsing due to corrosion of the positive electrode material and remarkably improves the stability of the battery during the cycle. The surface coating is used to attach the coating material, such as carbon and its derivatives, oxides, phosphates, and active material, to the surface of the cathode material, and it is a straightforward and effective modification method.

2.1. Carbon Coating. Carbon coating is a feasible measure to improve the ionic conductivity and cycle performance of NCA materials under different rates by increasing the electrical conductivity and changing the transmission mechanism [36].

NCA-graphene composite cathode materials are prepared by Yoon et al. [37] using high-energy mechanical milling from the mixture of NCA and graphene at 200 r/min under argon for 30 min. These results can be significantly improved compared with the NCA materials without coating, in which the NCA shows surface resistance of 11.8 Ω which is higher than that of the NCA-graphene composite (7.7 Ω). The characterization results show that the assembled battery can present excellent physicochemical and battery performance. Between 4.3 and 3 V at a constant current of 55.6 mA/g at 25°C, the NCA delivers a capacity of 172 mAh g^{-1} with a capacity retention of 91%, while the NCA-graphene composite shows a capacity of 180 mAh g^{-1} with a capacity retention of 97% after 80 cycles. The reasons can be mainly attributed to the graphene coating on the surface of NCA materials. On the one hand, the coating graphene can improve the surface conductivity of materials [38, 39]. On the other hand, the graphene layer provides a certain protection to the material and improves the cycle performance. These phenomena can be also detected and elaborated in the references. For example, Chung et al. [40] have adopted sodium dodecyl sulfate as the carbon source, as well as the NCA materials evenly mixed with sodium dodecyl sulfate in the air at 600°C for 5 h to get carbon-coated NCA/C materials. The capacity retention rate of NCA/C is 93% after 40 cycles at 0.1 C, which is higher than that of the uncoated material (86%). Liu et al. [41] reported the coated NCA composite material using 1.0 wt % sucrose and glucose as carbon sources after being calcined at 600°C for 4 h in an argon

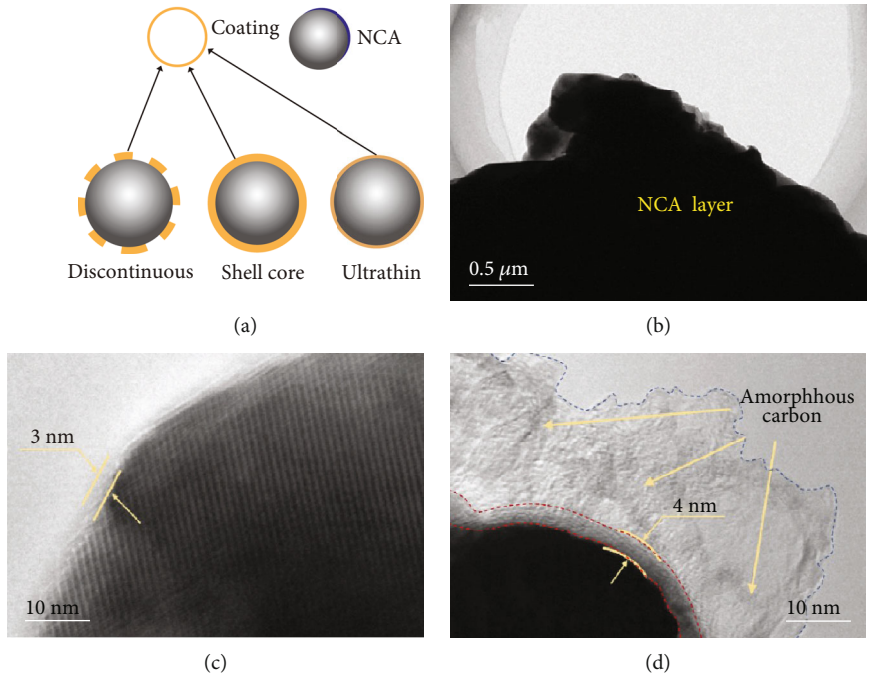

Figure 2: Types of electrode material surface coating (a). TEM images of NCA coated with different carbon sources: (b) bare; (c) glucose 1% NCA/C; (d) sucrose 1% NCA/C [41].

atmosphere. The battery performance indicates that the capacity retention of the composite cathodes coated by sucrose and glucose is about 88.3% and 70.4% after 200 cycles at 1.0 C, respectively, which are clearly higher than the uncoated one. Moreover, the battery performance can be tailored by the thickness of the carbon layer, which can be significantly observed by TEM technique. Figure 2 displays the TEM images of NCA materials coated by different carbon sources.

The amorphous carbon coating may cause more unfavorable Ni^{2+} content and exacerbate the Li^{+}/Ni^{2+} intermixing degree, resulting in the degradation of battery performance of NCA cathode material [42, 43]. The reason can be attributed to the reduction of Ni^{3+} to Ni^{2+} by the in situ carbonization of the carbon source. He et al. [44] developed an alternative method for carbon material coating without in situ carbonization and used separately synthesized graphene nanodots (GND) for the non-in situ coating process of NCA cathode materials. The study results show that the uniform distribution of 5 nm GND on the surface of $LiNi_{0.8}Co_{0.15}Al_{0.05}O_2$ particles can significantly improve the electron conductivity and exhibit a high discharge specific capacity of 150 m Ah g^{-1} at 5.0 C. The carbon coating improves the electron transport path on the surface of the NCA, transforms point-to-point conduction into face-to-face conduction, and significantly improves the conductivity, and the cycle performance of the material is also improved under high rate conditions. Moreover, it is worth noting that the carbon layer doped with N and P elements could improve the electrical conductivity of the materials by increasing the local electron density of the carbon material. Gao et al. [45] prepared high performance $LiNi_{0.8}Co_{0.15}Al_{0.05}O_2$ materials by coating the nitrous and phosphorus codoped nanocarbon coating (N/PC) on the surface, and the aniline was used as carbon source and nitrogen source and phytic acid as carbon source and phosphorus source. When the N/PC coating amount was up to 1.0 wt %, the materials can deliver the best electrochemical performance in which the capacity retention can retain at 90.7% after 200 cycles at 1.0 C that was significantly over 70.1% of the uncoated one.

2.2. Oxide Coating. As far as we know, oxides, such as Al_2O_3, MgO, TiO_2 [46], ZnO, ZrO_2 [47], SiO_2, CeO_2, and RuO_2 [48], can be widely used to modify the surface of NCA materials due to excellent electronic conductivity and good compatibility with electrolytes, which can significantly improve the cycle performance and rate performance of NCA materials by enhancing the electron transport and structural stability.

Xie et al. [49] proposed to prepare the SnO_2-coated Li-excess NCA material by synchronous bifunctional modification via the oxalate coprecipitation route. This bifunctionally modified NCA material can not only exhibit improved electrochemical performance but also exhibit improved storage stability. After 400 cycles at 1.0 C, the capacity decreases from 123.7 to 86.7 mAh g^{-1} with a capacity retention of 70.1%, in which excessive Li is believed to reduce the cationic mixing and SnO_2 modification is deemed to restrict the undesirable side reaction between active materials and electrolytes [50]. Liu et al. [51] have synthesized a multifunctional TiO_2 composite layer by the solid-state reaction to modify $LiNi_{0.8}Co_{0.15}Al_{0.05}O_2$ materials to enhance the surface and structural stability confirmed by electron microscopy and XPS measurements, in which the substitution of Ti in the crystal structure realizes the synergistic effect of the composite layer and titanium doping by enhancing surface and

structural stability via heterogeneous layer coating and bulk doping [52], and the electrochemical battery exhibits the highest initial capacities of 162.9 and 182.4 m Ah g^{-1} at 1.0 C and 0.1 C, and the discharge capacity retentions can reach 85.0% after 200 cycles at 1.0 C. Moreover, metal oxides doped with different metal elements can provide higher electronic conductivity. He et al. [53] adopted electronically conductive antimony-doped tin oxide (ATO) to coat the NCA cathode material by a wet chemical process. After being coated, the as-prepared ATO-coated NCA (ATO-NCA) material had a high discharge specific capacity of 145 mAh g^{-1} at a rate of 5.0 C, which is higher than that of the original NCA material (135.2 mAh g^{-1}). In addition, at 60°C and 1.0 C, the ATO-NCA material delivered the capacity retention of 91.7% after 200 cycles, which is much higher than that of the original NCA (70.9%). The significant improvements in cyclic and rate performance are mainly attributed to the ATO coating, which not only enhances electron transport but also effectively inhibits the adverse reactions between NCA materials and electrolytes. At the same time, the Li^+/Ni^{2+} mixing of the NCA material and the growth of the solid electrolyte interface (SEI) film can be effectively suppressed, and the cycle stability is significantly improved, especially at higher temperatures.

The oxide can also be coated directly with the cathode materials for sintering a precursor and colithium. An advantage of this new coating method is that it makes the coating uniform. Another is that the simultaneous production of the cathode material and the formation of the coating at the same heat treatment temperature result in a strong bond between the coating layer and the substrate. Therefore, the modified cathode material possesses a stable structure and exhibits excellent electrochemical performance during repeated charge and discharge. Zheng et al. [54] used the tetraethyl silicate (TEOS) as a silicon source to transform into a SiO_2 layer on the $NCA(OH)_2$ precursor surface. Then, the SiO_2-coated $NCA(OH)_2$ was mixed with Li salt and sintered to obtain a NCA composite directly. The rate and cycling performance of NCA are found to be successfully enhanced, especially in the sample with 3 mol % coating. In addition, due to the high-temperature treatment, Al was doped to SiO_2 as a fast ionic conductor. The result was an effective increase in the diffusion of lithium ions between the electrode and the electrolyte interface while protecting the body from direct contact with the electrolyte. Finally, the stability of the material was increased.

2.3. Phosphate Coating. Surface modification by phosphate has received widespread attention in recent years. The principle of phosphate-coated positive electrode material is the same as that of oxide coating, in which the phosphate has better ion transportability and thermal stability that can better improve the rate performance of the material. The commonly used phosphates are $AlPO_4$ [55], Li_3PO_4 [56, 57], $Ni_3(PO_4)_2$ [58], $Co_3(PO_4)_2$ [59], and so on.

Tang et al. [60] first coated an appropriate amount of $NH_4H_2PO_4$ on the surface of $Ni_{0.815}Co_{0.15}Al_{0.035}(OH)_2$ and then sintered it with Li_2CO_3 to prepare the composite (P-NCA), in which $NH_4H_2PO_4$ can react with residual lithium on the surface of the material to form a uniform Li_3PO_4 coating. The removal of lithium ions and the formation of the ion-conductive coating Li_3PO_4 promoted the transport of Li^+ to some extent. However, due to the limitation of lithium ion conductivity, the heavy Li_3PO_4 coating inevitably hindered the migration of lithium ions. The cycle stability of the coated Li $Ni_{0.815}Co_{0.15}Al_{0.035}O_2$ at room temperature and 55°C can be improved when the coating content reaches 3 wt %, at which point the DSC shows that the heat generation is considerably decreased from 757 J g^{-1} to 525 J g^{-1} for NCA and P-NCA. Qi et al. [55] successfully improved the electrochemical performance of $LiNi_{0.8}Co_{0.15}Al_{0.05}O_2$ coated with $AlPO_4$ composite by the wet coating process. The capacity retention was 86.9% after 150 cycles at 0.5 C, which is significantly higher than the 66.8% of the uncoated sample. In addition, the modified sample had better thermal stability and smaller resistance and charge transfer resistance, and the values of R_1 (0.569 Ω) and R_2 (51.6 Ω) of the coated sample were clearly smaller than those of the pristine sample (1.30 Ω and 83.7 Ω, respectively). This improved performance can be mainly attributed to the stable protective layer which can inhibit adverse reactions between NCA and electrolytes.

The phosphate coating can also improve the cycling performance of NCA in a wider cut-off voltage range. Liu et al. [61] first extended the charge and discharge cut-off voltage range to 1.5-4.8 V (vs. Li/Li^+) and prepared $BiPO_4$-coated NCA by a coprecipitation method, in which the assembled battery can deliver an initial discharge capacity of 325.0 mAh g^{-1}. It is very encouraging that the first two cycle discharge capacities surpassed the theoretical capacity of NCA (274 mAh g^{-1}) when the cut-off voltage was 1.5-4.8 V. These exceptionally high capacities may be caused by the formation of lithium-rich compounds during the charge and discharge process which is under further exploration. The most significant finding is that the charge and discharge platforms can be found at 2.3-2.5 V and 1.7 V, respectively, which contributes to the high capacity properties of NCA. Additionally, the existence of the $BiPO_4$ coating effectively protects NCA from electrolyte corrosion and improves the cycle performance of NCA. After the first 30 cycles, the capacity retention of $BiPO_4$-coated NCA materials increases to 81.48, 77.98, 75.20, and 69.11% in the voltage range of 1.5-4.3 V, 1.5-4.5 V, 1.5-4.6 V, and 1.5-4.8 V, respectively, while that of unmodified NCA materials was 77.99%, 72.08%, 63.35%, and 52.05% in the same voltage ranges.

With the expansion of $LiFePO_4$-positive materials, $FePO_4$ can potentially be used as a precursor for the preparation of $LiFePO_4$-positive materials, which has certain electrochemical activities. Therefore, surface modification by $FePO_4$ can effectively improve the cycling and thermal stability of NCA materials. Generally, there are two topics in terms of $FePO_4$ materials in LIBs, namely, uniformly distributed and highly crystalline nano-$FePO_4$ preparation and uniform surface moderation. Xia et al. [62] employed a general liquid-phase technology to prepare uniformly distributed and highly crystalline nano-$FePO_4$ powders, which were then used to coat the surface of $LiNi_{0.8}Co_{0.15}Al_{0.05}O_2$ (NCA) to adjust the interface property between electrodes and electrolytes. Among the samples with different coated $FePO_4$ contents,

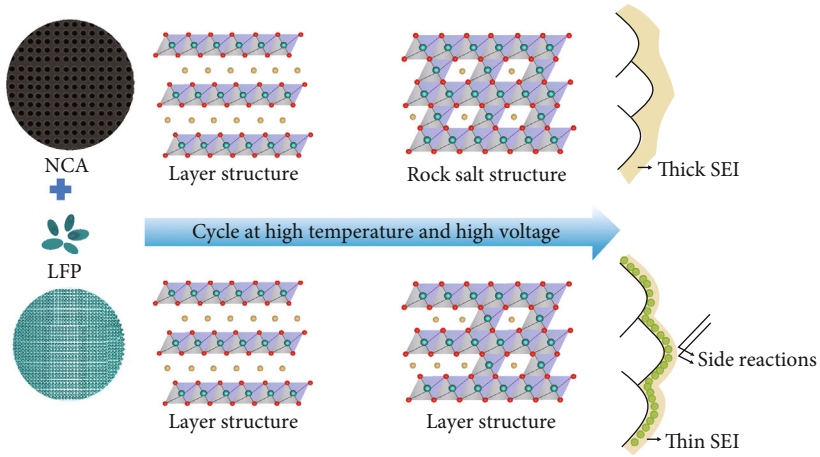

Figure 3: A scheme illustrating the effects of a lithium iron phosphate coating on NCA cathodes [68].

the cells with the NCA coated with 2 wt % $FePO_4$ presented the best electrochemical performance with an initial discharge specific capacity of 181.4 mAh g^{-1} and a capacity retention of 80.49% after 100 cycles at 1.0 C. Moreover, the solid-liquid interface membrane impedance (R_f) changed little during the cycles by the charge transfer resistance fitted from EIS patterns; however, the charge transfer resistance (R_{ct}) of the pristine sample clearly increased from 85 Ω to 187 Ω while the R_{ct} of the 2 wt % $FePO_4$-coated samples increased only slightly. These results reveal that the amorphous $FePO_4$ coating plays a key role to suppress R_{ct} from increasing during charge-discharge cycles by reducing the charge transfer resistance.

2.4. Active Material Coating. Different from other coatings, active materials, as conductor materials of Li^+, can better realize the insertion and extraction of Li^+ and improve the cycle performance and rate performance of NCA materials. At the same time, some lithium compounds can be used as electrode materials [63, 64], contributing capacity during charging and discharging cycles, thus reducing the impact of coating on the overall capacity loss of the material. Liu et al. [65] coated 3.0 wt % $LiCoO_2$ on the surface of NCA material by a molten salt method. Between 2.75 and 4.3 V and at 0.5 C, the initial discharge specific capacity of NCA/$LiCoO_2$ material was 163.6 mAh g^{-1} and the capacity retention rate was 95.8% after 50 cycles, whereas the undischarged material had an initial discharge specific capacity of 154.3 mAh g^{-1} and a capacity retention rate of 87.9%. The cycle and rate performance of the coated material were improved. The electrochemical impedance test results showed that the reduction of the NiO phase formed on the surface of the cladding was the main reason for the improved material properties.

NCA is a secondary particle aggregated by primary particles, and its structure has a significant influence on electrochemical performance, such as rate performance and cycle life. During the charge and discharge process, the internal stress of the positive electrode material changes due to the interaction between the lithium ions and the lattice structure, and this stress may cause structural damage of the secondary particles and accelerate the formation of cracks, yielding the material and the electrolyte. The side reaction is intensified. Yang et al. [66] introduced a filling and coating method using $LiNi_{0.333}Co_{0.333}Mn_{0.333}O_2$ to fill and coat the surface of the positive electrode material $LiNi_{0.815}Co_{0.15}Al_{0.035}O_2$; the thickness of the gap layer was approximately 10 nm, there was no capacity loss, and the capacity retention was 88.5% after 200 cycles. The cycle performance was greatly improved, and the polarization was significantly reduced compared with the original NCA. Furthermore, the mechanism of secondary particle fragmentation was further revealed by the in situ compression test. The secondary particle fracture is considered a fatigue process under long-term electrochemical reaction. The coated sample has a good elastic recovery ability, and the NCA with a filled coating can ensure a low residual lithium content and ensure a strong bonding force between adjacent crystal grains, which also improves the long-term cycle stability. Li-redox-active lithium iron phosphate (LFP) has excellent thermal and electrochemical stability as well as Li-redox activity at relatively high voltages, and it can be uniformly coated on the NCA surface by an industrially feasible melt mixing and calcination process. This reduces the side reaction between the NCA and the electrolyte and the degree of disorder of the cations in NCA [67]. Chen et al. [68] showed that the capacity of the full cell prepared by this simple method of NCA-LFP material was greatly improved at high temperature and higher charging voltage. After 100 charge and discharge cycles, NCA-LFP exhibited an excellent capacity retention of 95% at high charging voltage (4.5 V) and high temperature (55°C), which is 15% higher than in the original NCA cathode. This improvement in electrochemical performance and thermal stability at high voltages is attributed to the reduction in the degree of cation mixing in the NCA and the reduction in SEI film formation in the presence of the LFP coating, as shown in Figure 3.

2.5. Fluoride Coating. Fluoride is also one of the most widely used materials in the coating modification of lithium-ion battery cathode materials. A key factor in the electrochemical performance degradation of lithium-ion batteries is that

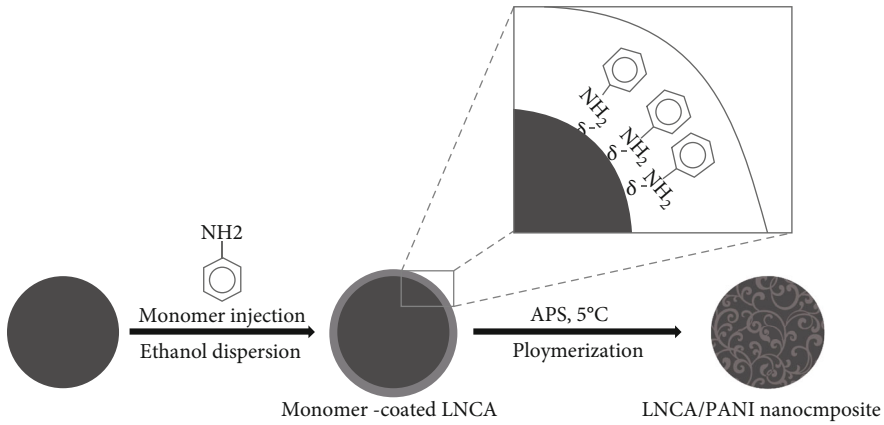

Figure 4: A scheme illustrating the LNCA material surface coated by polyaniline [80].

electrolyte $LiPF_6$ will decompose continuously during battery operation to produce highly corrosive hydrofluoric acid (HF), which causes the dissolution of transition metals in NCA cathode materials. The decomposition of $LiPF_6$ generates LiF and PF_5. The LiF is deposited on the surface of the active material, and it has a low Li^+ and electron permeability. Meanwhile, the PF_5 reacts with the trace amount of water in the electrolyte to form HF, which causes corrosion to the electrode material and further enhances the instability of the interface between electrode and electrolyte. Therefore, an important method to increase the capacity retention of lithium-ion batteries is to slow the dissolution of transition metals in the active materials. Fluoride-coated positive electrode materials are directly used in lithium-ion batteries. On the one hand, the common electrolyte for lithium-ion batteries is $LiPF_6$, and F^- can effectively suppress the occurrence of interfacial reactions [69]. On the other hand, the addition of F can lower the charge transfer resistance and improve the conductivity, thereby improving the rate performance and cycle performance of the cathode material [70].

The fluorides currently used for coating include AlF_3, MgF_2, CaF_2, YF_3, LaF_3, GaF_3, and LiF [71–75]. Lee et al. [76] mixed the homemade AlF_3 with NCA and obtained the NCA/AlF_3 material after high-speed ball milling (3400 r/min) for 5 min. The cycle performance rate performance and thermal stability of the coated material were improved, especially at high temperatures. Tested at 55°C and 1.0 C, the capacity retention of NCA/AlF_3 material after 500 cycles was 55.9%, much higher than the 11.7% for the raw materials. On the one hand, the coating inhibits the erosion of the HF electrode material, reduces the dissolution of the transition metal in the electrolyte, and thus reduces the growth of charge transfer resistance. On the other hand, the coating reduces the volume change of the material, thereby preventing the material from chalking during the cycle. Fluoride has a high electronegativity and forms a stable compound with 3D transition metal elements [77]. Furthermore, the mixture has desirable thermal stability at elevated temperatures for lithium-ion batteries. Liu et al. [78] used a solventing-out crystallization process to coat a 10-20 nm thick FeF_3 layer on NCA. The electrochemical properties of the battery significantly improved, where the discharge capacity of bare NCA decreased sharply from 180.9 to 81.8 mAh g^{-1}, with a retention of 45.2% after 100 cycles at 1.0 C and 55°C, while the discharge capacity of FeF_3-coated NCA decreased from 182.2 to 105.4 mAh g^{-1}, with a retention of 57.8%. When the cycle number increased from 2 to 50, the charge transfer resistance value of bare NCA increased from 64 Ω to 218 Ω, but that of coated NCA increased only from 58 Ω to 166 Ω. This indicates that the FeF_3 coating reduced the side reactions between the cathode and electrolyte, thus suppressing the impedance increase. The reason can be mainly attributed to the FeF_3 coating effectively improving the electrochemical properties of NCA, including the rate capability, cycle performance, and high-temperature property.

2.6. Polymer Coating. Some polymers have good electrical conductivity and can be used for the surface coating of NCA materials. In addition, the conductive polymer has a certain blocking effect of preventing intergranular cracking of the NCA particles. Among the conducting polymers, polyaniline (PANI) is popular due to its ease of coating, simple preparation, environmental stability, and low cost. NCA/PANI materials were prepared by Chung and Ryu [79] using in situ self-stabilizing dispersion polymerization to coat a layer of polyaniline on the surface of NCA material as shown in Figure 4. The synthesized NCA/PANI has a similar particle size to NCA and demonstrated good cycling performance compared with pristine NCA to 40 cycles. PANI (the emeraldine salt form) provides good contact between polymer and oxide particles, resulting in the observed increase in the electrical conductivity of the composite compared with the pristine NCA. Moreover, this material showed good reversibility for Li insertion in discharge cycles when used as the electrode of lithium-ion batteries. Poly(3-hexylthiophene-2,5-diyl) (P3HT), a conducting polymer studied extensively for its optoelectronic devices, offers several advantageous properties when used as a cladding material for lithium-ion battery cathode materials. Lai et al. [80] prepared P3HT for both surface protection and as a conductive layer for NCA. The thickness was carefully controlled to limit the ionic resistance while providing sufficient electronic conduction. The improved conduction

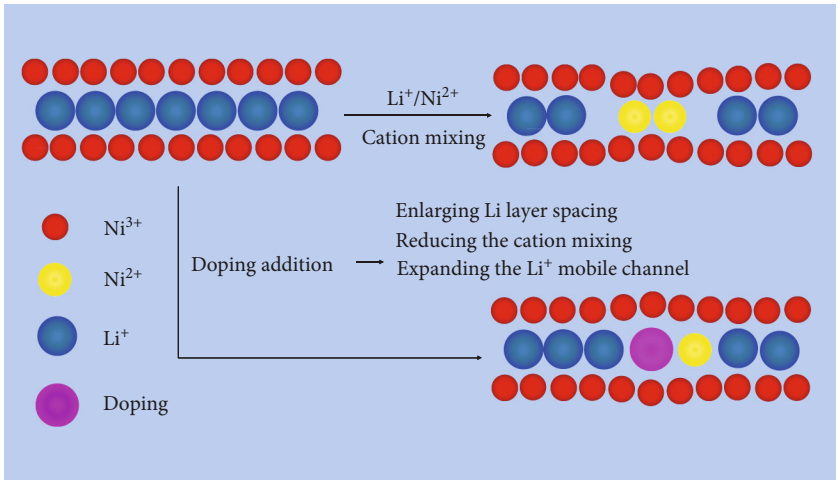

Figure 5: Possible function mechanism of doping in NCA [81].

enables higher power densities to be attained compared with the control NCA electrodes, which were made with the standard binder polymer. The dense P3HT coating provides limited spacing for ion transport of the bulky reactants generated from the electrolyte breakdown. In this way, the P3HT functions as an artificial SEI, protecting the NCA from degradation. The integration of P3HT with NCA enables the resulting material to perform as a high rate positive electrode for lithium-ion batteries. Moreover, the use of the P3HT-CNT binder system led to improved cycling for NCA at high power density with capacities of 80 mAh g^{-1} obtained after 1000 cycles at 16.0 C, a value that was 4 times greater than that achieved in the control electrode.

3. Doping and Functionalization

Unlike the surface coating, the problem of NCA is solved from the surface of the material, whereas the bulk phase is focused on improving the performance from the internal structure of the material. Primarily, the use of additional atomic doping combines the properties of foreign atoms with NCA to enhance the features of NCA or overcome the shortcomings of NCA. At present, there are two kinds of doping modifications for NCA cathode materials: cationic doping and anionic doping. Successful doping does not affect the structure of NCA-positive electrode materials, nor does it form impurities. Doping can also inhibit Ni^{2+} from occupying Li^+ vacancies, which reduces the phenomenon of cation mixing and increases the unit cell parameter c, reduces the irreversible capacity loss during charge and discharge, and improves the electrochemical performance of the material. The possible doping mechanism is shown in Figure 5.

3.1. Cationic Doping. Further research with alternative transition metal elements will help to optimize the structural design of the NCA-based materials to balance the specific capacity, cycle performance, and electrical conductivity of the materials. Mn and Ti have atomic radii similar to Ni and coordinate with oxygen to replace transition metal atoms in octahedral interstitial sites. Wan et al. [82] prepared a $LiNi_{0.85}Co_{0.1}Al_{0.05}O_2$ (NCA) cathode material by hydrothermal reaction and doping with the transition metals Mn and Ti, respectively. In the voltage range of 3.0-4.3 V, the initial discharge specific capacity of NCA-Ti and NCA-Mn was 179.6 mAh g^{-1} and 171.4 mAh g^{-1}, respectively, which was higher than that of undoped NCA (156.5 mAh g^{-1}). The octahedral lattice space occupied by lithium ions introduced by Mn^{4+} and Ti^{4+} increases the unit cell volume and enlarges the lithium layer spacing, thereby improving the diffusion of lithium ions and thus improving the electrochemical performance of the cathode material. Moreover, the SEI film resistance (R_1) values of the LIBs with the fresh NCA, NCA-Mn, and NCA-Ti electrodes were 31.1, 52.4, and 24.2 Ω, respectively. The smallest R_1 of the NCA-Ti electrode suggests that the NCA-Ti electrode has better electrochemical properties and abilities for rapid electron transport during the electrochemical Li^+ insertion/extraction reaction. Titanium ions with a large ionic radius can modify the oxygen crystal lattice, improve the local coordination environment of NCA, reduce the cation mixing, and make the material have better kinetics and thermodynamic properties and structural stability. Qiu et al. [83] demonstrated that the appropriate amount of Ti substitution could enable the NCA cathode to be operated with a high cut-off voltage. The XRD and TEM results showed Ti doping can effectively inhibit the mixing of Li^+/Ni^{2+} and the surface of the NiO phase on the surface of NCA kinetics and thermodynamics. At a high cut-off voltage of 4.7 V, 1% Ti-doped NCA (NCAT-1) had the highest reversible capacity of 198 mAh g^{-1} at 0.1 C, and its capacity retention after 100 cycles was 86.9%. In addition, NCAT-1 has a lower Li^+ diffusion coefficient and rate performance with higher voltage polarizability than NCA cathodes. The FeO_6 octahedron formed in the Fe-doped NCA material affects the edge-shared NiO_6 octahedron, which enhances electron localization, reduces the tendency to generate active oxygen species at the interface, inhibits oxidation of the electrolyte, and stabilizes the interface [84]. $LiNi_{0.8}Co_{0.15-y}Fe_yAl_{0.05}O_2$ (NCFA, $0 \le y \le$

Table 1: Crystallographic formula of the prepared samples before and after 10 cycles based on the ICP-AES results [92].

Samples	Crystallographic formula	
	Before cycling	After 10 cycles
NCA	$Li_{1.004}Ni_{0.803}Co_{0.147}Al_{0.046}O_2$	$Li_{0.994}Ni_{0.809}Co_{0.149}Al_{0.048}O_2$
NNCA	$Li_{1.002}Na_{0.009}Ni_{0.798}Co_{0.146}Al_{0.045}O_2$	$Li_{0.999}Na_{0.003}Ni_{0.802}Co_{0.149}Al_{0.047}O_2$
KNCA	$Li_{0.999}K_{0.008}Ni_{0.797}Co_{0.147}Al_{0.049}O_2$	$Li_{0.997}K_{0.008}Ni_{0.798}Co_{0.148}Al_{0.049}O_2$

0.15) cathode materials were systematically studied by Du et al. [85] using ball milling from the mixture of $Ni(OH)_2$, Co_3O_4, Al_2O_3, Fe_2O_3, and Li_2CO_3 under alcohol media for 8 h and then calcinated under flowing oxygen at 720°C for 8 h. The characterization results show that the assembled battery can present excellent physicochemical and battery performance when the Fe substitution is 0.075, the discharge capacity of NCFA can reach 167.2 mAh g^{-1} (NCA is 183.9 mAh g^{-1}), and the cycle performance is excellent. In addition, the capacity retention rate was 88.4% after 350 cycles (55.7% for NCA) due to the suppression of phase transitions and stable electrode-electrolyte interface. As the iron content increases, the (003) and (104) peaks move toward small angles, and these diffraction peaks are particularly sensitive to changes in the *c*-axis and the *a*-axis of the hexagonal unit cell [86, 87]. The refinement of the XRD pattern by the Rietveld method using GSAS software confirmed that the substitution of Fe might lead to an increase in *c*-axis and *a*-axis values. The increase in the *a* value and *c* value is probably because the ionic radius of Fe^{3+} (0.645 Å) is greater than Co^{3+} (0.545 Å). However, the *c*/*a* ratios of the two samples were similar, indicating that no disordered phase was formed in the presence of an appropriate amount of iron [88], indicating that NCFA still has an excellent lamellar structure.

Excessive element doping is an effective method to improve the structural stability of layered cathode oxides [89], and elements doped at the Li site have also proven to be a viable method to prevent the collapse of layered structures. Na-doped samples have good oxidation resistance, lower potential polarization, higher initial coulomb efficiency, better rate performance, and so on. These characteristics can also be detected and elaborated in the references. For example, Wang et al. [88] doped 1% (by weight) NaCl into $LiNi_{0.8}Co_{0.15}Al_{0.05}O_2$; the obtained Na-doped sample had superior cycle stability at 1.0 C, where the initial discharge specific capacity of the original NCA and the doped NCA did not differ significantly, 182.9 mAh g^{-1} and 183.9 mAh g^{-1}, respectively. After 300 cycles, the capacity of the doped NCA sample remained 81.6%, higher than in the original NCA (48.1%); by the columnar effect of the large radius of Na^+, the Na-doped NCA sample particles retained a complete spherical morphology even after many cycles. The incorporation of a large radius of alkali ions can increase the lithium layer spacing and reduce the degree of cation mixing by increasing the diffusivity of Li^+ in the bulk structure. In addition, potassium has similar chemistry to sodium and a larger ionic radius (1.38 Å) and lower electronegativity [90, 91]. Zhao et al. [92] anchored 1% K^+ to the Li^+ site of $LiNi_{0.8}Co_{0.15}Al_{0.05}O_2$ as an excellent structural stabilizer compared with the Na^+-doping material with a similarity to the original material and modification mechanism, and the K^+-doped cathode material exhibited higher initial coulombic efficiency and better rate performance; $Li_{0.99}K_{0.01}Ni_{0.8}Co_{0.15}Al_{0.05}O_2$ had a large initial discharge capacity of 216.8 mAh g^{-1} at 0.1 C and maintained 87.4% after 150 cycles of a stable cycle at 4.6 V high voltage and 1.0 C. The ICP-AES results are shown in Table 1. Moreover, Na^+ can migrate from the material to the electrolyte during the high-pressure cycle, and the migration of Na^+ causes the material to also undergo severe capacity decay. In contrast, K^+ with a larger ionic radius and lower migration ability can stabilize and inhibit the irreversible phase transition between H2 and H3 and the degradation of the host structure by occupying the lithium layer firmly. At the same time, K^+ in the Li^+ site prevents the formation of trivacancies in the highly delithiated state by alleviating the cation migration and the generation of the resistive spinel and rock salt phases during the high-pressure cycle, as shown in Figure 6. Considering the enhanced structural stability of the Ni-rich cathode material by K^+ anchoring under high-pressure cycling, it provides an extraordinary hint for the rational design of advanced cathode materials for the pursuit of high-energy density lithium-ion batteries.

3.2. Anionic Doping. Another method to improve the cycling stability of lithium-ion battery electrode materials is anion doping. The negative ions currently used are F^- [93, 94], Cl^- [95, 96], Br^- [97, 98], S^{2-} [99], PO_4^{3-} [100], and so on. In recent years, to improve the performance of NCA, F^- has been added to the list of anions deployed by cryogenic methods. F^- doping indicates that the process is a catalyst that promotes the growth of primary particles. The valence state of the surface nickel ions decreases, the spacing between the plates increases, and the increase in the impedance during the cycle is reduced, which is beneficial to inhibiting the degradation of NCA material. Huang et al. [94] prepared different amounts of NH_4F and NCA dispersed in anhydrous ethanol, and the mixture was continuously evaporated and dried. It was homogeneous and calcined in air at 420°C for 4 h to obtain an F-doped NCA material (NCAF). As the concentration of fluorine increased, some of the nickel ions were reduced, resulting in a decrease in the initial discharge capacity. NCAF had the best electrochemical performance when NH_4F was added at 2 mol %, and the cycle performance of NCAF was improved at room temperature, high temperature (55°C), and high cut-off potential (4.5 V).

In contrast, NCA modified with Br will have a more stable structure than N modified with F, and the electron affinity of Br is greater than O and F (Br: 342.54 kJ mol^{-1}, F:

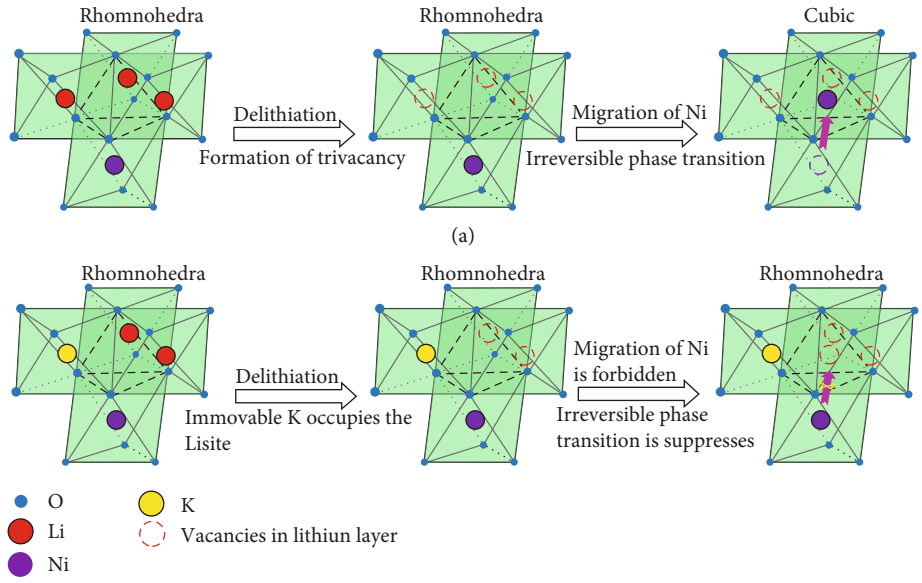

FIGURE 6: Schematic diagrams of the phase evolution routes for (a) potassium-free and (b) potassium-doped samples, which are built on an O_3-layered model with unrealistic radius ratios [92].

328.1 kJ mol^{-1}, and O: 141.3 kJ mol^{-1}), so M- (Ni, Co, Al) Br is stronger than the M- (Ni, Co, Al) O or M- (Ni, Co, Al) F bond. In addition, Br^- doping is expected to produce an NCA similar to the F^--doping mechanism. Furthermore, the ionic radius (0.196 nm) of Br^- is larger than F^- (0.133 nm) or O^{2-} (0.140 nm), and the NCA modified with Br^- may increase the Li^+ mobility. He et al. [101] modified the electrochemical properties of $LiNi_{0.815}Co_{0.15}Al_{0.035}O_2$ (NCA) cathode material by in situ Br^- doping. The effects of Br^- modification on the structure, morphology, and electrochemical properties of NCA cathode materials were systematically investigated. The results of structural characterization show that part of the Br^- doped into the bulk particles of NCA replaces O^{2-} at position 6c, thus forming a strong bond between the metal and Br^- by stabilizing the main structure and improving the stability of NCA against HF attack. At the same time, the gap spacing of the NCA is increased, and the growth of the primary particles is suppressed by the Br^- modification, providing a wider channel and a shorter path for Li^+. In addition, due to the incorporation of Br^-, the Ni^{3+} portion of the surface is reduced to Ni^{2+}, which also contributes to improving the structural stability of the NCA. The residual lithium acts as a stable LiBr rather than an unstable Li_2CO_3, which can suppress the reductive decomposition reaction of the electrolyte. Electrochemical tests show that 0.2 mol% Br^--doped NCA (NCABr-2) reduces potential polarization, decreasing the $R_{sf} + R_{ct}$ value and increasing the Li^+ diffusion coefficient. The capacity retention rate of NCABr-2 was 73.7% after circulating for 100 cycles at 0.5 C, which was higher than the 63.7% of the original NCA material. Moreover, Br^- doping can effectively improve the cycle performance of the NCA cathode material, and this performance is more obvious at high temperatures. The cycle retention of NCABr-2 at 55°C and 0.5 C was 75.7%, which was much higher than the 41.5% of pure NCA material. These results clearly show that Br^- doping contributes significantly to the structural stability and cycle performance of the NCA material.

Chen et al. [102] adopted a gradient boron-polyanion-doped nickel-rich $LiNi_{0.8}Co_{0.15}Al_{0.05}O_2$ cathode material. When the doping amount was 1.5% (molar percentage), the sample B0.015-NCA had the best cycle performance. It also worked well at high voltage (4.5 V) and high temperature (55°C). The SEM images analyzed the presence of cracks and thicker SEI layers on the elementary particles after 100 cycles at high temperature while the doped particles were intact and the SEI layer was thinner, which reduced the capacity/potential decay during charge and discharge. Electrochemical impedance spectroscopy confirmed that boron-polyanion doping could suppress the increase in impedance during high-temperature cycling. The advantages of gradient polyanion doping in a structure are mainly reflected in two aspects. On the one hand, the outer layer of boron-rich polyanion decreases the average valence of nickel ions and reduces the surface reaction of the material. The activity inhibits the decomposition of the organic electrolyte and plays a role in surface modification. On the other hand, due to the reduction of the Ni-O covalent bond and the introduction of the B-O covalent bond with high bond energy, the change in the 2p orbital of the O atom and the formation of cracks are effectively alleviated in the charge and discharge process.

4. Conclusions

Given that the NCA material is expected to become the future cathode material of the lithium-ion battery, it is necessary to pay attention to the practicability of materials. The modification methods of materials should also be designed with practicability in mind. It is essential to consider the

compatibility of the coated or doped NCA material with the electrolyte and the negative electrode material, compatibility with the battery manufacturing process, and adaptability. For the needs of large-scale production, the experimental conditions of the modification process should be as simple as possible, avoiding the use of more energy-intensive methods and saving costs. In addition, it is better to use modified materials that are relatively easy to obtain with a wide range of sources, which is conducive to the large-scale application of NCA materials and to meeting the demand for battery materials in various fields of society in the future. Moreover, the design of the material itself is also one of the methods to solve the current problem, and the coating and doping technology is more important for the modification of NCA materials with higher Ni content in terms of capacity and price.

Conflicts of Interest

The authors declare that they have no conflicts of interest.

Acknowledgments

This work was financially supported by the National Natural Science Foundation of China (Nos. 51874046 and 51404038), the Project of Scientific Research of Jingzhou (No. 2018029), and the Yangtze Youth Talents Fund (No. 2016cqr05).

References

[1] B. Scrosati and J. Garche, "Lithium batteries: status, prospects and future," *Journal of Power Sources*, vol. 195, no. 9, pp. 2419–2430, 2010.

[2] M. Bini, D. Capsoni, S. Ferrari, E. Quartarone, and P. Mustarelli, "Rechargeable lithium batteries: key scientific and technological challenges," *Rechargeable Lithium Batteries*, vol. 195, no. 9, pp. 1–17, 2015.

[3] G. E. Blomgren, "The development and future of lithium ion batteries," *Journal of the Electrochemical Society*, vol. 164, no. 1, pp. A5019–A5025, 2017.

[4] N. Nitta, F. Wu, J. T. Lee, and G. Yushin, "Li-ion battery materials: present and future," *Materials Today*, vol. 18, no. 5, pp. 252–264, 2015.

[5] F. Cheng, J. Liang, Z. Tao, and J. Chen, "Functional materials for rechargeable batteries," *Advanced Materials*, vol. 23, no. 15, pp. 1695–1715, 2011.

[6] K. Ozawa, "Lithium-ion rechargeable batteries with $LiCoO_2$ and carbon electrodes: the $LiCoO_2$/C system," *Solid State Ionics*, vol. 69, no. 3-4, pp. 212–221, 1994.

[7] T. F. Yi, P. P. Peng, X. Han, Y. R. Zhu, and S. Luo, "Interconnected Co_3O_4@$CoNiO_2$@PPy nanorod and nanosheet composite grown on nickel foam as binder-free electrodes for Li-ion batteries," *Solid State Ionics*, vol. 329, pp. 131–139, 2019.

[8] T. Ohzuku, A. Ueda, M. Nagayama, Y. Iwakoshi, and H. Komori, "Comparative study of $LiCoO_2$, $LiNi_{12}Co_{12}O_2$ and $LiNiO_2$ for 4 volt secondary lithium cells," *Electrochimica Acta*, vol. 38, no. 9, pp. 1159–1167, 1993.

[9] T. Ohzuku, A. Ueda, and M. Nagayama, "Electrochemistry and Structural Chemistry of $LiNiO_2$ ($R\bar{3}m$) for 4 Volt Secondary Lithium Cells," *Journal of the Electrochemical Society*, vol. 140, no. 7, pp. 1862–1870, 1993.

[10] E. Zhecheva and R. Stoyanova, "Stabilization of the layered crystal structure of $LiNiO_2$ by co-substitution," *Solid State Ionics*, vol. 66, no. 1-2, pp. 143–149, 1993.

[11] E. Levi, M. D. Levi, G. Salitra et al., "Electrochemical and in-situ XRD characterization of $LiNiO_2$ and $LiCo_{0.2}Ni_{0.8}O_2$ electrodes for rechargeable lithium cells," *Solid State Ionics*, vol. 126, no. 1-2, pp. 97–108, 1999.

[12] K. Zhu, T. Wu, Y. Zhu et al., "Layered Fe-substituted $LiNiO_2$Electrocatalysts for high-efficiency oxygen evolution reaction," *ACS Energy Letters*, vol. 2, no. 7, pp. 1654–1660, 2017.

[13] M. Song, I. Kwon, S. Shim, and J. H. Song, "Electrochemical characterizations of Fe-substituted $LiNiO_2$ synthesized in air by the combustion method," *Ceramics International*, vol. 36, no. 4, pp. 1225–1231, 2010.

[14] M. K. Majee, A. K. Nigam, and P. A. Bhobe, "Comparison of local crystal structure and magnetic properties of cation substituted $LiNiO_2$ compositions," *Materials Research Bulletin*, vol. 116, pp. 143–152, 2019.

[15] Z. Qiu, Y. Zhang, X. Huang et al., "Beneficial effect of incorporating Ni-rich oxide and layered over-lithiated oxide into high-energy-density cathode materials for lithium-ion batteries," *Journal of Power Sources*, vol. 400, pp. 341–349, 2018.

[16] H. S. Ko, J. H. Kim, J. Wang, and J. D. Lee, "Co/Ti co-substituted layered $LiNiO_2$ prepared using a concentration gradient method as an effective cathode material for Li-ion batteries," *Journal of Power Sources*, vol. 372, pp. 107–115, 2017.

[17] C. S. Yoon, U. H. Kim, G. T. Park et al., "Self-passivation of a $LiNiO_2$Cathode for a lithium-ion battery through Zr doping," *ACS Energy Letters*, vol. 3, no. 7, pp. 1634–1639, 2018.

[18] H. Ouyang, X. Li, Z. Wang, H. Guo, and W. Peng, "Electrochemical and structural analysis of Mg substitution in lithium-rich layered oxide for lithium-ion battery," *Ionics*, vol. 24, no. 11, pp. 3347–3356, 2018.

[19] Z. Y. Li, H. Guo, X. Ma et al., "Al substitution induced differences in materials structure and electrochemical performance of Ni-rich layered cathodes for lithium-ion batteries," *The Journal of Physical Chemistry C*, vol. 123, no. 32, pp. 19298–19306, 2019.

[20] M. S. Whittingham, "Ultimate limits to intercalation reactions for lithium batteries," *Chemical Reviews*, vol. 114, no. 23, pp. 11414–11443, 2014.

[21] S. Xia, F. Li, F. Cheng et al., "Synthesis of spherical fluorine modified gradient Li-ion battery cathode material $LiNi_{0.80-}Co_{0.15}Al_{0.05}O_2$ by simple solid phase method," *Journal of the Electrochemical Society*, vol. 165, no. 5, pp. A1019–A1026, 2018.

[22] W. Chen, Y. Li, D. Yang, X. Feng, X. Guan, and L. Mi, "Controlled synthesis of spherical hierarchical $LiNi_{1-x-y}Co_xAl_yO_2$ ($0<x, y<0.2$) via a novel cation exchange process as cathode materials for high-performance lithium batteries," *Electrochimica Acta*, vol. 190, pp. 932–938, 2016.

[23] J. Duan, P. Dong, D. Wang et al., "A facile structure design of $LiNi_{0.90}Co_{0.07}Al_{0.03}O_2$ as advanced cathode materials for lithium ion batteries via carbonation decomposition of $NaAl(OH)_4$ solution," *Journal of Alloys and Compounds*, vol. 739, pp. 335–344, 2018.

[24] N. M. Trease, I. D. Seymour, M. D. Radin et al., "Identifying the distribution of Al^{3+} in $LiNi_{0.8}Co_{0.15}Al_{0.05}O_2$," *Chemistry of Materials*, vol. 28, no. 22, pp. 8170–8180, 2016.

[25] K. J. Park, J. Y. Hwang, H. H. Ryu et al., "Degradation mechanism of Ni-enriched NCA cathode for lithium batteries: are microcracks really critical ?," *ACS Energy Letters*, vol. 4, no. 6, pp. 1394–1400, 2019.

[26] H. Chen, J. A. Dawson, and J. H. Harding, "Effects of cationic substitution on structural defects in layered cathode materials $LiNiO_2$," *Journal of Materials Chemistry A*, vol. 2, no. 21, pp. 7988–7996, 2014.

[27] J. Y. Liao and A. Manthiram, "Surface-modified concentration-gradient Ni-rich layered oxide cathodes for high-energy lithium-ion batteries," *Journal of Power Sources*, vol. 282, pp. 429–436, 2015.

[28] I. Hwang, C. W. Lee, J. C. Kim, and S. Yoon, "Particle size effect of Ni-rich cathode materials on lithium ion battery performance," *Materials Research Bulletin*, vol. 47, no. 1, pp. 73–78, 2012.

[29] F. Wu, J. Tian, Y. Su et al., "Effect of Ni^{2+} content on lithium/nickel disorder for Ni-rich cathode materials," *ACS Applied Materials & Interfaces*, vol. 7, no. 14, pp. 7702–7708, 2015.

[30] T. Nonaka, C. Okuda, Y. Seno, H. Nakano, K. Koumoto, and Y. Ukyo, "In situ XAFS and micro-XAFS studies on $LiNi_{0.8}Co_{0.15}Al_{0.05}O_2$ cathode material for lithium-ion batteries," *Journal of Power Sources*, vol. 162, no. 2, pp. 1329–1335, 2006.

[31] W. Liu, P. Oh, X. Liu, S. Myeong, W. Cho, and J. Cho, "Countering voltage decay and capacity fading of lithium-rich cathode material at 60 °C by hybrid surface protection layers," *Advanced Energy Materials*, vol. 5, no. 13, pp. 1500274–1500284, 2015.

[32] T. Nonaka, C. Okuda, Y. Seno, K. Koumoto, and Y. Ukyo, "X-ray absorption study on $LiNi_{0.8}Co_{0.15}Al_{0.05}O_2$ cathode material for lithium-ion batteries," *Ceramics International*, vol. 34, no. 4, pp. 859–862, 2008.

[33] G. V. Zhuang, G. Chen, J. Shim, X. Song, P. N. Ross, and T. J. Richardson, "Li_2CO_3 in $LiNi_{0.8}Co_{0.15}Al_{0.05}O_2$ cathodes and its effects on capacity and power," *Journal of Power Sources*, vol. 134, no. 2, pp. 293–297, 2004.

[34] W. L. Ong, S. M. Rupich, D. V. Talapin, A. J. H. McGaughey, and J. A. Malen, "Surface chemistry mediates thermal transport in three-dimensional nanocrystal arrays," *Nature Materials*, vol. 12, no. 5, pp. 410–415, 2013.

[35] D. Mohanty, K. Dahlberg, D. M. King et al., "Modification of Ni-rich FCG NMC and NCA cathodes by atomic layer deposition: preventing surface phase transitions for high-voltage lithium-ion batteries," *Scientific Reports*, vol. 6, no. 1, pp. 26532–26537, 2016.

[36] T. F. Yi, P. P. Peng, Z. Fang, Y. R. Zhu, Y. Xie, and S. Luo, "Carbon-coated $LiMn_{1-x}Fe_xPO_4$ ($0 \leq x \leq 0.5$) nanocomposites as high- performance cathode materials for Li-ion battery," *Composites Part B: Engineering*, vol. 175, pp. 107067–107076, 2019.

[37] S. Yoon, K. N. Jung, S. H. Yeon, C. S. Jin, and K. H. Shin, "Electrochemical properties of $LiNi_{0.8}Co_{0.15}Al_{0.05}O_2$-graphene composite as cathode materials for lithium-ion batteries," *Journal of Electroanalytical Chemistry*, vol. 683, pp. 88–93, 2012.

[38] Z. Jiang, Y. Li, J. Zhu et al., "Synthesis and performance of a graphene decorated $NaTi_2(PO_4)_3$/C anode for aqueous lithium-ion batteries," *Journal of Alloys and Compounds*, vol. 791, pp. 176–183, 2019.

[39] R. Fang, C. Miao, H. Mou, and W. Xiao, "Facile synthesis of $_2$@rGO composite with sandwich-like nanostructure as superior performance anodes for lithium ion batteries," *Journal of Alloys and Compounds*, pp. 152884–152891, 2019.

[40] Y. M. Chung, S. H. Ryu, J. H. Ju et al., "A surfactant-based method for carbon coating of $LiNi_{0.8}Co_{0.15}Al_{0.05}O_2$Cathode in Li ion batteries," *Bulletin of the Korean Chemical Society*, vol. 31, no. 8, pp. 2304–2308, 2010.

[41] Z. Liu, Z. Wang, T. Lu, P. Dai, P. Gao, and Y. Zhu, "Modification of $LiNi_{0.8}Co_{0.15}Al_{0.05}O_2$ using nanoscale carbon coating," *Journal of Alloys and Compounds*, vol. 763, pp. 701–710, 2018.

[42] X. Wang, L. Lv, Z. Cheng et al., "High-density monolith of N-doped holey graphene for ultrahigh volumetric capacity of Li-ion batteries," *Advanced Energy Materials*, vol. 6, no. 6, pp. 1502100–1502106, 2016.

[43] C. Li, B. Xie, Z. He, J. Chen, and Y. Long, "3D structure fungi-derived carbon stabilized stearic acid as a composite phase change material for thermal energy storage," *Renewable Energy*, vol. 140, pp. 862–873, 2019.

[44] X. He, G. Han, S. Lou et al., "Improved electrochemical performance of $LiNi_{0.8}Co_{0.15}Al_{0.05}O_2$Cathode material by coating of graphene nanodots," *Journal of the Electrochemical Society*, vol. 166, no. 6, pp. A1038–A1044, 2019.

[45] P. Gao, Y. Jiang, Y. Zhu, and H. Hu, "Improved cycle performance of nitrogen and phosphorus co-doped carbon coatings on lithium nickel cobalt aluminum oxide battery material," *Journal of Materials Science*, vol. 53, no. 13, pp. 9662–9673, 2018.

[46] R. Fang, W. Xiao, C. Miao et al., "Enhanced lithium storage performance of core-shell structural Si@TiO_2/NC composite anode via facile sol-gel and *in situ* N-doped carbon coating processes," *Electrochimica Acta*, vol. 317, pp. 575–582, 2019.

[47] Z. Wang, C. Miao, W. Xiao et al., "Effect of different contents of organic-inorganic hybrid particles poly(methyl methacrylate)-ZrO2 on the properties of poly(vinylidene fluoride-hexafluoroprolene)-based composite gel polymer electrolytes," *Electrochimica Acta*, vol. 272, pp. 127–134, 2018.

[48] W. Xiao, Z. Wang, Y. Zhang et al., "Enhanced performance of P(VDF-HFP)-based composite polymer electrolytes doped with organic-inorganic hybrid particles PMMA-ZrO_2 for lithium ion batteries," *Journal of Power Sources*, vol. 382, pp. 128–134, 2018.

[49] Z. Xie, Y. Zhang, A. Yuan, and J. Xu, "Effects of lithium excess and SnO_2 surface coating on the electrochemical performance of $LiNi_{0.8}Co_{0.15}Al_{0.05}O_2$ cathode material for Li-ion batteries," *Journal of Alloys and Compounds*, vol. 787, pp. 429–439, 2019.

[50] R. Li, C. Miao, M. Zhang, and W. Xiao, "Novel hierarchical structural SnS_2 composite supported by biochar carbonized from chewed sugarcane as enhanced anodes for lithium ion batteries," *Ionics*, pp. 1–9, 2019.

[51] B. S. Liu, X. L. Sui, S. H. Zhang et al., "Investigation on electrochemical performance of $LiNi_{0.8}Co_{0.15}Al_{0.05}O_2$ coated by heterogeneous layer of TiO_2," *Journal of Alloys and Compounds*, vol. 739, pp. 961–971, 2018.

[52] R. Li, W. Xiao, C. Miao, R. Fang, Z. Wang, and M. Zhang, "Sphere-like SnO_2/TiO_2 composites as high-performance anodes for lithium ion batteries," *Ceramics International*, vol. 45, no. 10, pp. 13530–13535, 2019.

[53] X. He, C. Du, B. Shen et al., "Electronically conductive Sb-doped SnO_2 nanoparticles coated $LiNi_{0.8}Co_{0.15}Al_{0.05}O_2$ cathode material with enhanced electrochemical properties for Li-ion batteries," *Electrochimica Acta*, vol. 236, pp. 273–279, 2017.

[54] J. C. Zheng, Z. Yang, Z. J. He, H. Tong, W. J. Yu, and J. F. Zhang, "In situ formed $LiNi_{0.8}Co_{0.15}Al_{0.05}O_2$@$Li_4SiO_4$ composite cathode material with high rate capability and long cycling stability for lithium-ion batteries," *Nano Energy*, vol. 53, pp. 613–621, 2018.

[55] R. Qi, J. L. Shi, X. D. Zhang et al., "Improving the stability of $LiNi_{0.80}Co_{0.15}Al_{0.05}O_2$ by $AlPO_4$ nanocoating for lithium-ion batteries," *Science China Chemistry*, vol. 60, no. 9, pp. 1230–1235, 2017.

[56] X. Zhang, G. Liu, S. Li, H. Dong, H. Liu, and J. Mei, "Preparation of a homogeneous Li_3PO_4 coating and its effect on the electrochemical properties of $LiNi_{0.8}Co_{0.15}Al_{0.05}O_2$," *Journal of Electronic Materials*, vol. 48, no. 7, pp. 4443–4451, 2019.

[57] Z. Wang, Z. Kou, C. Miao, and W. Xiao, "Improved performance all-solid-state electrolytes with high compacted density of monodispersed spherical $Li_{1.3}Al_{0.3}Ti_{1.7}(PO_4)_3$ particles," *Ceramics International*, vol. 45, no. 11, pp. 14469–14473, 2019.

[58] D. J. Lee, B. Scrosati, and Y. K. Sun, "$Ni_3(PO_4)_2$-coated $Li[Ni_{0.8}Co_{0.15}Al_{0.05}]O_2$ lithium battery electrode with improved cycling performance at 55 °C," *Journal of Power Sources*, vol. 196, no. 18, pp. 7742–7746, 2011.

[59] Y. R. Bak, Y. Chung, J. H. Ju, M. J. Hwang, Y. Lee, and K. S. Ryu, "Structure and Electrochemical Performance of $LiNi_{0.8}Co_{0.15}Al_{0.05}O_2$ Cathodes Before and After Treatment with $Co_3(PO_4)_2$ or $AlPO_4$ by *in situ* Chemical Method," *Journal of New Materials for Electrochemical Systems*, vol. 14, no. 4, pp. 203–207, 2011.

[60] Z. F. Tang, R. Wu, P. F. Huang, Q. S. Wang, and C. H. Chen, "Improving the electrochemical performance of Ni-rich cathode material $LiNi_{0.815}Co_{0.15}Al_{0.035}O_2$ by removing the lithium residues and forming Li_3PO_4 coating layer," *Journal of Alloys and Compounds*, vol. 693, pp. 1157–1163, 2017.

[61] W. Liu, H. Guo, M. Qin et al., "Effect of voltage range and BiPO4Coating on the electrochemical properties of $LiNi_{0.8}Co_{0.15}Al_{0.05}O_2$," *ChemistrySelect*, vol. 3, no. 26, pp. 7660–7666, 2018.

[62] S. Xia, F. Li, F. Chen, and H. Guo, "Preparation of $FePO_4$ by liquid-phase method and modification on the surface of $LiNi_{0.80}Co_{0.15}Al_{0.05}O_2$ cathode material," *Journal of Alloys and Compounds*, vol. 731, pp. 428–436, 2018.

[63] W. Xiao, Z. Wang, C. Miao et al., "High performance composite polymer electrolytes doped with spherical-like and honeycomb structural $Li_{0.1}Ca_{0.9}TiO_3$ particles," *Frontiers in Chemistry*, vol. 6, pp. 525–531, 2018.

[64] T. F. Yi, J. Mei, P. P. Peng, and S. Luo, "Facile synthesis of polypyrrole-modified $Li_5Cr_7Ti_6O_{25}$ with improved rate performance as negative electrode material for Li-ion batteries," *Composites Part B: Engineering*, vol. 167, pp. 566–572, 2019.

[65] W. Liu, G. Hu, K. Du, Z. Peng, Y. Cao, and Q. Liu, "Synthesis and characterization of $LiCoO_2$-coated $LiNi_{0.8}Co_{0.15}Al_{0.05}O_2$ cathode materials," *Materials Letters*, vol. 83, pp. 11–13, 2012.

[66] C. Yang, R. Shao, Y. Mi et al., "Stable interstitial layer to alleviate fatigue fracture of high nickel cathode for lithium-ion batteries," *Journal of Power Sources*, vol. 376, pp. 200–206, 2018.

[67] B. Xu, P. Dong, J. Duan, D. Wang, X. Huang, and Y. Zhang, "Regenerating the used $LiFePO_4$ to high performance cathode via mechanochemical activation assisted V^{5+} doping," *Ceramics International*, vol. 45, no. 9, pp. 11792–11801, 2019.

[68] J. Chen, L. Zhu, D. Jia et al., "$LiNi_{0.8}Co_{0.15}Al_{0.05}O_2$ cathodes exhibiting improved capacity retention and thermal stability due to a lithium iron phosphate coating," *Electrochimica Acta*, vol. 312, pp. 179–187, 2019.

[69] J. S. Park, A. U. Mane, J. W. Elam, and J. R. Croy, "Amorphous metal fluoride passivation coatings prepared by atomic layer deposition on LiCoO2for Li-ion batteries," *Chemistry of Materials*, vol. 27, no. 6, pp. 1917–1920, 2015.

[70] P. Yue, Z. Wang, X. Li et al., "The enhanced electrochemical performance of $LiNi_{0.6}Co_{0.2}Mn_{0.2}O_2$ cathode materials by low temperature fluorine substitution," *Electrochimica Acta*, vol. 95, pp. 112–118, 2013.

[71] Z. Zhu, F. Cai, and J. Yu, "Improvement of electrochemical performance for AlF_3-coated $Li_{1.3}Mn_{4/6}Ni_{1/6}Co_{1/6}O_{2.40}$ cathode materials for Li-ion batteries," *Ionics*, vol. 22, no. 8, pp. 1353–1359, 2016.

[72] L. Chen, Y. Yang, Z. Wang et al., "Enhanced electrochemical performances and thermal stability of $LiNi_{1/3}Co_{1/3}Mn_{1/3}O_2$ by surface modification with YF_3," *Journal of Alloys and Compounds*, vol. 711, pp. 462–472, 2017.

[73] C. D. Li, Z. L. Yao, J. Xu, P. Tang, and X. Xiong, "Surface-modified $Li(Li_{0.2}Mn_{0.54}Ni_{0.13}Co_{0.13})O_2$ nanoparticles with LaF_3 as cathode for Li-ion battery," *Ionics*, vol. 23, no. 3, pp. 549–558, 2017.

[74] A. Kraytsberg, H. Drezner, M. Auinat et al., "Atomic layer deposition of a particularized protective MgF2Film on a Li-ion battery $LiMn_{1.5}Ni_{0.5}O_4$Cathode powder material," *ChemNanoMat*, vol. 1, no. 8, pp. 577–585, 2015.

[75] X. Liu, J. Liu, T. Huang, and A. Yu, "CaF_2-coated $Li_{1.2}Mn_{0.54}Ni_{0.13}Co_{0.13}O_2$ as cathode materials for Li-ion batteries," *Electrochimica Acta*, vol. 109, pp. 52–58, 2013.

[76] S. H. Lee, C. S. Yoon, K. Amine, and Y. K. Sun, "Improvement of long-term cycling performance of $Li[Ni_{0.8}Co_{0.15}Al_{0.05}]O_2$ by AlF_3 coating," *Journal of Power Sources*, vol. 234, pp. 201–207, 2013.

[77] C. Li, M. Wang, B. Xie, H. Ma, and J. Chen, "Enhanced properties of diatomite-based composite phase change materials for thermal energy storage," *Renewable Energy*, vol. 147, pp. 265–274, 2020.

[78] W. Liu, X. Tang, M. Qin, G. Li, J. Deng, and X. Huang, "FeF_3-coated $LiNi_{0.8}Co_{0.15}Al_{0.05}O_2$ cathode materials with improved electrochemical properties," *Materials Letters*, vol. 185, pp. 96–99, 2016.

[79] Y. M. Chung and K. S. Ryu, "Surface coating and electrochemical properties of $LiNi_{0.8}Co_{0.15}Al_{0.05}O_2$ polyaniline composites as an electrode for Li-ion batteries," *Bulletin of the Korean Chemical Society*, vol. 30, no. 8, pp. 1733–1737, 2009.

[80] C. H. Lai, D. S. Ashby, T. C. Lin et al., "Application of poly(3-hexylthiophene-2,5-diyl) as a protective coating for high rate cathode materials," *Chemistry of Materials*, vol. 30, no. 8, pp. 2589–2599, 2018.

[81] H. Xie, K. Du, G. Hu, Z. Peng, and Y. Cao, "The Role of Sodium in $LiNi_{0.8}Co_{0.15}Al_{0.05}O_2$ Cathode Material and Its Electrochemical Behaviors," *The Journal of Physical Chemistry C*, vol. 120, no. 6, pp. 3235–3241, 2016.

[82] D. Y. Wan, Z. Y. Fan, Y. X. Dong et al., "Effect of metal (Mn, Ti) doping on NCA cathode materials for lithium ion batteries," *Journal of Nanomaterials*, vol. 2018, 9 pages, 2018.

[83] Q. Q. Qiu, Z. Shadike, Q. C. Wang et al., "Improving the electrochemical performance and structural stability of the $LiNi_{0.8}Co_{0.15}Al_{0.05}O_2$ cathode material at high-voltage charging through Ti substitution," *ACS Applied Materials & Interfaces*, vol. 11, no. 26, pp. 23213–23221, 2019.

[84] R. Fang, W. Xiao, C. Miao et al., "Fabrication of Si-SiO_2@-Fe/NC composite from industrial waste AlSiFe powders as high stability anodes for lithium ion batteries," *Electrochimica Acta*, vol. 324, pp. 134860–134869, 2019.

[85] F. Du, R. Chen, Y. Zhuang et al., "Effect of substitution of cobalt with iron on electrochemical behavior and solid electrolyte interface of $LiNi_{0.8}Co_{0.15}Al_{0.05}O_2$," *Applied Surface Science*, vol. 484, pp. 374–382, 2019.

[86] B. Huang, X. Li, Z. Wang, H. Guo, and X. Xiong, "Synthesis of Mg-doped $LiNi_{0.8}Co_{0.15}Al_{0.05}O_2$ oxide and its electrochemical behavior in high-voltage lithium-ion batteries," *Ceramics International*, vol. 40, no. 8, pp. 13223–13230, 2014.

[87] W. S. Yoon, K. Y. Chung, J. McBreen, and X. Q. Yang, "A comparative study on structural changes of $LiCo_{1/3}Ni_{1/3}Mn_{1/3}O_2$ and $LiNi_{0.8}Co_{0.15}Al_{0.05}O_2$ during first charge using in situ XRD," *Electrochemistry Communications*, vol. 8, no. 8, pp. 1257–1262, 2006.

[88] Y. Y. Wang, Y. Y. Sun, S. Liu, G. R. Li, and X. P. Gao, "Na-doped $LiNi_{0.8}Co_{0.15}Al_{0.05}O_2$ with excellent stability of both capacity and potential as cathode materials for Li-ion batteries," *ACS Applied Energy Materials*, vol. 1, no. 8, pp. 3881–3889, 2018.

[89] H. Liu, M. Wolf, K. Karki et al., "Intergranular cracking as a major cause of long-term capacity fading of layered cathodes," *Nano Letters*, vol. 17, no. 6, pp. 3452–3457, 2017.

[90] Q. Li, G. Li, C. Fu, D. Luo, J. Fan, and L. Li, "K(+)-doped $Li_{1.2}Mn_{0.54}Co_{0.13}Ni_{0.13}O_2$: a novel cathode material with an enhanced cycling stability for lithium-ion batteries," *ACS Applied Materials & Interfaces*, vol. 6, no. 13, pp. 10330–10341, 2014.

[91] M. N. Ates, Q. Jia, A. Shah, A. Busnaina, S. Mukerjee, and K. M. Abraham, "Mitigation of layered to spinel conversion of a Li-rich layered metal oxide cathode material for Li-ion batteries," *Journal of the Electrochemical Society*, vol. 161, no. 3, pp. A290–A301, 2014.

[92] J. Zhao, Z. Wang, J. Wang et al., "Anchoring K^+in Li^+Sites of $LiNi_{0.8}Co_{0.15}Al_{0.05}O_2$ Cathode material to suppress its structural degradation during high-voltage cycling," *Energy Technology*, vol. 6, no. 12, pp. 2358–2366, 2018.

[93] L. Zhu, Y. Liu, W. Wu, X. Wu, W. Tang, and Y. Wu, "Surface fluorinated $LiNi_{0.8}Co_{0.15}Al_{0.05}O_2$as a positive electrode material for lithium ion batteries," *Journal of Materials Chemistry A*, vol. 3, no. 29, pp. 15156–15162, 2015.

[94] Y. Huang, S. D. Gong, R. Huang et al., "Polyhedral oligomeric silsesquioxane containing gel polymer electrolyte based on a PMMA matrix," *RSC Advances*, vol. 5, no. 57, pp. 45908–45918, 2015.

[95] X. Li, F. Kang, W. Shen, and X. Bai, "Improvement of structural stability and electrochemical activity of a cathode material $LiNi_{0.7}Co_{0.3}O_2$ by chlorine doping," *Electrochimica Acta*, vol. 53, no. 4, pp. 1761–1765, 2007.

[96] W. K. Kim, D. W. Han, W. H. Ryu, S. J. Lim, J. Y. Eom, and H. S. Kwon, "Effects of Cl doping on the structural and electrochemical properties of high voltage $LiMn_{1.5}Ni_{0.5}O_4$ cathode materials for Li-ion batteries," *Journal of Alloys and Compounds*, vol. 592, pp. 48–52, 2014.

[97] Y. Qi, Y. Huang, D. Jia, S. J. Bao, and Z. P. Guo, "Preparation and characterization of novel spinel $Li_4Ti_5O_{12-x}$ Br_x anode materials," *Electrochimica Acta*, vol. 54, no. 21, pp. 4772–4776, 2009.

[98] T. F. Yi, Y. R. Zhu, W. Tao, S. Luo, Y. Xie, and X. F. Li, "Recent advances in the research of $MLi_2Ti_6O_{14}$ (M = 2Na, Sr, Ba, Pb) anode materials for Li-ion batteries," *Journal of Power Sources*, vol. 399, pp. 26–41, 2018.

[99] Y. Yan, Y. X. Yin, S. Xin, Y. G. Guo, and L. J. Wan, "Ionothermal synthesis of sulfur-doped porous carbons hybridized with graphene as superior anode materials for lithium-ion batteries," *Chemical Communications*, vol. 48, no. 86, pp. 10663–10665, 2012.

[100] H. Z. Zhang, Q. Q. Qiao, G. R. Li, and X. P. Gao, "PO_4^{3-} polyanion-doping for stabilizing Li-rich layered oxides as cathode materials for advanced lithium-ion batteries," *Journal of Materials Chemistry A*, vol. 2, no. 20, pp. 7454–7460, 2014.

[101] S. He, A. Wei, W. Li et al., "An in-depth analysis detailing the structural and electrochemical properties within Br^- modified $LiNi_{0.815}Co_{0.15}A_{0.035}O_2$ (NCA) cathode material," *Electrochimica Acta*, vol. 318, pp. 362–373, 2019.

[102] T. Chen, X. Li, H. Wang et al., "The effect of gradient boracic polyanion-doping on structure, morphology, and cycling performance of Ni-rich $LiNi_{0.8}Co_{0.15}Al_{0.05}O_2$ cathode material," *Journal of Power Sources*, vol. 374, pp. 1–11, 2018.

Hindawi
International Journal of Photoenergy
Volume 2019, Article ID 3792942, 7 pages
https://doi.org/10.1155/2019/3792942

Research Article

Electrochemical Performance of Hybrid Cationic Aqueous-Based Rechargeable Battery with Different Current Collectors and Electrolytes

Shang Chen,[1] Fang Tang,[1] Ting He,[1] Huanhuan Zhang,[1] Shanshan Deng,[1] Yukang Li,[1] Xianwen Wu,[1] Qiaobao Zhang,[2,3] Yanhong Xiang,[4] and Wenbin Yan[1]

[1]*School of Chemistry and Chemical Engineering, Jishou University, Jishou Hunan 416000, China*
[2]*Key Laboratory of Testing Technology for Manufacturing Process, Southwest University of Science and Technology, Mianyang 621010, China*
[3]*Department of Materials Science and Engineering, College of Materials, Xiamen University, Xiamen 361005, China*
[4]*School of Physics, Mechanical and Electrical Engineering, Jishou University, Jishou 416000, China*

Correspondence should be addressed to Xianwen Wu; wxwcsu2011@163.com, Yanhong Xiang; 420228446@qq.com, and Wenbin Yan; jishouyanwenbin@163.com

Received 14 August 2019; Accepted 5 November 2019; Published 23 December 2019

Guest Editor: Yi Long

Different zinc foils as anode current collectors by electrowinning in various electrolytes with additives were prepared, which were evaluated through X-ray diffraction (XRD), scanning electron microscopy (SEM), float charge, and Tafel curve tests. The effect of different cathode current collectors, electrolytes, and the as-prepared zinc foils as the anode on the coulombic efficiency and the cycling performance of aqueous batteries were investigated. The results indicate that the initial coulombic efficiency and discharge capacity of the battery with 1 mol/L $ZnSO_4$ and 2 mol/L Li_2SO_4 are 94.31% and 105.7 mAh/g using graphite as the current collector, which are much higher than 68.20% and 71.0 mAh/g using conductive polyethylene, respectively, attributed to the smaller polarization and electrochemical transfer impedance (R_{ct}) of the former. However, the capacity retention of the latter is much higher than that of the former, especially using the high-concentration-lithium-based hybrid electrolyte, of which it is up to 74.63% even after 500 cycles. Moreover, the cycling performance of a battery with as-prepared zinc foil adding thiourea and gelatin into electrolyte during electrowinning is much better than that without additives, which is due to the smaller corrosion rate and side reaction.

1. Introduction

The energy problems have been paid more and more attention recently. All kinds of energy including solar energy have been developed [1–4]. Although lithium ion batteries (LIBs) based on organic electrolyte have gained great improvement as one of the most competitive energy conversion and storage systems with high energy/power density [5–7], their cost, safety, and large-rate charge/discharge characteristics are still the challenging issues which need to be solved in view of their large-scale use in electric vehicles and smart grids [8–13].

On the contrary, the aqueous rechargeable batteries are much safer and cheaper than LIBs since it was first proposed by Dahn's group in 1994 [14]. Many efforts have been made to improve the electrochemical performance, and a series of aqueous rechargeable battery systems have been constructed and investigated [15–18]. However, the aqueous rechargeable batteries at present still suffer from very poor cycling and rate performance due to the side reactions such as the serious oxygen evolution and so on. The main bottleneck for the practical application is associated with selection about the electrode materials.

In recent years, many studies have showed that zinc as the anode exhibits excellent reversibility, high overpotential for hydrogen evolution in a weak acidic environment. Based on the defects and limitations of aqueous rechargeable

lithium ion batteries (ARLIBs), a hybrid cationic aqueous-based rechargeable battery system based on lithium intercalation cathode with undoped $LiMn_2O_4$ and low equilibrium potential and low-cost zinc anode was first reported by Chen's group [19]. Since then, they have attracted increasing concerns about aqueous batteries [20, 21] and the similar systems such as $Na_{0.44}MnO_2$//Zn [22], $LiMnPO_4$//Zn [23], $LiCo_{1/3}Mn_{1/3}Ni_{1/3}PO_4$//Zn [24], and so on [25–28].

However, the hydrogen evolution, zinc corrosion, and zinc dendrite could not be ignored in the hybrid cationic aqueous-based rechargeable battery, which takes place as the side reaction in the anode. Wu et al. [29] studied the effect of different zinc anodes on the electrochemical performance in the previous report and found that the surface morphology of zinc anode could affect the cycling performance.

In this paper, the different zinc foils were prepared by adding different additives into the electrolyte during electrowinning. The structure, morphology, and corrosion performance of the zinc anodes were compared, and the float charge and the cycling performance of batteries were discussed. Meanwhile, the effect of different cathode current collectors and electrolytes on the coulombic efficiency and the cycling performance of the battery were studied systematically.

2. Experimental

Zinc foil was prepared by electrowinning under the following conditions, aluminum plate and lead plate were used as the cathode and anode, respectively, and 58 g/L Zn^{2+} and 150 g/L H_2SO_4 were used as the electrolyte, including some additives like thiourea (TU) and getatin (GL) in order to improve the morphology and the electrodeposition process of zinc.

The cathode electrode was prepared by casting slurries of $LiMn_2O_4$ (MTI Co.), KS-6 (Alfa Aesar Co.), and polyvinylidene fluoride (PVDF, Arkema Inc.) (86 : 7 : 7 wt.%) in N-methyl-2-pyrrolidinone (NMP, Sigma-Aldrich Co.) on graphite or conductive polyethylene (abbreviated for PE) foil (SGL Group Co.) and dried in a vacuum oven at 60°C for 6 h. The cathode electrode with disks of 14 mm diameter was cut and then soaked in electrolyte under vacuum for 10~15 min. The electrolyte was prepared by dissolving zinc sulfate and lithium sulfate (analytical grade from Aldrich) in deionized water and adjusting the solution of pH to 4. Similarly, the zinc foil was used as an anode current collector, and AGM (Absorbed Glass Mat, NSG Corporation) wet with the above electrolyte was used as a separator. Lastly, the galvanostatic charge-discharge test for coin-type batteries was performed with a battery tester (Land in China) in the potential range of 1.4~2.1 V at room temperature at 4 *C*-rate. The float charge performance was measured to investigate the side reaction based on the result of float charge current density. First, the battery was cycled for 3 times at 0.2 *C*-rate between 1.4 and 2.1 V and then charged to 2.1 V and the last charged at 2.1 V with the constant voltage for 24 h at 60°C.

The Tafel curve was used to evaluate the corrosion performance in a three-electrode system. The working electrode is zinc anode after electrowinning ($d = 5$ mm), the counter electrode is platinum wire ($d = 8$ mm), and the reference electrode is Hg/Hg_2SO_4.

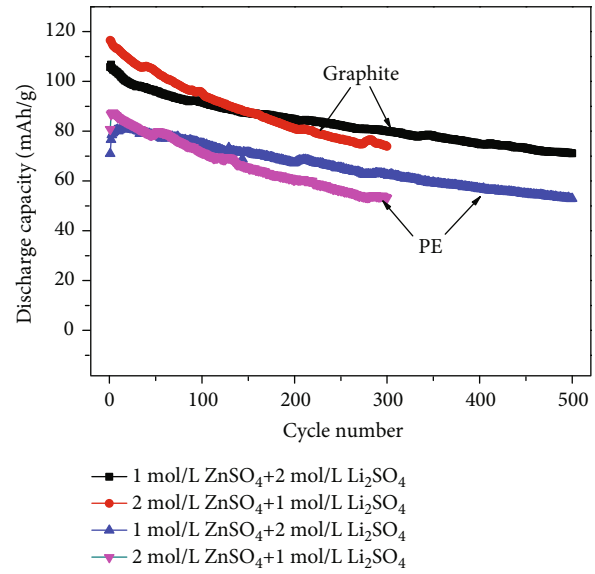

FIGURE 1: The cycling performance of $LiMn_2O_4$//Zn at 4 *C*-rate with different cathode current collectors.

To identify the phase constitutions, the as-prepared zinc foils were characterized by X-ray diffraction (XRD, D8 Discover, Bruker) employing Cu Kα ($\lambda = 0.15406$ nm) radiation from 20° to 90°. Field emission scanning electron microscopy (FE-SEM, Leo-1530, Zeiss) with an accelerating voltage of 20 kV was conducted to investigate the morphology of zinc foil after electrowinning.

3. Results and Discussion

3.1. Effect of Different Cathode Current Collectors and Electrolyte on the Electrochemical Performances. The charge/discharge performance of $LiMn_2O_4$//Zn at 4 *C*-rate with two different cathode current collectors was evaluated between 1.4 and 2.1 V at room temperature. Obviously, with the cycle number increasing as shown in Figure 1, the discharge capacity of the battery with the same electrolytes using graphite as the cathode current collector fades gradually, while the capacity of the battery using PE increases at the beginning and then decreases correspondingly. Meanwhile, the battery using graphite shows higher charge/discharge capacities than that with PE, and the initial charge/discharge capacities of the former with 1 mol/L $ZnSO_4$ and 2 mol/L Li_2SO_4 are 112.1 mAh/g and 105.7 mAh/g, respectively, with a capacity retention of 67.22% even after 500 cycles, while that of the latter delivers 104.0 mAh/g and 71.0 mAh/g, respectively, and the capacity retention is up to 74.63% after 500 cycles compared to the initial discharge capacity, indicating a much better cycling stability than the battery with graphite as the current collector. However, from Figure 2(a), it can be seen that the charge capacities of both batteries using graphite and PE with the same electrolyte are nearly the same, while the initial coulombic efficiencies are 94.31% and 68.20%,

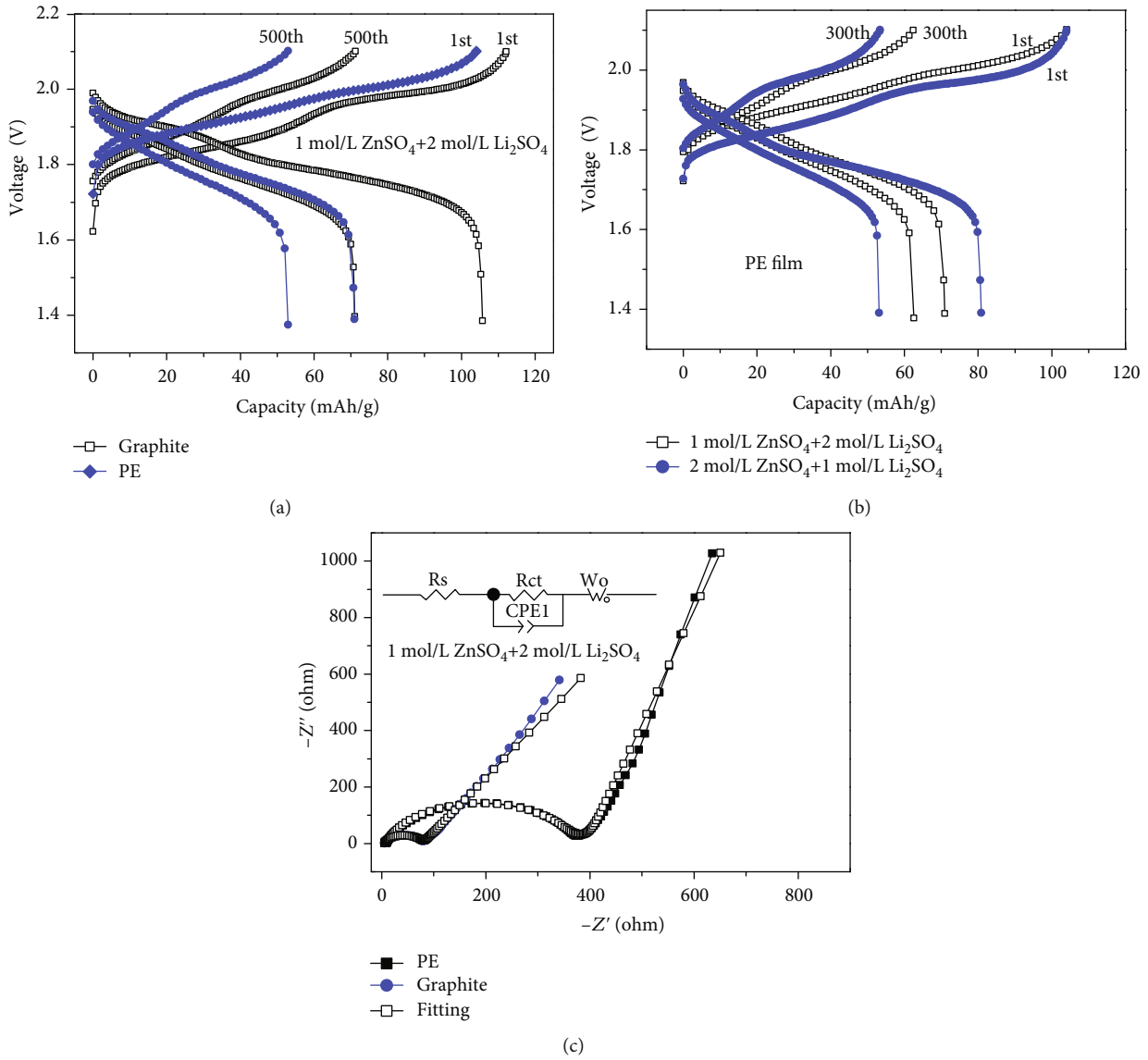

Figure 2: The charge/discharge curves of $LiMn_2O_4$//Zn at 4 C-rate (a) with different cathode current collectors (b) with different electrolytes and (c) EIS spectra before cycling.

respectively. That is to say, the increased coulombic efficiency is due to the higher discharge capacity of the battery with graphite. In addition, the charge/discharge plateau was compared to each other in Figure 2(a). The charge plateau of the battery using PE is much higher, while the discharge plateau is much lower than that using graphite, indicating the larger polarization for the former with PE. In order to further confirm this, the electrochemical impedance spectroscopy (EIS) measurements simulated by Zview 2.0 were performed for the batteries before cycling with 1 mol/L $ZnSO_4$ and 2 mol/L Li_2SO_4, and the parameter results are listed in Table 1. As can be seen from Figure 2(c), the curve consists of two parts, a semicircle at high frequency and a sloping line at low frequency. The semicircle corresponds to the charge transfer resistance (R_{ct}) and double layer capacitance (C_{dl}). The sloping line represents the Warburg impedance (Z_ω), which is related to the diffusion coefficient of Li^+ in the solid phase.

Table 1: Impedance parameters of equivalent circuit of $LiMn_2O_4$//Zn.

Current collector	R_s (Ω)	R_{ct} (Ω)
Graphite	4.787	74.57
PE	8.613	347.7

However, the R_{ct} is only 74.57 Ω for the battery with graphite, which is much smaller than that of 347.7 Ω with PE. The smaller polarization for the battery with graphite is mainly attributed to the smaller charge transfer resistance (R_{ct}) than that with PE.

Furthermore, the cycling performance and the charge-discharge curves of the batteries with different electrolytes are compared in Figures 1 and 2(b). When using the same cathode current collectors of PE, it delivers the higher initial

discharge capacity with high-concentration zinc-based electrolyte than that with high-concentration lithium-based electrolyte although the charge capacity is nearly the same, while the capacity retention of the former is much worse than the latter after 300 cycles, demonstrating the worse cycling stability, which is attributed to the high polarization with high-concentration zinc-based electrolyte. However, the coulombic efficiency of the former with 77.72% is much higher than the latter with 68.20%; the reason should be further investigated.

In fact, the charge-discharge mechanism is different from the traditional "rocking-chair" type battery [30, 31]. During the charge/discharge process, the hybrid lithium and zinc coexist in the electrolyte, and the lithium ions are deintercalated from the cathode of $LiMn_2O_4$ first and dissolved into the weak acid electrolyte, accompanied by releasing electrons. While zinc ions accept electrons from the external circuit, depositing onto the surface of a zinc current collector, of which the opposite process will take place during the discharge process. We note that the deposited material composition in the charge process is the same as the zinc current collector in the anode side. Previous research [29] indicates that it is easy for zinc to be corroded by acid electrolyte and the cycling performance of the battery with different surface morphologies of zinc is different. Herein, we prepared different zinc anodes by electrowinning below.

3.2. The XRD and SEM of Zinc during Electrowinning. Organic additives are most widely investigated for controlling the various qualities of electrowinning metal. It can usually reduce the grain size and change the morphology of deposited metals and the orientation growth of lattice plane using different additives. The reduction of grain size by different organic additives is mainly related to the synergistic effect [21]. Considering these, TU and GL have been used in this paper.

Figure 3 shows the XRD patterns of zinc foils. As can be seen, all peaks are indexed with that of the JCPDS 87-0713, and no impurity peaks can be found. However, compared with the electrowinning zinc from a sulfate solution containing 58 g/L Zn^{2+} and 150 g/L H_2SO_4 without additives, the (002), (100), and (101) peak intensity of zinc adding TU in the electrolyte has been increased a lot, which means that the preferred orientation of zinc particles happens in these planes after adding TU. Furthermore, XRD patterns of electrowinning zinc adding TU and GL have been characterized. To our surprise, the (002) plane has been inhibited to a certain extent, while the peak intensity of (100) and (101) has been increased continually. In order to find out the differences, SEM images of the electrowinning zinc have been tested, as indicated in Figure 4. The deposited zinc without additives is furry in Figure 4(a), which is due to the hydrogen evolution probably during the electrowinning. However, the zinc surface is very compact after adding the single GL in Figure 4(b), while the finest particles like leaves are formed due to the addition of GL in the electrolyte in Figure 4(c). As the mixture of TU and GL is added into the electrolyte in Figure 4(d), it shows a similar

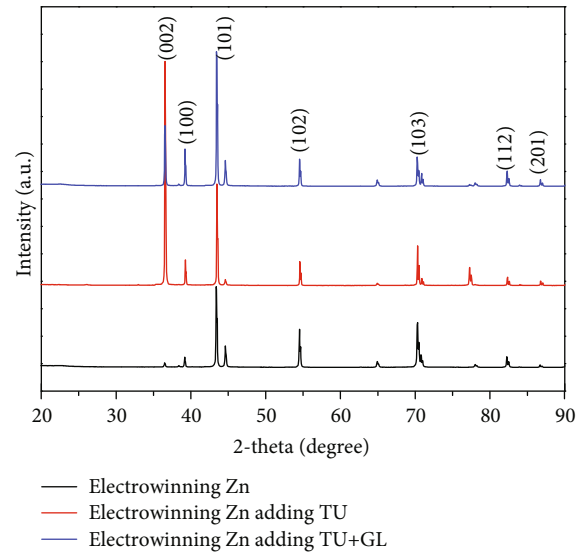

Figure 3: XRD patterns of zinc foil by electrowinning.

synergetic effect on the morphology, resulting in the smooth and compact zinc.

3.3. The Electrochemical Performance of Battery with Electrowinning Zinc. To further compare the difference of the zinc foils by electrowinning with or without mixed additives, galvanostatic charge/discharge was conducted between 1.4 and 2.1 V at 4 *C*-rate. As shown in Figure 5(a), there are two distinguished plateaus using the electrowinning zinc adding TU and GL that reflect two-stage Li-ion extraction/insertion behavior and are consistent with the previous reports [27]. In Figure 5(b), the capacity retentions after 300 cycles are 1.62%, 34.88%, and 45.63%, respectively, for three parallel batteries, of which the zinc current collectors were cut from the same piece of zinc foil by electrowinning from a sulfate solution containing 58 g/L Zn^{2+} and 150 g/L H_2SO_4 without additives in the electrolyte, and the consistency of the zinc is very bad. However, it is noted that the specific discharge capacity of the battery using electrowinning zinc adding TU and GL delivers 78.5 mAh/g after 300 cycles and the capacity retention is up to 70.88% with a much better stability.

A float charge test is used here for evaluating the side reactions of the battery; the float charge measurement with different electrowinning zinc was performed with 1 mol/L $ZnSO_4$ and 2 mol/L Li_2SO_4 as illustrated in Figure 6(a). Obviously, the float charge current densities are 13.0 and 9.5 mA/g for the battery using electrowinning zinc adding TU and GL compared with that without additives. Furthermore, the Tafel curves of different zinc current collectors were tested as shown in Figure 6(b). The corrosion potential (-1.427 V) of electrowinning zinc with mixed additives in the electrolyte in Table 2 is a little higher than that (-1.434 V) without additives, indicating that it is easy to be dissolved into the electrolyte for the former zinc, while the corrosion current (79.926 μA) of the former is much lower than the latter (2173.021 μA), which is consistent with the float charge result, demonstrating the smaller side reaction.

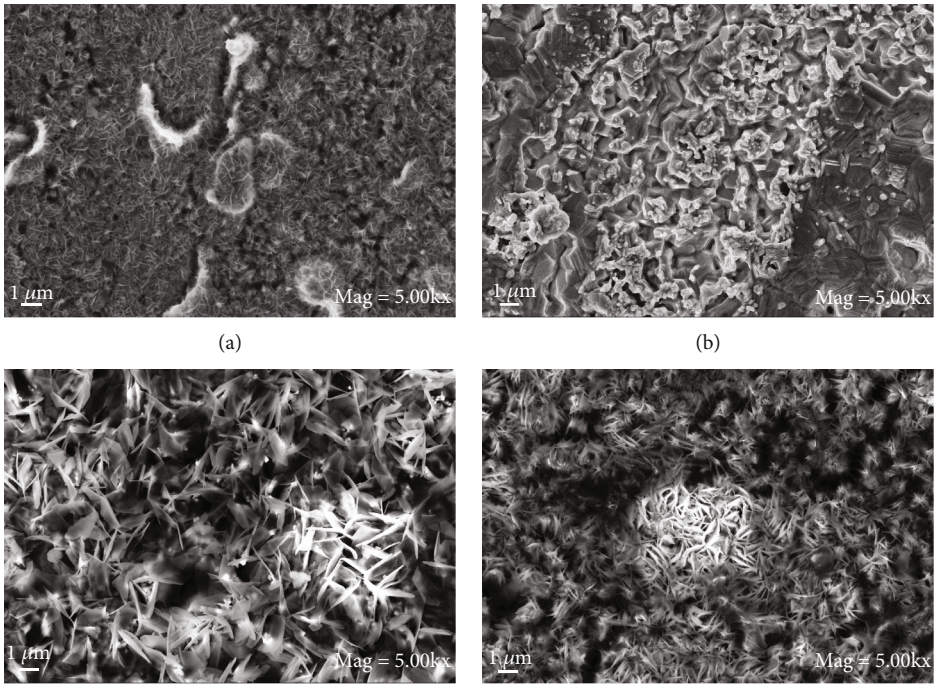

Figure 4: SEM images of zinc foils by electrowinning (a) without additives; (b) gelatin; (c) thiourea; (d) gelatin+thiourea.

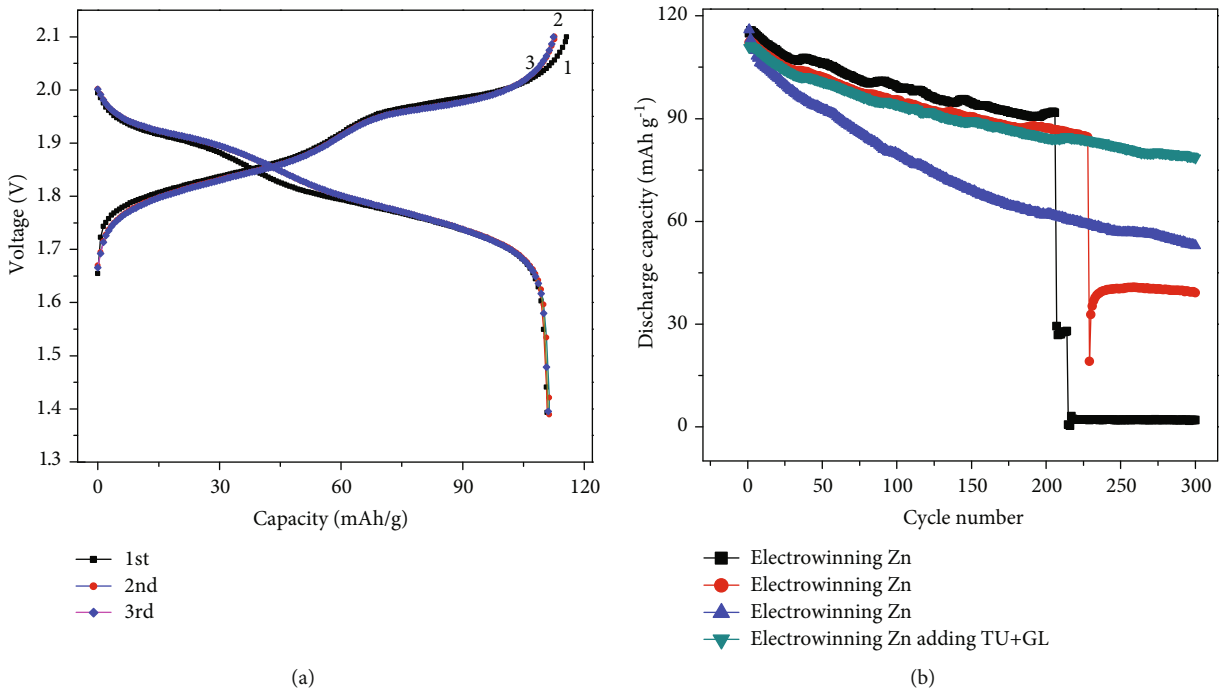

Figure 5: The cycling performance of $LiMn_2O_4$//Zn at 4 *C*-rate with different zinc foils by electrowinning as the anode.

4. Conclusions

The hybrid cationic aqueous battery based on Li^+ insertion/extraction at cathode and Zn^{2+} dissolution/deposition at anode is built up. It is found that graphite as the cathode current collector increases the initial coulombic efficiency and discharge capacity compared to that with PE, while high-concentration lithium-based hybrid electrolyte improve the cycling performance of the battery compared to that with high-concentration zinc-based hybrid electrolyte. The hybrid electrolyte additives improve the morphology of the zinc foil, furtherly improving the cycling performance of the battery.

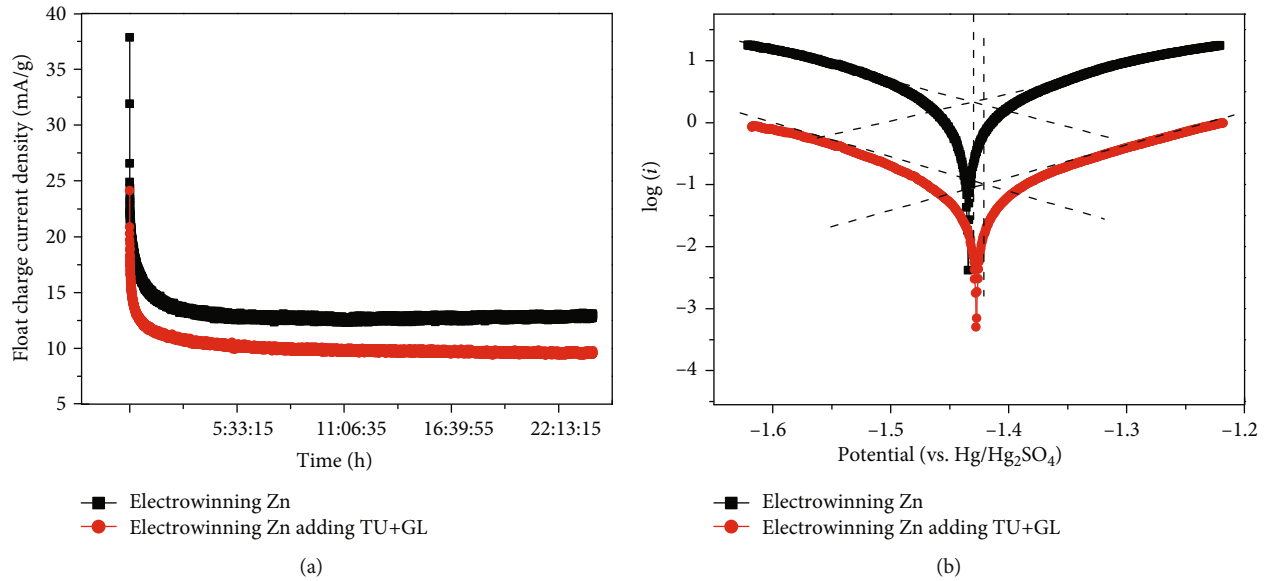

FIGURE 6: (a) The float charge process of $LiMn_2O_4$//Zn at 0.2 *C*-rate at high temperature and (b) the Tafel curves of different zinc current collectors by electrowinning with or without additives.

TABLE 2: The corrosion potential and corrosion current of different zinc foils.

	Corrosion potential (V)	Corrosion current (μA)
Electrowinning Zn	-1.434	2173.021
Electrowinning Zn adding additives	-1.427	79.926

The excellent reversibility and good cycling properties indicate that $LiMn_2O_4$//Zn based on hybrid aqueous electrolyte is a promising battery system for large-scale energy storage/conversion devices.

Data Availability

The data used to support the findings of this study are available from the corresponding author upon request. All of the data used to support the findings of this study are included within the article.

Conflicts of Interest

The authors declare that they have no conflicts of interest.

Authors' Contributions

Shang Chen and Fang Tang contributed equally to this work.

Acknowledgments

This research was financially supported by the Undergraduate Innovation Project of Hunan Province (No. S201910531033), the Opening Project of the Key Laboratory of Testing Technology for Manufacturing Process, Southwest University of Science and Technology (Grant No. 16kfzk02), the Natural Science Foundation of Hunan Province (Nos. 2018JJ3415 and 2018JJ34157), the Key Project of Hunan Province Education Department (No. 18A285), the Key Planned Science and Technology Project of Xiangxi Tujia and Miao Autonomous Prefecture (No. 2018GX2001), the Program of Young Talent Support of Huxiang in Hunan Province (2018RS3098), and the National Natural Science Foundation of China (Nos. 21566010, 51704124, and 51762017), which were greatly appreciated.

References

[1] C. Li, B. Xie, J. Chen, Z. He, Z. Chen, and Y. Long, "Emerging mineral-coupled composite phase change materials for thermal energy storage," *Energy Conversion and Management*, vol. 183, pp. 633–644, 2019.

[2] C. Li, B. Xie, D. Chen et al., "Ultrathin graphite sheets stabilized stearic acid as a composite phase change material for thermal energy storage," *Energy*, vol. 166, pp. 246–255, 2019.

[3] C. Li, B. Xie, Z. He, J. Chen, and Y. Long, "3D structure fungi-derived carbon stabilized stearic acid as a composite phase change material for thermal energy storage," *Renewable Energy*, vol. 140, pp. 862–873, 2019.

[4] C. Li, B. Zhang, B. Xie et al., "Stearic acid/expanded graphite as a composite phase change thermal energy storage material for tankless solar water heater," *Sustainable Cities and Society*, vol. 44, pp. 458–464, 2019.

[5] X. Wu, Y. Li, S. Zhao et al., "Fabrication of F-doped, C-coated $NiCo_2O_4$ nanocomposites and its electrochemical performances for lithium-ion batteries," *Solid State Ionics*, vol. 334, pp. 48–55, 2019.

[6] R. Li, W. Xiao, C. Miao, R. Fang, Z. Wang, and M. Zhang, "Sphere-like SnO_2/TiO_2 composites as high-performance anodes for lithium ion batteries," *Ceramics International*, vol. 45, no. 10, pp. 13530–13535, 2019.

[7] Y. Zhang, T. Ren, J. Zhang et al., "The role of boracic polyanion substitution on structure and high voltage electrochemical performance of Ni-Rich cathode materials for lithium ion batteries," *Journal of Alloys and Compounds*, vol. 805, pp. 1288–1296, 2019.

[8] S. Zheng, D. Liu, L. Tao et al., "Electrochemistry and redox characterization of rock-salt-type lithium metal oxides $Li_{1+z/3}Ni_{1/2-z/2}Ti_{1/2+z/6}O_2$ for Li-ion batteries," *Journal of Alloys and Compounds*, vol. 773, pp. 1–10, 2019.

[9] L. Wu, J. Zheng, L. Wang et al., "PPy-encapsulated SnS2 Nanosheets Stabilized by Defects on a TiO2 Support as a Durable Anode Material for Lithium-Ion Batteries," *Angewandte Chemie International Edition*, vol. 58, no. 3, pp. 811–815, 2019.

[10] L. Wu, Y. Hu, X. Zhang, J. Liu, X. Zhu, and S. Zhong, "Synthesis of carbon-coated Na_2MnPO_4F hollow spheres as a potential cathode material for Na-ion batteries," *Journal of Power Sources*, vol. 374, pp. 40–47, 2018.

[11] L. Wu, S. Shi, X. Zhang et al., "Room-temperature pre-reduction of spinning solution for the synthesis of $Na_3V_2(PO_4)_3$/C nanofibers as high-performance cathode materials for Na-ion batteries," *Electrochimica Acta*, vol. 274, pp. 233–241, 2018.

[12] J. Leng, Z. Wang, J. Wang et al., "Advances in nanostructures fabricated *via* spray pyrolysis and their applications in energy storage and conversion," *Chemical Society Reviews*, vol. 48, no. 11, pp. 3015–3072, 2019.

[13] J. Leng, Z. Wang, X. Li et al., "A novel dried plum-like yolk–shell architecture of tin oxide nanodots embedded into a carbon matrix: ultra-fast assembly and superior lithium storage properties," *Journal of Materials Chemistry A*, vol. 7, no. 10, pp. 5803–5810, 2019.

[14] W. Li, J. R. Dahn, and D. S. Wainwright, "Rechargeable lithium batteries with aqueous electrolytes," *Science*, vol. 264, no. 5162, pp. 1115–1118, 1994.

[15] S. Yang, M. Zhang, X. Wu et al., "The excellent electrochemical performances of $ZnMn_2O_4/Mn_2O_3$: the composite cathode material for potential aqueous zinc ion batteries," *Journal of Electroanalytical Chemistry*, vol. 832, pp. 69–74, 2019.

[16] Z. He, M. Li, Y. Li et al., "ZrO_2 nanoparticle embedded carbon nanofibers by electrospinning technique as advanced negative electrode materials for vanadium redox flow battery," *Electrochimica Acta*, vol. 309, pp. 166–176, 2019.

[17] X. Wu, Y. Xiang, Q. Peng et al., "green-low-cost rechargeable aqueous zinc-ion batteries using hollow porous spinel ZnMn2O4as the cathode material," *Journal of Materials Chemistry A*, vol. 5, no. 34, pp. 17990–17997, 2017.

[18] Z. Jiang, Y. Li, J. Zhu et al., "Synthesis and performance of a graphene decorated $NaTi_2(PO_4)_3$/C anode for aqueous lithium-ion batteries," *Journal of Alloys and Compounds*, vol. 791, pp. 176–183, 2019.

[19] J. Yan, J. Wang, H. Liu, Z. Bakenov, D. Gosselink, and P. Chen, "Rechargeable hybrid aqueous batteries," *Journal of Power Sources*, vol. 216, pp. 222–226, 2012.

[20] C. Lu, T. K. A. Hoang, T. N. L. Doan et al., "Rechargeable hybrid aqueous batteries using silica nanoparticle doped aqueous electrolytes," *Applied Energy*, vol. 170, pp. 58–64, 2016.

[21] K. E. K. Sun, T. K. A. Hoang, T. N. L. Doan et al., "Suppression of dendrite formation and corrosion on zinc anode of secondary aqueous batteries," *ACS Applied Materials & Interfaces*, vol. 9, no. 11, pp. 9681–9687, 2017.

[22] X. Wu, Y. Li, Y. Xiang et al., "The electrochemical performance of aqueous rechargeable battery of $Zn/Na_{0.44}MnO_2$ based on hybrid electrolyte," *Journal of Power Sources*, vol. 336, pp. 35–39, 2016.

[23] M. Minakshi, P. Singh, S. Thurgate, and K. Prince, "Electrochemical behavior of olivine-type $_{LiMnPO[sub\ 4]}$ in aqueous solutions," *Electrochemical and Solid-State Letters*, vol. 9, no. 10, pp. A471–A474, 2006.

[24] S. Kandhasamy, A. Pandey, and M. Minakshi, "Polyvinylpyrrolidone assisted sol-gel route $LiCo_{1/3}Mn_{1/3}Ni_{1/3}PO_4$ composite cathode for aqueous rechargeable battery," *Electrochimica Acta*, vol. 60, pp. 170–176, 2012.

[25] X. Zhu, X. Wu, T. N. L. Doan, Y. Tian, H. Zhao, and P. Chen, "Binder-free flexible $LiMn_2O_4$/carbon nanotube network as high power cathode for rechargeable hybrid aqueous battery," *Journal of Power Sources*, vol. 326, pp. 498–504, 2016.

[26] L. Shan, J. Zhou, M. Han et al., "Reversible Zn-driven reduction displacement reaction in aqueous zinc-ion battery," *Journal of Materials Chemistry A*, vol. 7, no. 13, pp. 7355–7359, 2019.

[27] L. Shan, J. Zhou, W. Zhang et al., "Highly reversible phase transition endows V6O13with enhanced performance as aqueous zinc-ion battery cathode," *Energy Technology*, vol. 7, no. 6, article 1900022, 2019.

[28] C. Li, X. Shi, S. Liang et al., "Spatially homogeneous copper foam as surface dendrite-free host for zinc metal anode," *Chemical Engineering Journal*, vol. 379, article 122248, p. 122248, 2020.

[29] X. Wu, Y. Li, C. Li et al., "The electrochemical performance improvement of $LiMn_2O_4$/Zn based on zinc foil as the current collector and thiourea as an electrolyte additive," *Journal of Power Sources*, vol. 300, pp. 453–459, 2015.

[30] Z. Liu, W. Peng, K. Shih et al., "A MoS_2 coating strategy to improve the comprehensive electrochemical performance of $LiVPO_4F$," *Journal of Power Sources*, vol. 315, pp. 294–301, 2016.

[31] Z. He, X. Wu, Z. Yi, X. Wang, and Y. Xiang, "Silicon/graphene/carbon hierarchical structure nanofibers for high performance lithium ion batteries," *Materials Letters*, vol. 200, pp. 128–131, 2017.